SUBTASK 4.8 – FATE AND CONTROL OF MERCURY AND TRACE ELEMENTS

Final Report

(for the period July 1, 2009, through December 31, 2011)

Prepared for:

AAD Document Control

U.S. Department of Energy
National Energy Technology Laboratory
626 Cochrans Mill Road
PO Box 10940, MS 921-107
Pittsburgh, PA 15236-0940

Cooperative Agreement No.: DE-FC26-08NT43291
DOE Technical Monitor: Andrew O'Palko

Prepared by:

John H. Pavlish
Nicholas B. Lentz
Christopher L. Martin
Nicholas V.C. Ralston
Ye Zhuang
Lucinda L. Hamre

Energy & Environmental Research Center
University of North Dakota
15 North 23rd Street, Stop 9018
Grand Forks, ND 58202-9018

2011-EERC-12-09 December 2011

DOE DISCLAIMER

ACKNOWLEDGMENT

This subtask was funded through the Energy & Environmental Research Center (EERC)–U.S. Department of Energy (DOE) National Energy Technology Laboratory Joint Program on Research and Development for Fossil Energy-Related Resources Cooperative Agreement No. DE-FC26-08NT43291. However, any opinions, findings, conclusions, or recommendations expressed herein are those of the authors(s) and do not necessarily reflect the views of DOE.

EERC DISCLAIMER

SUBTASK 4.8 – FATE AND CONTROL OF MERCURY AND TRACE ELEMENTS

ABSTRACT

The Center for Air Toxic Metals® (CATM®) Program at the Energy & Environmental Research Center (EERC) continues to focus on vital basic and applied research related to the fate, behavior, measurement, and control of trace metals, especially mercury, and the impact that these trace metals have on human health and the environment. For years, the CATM Program has maintained an international perspective, performing research and providing results that apply to both domestic and international audiences, with reports distributed in the United States and abroad. In addition to trace metals, CATM's research focuses on other related emissions and issues that impact trace metal releases to the environment, such as SO_x, NO_x, CO_2, ash, and wastewater streams. Of paramount interest and focus has been performing research that continues to enable the power and industrial sectors to operate in an environmentally responsible manner to meet regulatory standards.

The research funded by the U.S. Department of Energy's (DOE's) National Energy Technology Laboratory (NETL) through CATM has allowed significant strides to be made to gain a better understanding of trace metals and other emissions, improve sampling and measurement techniques, fill data gaps, address emerging technical issues, and develop/test control technologies that allow industry to cost-effectively meet regulatory standards.

The DOE NETL–CATM research specifically focused on the fate and control of mercury and trace elements in power systems that use CO_2 control technologies, such as oxycombustion and gasification systems, which are expected to be among those technologies that will be used to address climate change issues. In addition, research addressed data gaps for systems that use conventional and multipollutant control technologies, such as electrostatic precipitators, selective catalytic reduction units, flue gas desulfurization systems, and flue gas-conditioning methods, to understand mercury interactions, develop better control strategies and, in some cases, prevent mercury from being reemitted. This research also addressed stakeholder concerns and questions related to sampling and analytical methods for mercury, especially for continuous mercury monitors and sorbent trap methods for future compliance. Advancements were made toward the development of a much simpler dry-based method for measurement of halogens and trace metals. Finally, this research resulted in significant outcomes related to mercury and selenium concentrations in freshwater fish and how it is associated with other elements, thereby potentially impacting health; this has greatly enhanced the understanding of the second-order mechanism of mercury toxicity. The outcomes of this research have been shared with stakeholders in various domestic and international forums, working groups, conferences, educational settings, and published documents, with information available and accessible to those most impacted or interested in timely and current results on toxic metals.

This subtask was funded through the EERC–DOE Joint Program on Research and Development for Fossil Energy-Related Resources Cooperative Agreement No. DE-FC26-08NT43291.

TABLE OF CONTENTS

Continued…

TABLE OF CONTENTS (continued)

Continued….

TABLE OF CONTENTS (continued)

LIST OF FIGURES

Continued…

LIST OF FIGURES (continued)

Continued…

LIST OF FIGURES (continued)

Continued…

LIST OF FIGURES (continued)

Continued…

LIST OF FIGURES (continued)

Continued…

LIST OF FIGURES (continued)

LIST OF TABLES

Continued…

LIST OF TABLES (continued)

NOMENCLATURE

AA	atomic absorption
AC	activated carbon
ACI	activated carbon injection
AHPC	advanced hybrid particle collector
AHX	aluminum heat exchanger
AMC	amalgam corrosion
APH	air preheater
ARL	Analytical Research Laboratory
AS	activated site
ASTM	ASTM International
BAC	brominated activated carbon
CAPD	Coal Ash Properties Database
CATM	Center for Air Toxic Metals
CCOFA	close-coupled overfire air
CCP	coal combustion product
CCPS	coal combustion product sample
CCR	coal combustion residue
CCS	carbon capture and sequestration
CEM	continuous emission monitor
CID	collision-induced dissociation
CMM	continuous mercury monitor
COPC	constituents of potential concern
CS	consumed site
CTF	combustion test facility
CVAAS	cold-vapor atomic absorption spectrometer
CVAFS	cold-vapor atomic fluorescence spectrometer
Cys	cysteine
dNm^3	dry normalized cubic meter
DI	deionized
DOE	U.S. Department of Energy
DMA	direct mercury analyzer
EERC	Energy & Environmental Research Center
EGU	electric utility steam-generating units
EPA	U.S. Environmental Protection Agency
EPRI	Electric Power Research Institute
ESI	electrospray ionization
ESP	electrostatic precipitator
ESP-CS	cold-side electrostatic precipitator
FAMS	flue gas absorbent mercury speciation
FDA	Food and Drug Administration
FF	fabric filter
FGD	flue gas desulfurization
GFAA	graphite furnace atomic absorption

GSH	glutathione
GTI	Gas Technology Institute
HAG	high-acid gas
HAP	hazardous air pollutant
HCl	hydrochloric acid
HF	hydrofluoric acid
HPFBG	high-pressure fluidized-bed gasifier
IC	ion chromatograph
ICP–MS	inductively coupled plasma–mass spectrometry
ICR	information collection request (EPA's)
IGCC	integrated gasification combined cycle
IPCC	Intergovernmental Panel on Climate Change
LAG	low-acid gas
LC	liquid chromatography
LDDS	liquid desiccant dehumidification system
LEAF	Leaching Environmental Assessment Framework
LME	liquid metal embrittlement
LNB	low-nitrogen oxide burner
LOAEL	lowest observed adverse effect levels
LOI	loss on ignition
LTL	long-term leaching
M26A	EPA Method 26A (for halogens)
M29	EPA Method 29 (for multimetals)
M30b	EPA Method 30b (for mercury)
M5	EPA Method 5 (for particulates)
MACT	Maximum Achievable Control Technology
MDEA	methyldiethanolamine
MEA	monoethanolamine
ME-ST	multielement sorbent trap (method)
MFC	mass flow controller
MPCA	Minnesota Pollution Control Agency
MMBtu	million Btu
MS	mass spectrometry
MW	megawatt
NAS	National Academy of Sciences
NATA	National Air Toxics Assessment
NDIC	North Dakota Industrial Commission
NESHAP	National Emission Standards for Hazardous Air Pollutants
NETL	National Energy Technology Laboratory
NIST	National Institute of Standards and Technology
NOAA	National Oceanic and Atmospheric Administration
NOAEL	no observed adverse effect levels
NODA	Notice of Data Availability
NSPS	New Source Performance Standards
OFA	overfire air
OH	Ontario Hydro

ORD	Office of Research and Development
OSWER	Office of Solid Waste and Emergency Response
pc	pulverized coal
PM	particulate matter
PRB	Powder River Basin
PS	potential site
PTC	particulate test combustor
QA/QC	quality assurance/quality control
RFG	recirculation flue gas
ROS	reactive oxygen species
SAB	Science Advisory Board
SBC	sodium bicarbonate
SCR	selective catalytic reduction
SDA	spray dryer absorber
SEA	sorbent enhancement additive
Se-HBV	selenium-health benefit value
Sec	selenocysteine
SEM	scanning electron microscopy
Ser	serine
SGLP	synthentic groundwater leaching procedure
SOFA	separated overfire air
SOS	synergies of sequestration
SSTP	site-specific test plan
ST	sorbent trap
STAR	Science To Achieve Results
TBtu	trillion British thermal units
TCLP	toxicity characteristic leaching procedure
TVA	Tennessee Valley Authority
UND	University of North Dakota
UNEP	United Nations Environmental Programme
USGS	U.S. Geological Survey
XRF	x-ray fluorescence

SUBTASK 4.8 – FATE AND CONTROL OF MERCURY AND TRACE ELEMENTS

EXECUTIVE SUMMARY

To address current and future environmental issues and the needs of electric and energy production in the United States, the Energy & Environmental Research Center (EERC) established a Center for Air Toxic Metals® (CATM®) Program targeted at conducting research on air toxic metals, in particular mercury. As part of this program, the U.S. Department of Energy (DOE) provided funding to develop improved measurement and sampling methods, investigate transformation of metals in energy conversion systems, and develop and test control technologies that apply to both traditional and advanced combustion systems, with and without CO_2 cocontrol. Efforts were also focused on addressing ongoing environmental concerns related to mercury toxicity and potential impacts of trace metals in the environment. Research outcomes were communicated to regulatory bodies, commerce, government, industrial, and environmental groups as well as educational institutes.

Specific research activities focused on developing an understanding of and controlling mercury emissions in power systems that use CO_2 reduction technologies, understanding mercury behavior and controlling multiple trace metals concurrently in conventional and advanced systems, evaluating and developing better measurement and analytical methods for emerging power systems, developing a better understanding of the complex interactions between mercury and selenium and the mechanisms in toxicity and in freshwater fish, and ensuring that outreach and educational venues were effectively used to communicate research findings.

As the United States moves toward use of advanced energy systems and greenhouse gas control and reduction strategies (especially those that involve CO_2 control and sequestration), it is critical that sound scientific research be conducted. To address broad and emerging issues, the research focused on the following specific topics and activities.

ACTIVITY 1 – MANAGEMENT, REPORTING, AND EMERGING MERCURY STUDIES

Overall management of all research activities was performed under this activity, with direction provided on emerging issues. Quarterly and technical reporting were performed.

CATM research is guided by several means, including a Research Advisory Council (RAC) that provides input into research priorities, concepts, development of research needs, and feedback regarding emerging issues faced by power generators, industry, and the government. A RAC was maintained throughout, with the chair being a representative from DOE's National Energy Technology Laboratory (NETL).

ACTIVITY 2 – FATE AND CONTROL OF MERCURY AND TRACE ELEMENTS IN POWER SYSTEMS WITH CO_2 TECHNOLOGIES

Research in this area focused on gaining additional information related to mercury and trace metals in advanced and conventional power systems that target CO_2 reduction. The impact that CO_2 reduction technologies have on mercury behavior and control is unknown, but it is suspected to be significant as process conditions and configurations are significantly different compared to conventional power systems. Special emphasis on research within this activity focused on oxycombustion and near-commercial CO_2 control technologies, such as ZGCC and amine-based solvent that can be integrated into existing power systems.

Research was performed to validate mercury measurement techniques and to establish mercury partitioning in CO_2 control applications. In addition, Hg control technologies were also developed and evaluated in CO_2 control scenarios.

ACTIVITY 3 – FATE AND CONTROL OF MERCURY AND TRACE ELEMENTS IN POWER SYSTEMS WITH CONVENTIONAL AND MULTIPOLLUTANT CONTROL TECHNOLOGIES

Under this activity, the EERC continued to develop and test new and advanced technologies, including sorbents, for mercury and trace element control in power systems equipped with conventional and multipollutant emission control devices. These include power systems with individual or combinations of fabric filters, electrostatic precipitators (ESPs), selective catalytic reduction (SCR) units, wet and dry scrubbers, or other multipollutant technologies that can capture/reduce particulate, NO_x, SO_x, trace elements, etc. The likely issuance of a Maximum Achievable Control Technology (MACT) standard will require that all existing 1200-plus units in the United States now also meet Hg and trace element limits.

Areas that continue to provide challenges to mercury capture in conventional systems are those that either have concentrations of SO_3 that are naturally high because of transformation mechanisms within the system or that use SO_3 injection as a means of flue gas conditioning. Several approaches were pursued to improve the sorbent-based removal of mercury from these systems. A number of novel mercury sorbents were evaluated, and sorbent–mercury modeling was used to optimize performance of sorbent injection systems.

Another area of concern is mercury and trace element capture across systems with wet flue gas desulfurization (FGD) systems. Power plants burning high-sulfur coals are now required to install and operate FGD systems. EPA information collection request (ICR) data suggest that up to 95% mercury capture is possible if these plants are also equipped with SCRs. However, the actual level of capture is highly variable and site-specific, with many plants only able to achieve 60%–70% mercury removal because of insufficient mercury oxidation or reemission of mercury from the FGD slurry. Research focused on improving the retention of mercury in wet FGD systems and the resulting impact of these technologies on trace element separation from FGD wastewater.

The final area of emphasis within this activity concerns selenium control in conventional power plants. Selenium is the next most volatile trace element in coal following mercury, and while it is an essential micronutrient for life, selenium can be toxic at elevated concentrations. The liquid-phase release of selenium to the environment is already strictly controlled, and proposed EPA regulations for coal-fired power plants also include surrogate reductions for vapor-phase emissions. Like mercury and other trace elements of concern, the transport and capture of selenium within air pollution control devices is strongly dependent on the specific chemical species and its physical form. Research was conducted to evaluate the reactivity of selenium with conventional mercury sorbents and to consider the role of selenium's thermophysical properties on capture.

ACTIVITY 4 – DEVELOPMENT AND TESTING OF SAMPLING AND ANALYTICAL METHODS FOR MERCURY AND TRACE ELEMENTS

To support the research activities, the EERC evaluated, tested, and developed trace element measurement techniques that can be used in oxycombustion and advanced power systems.

ACTIVITY 5 – FATE OF MERCURY AND TRACE ELEMENTS IN THE ENVIRONMENT

Research in this area focused on addressing trace metal behavior in the environment and the stability of mercury in various natural conditions as well as environmental management of by-products produced from power systems. Research also focused on mercury–selenium interactions, with an emphasis on fish in freshwater lakes.

ACTIVITY 6 – EDUCATION AND OUTREACH

Key research findings were presented, communicated, and shared with regulatory bodies, commerce, government, industry, and environmental groups as well as educational institutes.

RESEARCH HIGHLIGHTS

Results and findings of research outcomes can be found throughout the report. Below are highlights of research outcomes and key findings for the research activities described above:

- Experimental data indicate that mercury measurements with continuous mercury monitors (CMMs) in flue gas with variable and/or highly concentrated CO_2 may require modifications. Highly concentrated CO_2 streams affect the accuracy of the mass flow rate and the subsequent gaseous mercury measurement, although this is specific to the type of CMM used.

- Mercury sampling data indicate that both CMM and sorbent trap methods are capable of providing accurate mercury measurement in a reducing syngas stream, while results of wet-chemistry methods such as U.S. Environmental Protection Agency (EPA) Method 29, show interference from reactions between syngas constituents and reagents used in the wet-chemistry sampling.

- Measurement of trace metals and halogens using Methods 29 and 26a, respectively, is cumbersome and costly. Shipping of hazardous chemicals and samples makes EPA reference methods hard to mobilize in the field. A novel multielement sorbent trap (ME-ST) method was developed by CATM that has lower detection limits and uses no hazardous chemicals. The ME-ST method is now under field evaluation.

- Mercury enrichment was observed during oxycombustion tests. Both the total amount of mercury increased as well as the form changed, implying control implications.

- Other than PM, the emission rates of most hazardous air pollutants (HAPs) are lower under oxycombustion conditions than those of air-blown combustion.

- Copper-based nanoscale sorbents show reasonable mercury capture in a reducing syngas stream.

- The applied model for calculating in-flight mercury capture with activated carbon (AC) was shown to qualitatively predict the limiting factors for mercury capture with a variety of coal flue gases. Furthermore, the insights provided by the sensitivity study of mercury capture result in optimization recommendations that are in agreement with those gained from field experience.

- The inorganic sorbents that were investigated for mercury control in flue gas appear to have reasonable reaction kinetics, but far less capacity for mercury capture than AC. Activation methods could be pursued in future work to increase the number of active sites on the sorbent.

- AC sorbents that were investigated because of their extreme physical toughness were found to have poor reactivity and limited active sites. These carbons perhaps may serve as novel catalyst supports but do not appear to be suitable mercury sorbents.

- Additives for preventing the reemission of elemental mercury in wet scrubbers were evaluated for their effect on mercury and selenium precipitation from the scrubber slurry. Their effects on mercury or selenium precipitation were small with a simulated slurry of $CaSO_4$; however, the EERC additive was observed to improve mercury precipitation under basic conditions with a $Ca(OH)_2$ slurry.

- The capture of flue gas selenium across wet scrubbers may be affected by the saturation properties of SeO_2/H_2SeO_3. Measurements of the SeO_2 saturation boundary show that the saturation limits for H_2SeO_3 can be exceeded in FGD systems that

quench the flue gas to temperatures below 180°F. This implies that some condensed selenium could slip through wet scrubbers in an analogous manner to SO_3/H_2SO_4.

- Measurements regarding selenium vapor interactions in flue gas suggest that vapor-phase control of selenium may be more difficult than for mercury. Selenium can be captured on AC; however, AC is generally not as efficient for selenium capture as it is for mercury.

- No mercury capture was seen across an amine scrubber used for CO_2 control. Steel coupon corrosion studies showed very little corrosion, with small amounts of monoethanolamine and mercury present in a CO_2–water vapor environment.

- While the EPA-approved method to assess leachability of trace elements in coal residuals is comprehensive, it is costly and complicated and requires very skilled personnel to avoid biases. For some residuals, sample conditions could not be maintained as prescribed by the method. The generation of titration pretest pH curves is a labor-intensive process that commonly does not accurately predict the leachate pH behavior of the reactive coal combustion products (CCPs). pH-dependent leaching tests from the leaching framework can provide information over a range of pH values. However, the data must be interpreted with regard the management of the CCP.

- Mercury emission control strategies can alter the total element concentrations of some elements in the CCPs, specifically arsenic, beryllium, fluoride, lead, manganese, mercury, and selenium. Many of the elements leached less than 5% of the total amount in the CCP. Several elements were not detected in any of the leaching tests performed on individual CCPs. Up to 60% of the total Se and S (measured as sulfate in the leachates) leached from the CCPs. The highest percentage of Se or S leached occurred in the pH range of 8–9.

- Hg can sequester Se, thereby creating the potential for toxicity within organisms. Sufficient data were obtained to posit a model that shows this interaction and the means of the second-order toxicity effect.

- The most important aspects of the seafood and freshwater fish consumption issue involve MeHg binding to Se, the molecular target of MeHg toxicity. Findings indicate that high MeHg accumulation in fish from certain lakes can result in high Hg:Se molar ratios that approach levels potentially associated with adverse health effects, especially in sensitive subpopulations of consumers. However, the relative percentage of water bodies in the United States that may contain fish that pose such risks appears to be quite low, probably less than 5% and possibly less than 2%.

- As a supplement to a parallel, but separate, project funded by the National Oceanic and Atmospheric Administration, a documentary on the health benefits of eating ocean fish, fact sheets, a brochure, and a Web site were created to supplement information provided in the documentary; this includes data from this project. Information was provided to the United Nations Environmental Programme mercury program on

mercury control technologies, which will be distributed worldwide. Research results were presented at numerous venues, and several peer-reviewed papers were published.

This subtask was funded through the EERC–DOE Joint Program on Research and Development for Fossil Energy-Related Resources, Cooperative Agreement No. DE-FC26-08NT43291.

SUBTASK 4.8 – FATE AND CONTROL OF MERCURY AND TRACE ELEMENTS

1.0 INTRODUCTION

In the United States, a real need exists to find viable and economical emission control technologies for trace metals to meet the requirements of the Clean Air Act Amendments and state-imposed legislation. The Energy & Environmental Research Center (EERC) has been fully involved in these discussions and in technology development and testing efforts for over 15 years, with a special emphasis on trace metal chemistry, especially for mercury.

The Center for Air Toxic Metals® (CATM®) Program at the EERC is respected as one of the world's premier mercury research centers, with a broad focus on vital basic and applied research related to the fate, behavior, measurement, and control of all trace metals and the impacts that these trace metals have on human health and the environment. In addition to trace metals, CATM's research focuses on other related emissions and issues that impact trace metal releases to the environment, such as SO_x, NO_x, CO_2, ash, and wastewater streams.

Of paramount concern has been the ability to meet regulatory standards and enable the power and industrial sectors to operate in an environmentally responsible manner; environmental research into trace metal behavior continues to be a driver in this domain, and CATM researchers have contributed significant findings in this area as well.

Over the course of CATM's research program, significant strides have been made to gain a better understanding of transformation of trace metals and their emissions and, ultimately, to enable development of control technologies In addition, over the past several years, CATM's research has contributed valuable insight into toxicity mechanisms, especially for mercury. As the United States moves forward on implementing regulations that have wide implications for our country, frameworks are being established for global environmental regulations, such as the binding global mercury rule that is being developed by the United Nations Environmental Programme (UNEP). Further work continues this year toward establishing the priorities and structure for this binding international treaty (1), with CATM's involvement in a working group to provide research into this venue. From the beginning, the CATM Program has maintained an international perspective, performing research and providing results that apply to both domestic and international audiences, with reports distributed in the United States and abroad.

The research presented in this report is in response to stakeholders who have a clear picture of the most pressing research needs. CATM's Director and researchers continue to have an ongoing dialogue with the research community and utility/industrial stakeholders to identify data gaps and technical questions that are yet to be addressed concerning the availability and effectiveness of control technologies, the atmospheric transport and deposition of different forms of trace metals, the ability to adequately and appropriately measure these forms for compliance and research purposes, and the ability to make decisions about environmental impacts of trace metals and other constituents in emissions from power and industrial systems.

CATM's current research continues to focus on the fate and control of mercury and trace elements in power systems that use CO_2 technologies, such as oxycombustion and gasification systems, which are expected to be among those technologies that will be used to address climate change issues. In addition, research continues to address data gaps for systems that use conventional and multipollutant control technologies, such as electrostatic precipitators (ESPs), selective catalytic reduction (SCR) units, flue gas desulfurization (FGD) systems, and flue gas-conditioning methods, to understand mercury interactions and develop better control strategies and, in some cases, prevent mercury from being reemitted. As many utilities and researchers have noted, significant questions remain in sampling and analytical methods for mercury, especially when continuous mercury monitor (CMM) and sorbent trap (ST) methods are used for future compliance testing. Finally, the fate of mercury and trace elements in the environment is an area that continues to require study to further the understanding of mercury in freshwater fish and how it is associated with other elements, thereby potentially impacting health.

Research under this project focused on the following specific topics and activities.

Activity 1 – Management, Reporting, and Emerging Mercury Studies. Overall management of all research activities was performed under this activity, with direction provided on emerging issues. Quarterly and technical reporting were performed.

CATM research is guided by several means, including a Research Advisory Council (RAC) that provides input into research priorities, concepts, development of research needs, and feedback regarding emerging issues faced by power generators, industry, and the government. A RAC was maintained throughout, with the chair being a representative from the U.S. Department of Energy's (DOE's) National Energy Technology Laboratory (NETL).

Activity 2 – Fate and Control of Mercury and Trace Elements in Power Systems with CO_2 Technologies. Research in this area focused on gaining additional information related to mercury and other trace metals in advanced and conventional power systems that target CO_2 reduction. The impact that CO_2 reduction technologies have on mercury behavior and control is unknown, but it is suspected to be significant as process conditions and configurations are significantly different compared to conventional power systems. Special emphasis on research within this activity focused on oxycombustion and near-commercial CO_2 control technologies that can be integrated into existing power systems.

One effort is to validate mercury-sampling technologies in a CO_2-enriched flue gas and characterize transformation and partitioning of mercury and other trace elements during oxygen-blown combustion. Another focus is to develop novel sorbents for mercury adsorption in a coal gasification process which is considered as an advanced power generation technology with low hazardous emissions and higher overall efficiency.

Chemically active agents, such as monoethanolamine (MEA) and methyldiethanolamine (MDEA), have been sucessfully applied in industry processes for CO_2 stripping. Research has been performed to characterize mercury species across the CO_2 stripping tower.

Details of this research are discussed in Section 4.0.

Activity 3 – Fate and Control of Mercury and Trace Elements in Power Systems with Conventional and Multipollutant Control Technologies. Under this activity, the EERC continued to develop and test new and advanced technologies, including sorbents, for mercury and trace element control in power systems equipped with conventional and multipollutant emission control devices. These include power systems with individual or combinations of fabric filters, electrostatic precipitators (ESPs), SCRs, wet and dry scrubbers, or other multipollutant technologies that can capture/reduce particulate, NO_x, SO_x, trace elements, etc. The likely issuance of a maximum achievable control technology (MACT) standard will require that all existing 1200-plus units in the United States now also meet Hg and trace element limits.

Areas that continue to provide challenges to mercury capture in conventional systems are those that either have concentrations of SO_3 that are naturally high because of transformation mechanisms within the system or that use SO_3 injection as a means of flue gas conditioning. Several approaches were pursued to improve the sorbent-based removal of mercury from these systems. A number of novel mercury sorbents were evaluated, and sorbent-mercury modeling was used to optimize performance of sorbent injection systems.

Another area of concern is mercury and trace element capture across systems with wet flue gas desulfurization (FGD) systems. Power plants burning high-sulfur coals are now required to install and operate FGD systems. EPA information collection request (ICR) data suggest that up to 95% mercury capture is possible if these plants are also equipped with SCRs. However, the actual level of capture is highly variable and site-specific, with many plants only able to achieve 60%–70% mercury removal because of insufficient mercury oxidation or reemission of mercury from the FGD slurry. Research focused on improving the retention of mercury in wet FGD systems and the resulting impact of these technologies on trace element separation from the FGD wastewater.

The final area of emphasis within this activity concerns selenium control in conventional power plants. Selenium is the next most volatile trace element in coal following mercury, and while it is an essential micronutrient for life, selenium can be toxic at elevated concentrations. The liquid-phase release of selenium to the environment is already strictly controlled, and proposed EPA regulations for coal-fired power plants also include surrogate reductions for vapor-phase emissions. Like mercury and other trace elements of concern, the transport and capture of selenium within air pollution control devices is strongly dependent on the specific chemical species and its physical form. Research was conducted to evaluate the reactivity of selenium with conventional mercury sorbents and to consider the role of selenium's thermophysical properties on capture.

Details of this research are discussed in Section 5.0.

Activity 4 – Development and Testing of Sampling and Analytical Methods for Mercury and Trace Elements. To support the research activities, the EERC evaluated, tested, and developed trace element measurement techniques that can be used in oxycombustion and advanced power systems. Details of this research are discussed in Section 6.0.

Activity 5 – Fate of Mercury and Trace Elements in the Environment. Research in this area focused on addressing trace metal behavior in the environment and the stability of mercury

in various natural conditions as well as environmental management of by-products produced from power systems. Research also focused on mercury–selenium interactions, with an emphasis on fish in freshwater lakes. Details of this research are discussed in Section 7.0.

Activity 6 – Education and Outreach. Key research findings were presented, communicated, and shared with regulatory bodies, commerce, government, industry, and environmental groups as well as educational institutes.

Reference

1. Mercury Coalition Urges World Governments to Negotiate Strong Treaty. *PR Newswire* [online]; Posted Oct 31, 2011, www.zeromercury.org (accessed Nov 9, 2011).

2.0 PROJECT BACKGROUND

Energy and chemical production and chemical-related environmental issues—especially as they pertain to toxic trace metals—have gained worldwide attention. To establish a strong sustained research program targeting critical, timely air toxic issues, in 1992, the CATM Program was established as one of the Centers of Excellence within the EERC. The base program was originally established with federal funding through EPA. The funding for the research reported here has been provided through DOE NETL Agreement No. DE-FC26-08NT43291.

A CATM Affiliates Program was established in 1993 to provide a parallel, but separate, program to direct CATM research with a focus on emerging needs of most importance to its members, who have traditionally been in power and industrial sectors. These projects are more narrowly focused on a specific issue or application, as is fitting for projects with commercial funding.

Since its establishment in 1992, CATM has used a multifaceted approach to answer many critical questions and continues to address issues related to toxic metal transformations and pathways; sampling, measurement, and analysis of toxic metal emissions; control technologies; computer modeling; and health risks related to toxic concentrations of trace metals. CATM takes a comprehensive "cradle-to-grave" approach to solve air toxic metal emission problems that includes putting this information in the hands of stakeholders through technology transfer, workshops, conferences, training material and courses, and support for general public outreach and education.

The research conducted through CATM has been considered, used, and cited by policymakers, industry leaders, researchers, conservationists, and academia to better understand the science of trace metals and to develop means to protect the environment and public health. The EERC's research has contributed to the body of science supporting federal and state rules and guidelines, new methods for measurement and analysis of trace metals, numerous control technologies related to mercury and other trace metals, and emerging health research to better understand the toxicity of mercury. Throughout the years, CATM has been a source of sound scientific information for the general scientific community, industry leaders, and the public to answer questions and provide results germane to trace metals.

Perhaps the most important function that CATM's researchers have provided, through previous funding and that provided by this project, are the thousands of responses to inquiries from a very diverse group of stakeholders regarding trace metal regulatory development, trace metal behavior, effective control strategies, potential economic costs of implementation, and other pressing matters. This feedback has taken many forms: one-on-one conversations, working groups, conference calls, and other forms of communication. It has been an inherent part of the CATM Program to provide information and direction to these stakeholders as they continue to search for answers to complex questions. CATM researchers have responded to thousands of inquiries from stakeholders who seek to evaluate and sift through reams of data, which often appear to conflict.

Through this ongoing dialogue, as well as participation in conferences, working groups, industrial meetings, research paper development and review, etc., CATM researchers have kept a focus on the emerging trace metal research needs that are most pressing to ensure that limited funds are directed to those issues that are likely to have the most impact to affected stakeholders.

Among the needs most often expressed to CATM researchers are a deeper understanding of trace metal behaviors, especially in advanced energy production systems and industrial flue gases; this need has become more urgent in light of pending regulation and the emphasis on technologies for CO_2 capture and sequestration (CCS), which is an area with significant data gaps. As regulatory measures move from discrete rules/laws that cover one specific emission to a multipollutant approach, greater attention is needed to development and application of approaches that concurrently lower several emissions in an economical way, with minimal negative impacts to downstream processes and equipment. New EPA regulatory emission limits are very low, meaning that there must be confidence in measurement and analytical techniques, as well as continued development of methods that have the potential to be adopted as alternate measurement methods by EPA and other regulatory agencies; those that can be used with greater confidence, flexibility, and speed and at a lower cost are especially needed. New and revised EPA emission limits also mean that wet FGDs will likely be installed on many more coal-fired electric generating units in the near future; understanding the mechanisms by which mercury is reemitted and preventing this phenomenon involve complex chemical reactions. Finally, as always, environmental and health impacts continue to be pressing needs.

CATM's research through this project has focused on providing sound data and technological advances in these areas.

3.0 PROGRAMMATIC STRUCTURE

To accomplish the long-term mission and overall goal of CATM, the EERC fosters partnerships through relationships with industry, academia, and government to perform multidisciplinary, multiclient research. CATM is at the focal point or hub of these partnerships, which are key to an effective research and development program.

CATM is structured to leverage complementary research performed throughout the EERC to leverage funding and to gather additional trace metal research from projects that have a different focus. Figure 3-1 illustrates the interactive nature of the stakeholders involved in the CATM base program and the separate, parallel CATM Affiliates Program as reflected over the course of this project. Industry cost-share projects shown are just a few of the hundreds of projects that have been conducted in connection with the CATM Program and complementary research at the EERC.

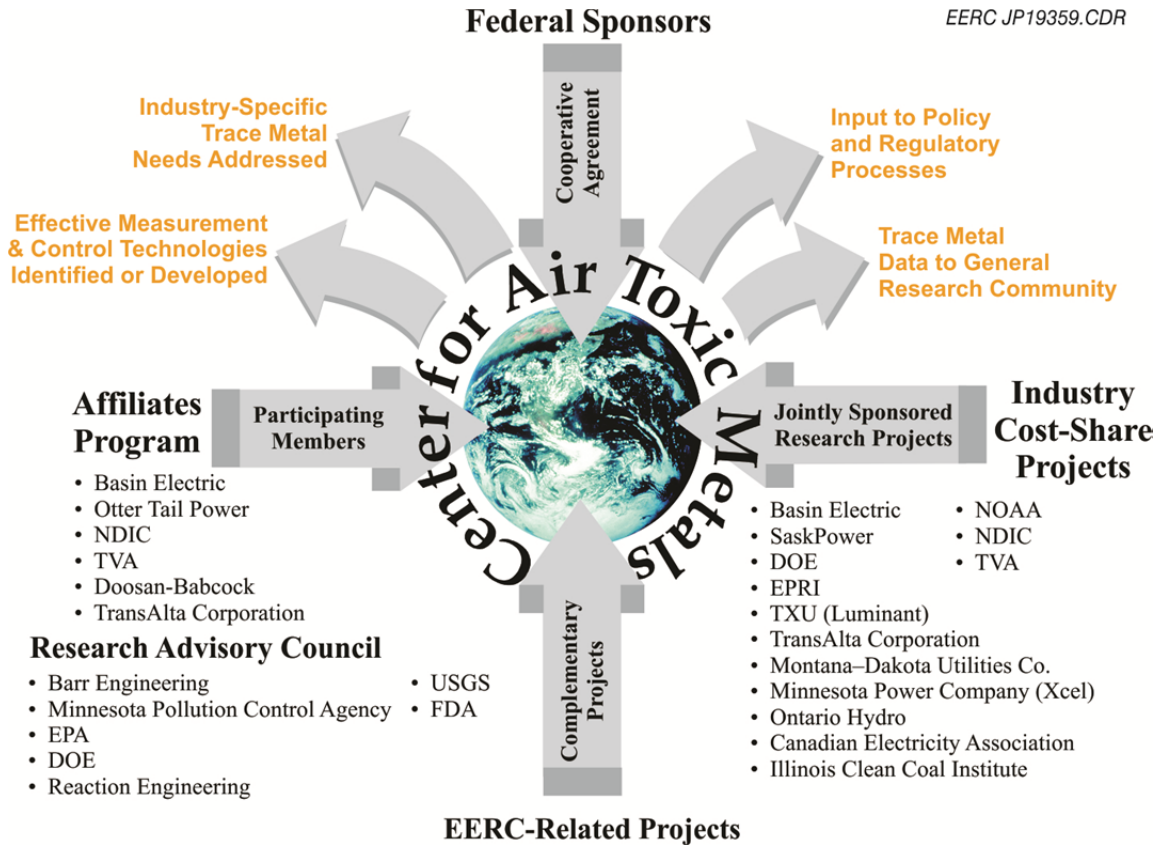

Figure 3-1. CATM's multiclient program is at the focal point of its research (abbreviations are as follows: NDIC = North Dakota Industrial Commission, TVA = Tennessee Valley Authority, USGS = U.S. Geological Survey, FDA = Food and Drug Administration, NOAA = National Oceanic and Atmospheric Administration, and EPRI = Electric Power Research Institute).

The CATM base program has been funded by EPA and DOE directly (currently under Agreement No. DE-FC26-08NT43291) and many entities, both public and private, in the past and is expected to continue to have a varied base of support.

The CATM Affiliates Program typically funds smaller, more focused, discrete projects that more closely meet the needs of industry; Affiliate support allows leveraging of partner membership funds against other public and private funding sources that require matching funds. This could include matching funds for established federal programs at the EERC or for various solicitations funded by state and private industry. Affiliate memberships also provide funding for small projects to meet emerging needs throughout the year.

CATM has two important committees that, on an ongoing basis, provide a partnership that is focused on pollution prevention, control technologies, and related environmental issues. This coordinated partnership is known as CATM's Research Advisory Council and comprises the Partners Advisory Committee and the Science Advisory Committee:

- The Partners Advisory Committee comprises Affiliate members, bringing acute awareness of the needs of industry, and the Project Manager from the federal agency that funds CATM's base program; together, these partners have been key in establishing priorities and overseeing research progress.

- The Science Advisory Committee, which comprises experts from industry, government, and academia, provides regulatory and scientific feedback, shares information regarding issues and research conducted by other organizations, and provides formative peer critique of the research approach and outcomes of the CATM Program. This committee has ensured that the research activities identified and conducted through CATM are scientifically valid, have a strong experimental plan, utilize appropriate analytical techniques, and meet overall quality control guidelines.

To support the mission of CATM, the program is managed as follows and has a focus on the following research areas:

- *Research Area 1, Transformation Mechanisms – Dr. Ye Zhuang, Program Area Manager*. Research in this area focuses on developing an in-depth understanding of the fate and transformation of trace metals throughout industrial processes and energy conversion systems, including theoretical, mechanistic, and applied explanations and predictions.

- *Research Area 2, Sampling and Analytical Methods – Dr. Nicholas Lentz, Program Area Manager*. Research in this area focuses on developing sampling and measurement techniques that are valid, reliable, and able to meet the measurement limits needed for scientific study and regulatory compliance.

- *Research Area 3, Control Technologies – Dr. Christopher Martin, Program Area Manager*. Research in this area is focused on developing novel and effective capture

technologies to reduce emissions from industrial processes and energy conversion systems, with a goal of technologies that are commercialized.

- *Research Area 4, Environmental and Health Effects – Dr. Nicholas Ralston, Program Area Manager*. Research in this area is focused on developing an understanding of the interrelationship that exists between emissions from industrial processes and energy conversion systems and their effect on the environment and/or health.

- *Research Area 5, Technology Commercialization and Education – Mr. John Pavlish, Program Area Manager*. Through this area, CATM research is disseminated within the United States and internationally through various venues, such as conferences, peer-reviewed journals, newsletters, etc. Technology partners are sought to commercialize technologies developed throughout the CATM Program.

NOTE: Further information regarding CATM's goals, structure, past research, and downloadable reports, newsletters, etc., can be obtained at www.undeerc.org/catm.

CATM uses a cradle-to-grave approach to solve scientific and environmental issues related to the production of energy and industrial processes. As mentioned above, research priorities are identified and refined through interaction with numerous levels of stakeholders and scientific personnel. For this project, CATM's research addressed the following high-level goals:

- Further the current understanding of the behavior and fate of potentially toxic elements and other related emissions.

- Develop advanced sampling and analytical methods to accurately measure toxic elements of low concentrations in challenging and under real-world conditions.

- Predict the fate of toxic elements of concern, and address environmental and operational issues related to these elements.

- Evaluate existing and develop new control technologies that are cost-effective to enable industries to meet regulatory standards and/or to address operational issues/limitations.

- Investigate the environmental and health impacts of various releases to the environment.

- Inform funding agencies, the general research community, regulatory bodies, and the public and contextualize many of the "hot topics" pertaining to trace metals and other elements.

- Keep stakeholders informed of CATM progress and results through various means, and seek feedback regarding emerging research needs.

4.0 FATE AND CONTROL OF MERCURY AND TRACE ELEMENTS IN POWER SYSTEMS WITH CO_2 TECHNOLOGIES

4.1 Background

Environmental concerns over rising CO_2 concentrations in the Earth's atmosphere are driving efforts to reduce anthropogenic emissions of CO_2. Currently, levels of CO_2 are over 30% higher than preindustrial levels (~280 ppm). The Intergovernmental Panel on Climate Change (IPCC) indicated that atmospheric CO_2 will be double the preindustrial level by the end of the 21st century based on the current trajectory of energy usage and carbon emissions. Approximately three-fourths of the increase in atmospheric CO_2 is attributable to burning fossil fuels (1).

Public awareness and regulation have imposed pressure on various industries to seek effective ways to reduce their emissions of CO_2. Incremental reductions of CO_2 emissions can be achieved by improving power plant efficiency and increasing the use of gas combined-cycle combustion systems, Meanwhile, greenhouse gas emissions from energy production can be reduced by the use of alternative energy sources, including nuclear power and renewable energy. However, until these sources can reliably produce significant amounts of energy, the immediate energy demand is likely to be met by conventional fossil fuel combustion.

4.1.1 Oxycombustion

In order to attain a significant reduction in CO_2 emissions, direct capture and sequestration of CO_2 from fossil fuel combustion is necessary (2). Technologies that have been developed for CCS include postcombustion capture using liquid solvent and solid sorbents, integrated gasification combined cycle followed by CO_2 capture, oxygen combustion (referred to as oxycombustion or oxyfuel combustion) with recycle flue gas, and chemical looping using an oxidant intermediate to oxidize fuel. Among these, oxycombustion is considered one of the most promising technologies for coal-fired power plants, since its cost potentially could be less than, or comparable to, that of conventional air-fired combustion with amine-based CO_2 capture (3–4).

The basic principle of oxycombustion is to burn coal in a mixture of oxygen and recycled flue gas. The produced flue gas is composed primarily of CO_2, H_2O, and small quantities of O_2, Ar, N_2, and trace gases, like SO_2 and NO_x. The CO_2-rich gas is then cooled to remove water and is directly compressed for CO_2 sequestration—no CO_2 separation is required.

The characteristics of oxycombustion are different from that of air-blown conventional combustion because of higher CO_2 levels and flue gas recirculation. Coal devolatilization in an O_2/CO_2 environment such as oxycombustion was reported to be greater than in an O_2/N_2 environment typical of conventional air combustion because of char gasification by CO_2 (5), and significant CO oxidation was observed in the boundary layer at higher oxygen levels and higher char combustion temperatures (6). Approximately 30% O_2 is needed to maintain an adiabatic flame temperature similar to conventional air combustion. Heat transfer in an oxycombustion system is expected to be different from air-blown combustion because of the changed emissivity and heat capacity of flue gas (2), although pilot-scale testing data indicate that, by adjusting

burner hardware and oxygen input, combustion performance comparable to air firing can be obtained, while heat absorption in the boiler and convection pass is maintained similar to air-blown combustion (7).

Formation of gaseous emissions also changes during oxycombustion. NO_x emissions from oxycombustion systems can be reduced to less than one-third that of combustion in air (8–9), which can be ascribed to 1) reduced thermal NO_x formation because of the elimination of atmospheric nitrogen, 2) reduction of recycled NO_x as it is reburned in the volatile matter release region of the flame (10), and 3) reaction between recycled NO_x and char (11).

SO_2 concentrations in oxycombustion flue gas are known to be higher than those with air combustion because of flue gas recirculation, which enhances sulfur retention by fly ash and results in decreased SO_2 emissions per unit of energy of the fuel combusted (9, 12). Meanwhile, model simulations indicate that SO_3 concentrations are about four times greater than the concentrations seen in conventional air firing (13).

In addition, mercury, another toxic air pollutant that has been regulated by EPA, has not been fully investigated for its transformation mechanisms and ultimate fate in oxycombustion conditions. It is well known that mercury causes corrosion of metal through embrittlement and could cause significant damage to CO_2-processing units (14). As a result of changed flue gas characteristics, including constituents and time–temperature profiles during oxycombustion, mercury transformations are likely to be very different from those in conventional air combustion. Limited, and somewhat questionable, data on mercury speciation in oxycombustion conditions have been published. Experimental data indicate that elevated CO_2 concentrations potentially enhance mercury retention on fly ash, while high O_2 concentrations may promote mercury vaporization and emission (15). Additional mercury oxidation has been observed in oxycombustion as a result of mercury chlorination (16). Besides expected changes in mercury transformations in oxycombustion, existing sampling methodology also needs to be validated, and additional modifications may be needed to mercury-sampling systems in order to ensure unbiased measurement of mercury speciation in oxycombustion flue gas.

To fully understand transformation and partitioning of mercury and other trace elements during oxygen-blown combustion, the EERC performed a series of experimental studies to 1) evaluate the measurement validity of CMMs in a simulated oxycombustion flue gas with varied CO_2 concentrations and 2) investigate mercury transformation in actual oxy–coal combustion with flue gas recirculation.

4.1.2 Coal Gasification

Coal gasification technology, in particular integrated gasification combined cycle (IGCC), is considered an advanced power generation technology that can offer many advantages over conventional power system, including 1) low emissions of various air pollutants, such as sulfur compounds; 2) higher overall efficiency approaching 40%–45%; and 3) lower water requirements. However, because of limited full-scale applications, most mercury-related studies have focused on understanding mercury–flue gas chemistry and developing corresponding mercury control strategies for conventional coal combustion scenarios.

In the process of compression, in these systems, deposition of liquid Hg^0 in gasification equipment, such as aluminum heat exchangers (AHXs), can compromise their structural integrity. One mechanism by which this can occur is referred to as liquid metal embrittlement (LME), which has been responsible for a number of failures of aluminum equipment in the gas-processing industry over the past 30 years. A second mechanism by which mercury can attack aluminum is amalgam corrosion (AMC), which requires both mercury and water in order to oxidize and, thus, degrade aluminum equipment. Up to now, there are limited data, yet growing research efforts have pursued a better understanding of mercury behavior in these environments to develop control technologies applicable to advanced power systems, such as coal gasification systems.

Through years of research, it is widely agreed that mercury in coal is expected to be totally vaporized during the gasification process.

One possible reaction scheme was proposed by Sekine et al. (17):

1. Hg in coal reacts with steam to form $Hg(OH)_2$
2. $Hg(OH)_2$ changes to HgO by heating
3. HgO decomposes to Hg and O_2 at 500°C

Extensive thermodynamic calculations (18–21) suggest that all vaporized mercury should be in the form of $Hg^0_{(g)}$ that is stable in typical reducing syngas from a coal gasifier and HgS could only be formed at temperatures below 50°C (22). Bench-scale experiments indicate that fly ash may have the capability to promote heterogeneous mercury oxidation in reducing syngas environments, depending on the reaction temperature and flue gas composition: mercury capture on model fly ash increased from 55% at 250°C to 92% at 750°C (23). An experimental study by Reed et al. (22) suggested that carbonaceous dust can efficiently capture mercury on a hot filter surface that was maintained below 200°C. On the other hand, the investigation done by Meij (24) indicated that there was no evidence of any significant Hg removal at a hot-gas filter temperature of 580°C.

Data on mercury emission in full-scale coal gasification systems are limited, since only a few systems of this scale are in operation. The EPA information collection request (ICR) (25) data showed ~60% of the mercury was emitted at the stack during coal gasification, mostly in the elemental form (26). Mercury stack emission measured at two large-scale IGCC power plants—Polk Power Plant and Wabash Power Plant—indicated ~74%–92% Hg^0, while the mercury mass balance was in the range of 58%–67% (27). Mercury sampling data on a full-scale coal gasifier at Sasol showed that mercury was predominantly associated with the crude gas stream, with a small portion associated with the ash fraction, and less to the liquid hydrocarbon coproduction fractions (28). The low mass balance values in mercury speciation data from full-scale gasification systems are ascribed to the problem associated with mercury sampling in pressurized reducing environments. Measurement uncertainties suggest that research effort is needed to establish a validated mercury-sampling protocol for coal gasification applications.

Sorbent-based control technologies are considered the most applicable for gasification applications since a relatively small volume of gas is treated, compared to the flue gas stream in

a conventional coal-fired boiler system The high pressure inherent in coal gasification systems also facilitates the use of fixed beds, which may be problematic in conventional combustion systems that have pressure drop limitations. Mercury capture in syngas can take place in a wide temperature range from 40° up to 540°C. Both standard AC and sulfur-impregnated AC beds can effectively capture mercury in syngas at temperatures below 150°C and provide fairly long-term mercury removal. For example, Gas Technology Institute (GTI) used a sulfur-impregnated sorbent to capture mercury in its syngas stream and attained 9.6 wt% of mercury in the packed sorbent after 18 months of operation (29). Eastman Chemical has reported 90%–95% mercury removal with sulfur-impregnated AC in cooled syngas at 50°C (30).

While cold-gas-cleaning technologies may offer effective removal of unwanted mercury, the overall efficiency of the systems is lowered when the flue gas is cooled to below 150°C. Sorbents that can remove mercury at elevated temperatures preserve the high thermal efficiency of the gasification system and will become a potential option for mercury capture in the near term. Unfortunately, mercury reduction in hot flue gas >540°C presents many challenges mainly because mercury is likely to exist in the difficult-to-capture elemental form under the reducing conditions of coal gasification (23, 31). Therefore, research has more recently focused on warm-gas cleanup, with temperatures ranging from 150° to 370°C.

Many sorbents, such as ACs, metal oxides, metal sulfides, and metals, have been tested at elevated temperatures. Unpromoted carbon-based sorbents have shown poor capacities for mercury: only ~60 μg/g at 204°C in a nitrogen environment (32). Musich et al. (33) tested a treated granular carbon in syngas at 260°C, showing good capture but with short breakthrough times and subsequent desorption.

Metal sorbents have received extensive attention since an amalgam could be formed between metal and mercury at elevated temperatures. Theoretical calculations (34) indicated that the interaction of noble metals with mercury increases in the order Ag > Au > Cu > Ni > Pt > Pd, and the binding is strongest when the mercury occupies fourfold hollow sites in one of the faces of the crystal structure. The capture mechanism for these metals is formation of an alloy or amalgam, where the mercury is not converted to a higher oxidation state because of little charge transfer from the Hg to metal matrix, but rather binding results from a small amount of charge transfer to provide a metallic type of bonding with delocalized electrons in conduction bands. The transfer of charge from Hg to the metal is higher for Pt and Pd, giving stronger binding (1 eV), and is least for Ag. Granite et al. (35) evaluated capacities of metal-based sorbents (Pd, Pt, and Ir) for Hg^0 capture in a simulated syngas in the temperature range of 204°–371°C. Palladium (5% palladium on alumina) demonstrated the highest mercury adsorption capacity of 900 μg/g at 288°C and could be partially regenerated by heating at 430°C. Poulston et al. (36) further indicated that Hg removal capacity of Pd increased with metal loading, although it decreased with sorbent temperature, possibly due to either deamalgamation or accelerated competitive adsorption of flue gas constituents at elevated temperatures.

Sugier and LaVilla patented the use of sulfided copper on a solid support, such as alumina, with a small amount of silver catalyst to capture mercury (37). The sorbent was used successfully for mercury capture in natural gas–steam mixtures at 35 bar but was not tested in hydrogen. Elevated temperatures and reducing environments have proven to be challenging and will need

significantly more research to arrive at acceptable mercury control strategies with reasonable cost.

CO_2 capture from plants of conventional pulverized fuel technology with scrubbing of the flue gas for CO_2 removal is another important approach for CO_2 reduction. Chemically active agents, such as monoethanolamine (MEA) and methyldiethanolamine (MDEA), are suited to the lean combustion CO_2 concentrations of flue gas but require a large amount of energy to regenerate the solvent (in the solvent stripper), this being as much as 80% of the total energy of the process. Interactions between the CO_2 capture system and the control of other emissions, such as acid gases, are observed. SO_2 and NO_2 react with MEA to form heat-stable salts that reduce the CO_2 absorption capacity of the solvent. Gas cleaning to 10-ppm levels is desirable to avoid the loss of costly solvent (38). However, no data regarding mercury species across the amine scrubber have been reported.

Another issue for CO_2 capture with amine-based solvent is equipment corrosion, which has long been a problem in refineries and gas plants. Corrosion in amine systems is usually produced by carbon dioxide and hydrogen sulfide in gas systems as well as from heat-stable salts produced by amine degradation rather than by the amine itself (39). The corrosion mechanism within the amine absorber and stripper columns is relatively well understood, while corrosion downstream of the amine stripper before the CO_2 compression step where the environment is at a relatively low temperature, an essentially pure CO_2 stream saturated with water vapor, with the possible presence of tens of ppm elemental mercury, is not well studied. Corrosion by CO_2 itself has been studied at much higher temperatures (900°–1000°C [1690°–1870°F]) (40).

Little information is available regarding the involvement of Hg in low-temperature corrosion. One set of experiments suggests that metallic mercury forms an amalgam with Fe, Cr, or Ni in stainless steel, with subsequent corrosion from liquid water catalyzed by the Hg (41). More research on Hg-induced corrosion on CO_2 reduction equipment is needed.

4.2 Objectives

Any CO_2 control technologies will most likely change characteristics of post combustion flue gas, such as the time–temperature profile, flue gas constituents, and their concentrations. Subsequently, these changes will affect transformation mechanisms of trace elements, including mercury and selenium; pose challenges for speciation measurement of elements of interest; and require the development of new control technologies for mercury reduction.

This activity addressed critical issues regarding measurement, physical/chemical transformations, and control technologies for mercury as CO_2 reduction strategies are applied to a power plant. Specific objectives include:

- Develop and validate mercury-sampling technologies in a coal flue gas with an elevated CO_2 concentration.

- Establish mercury speciation and partitioning in an oxygen-coal combustion system.

- Develop and validate mercury sampling technologies in a coal–derived synthetic gas stream.

- Develop low-cost sorbents for mercury capture that are applicable to coal gasification environments.

- Characterize Hg-induced material corrosion in an elevated CO_2 environment.

4.3 Mercury Measurement and Control in a CO_2-Enriched Flue Gas

4.3.1 Experimental Approach

A series of bench-scale experiments were performed to evaluate and/or develop mercury CMM sampling protocols applicable for CO_2-enriched flue gases. The test flue gas constituents came from the EERC's bench-scale simulator, which has proven effective in a variety of projects on mercury measurement and control (42, 43). Elemental mercury vapor and other typical flue gas constituents such as O_2, CO_2, H_2O, N_2, CO, SO_2, NO, NO_2, and hydrochloric acid (HCl) can be metered using mass flow controllers to produce a simulated flue gas stream with widely variable yet tightly controlled flue gas compositions. Details of the experimental apparatus have been described elsewhere (44).

Series I Tests – Mercury Measurement of CMMs at Elevated CO_2 Levels

The Series I tests were designed to characterize the direct response of CMMs used in a gas stream containing only O_2, N_2, Hg, and various CO_2 levels ranging from 0% to 100%, as shown in Table 4-1.

Two different CMMs were evaluated in this study:

- A Sir Galahad, manufactured by P S Analytical
- A DM-6B from Horiba

Table 4-1. Series I Test, Bench-Scale Simulated Flue Gas Composition and Correction Factor for the Mass Flow Controller (MFC)

Test Gas	A	B	C	D	E
Hg^0, µg/m^3	12.5 ± 1.0				
O_2, %	0	5	0	5	0
CO_2, %	0	12	22	80	100
N_2, %	100	83	78	15	0
Correction Factor for MFC	1.000*	0.9691	0.9439	0.7957	0.7450*

* Provided by manufacturer.

The Sir Galahad analyzer uses cold-vapor atomic fluorescence (CVAF) as a means of mercury detection with a mass flowmeter to determine the sampling flow rate of flue gas. The DM-6B uses dual-beam cold-vapor atomic absorption spectroscopy (CVAAS) for mercury detection with a rotameter for measuring flue gas flow rate. Figures 4-1a and b depict the sampling flowchart of the Sir Galahad analyzer and the DM-6B, respectively.

Series II Tests – Mercury Measurement with Preconditioning Unit and CMM

In order to measure mercury with a CMM in actual flue gas, a pretreatment/conversion system is required to remove acid gases that may interfere with the instrument and to speciate mercury.

Conversion systems are available from several companies that use varied methods, including wet-chemistry, thermal catalytic, and thermal dilution. Systems that use a wet-chemistry conversion unit ahead of the CMM are the main focus for this research. In these systems, as ~0.5l pm flue gas flows through the pretreatment/conversion unit, 20% sodium hydroxide and 5% sodium thiosulfate are used in the Hg^0 side to selectively scavenge any Hg^{2+}, so that only Hg^0 is transferred to the downstream CMM. In the other parallel side, 20% sodium hydroxide and 2% stannous chloride are used to reduce Hg^{2+} to Hg^0 for the total gaseous mercury measurement. Both solutions were continually refreshed at a flow rate of 10 mL per minute during sampling time. Oxidized mercury is calculated by difference between the two measurements. The wet-chemistry pretreatment/conversion unit is also capable of removing acid gas components, including CO_2, from the flue gas stream.

The Series II tests were designed to determine possible side effects of concentrated CO_2 on the wet-chemistry conversion unit and subsequent mercury measurements. Simulated flue gases with various levels of CO_2 (listed in Table 4-2) flowed through the wet-chemistry conversion unit and were measured with both the Sir Galahad and DM-6B at the outlets of the wet-chemistry conversion system.

Meanwhile, concentrations of CO_2, O_2, NO/NO_2, and SO_2 were also monitored using a gas analyzer (Testo 350-XL) at the impinger outlets. At the end of each test, the impinger effluents were collected for pH measurement and chemical analyses.

Series III Tests – Mercury Measurement with Flue Gas Dilution, Wet Conversion, and CMMs

For this series of tests, a flue gas dilution unit was installed prior to the wet-chemistry conversion unit to minimize the side effects of concentrated CO_2 and other acid gases on mercury measurement. Flue gas was diluted with N_2 at a 35:1 ratio, and the diluted flue gas was introduced to the wet-chemistry pretreatment/conversion unit followed by a CMM for mercury measurement. The system was tested in simulated flue gas containing 90% CO_2, 6% O_2, 5000 ppm SO_2, 500 ppm NO, and 20 ppm HCl.

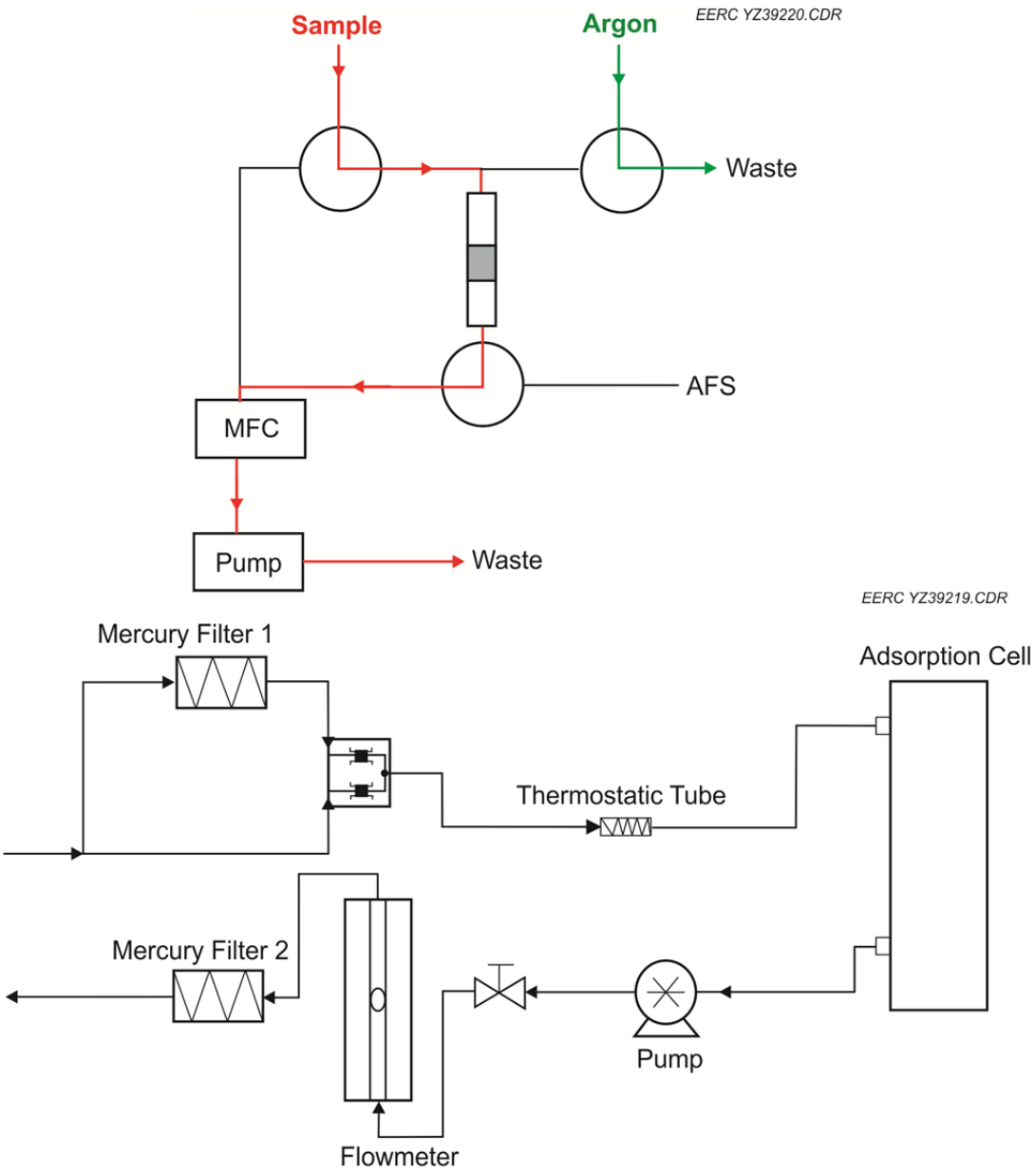

Figure 4-1. Sampling flowchart of the Sir Galahad analyzer (top) and sampling flowchart of the DM-6B analyzer (bottom).

Series IV Tests – Mercury Breakthrough Tests with AC in CO_2-Enriched Flue Gas

At the end of this study, a thin-bed mercury breakthrough test was performed with lignite-derived AC in a simulated combustion flue gas at a high concentration of CO_2 typical of an oxycombustion system, and the derived results were compared with the breakthrough data from conventional air combustion flue gases.

Table 4-2. Series II Tests, Bench-Scale Simulated Flue Gas Compositions

Test Gas	F	G	H	I	J	K	L
O_2, %	0	5	5	5	5	5	5
CO_2, %	0	0	12	22	40	80	80
N_2, %	100	95	83	73	55	15	15
NO, ppm	–	–	–	–	–	–	350
SO_2, ppm	–	–	–	–	–	–	1100
HCl, ppm	–	–	–	–	–	–	11
Hg^0, μg/m^3	12.5 ± 1.0						

4.3.2 Results and Discussions

Series I Tests

Plotted in Figure 4-2a are the mercury concentrations measured with the DM-6B mercury analyzer in simulated flue gases only containing O_2, N_2, and CO_2 under the conditions shown in Table 4-1. The CMM data were very stable—around 12.5 μg/m^3 of mercury under all testing conditions—proving that the dual-beam CVAAS of the DM-6B responded correctly and consistently at various CO_2 levels.

Conversely, the responses of the Sir Galahad unit, as plotted in Figure 4-2b, were quite scattered, depending upon the CO_2 concentrations in the gas stream: CMM data in a CO_2-free gas stream were around 12.5 μg/m^3, as expected, indicating that the CVAF of the Sir Galahad functioned properly. As CO_2 concentrations increased from 12% to 22%, the mercury measured by the Sir Galahad averaged acceptable levels of 11.3 and 11.6 μg/m^3, respectively. However, as CO_2 concentrations in the flue gas further increased to 80% and 100%, which are typical levels of high-purity CO_2 streams needed for CCS, the CMM data for the Sir Galahad became biased, measuring around 9 μg/m^3, which is much lower than the expected 12.5 ± 1.0 μg/m^3. The reason for this low bias was determined and has been attributed to biased signals of the MFC that is usually calibrated with a pure nitrogen stream, which generates comparable flow rate signals that are typical of coal air combustion flue gas. Testing showed that, with elevated CO_2 in the flue gas, a correction factor is required for the MFC in order to offset the signal difference introduced by the variable flue gas properties/compositions. The correction factors under varied CO_2 levels were calculated by summation of the MFC signals of each individual flue gas constituent fraction in the simulated flue gas, with the results shown in Table 4-1. The Sir Galahad data were then recalculated with the correction factors and replotted in Figure 4-2c, showing that mercury measurement data were consistently around 12.5 ± 1.0 μg/m^3 after the adjustment. From these tests, it is concluded that CMMs that use an MFC for flow rate measurement must be corrected to compensate for the signal difference introduced by increased CO_2 levels, but no correction is needed for CMMs that use a rotameter, such as the DM-6B unit.

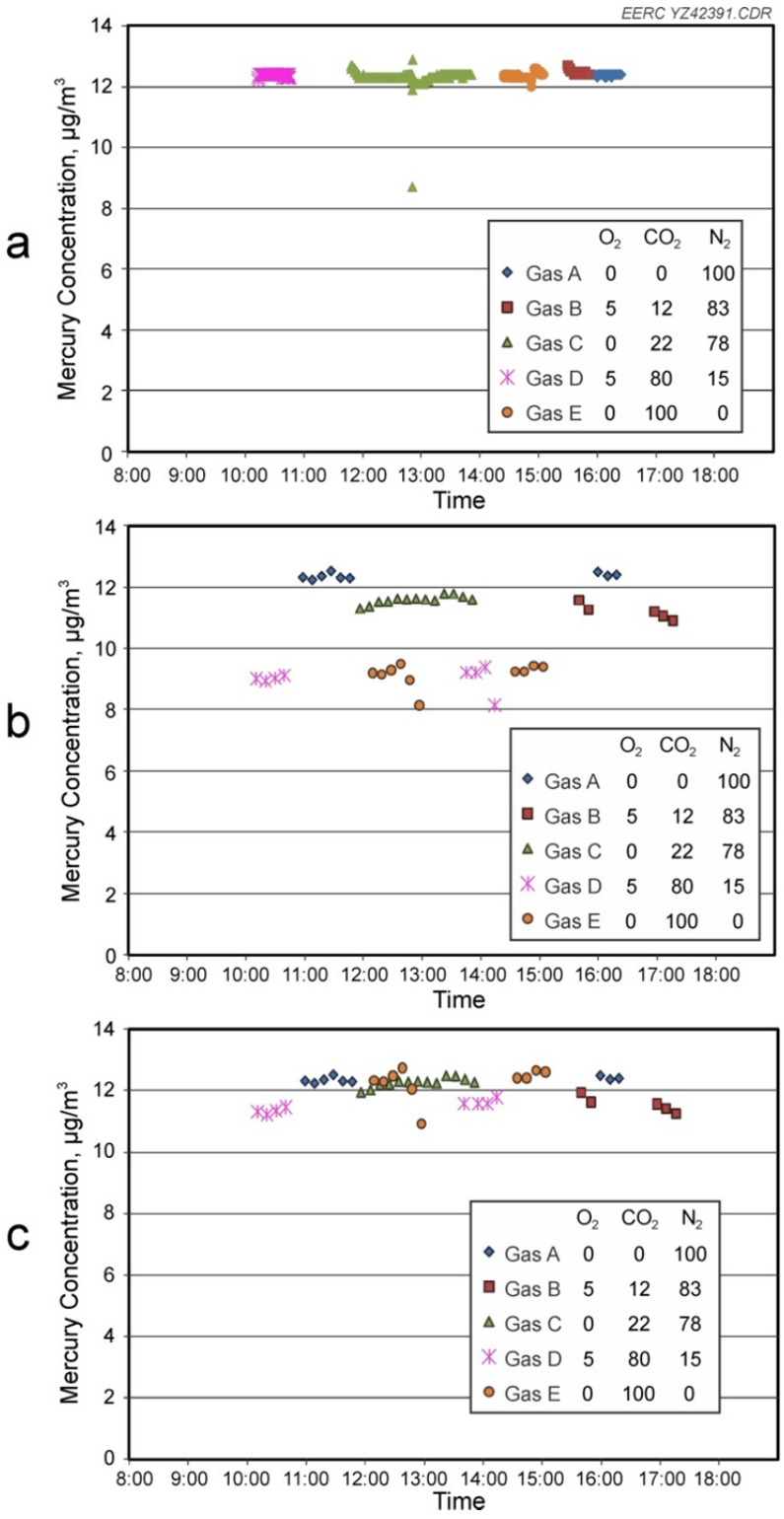

Figure 4-2. CMM response of the DM-6B with respect to various CO_2 concentrations, without any flow rate correction (a); CMM response of the Sir Galahad with respect to various CO_2 concentrations, without any flow rate correction (b); and CMM response of the Sir Galahad with respect to various CO_2 concentrations, with flow rate correction (c).

Series II Tests

Series II tests were designed to determine possible side effects of concentrated CO_2 on the wet-chemistry conversion unit and subsequent mercury measurements. Table 4-3 lists measured gas concentrations of $Hg^0/Hg_{(g)}$, CO_2, O_2, NO/NO_2, and SO_2 at the impinger outlets for each test condition. Averaged speciated mercury data from both the Sir Galahad and the DM-6B are also plotted in Figure 4-3 for each gas condition. Table 4-3 also shows the pH value and total carbon values of the impinger solutions.

CMM measurements in flue gas containing only 12% CO_2 were consistently around 12 $\mu g/m^3$, the same as the inlet mercury concentration. With the pH of the impinger solutions maintained at 13–14, most of the incoming CO_2 was removed by the NaOH in the impinger solutions, yielding results similar to the CO_2-free gas streams. The experimental data indicate that the wet-chemistry conversion unit functioned properly and did not introduce any mercury measurement bias in typical flue gas containing 12% CO_2 (Flue Gases F, G, and H). Since the wet-conversion unit was capable of removing up to 20% of CO_2 in the gas stream, the gas volume downstream of the conversion unit was reduced, subsequently concentrating mercury in the flue gas. Therefore, all CMM data have been corrected based on the changes of CO_2 across the conversion system to offset this biased concentrating effect.

However, as the CO_2 concentrations increased to 22% or higher (Flue Gases I, J, K, and L), both Hg^0 and $Hg_{(g)}$ measurements became inconsistent and scattered, varying from 10 to 15 $\mu g/m^3$. CO_2 measurements taken at the outlet of the wet conversion unit indicate that up to 20% of the total CO_2 dissolved into the chemical solution containing 20% NaOH, resulting in a continued decrease of pH value from 12.0 to 9.4, yielding 1.5%–2.0% total carbon in the impinger solution, as shown in Table 4-3.

Another observation showed that a white and/or yellowish solid precipitated out of the impinger solutions, on both the Hg^0 and $Hg_{(g)}$ sides, during the elevated CO_2 gas testing. Chemical analysis of the solid samples (listed in Table 4-3) indicates sodium compounds in the Hg^0 side, with both sodium and stannous compounds observed in the $Hg_{(g)}$ side. This indicates that the white precipitate was likely sodium bicarbonate, which formed via the following reactions:

$$CO_{2(g)} + 2NaOH_{(aq)} \rightarrow Na_2CO_{3(aq)} + H_2O \qquad \text{[Eq. 1]}$$

$$Na_2CO_{3(aq)} + CO_{2(g)} + H_2O \leftrightarrow 2NaHCO_{3(s)} \qquad \text{[Eq. 2]}$$

The precipitate will begin to form when the solution becomes saturated with Na_2CO_3. This reaction pathway is consistent with the lower pH values, which verify that the hydroxide ions were consumed in the reaction.

On the $Hg_{(g)}$ impinger side, two possible reactions can cause a precipitate: a sodium bicarbonate precipitate can form via the pathway shown in Equations 1 and 2, or the other possibility is a $SnO \cdot H_2O_{(s)}$ precipitate that can be formed if there is no excess of hydroxide in

Table 4-3. Analysis Results of Series II Tests

Test Gas		F	G	H	I	J	K	L
Impinger Outlet Gas	Hg^0	100% N_2 11.9 μg/m^3 Hg	5% O_2 95% N_2 11.0 μg/m^3 Hg	6.2% O_2 1.1% CO_2 12.1 μg/m^3 Hg Balance N_2	NA* 12.0 μg/m^3 Hg	11.7% O_2 16.4% CO_2 10.1 μg/m^3 Hg Balance N_2	8.6% O_2 66.8% CO_2 9.0–13.7 μg/m^3 Hg Balance N_2	9.8% O_2 60.6% CO_2 11.2 μg/m^3 Hg Balance N_2 300 ppm NO 4 ppm NO_2 0 ppm SO_2
	$Hg_{(g)}$	100% N_2 12.0 μg/m^3 Hg	5% O_2 95% N_2 11.1 μg/m^3 Hg	6.2% O_2 1.1% CO_2 12.2 μg/m^3 Hg Balance N_2	5.8% O_2 10.4% CO_2 12.0 μg/m^3 Hg Balance N_2	6.8% O_2 28.0% CO_2 11.8 μg/m^3 Hg Balance N_2	8.0% O_2 69.7% CO_2 10.8–13.0 μg/m^3 Hg Balance N_2	7.2% O_2 75% CO_2 14.6 μg/m^3 Hg Balance N_2 379 ppm NO 3 ppm NO_2 0 ppm SO_2
C Content in Impinger Effluent, wt%	Hg^0	~ 0	~ 0	1.20	2.04	2.04	1.44	1.54
	$Hg_{(g)}$	~ 0	~ 0	1.48	1.23	2.03	1.03	1.33
pH of Impinger Effluent	Hg^0	14	14	14	12	9.9	9.4	9.6
	$Hg_{(g)}$	14	13	13	12	9.9	9.5	9.4
Impinger Precipitate	Hg^0	None	None	None	Opaque crystal 7.6 wt% Na	None	White powder 25.4 wt% Na	Opaque crystal 22.7 wt% Na
	$Hg_{(g)}$	None	None	None	White crystal 6.4 wt% Na 0.24 wt% Sn	Yellow powder 10.6 wt% Na 38.4 wt% Sn	Yellow/white powder 32.3 wt% Na 13.4 wt% Sn	Yellow/white powder 17.3 wt% Na 9.1 wt% Sn

* Not applicable.

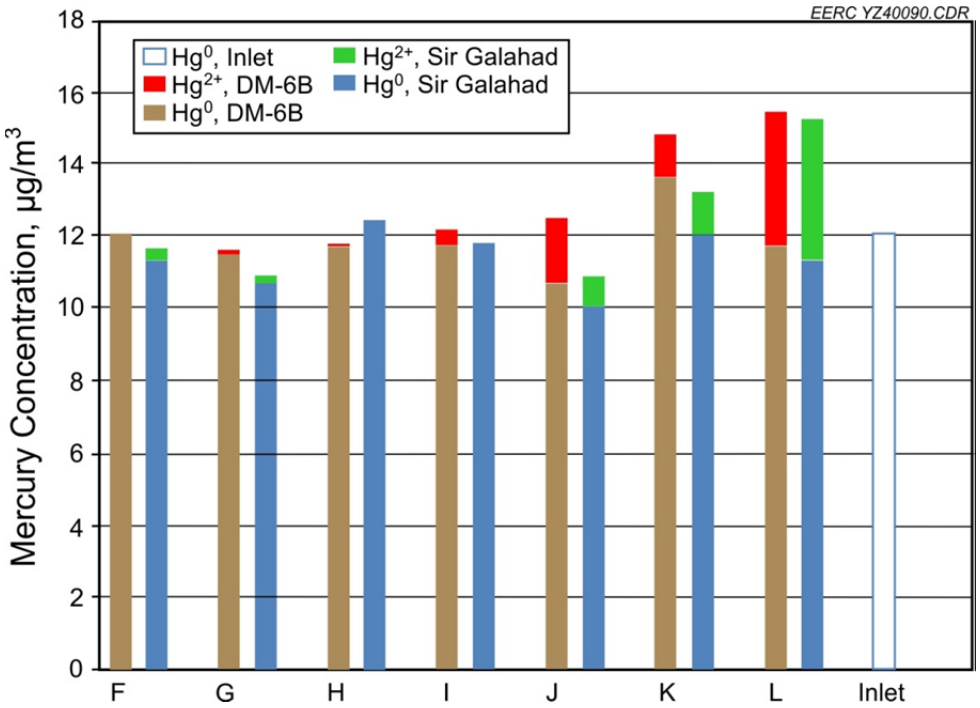

Figure 4-3. Comparison of mercury measurement for Sir Galahad and DM-6B instruments in flue gas with varied CO_2 concentrations.

solution, which causes the tin hydroxide to shift back to the tin-based solid and to precipitate out of solution. When stannous chloride is added to a sodium hydroxide solution, the stannous chloride reacts with the hydroxide ion to form $SnO{\cdot}H_2O_{(s)}$, as shown in Equation 3:

$$SnCl_{2(aq)} + 2NaOH_{(aq)} \rightarrow SnO{\cdot}H_2O_{(s)} + 2NaCl_{(aq)} \qquad \text{[Eq. 3]}$$

The solid is a milky white/yellow precipitate that is commonly seen when the stannous chloride is initially introduced to the solution. In the presence of excess hydroxide, the precipitate will go into solution by reacting with hydroxide ions, as seen in Equation 4:

$$SnO{\cdot}H_2O_{(s)} + NaOH_{(aq)} \leftrightarrow NaSn(OH)_{3(aq)} \qquad \text{[Eq. 4]}$$

As a result of the formation of the sodium bicarbonate (white precipitate) that consumed the excess hydroxide ions in solution, the dissolved tin hydroxide shifted back to the tin-based solid $SnO{\cdot}H_2O_{(s)}$ (yellow precipitate) and precipitated out of solution.

Series III Tests

In order to overcome the precipitate formation and to obtain correct mercury measurement with the CMM, either more moles of reagent are needed, or the CO_2 concentration has to be diluted before it passes through the impingers. Since it is not cost-effective to increase the reagent concentrations or quantity, flue gas dilution would appear to be the preferred way to

overcome the sampling issue. Figure 4-4 shows the plot of the mercury CMM data when a dilution/wet-chemistry conversion unit is used in a typical CO_2-enriched flue gas. Note that the inlet Hg^0 concentration was changed to 20.8 ± 1.0 μg/m^3 during the Series III test, since the total gas flow rate was reduced to accommodate the flue gas matrix. With a 35:1 nitrogen dilution, no precipitation was noticed in the wet-chemistry conversion unit, and the CMM measurements indicate a consistent and reasonable measurement of mercury species data for flue gas containing 90% CO_2, 5000 ppm SO_2, and 500 ppm NO. With the addition of 20 ppm of HCl into the flue gas stream, although the $Hg_{(g)}$ measurement showed the same values, the Hg^0 measurement was lower than expected, indicating possible mercury oxidation within the diluter.

From this experiment, it appears that mercury speciation measurement is not reliably accurate under what would be considered typical oxycombustion conditions, and further development on mercury measurement is needed to obtain reliable speciation data. Figure 4-5 shows the plot of mercury measurements in a CO_2-enriched flue gas (fly ash-free) using the Ontario Hydro (OH) method compared to those taken using a CMM preceded by a wet conversion unit. A 1-hour OH method sample was taken of flue gas at the outlet of the OH method's impinger train; several flue gas constituents, including O_2, CO_2, $Hg_{(g)}$, NO/NO_2, and SO_2, were monitored continuously during the sampling period. Mercury sampling was conducted simultaneously using a CMM, with the flue gas diluted to a 35:1 ratio before being measured by the wet conversion/CMM unit. Flue gas sampling with Testo 350-XL at the outlet of the OH impinger train indicated that mercury vapor and SO_2 were effectively adsorbed by the OH method's impinger solution and no breakthroughs of mercury or SO_2 were observed at the conclusion of the sampling period. The reason is that the chemical solutions used in OH method impingers are 1) 1N KCl solution, 2) 5% HNO_3/10% H_2O_2 solution, and 3) 10% H_2SO_4/4% $KMnO_4$ solution, and they are not as basic as the 20% NaOH solution in the CMM wet conversion unit. As a result, no significant CO_2 scrubbing occurred across the OH method impingers. The Testo data also showed that, at the outlet of the impinger trains, significant oxidation of NO to NO_2 had occurred in the flue gas.

These mercury data indicate that the OH method is capable of providing valid mercury speciation data within the 1-hour sampling period but that the CMM can only provide accurate measurement of $Hg_{(g)}$ with biased high oxidized Hg in this environment. Additional research is needed to optimize CMM measurement techniques for both wet and dry conversion units and to evaluate the applicability of sorbent trap measurements taken in elevated CO_2 conditions.

Series IV Mercury Breakthrough Tests with AC

As CO_2 control technologies are applied, flue gas characteristics will change. For example, oxycombustion with flue gas recirculation will not only enrich CO_2 concentrations but also other acid gases such as SO_2, SO_3, and HCl. These acid gases are known to impact mercury capture by AC. Therefore, mercury speciation and reduction strategies need to be reevaluated. Figure 4-6 shows a breakthrough plot for mercury capture with AC under flue gases enriched with 72%–80% CO_2 and varied levels of H_2O and NO_2. Also included in Figure 4-6 are the mercury breakthrough curves of a similar AC in typical flue gases (Flue Gases IV and V) from air-blown combustion of high-sulfur and low-sulfur coals, respectively.

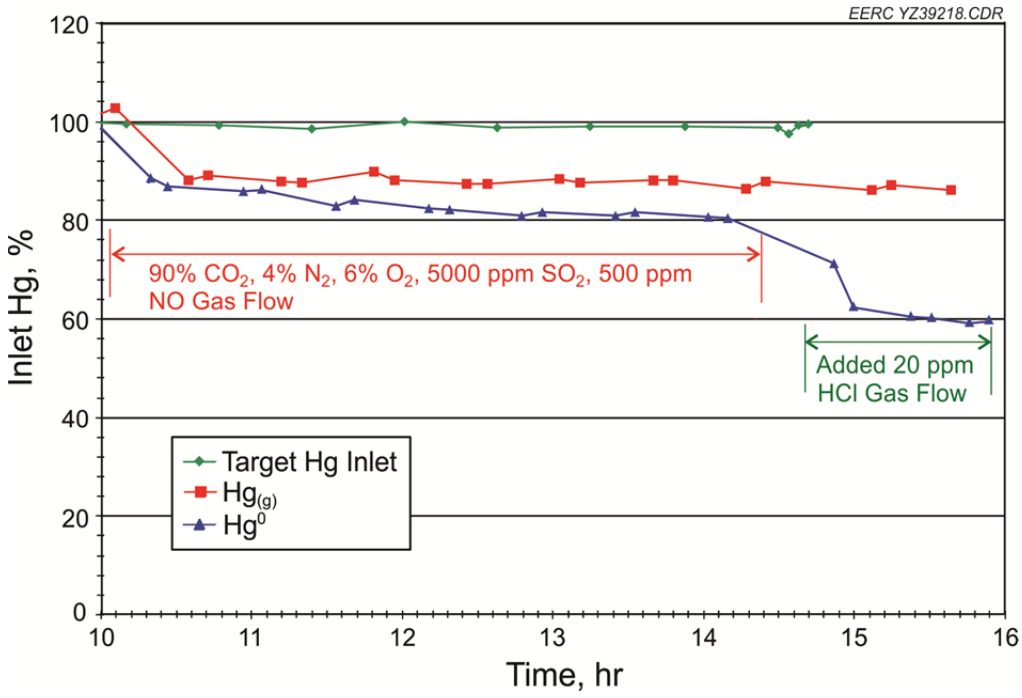

Figure 4-4. Mercury CMM data when using a dilution/wet-chemistry conversion unit in a typical CO_2-enriched flue gas with a PSA Sir Galahad.

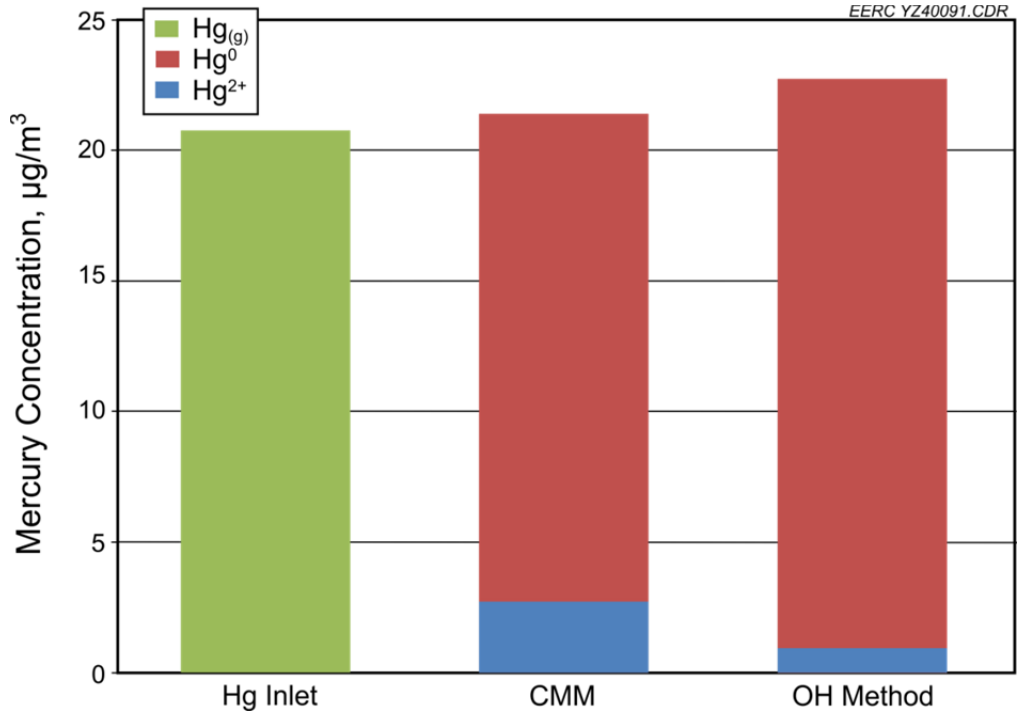

Figure 4-5. Comparison of mercury measurement with a CMM and the OH method in CO_2-enriched flue gas (with composition of 5% O_2, 80% CO_2, 10% H_2O, 400 ppm NO, 4000 ppm SO_2, and 40 ppm HCl).

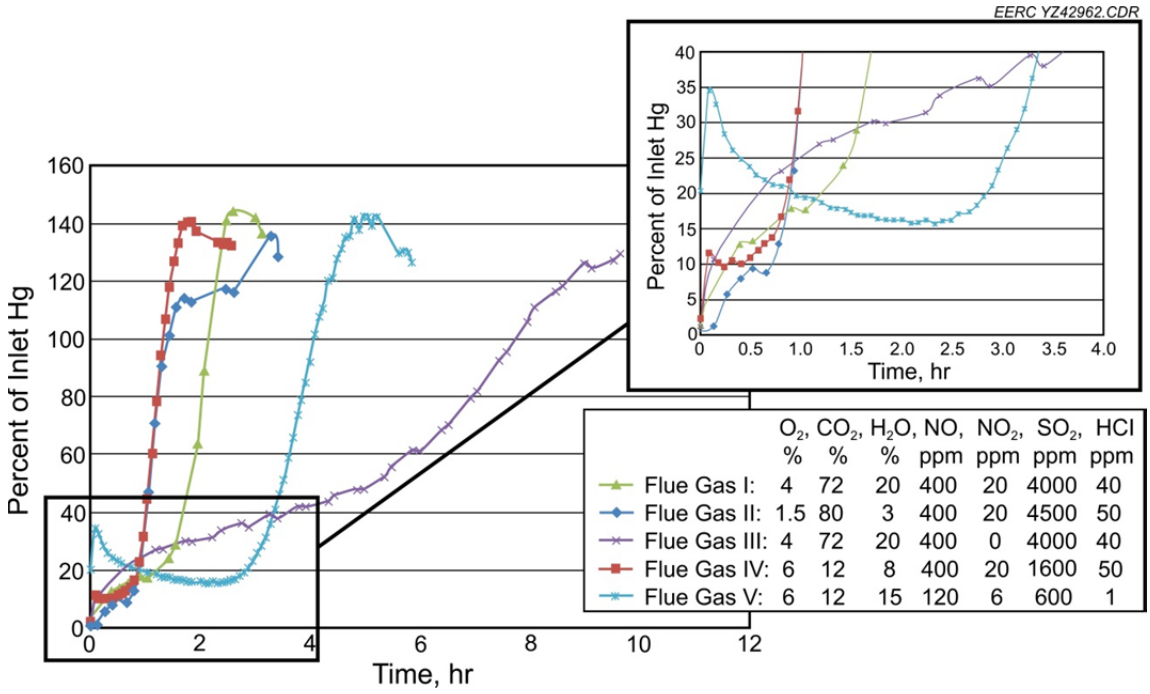

Figure 4-6. Comparison of mercury breakthrough with AC sorbent in different flue gases.

As a result of elevated CO_2 and other acid gases, mercury breakthrough in Flue Gases I, II, and III took place immediately, without an initial induction period. The 100% mercury breakthroughs of Flue Gases I and II were attained within 2 hours, similar to the results of typical high-sulfur, air-blown combustion flue gas. However, the mercury breakthrough in Flue Gas I with 20% H_2O was slower than that of Flue Gas II with only 3% H_2O, which is in contrast to the moisture effect on mercury capture with AC as seen in typical coal flue gas; additional experimental data are needed to verify this observation. The fact that no initial induction period was observed in the elevated CO_2 stream seems to indicate that the reactivity of Hg^0 to AC was enhanced compared to that in conventional coal flue gas where AC needs to be promoted by the flue gas constituent, such as HCl, for Hg adsorption. Flue Gas III contained 72% CO_2, 20% H_2O, 4000 ppm SO_2, 40 ppm HCl, 400 ppm NO, and 0 ppm NO_2. In this flue gas mixture, the intial intake of Hg is slower than that in Gases I and II, however, 100% mercury breakthrough was reached after approximately 7.5 hours, probably as a result of less sulfate formation on carbon surfaces in the absence of NO_2. In summary, AC performance on mercury capture in flue gas with enriched CO_2 and other acid gases are expected to be similar to that obtained in high-acid-gas streams, which may impose additional challenges on mercury capture in oxycombustion with low-sulfur coal. Meanwhile, Hg/AC kinetics need to be further evaluated in the elevated CO_2 environment.

4.3.3 Conclusions

Experimental data indicate that mercury measurements with CMMs in flue gas with variable and/or highly concentrated CO_2 may require modifications and additional validation

testing. Highly concentrated CO_2 streams affect the accuracy of the mass flow rate measurement and the subsequent gaseous mercury measurement, although this is specific to the type of CMM used. Concentrated CO_2 streams also led to solid precipitate in the wet-chemistry conversion unit and resulted in a biased measurement of gas-phase mercury. Flue gas dilution appears to provide accurate measurement of total gas-phase mercury and is applicable to mercury measurement in highly concentrated CO_2 streams, although mercury speciation still appears to be an issue. Bench-scale mercury breakthrough tests with AC under CO_2-enriched conditions show similar performance to those observed under typical high-acid-gas coal combustion conditions.

4.4 Transformation of Hazardous Air Pollutants in Oxygen-Fired Coal Combustion with Flue Gas Recycling

4.4.1 Experimental Approach

In order to characterize the transformation of a variety of hazardous air pollutants (HAPs) during oxygen–coal combustion and understand the impacts of different flue gas recycling scenarios on these HAPs, the EERC modified an existing pilot-scale combustion system for oxygen firing, which includes a 550,000-Btu/hr pulverized coal (pc)-fired combustor followed by an electrostatic precipitator (ESP) for particulate matter (PM) control and a wet scrubber for SO_2 capture. As shown in Figure 4-7, during the oxygen-blown test, part of the postcombustion flue gas was recycled and mixed with oxygen stream to maintain flame temperature and stability in coal combustion. Two different scenarios of recirculation flue gas (RFG) were evaluated: flue gas was recycled either from 1) the outlet of the ESP or 2) the outlet of the wet scrubber, separately, to investigate the corresponding effect on the transformation of HAPs. The postcombustion flue gas passed through a series of heat exchangers to control temperature to ~300°F, and the cooled flue gas was then introduced into the ESP followed by the wet scrubber. A direct-contact cooling unit was used to cool the RFG before it was mixed with oxygen and recycled to the primary and secondary oxidizer streams. For safety purposes, the oxygen levels in the primary and secondary streams were controlled around 23.0 ± 1.0% and 28 ± 0.8% using the oxygen sensors and the oxygen flow controls.

The pilot-scale combustion facility is fully instrumented to provide online analysis of the flue gas, which was drawn from the furnace exit, the outlet of the ESP, and the outlet of the wet scrubber. The sampled flue gas was filtered; transported in a heated sample line to the gas quenching unit; and passed to a series of gas analyzers for measuring O_2, CO, CO_2, NO_x, and SO_2 simultaneously. All system temperatures, pressures, and flue gas analyses were recorded continuously to chart recorders and the system's computer-controlled data acquisition system. Other than the routine flue gas measurement, flue gas samples were collected at the ESP inlet, the ESP outlet, and the scrubber outlet for analyses of SO_3, H_2O, PM, HCl, and mercury. Table 4-4 summarizes the test scenarios and sampling activities. A high-sulfur eastern bituminous coal was selected for the test.

For comparison purposes, an air-blown coal combustion test was also performed to establish a baseline condition, of which the bituminous coal was fed into the pc combustor at the same fuel firing rate as that of oxycombustion test.

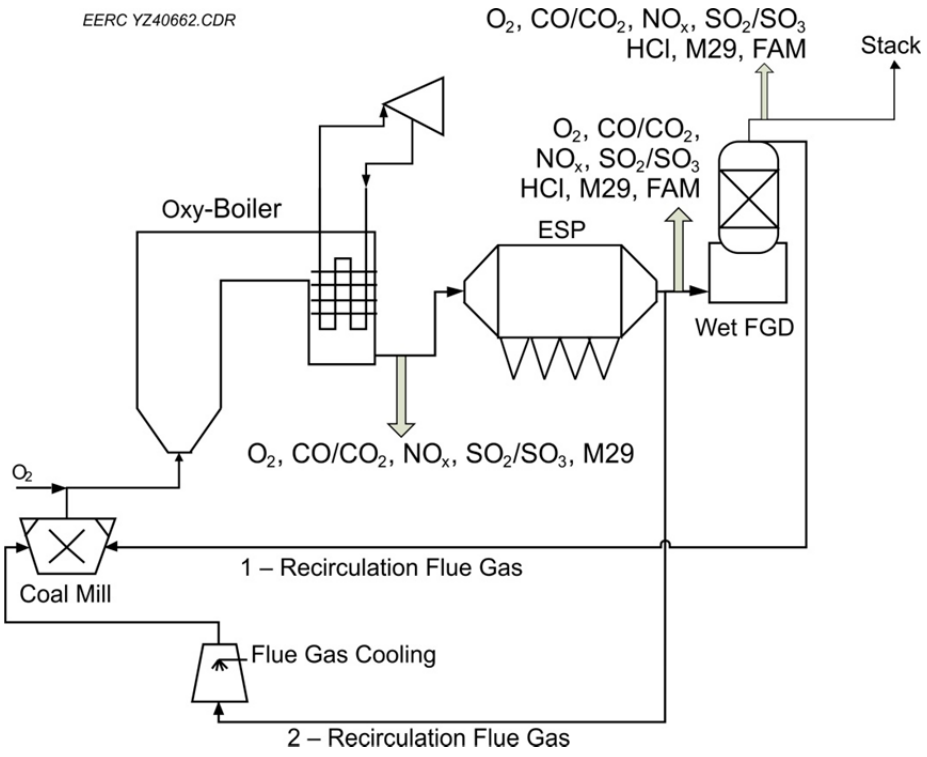

Figure 4-7. Experimental schematic diagram.

4.4.2 Results and Discussions

A high-sulfur bituminous coal was combusted during the test and analyzed for proximate/ultimate and trace elements of interest as listed in Tables 4-5 and 4-6. The test coal has also been ashed and analyzed for major inorganic elements, and the results are summarized in Table 4-7.

Table 4-8 lists combustion parameters for air-blown and oxygen-blown with RFG from the outlet of the ESP and the outlet of the wet scrubber, respectively. The coal feed rate was maintained at the same 54 lb/hr, equivalent to 5.92×10^5-Btu/hr firing rate, for all test conditions. While the actual amounts of O_2 feed were adjusted to match the fuel firing rate, the amounts of RFG were adjusted, and the subsequent average O_2 feed into the combustor during oxycombustion was 26.2% and 28.3%, respectively, for RFG at the ESP outlet and the scrubber outlet. The higher levels of O_2 in the feed gas during oxycombustion indicate that the amount of RFG feeding into the combustion was less than the corresponding nitrogen used in air-blown combustion. As a result, the total volume of flue gas generated during oxycombustion was expected to be ~ 75%–80% of the total flue gas generated in the air-blown combustion test, which has been proved by the measured flue gas flow rate at the furnace exit as shown in Table 4-8.

Table 4-4. Test Scenario and Sampling Activities

Test No.	Combustion	Recirculation of Flue Gas	Sampling Activity
I	Air-blown	NA	O_2, CO_2, CO, SO_2/SO_3, NO_x, HCl, H_2O, PM, and Hg
II	Oxygen/recycled flue gas	ESP outlet	
III	Oxygen/recycled flue gas	Wet scrubber outlet	

Table 4-5. Proximate/Ultimate Analysis Results of the Tested Bituminous Coal

Proximate Analysis, wt%, as-received	
Moisture	6.7
Volatile Matter	33.52
Fixed Carbon	47.51
Ash,	12.27
Ultimate Analysis, wt%, dry	
Hydrogen	5.32
Carbon	62.85
Nitrogen	1.34
Sulfur	3.63
Oxygen	14.59
Ash	12.27
Heating Value, Btu/lb	10,963

Table 4-6. Trace Element Analysis of the Tested Bituminous Coal, µg/g, dry

Coal	Sb	As	Be	Cd	Cr	Co	Mn	Hg	Ni	Se	Pb	Cl
Illinois	0.26	3.17	0.95	0.29	14.9	5.69	33.0	0.08	22.2	1.26	7.62	137

Table 4-7. Major Inorganic Elements of the Tested Bituminous Coal

Oxides	wt%
SiO_2	53.08
Al_2O_3	23.52
Fe_2O_3	16.98
TiO_2	0.86
P_2O_5	0.24
CaO	2.15
MgO	1.06
Na_2O	0.20
K_2O	1.94

Table 4-8. Combustion Conditions under a CO_2 Environment

	Air-Blown	Oxygen-Blown with RFG at ESP Outlet	Oxygen-Blown with RFG at Wet Scrubber Outlet
Combustion Parameter			
Fuel Feed Rate, lb/hr	54	54	54
Feed O_2, %	21	26.2	28.3
Feed N_2, %	79	5.3	7.2
Feed CO_2, %	0	68.5	64.5
Feed Others	–	SO_2, NO_x	SO_2, NO_x
Combustion Temperature, °F	2082 ± 8.4	1967 ± 10.9	2037
Equivalence Ratio	0.83	0.93	0.93
Flue Gas Flow Rate at Furnace Exit, scfm	118 ± 1.1	90 ± 4.0	82.9 ± 3.9
Flue Gas O_2 at Furnace Exit, %	3.7 ± 0.3	4.9 ± 0.4	5.1 ± 0.5
Flue Gas CO_2 at Furnace Exit, %	14.7 ± 2.5	71.4 ± 1.2	72.8 ± 2.7
Flue Gas CO at Furnace Exit, ppm	17.7 ± 1.8	78.1 ± 26.4	56.6 ± 12.6
Flue Gas H_2O at Furnace Exit, %	8.5	~18	~15
PM at Furnace Exit, g/m^3	8.46	13.9	13.3
LOI in Ash, %	0.74	2.24	1.38

Combustion equivalence ratio, defined as the actual fuel-to-oxidizer divided by the stoichiometric fuel-to-oxidizer was used to evaluate feed of O_2 versus fuel. 0.93 was obtained during oxycombustion compared to 0.83 in air combustion mode. The measured combustion equivalence ratio indicates that, under the same firing rate, slightly less O_2 was fed into oxycombustion than under air firing, which partially cause higher CO_2 concentrations in the flue gas: 78.1–56.6 ppm during oxycombustion compared to 17.7 ppm in air-blown mode. Corresponding higher values of loss on ignition (LOI), as listed in Table 4-8, were observed for ash generated in oxycombustion than air-blown combustion. The oxycombustion temperature was slightly lower than the air-fired temperature, presumed partially due to the higher specific heat of CO_2. The observed combustion performance indicates insufficient burnout during oxycombustion, which may be ascribed to the lower O_2 diffusivity and less efficient O_2 mixing in a CO_2-enriched combustion zone.

Achieving high levels of CO_2 in the postcombustion flue gas is the main focus of the oxy-blown combustion, while the concentration of CO_2 is affected by air infiltration of the combustion system. The highest CO_2 attained at the furnace exit during oxycombustion was ~70% and further decreased to 65%–68% at the stack. In comparison with the ASPEN simulation results performed by McCauley et al. (7), it indicates that the EERC's unit has an approximately 8.5% air leakage through the entire combustion system. Further oxygen measurement along the system indicates that ~6% air infiltration was from the combustor, while the rest of the air leakage occurred between the convection duct and stack.

As the result of the low volumetric flue gas flow, the moisture content and dust loading during oxycombustion were higher than that in air-blown combustion.

Emission Characteristics of HAPs During Oxycombustion

In general, HAP emissions from oxycombustion were lower than that of air-blown combustion mainly because of the concentrated air pollutants in the flue gas and the reduced volume of flue gas being treated.

NO_x Emission

Plotted in Figure 4-8 is the NO_x concentration distribution for the systems. With ~70%–80% flue gas recycling during oxycombustion, NO_x concentrations in oxycombustion flue gas increased slightly, mainly due to the concentrating effect by the reduced gas volume generated from oxycombustion. The actual NO_x stack emissions during oxycombustion were in the range of 0.04–0.07 lb/MMBtu, and ~90% NO_x reduction was achieved compared to the NO_x emission from air-blown combustion. The main reason for the observed NO_x removal can be attributed to 1) reduced thermal NO_x formation because of the elimination of atmospheric nitrogen, 2) reduction of recycled NO_x as it is reburned in the volatile matter release region of the flame, and 3) the reaction between recycled NO_x and char.

SO_x Emission

SO_2 distributions and emissions between oxy-fired and air-fired mode are plotted in Figure 4-9. For conventional air-blown combustion, the high-sulfur coal generated ~3500 ppm SO_2. With the aid of the high-efficiency packed-tower wet scrubber, SO_2 concentration in the stack exhaust was reduced to 184.5 ppm, equivalent to 0.34 lb/MMBtu. With flue gas recycling at the outlet of the ESP during oxycombustion, the concentrations of SO_2 in flue gas prior to the wet scrubber were elevated compared to that of air-blown combustion. The highest SO_2 concentration was >7000 ppm at the furnace exit. In spite of the extremely high level of SO_2 in the flue gas, the emission of SO_2 from the wet scrubber was kept as low as 3 ppm, equivalent to 2.2×10^{-4} lb/MMBtu, which was due to the high liquid/gas ratio of the wet scrubber since only ~12% of the flue gas generated during oxycombustion flowing through the wet scrubber and the majority was recycled back to the combustor prior to the desulfurization unit. For the test where the RFG took place at the scrubber outlet, not much SO_2 enrichment was observed since most of the SO_2 had already been captured within the wet scrubber. The average SO_2 concentration in flue gas was ~4200 ppm prior to the wet scrubber and decreased to ~56 ppm at the scrubber outlet, equal to 0.015 lb/MMBtu. Again, the improved performance of wet scrubber was because the total gas volume across the wet scrubber was 82.9 scfm, less than the 118 scfm during air-blown combustion.

One concern for oxycombustion has been possible elevated SO_3 in flue gas because of 1) concentrated SO_2 because of the flue gas recycling and 2) the extended residence time of flue gas within the unit. Both factors could potentially enhance SO_3 formation in flue gas. To address the concern of SO_3, SO_3 condensation sampling was conducted at the outlet of the ESP for the

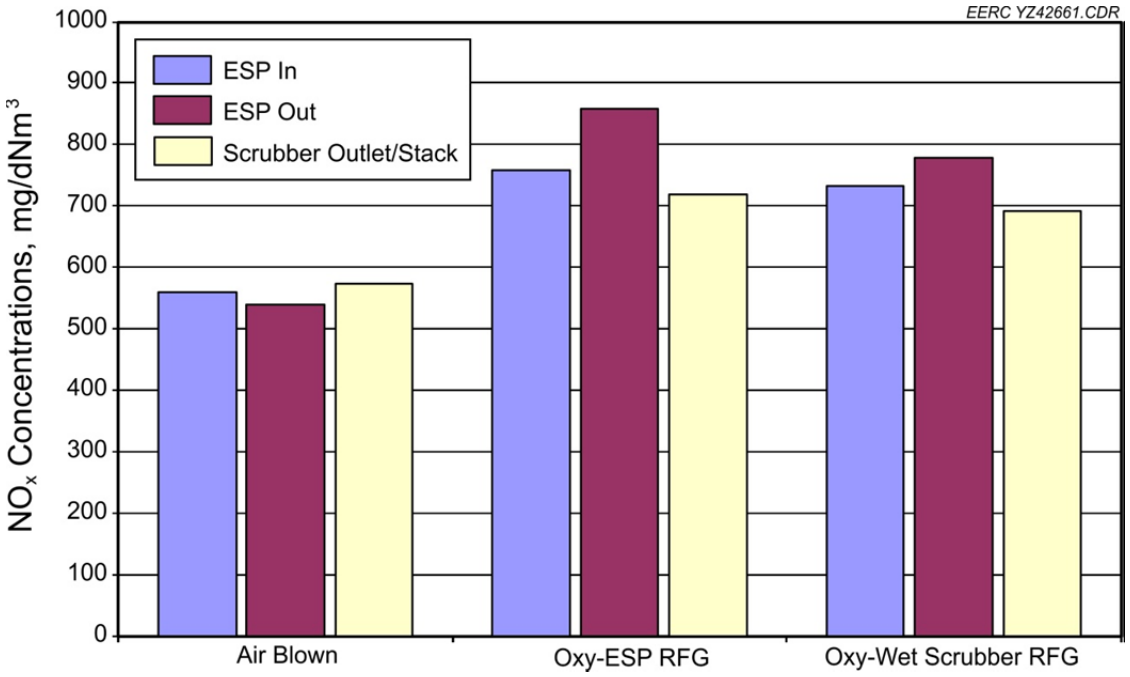

Figure 4-8. NO_x concentration and emission rates during air-blown and oxygen-blown combustion.

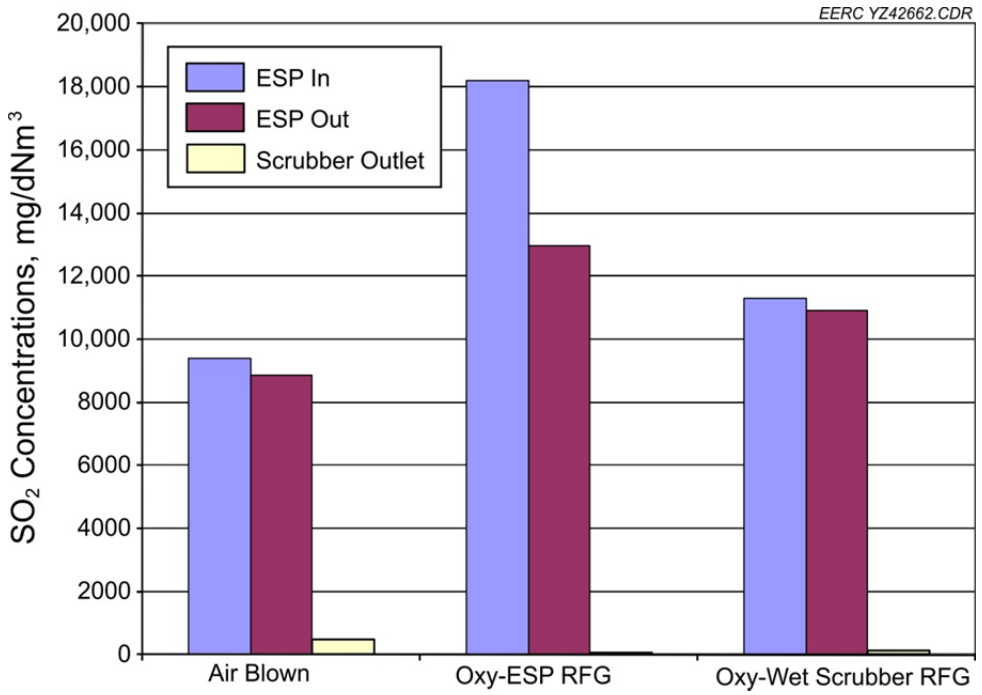

Figure 4-9. SO_2 concentration and emission rates during air-blown and oxygen-blown combustion.

three test conditions; the resulting SO_3 data are plotted in Figure 4-10. It appears that SO_3 concentrations during oxycombustion tests were somewhat higher than that of air-blown combustion, and there was no significant difference on SO_3 concentrations caused by RFG at either the ESP outlet or the scrubber outlet. Considering the fact that the system contained higher SO_2 concentrations for the test with the ESP recycling than that of wet scrubber recycling, it seems that the extended residence time may be the main reason for elevated SO_3 in the flue gas. The conversion of SO_2 to SO_3 was 0.24% during air-blown combustion and increased to 0.32%–0.34% after switching to oxycombustion. The observed SO_2/SO_3 conversion is much lower than the 5%–6% reported by Tan et al. (45), while the reason can be ascribed to the 35% O_2 presence in their experiment comparing to 26%–28% in the present study. The concentrated SO_2 and SO_3during oxycombustion may also enhance sulfur retention on the tested fly ash since the bituminous coal has a fair amount of calcium. Sulfate analysis of the fly ash showed that the sulfate concentration was 52.3 and 22.6 mg/g for oxycombustion with ESP RFG and wet scrubber RFG, respectively, higher than the 13.9 mg/g sulfate in the fly ash generated in the air-blown combustion test.

SO_3 equilibrium vapor concentration depends on temperature and moisture content of the flue gas and was calculated using the equation proposed by Banchero and Verhoff (46). The equilibrium SO_3 vapor concentration is ~16 ppm for the ESP outlet flue gas that was at 300°F and with 20% moisture content. The calculation result indicates the test flue gas was saturated with SO_3 and SO_3 condensation most likely occurred. Therefore, acid gas corrosion of plant equipment needs to be addressed for oxycombustion.

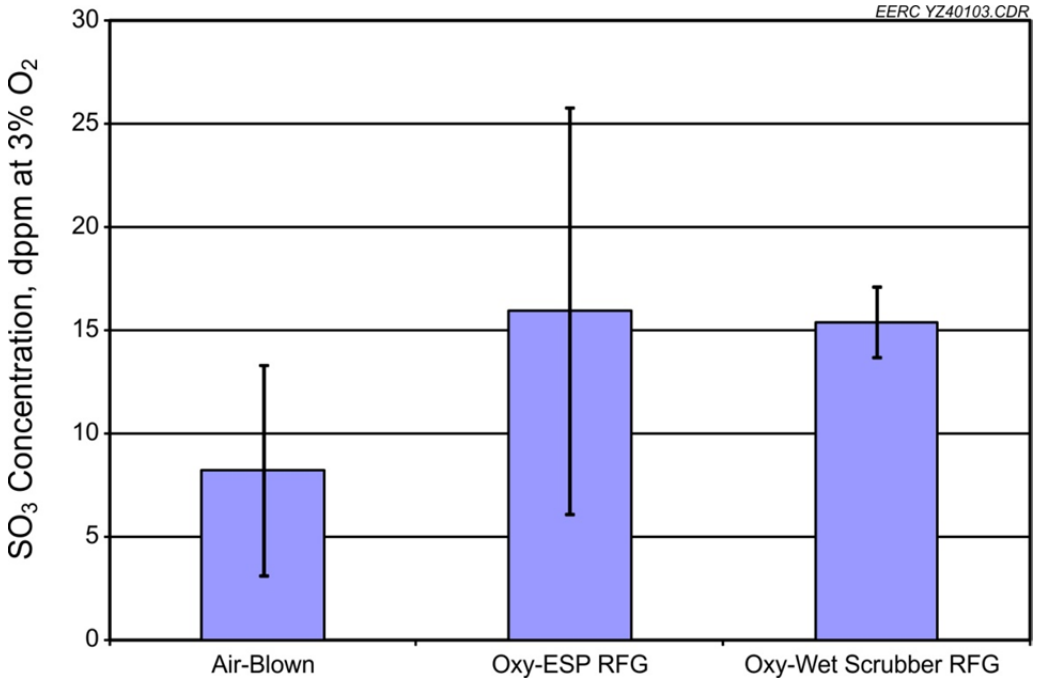

Figure 4-10. SO_3 concentrations at the ESP outlet during air-blown and oxygen-blown combustion.

HCl Emission

HCl is another air pollutant under strict regulation under MACT Standards. HCl sampling using the EPA Method 26 was conducted at the inlet and outlet of the ESP during the tests, and the results are plotted in Figure 4-11, showing an enrichment of HCl during oxycombustion. Meanwhile, analysis on resulting fly ashes showed no detectable chloride on the collected ashes from both air-blown and oxy-blown combustions. Assuming all HCl in the RFG was removed either by the flue gas direct cooling system or by the wet scrubber for oxycombustion with RFG at the ESP outlet and the scrubber outlet, respectively, the reason for the enriched HCl in flue gas during oxycombustion was most likely due to concentrating effect of the reduced gas volume during oxycombustion. However, additional HCl data in flue gas at the scrubber outlet will be helpful to fully understand the fate of HCl in a combustion system.

Mercury Emission

EPA Method 29 samples were collected for each of the three test conditions at the inlet and outlet of the ESP and the scrubber outlet, respectively, to establish mercury partitioning between total gas-phase mercury vs. particulate-bound mercury. EPA Method 30B samples were also collected at the ESP outlet and the scrubber outlet under the same three test conditions, not only for the comparison with Method 29 results, but also to provide gas-phase mercury speciation data. A summary of the obtained mercury data is plotted in Figure 4-12.

The air-blown combustion flue gas contained a total mercury value of 11.4 μg/dNm^3 with 97% gas-phase mercury, which matched the theoretical expectation based on mercury content in coal and proximate/ultimate data. There was virtually no mercury capture across the ESP since most of the mercury was in the gas phase. Both Method 29 and Method 30B data indicated mercury reduction, in the range of 40%–50%, occurred through the wet scrubber because ~52% gaseous mercury was in the soluble oxidized form. Mercury speciation data obtained during the conventional air-blown combustion are consistent with mercury emission data published elsewhere (47), indicating a representative combustion was established and the mercury speciation measurement was valid.

As for oxy-blown combustion with RFG either from the ESP outlet or the scrubber outlet, mercury concentrations in the flue gas at the ESP inlet were ~20 μg/dNm^3, almost double compared to total mercury data in the air-blown combustion test, which can be ascribed to the accumulative effect of flue gas recycling and the reduced gas volume during oxycombustion. The mercury data from oxycombustion with RFG at the scrubber outlet were consistently lower than that of RFG from the ESP outlet, mainly due to the fact that part of the mercury was captured by the wet scrubber before it was recycled back to combustion.

Mercury speciation data also indicated that $Hg_{(g)}$-to-$Hg_{(p)}$ conversion and Hg^0-to-Hg^{2+} oxidation took place upstream of the wet scrubber, most likely due to the continuous interactions with enriched HCl, unburned carbon (higher LOI during oxycombustion), and other reagents in the flue gas. As a result, mercury reductions of ~14.5% across the ESP and ~77% across the wet scrubber were achieved for oxycombustion. The overall mercury capture across the oxycombustion system was 80.9%, much higher than the 40.4% mercury removal by the air-blown combustion system.

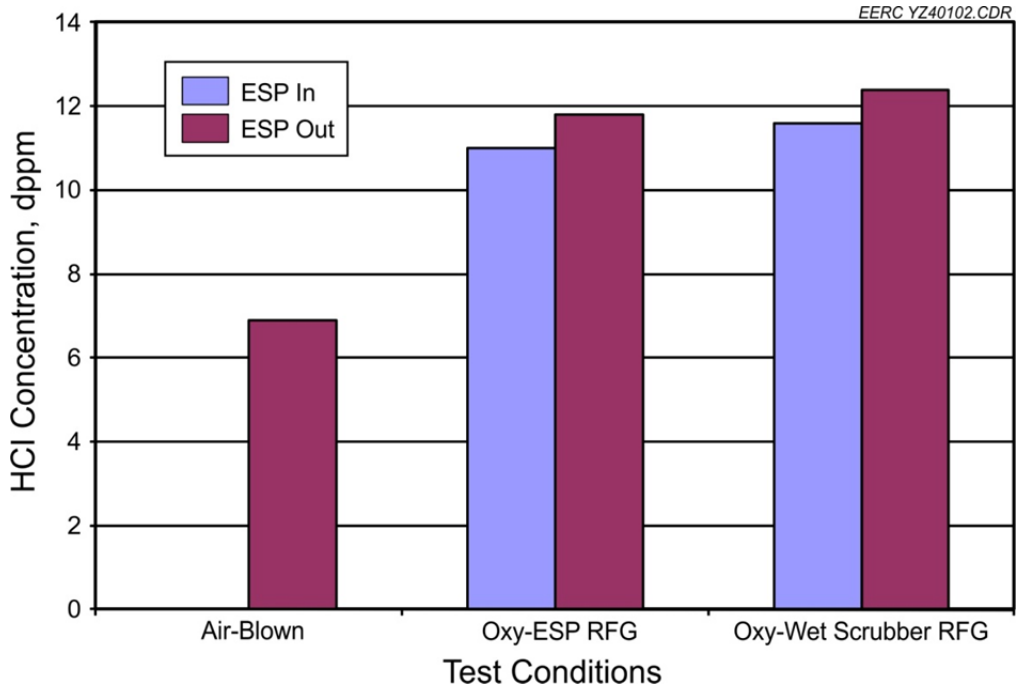

Figure 4-11. HCl emissions during air-blown and oxygen-blown combustion.

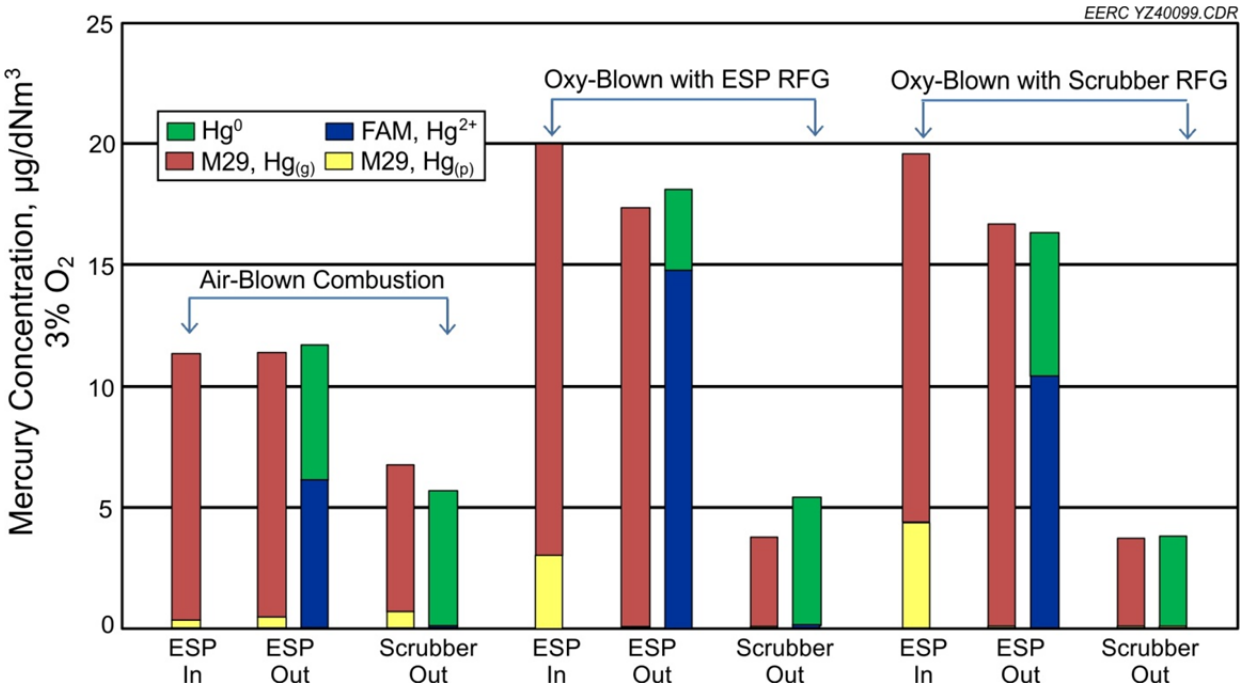

Figure 4-12. Mercury species partitioning during air-blown and oxygen-blown combustion.

Table 4-9 summarizes the emission rates of HAPs at the stack for both air-blown and oxy-blown combustion tests.

Table 4-9. Stack Emissions of HAPs, lb/MMBtu

	SO_2	SO_3	NO_x	HCl	Hg	PM
Air-Blown	0.34	0.02	0.39	7.2×10^{-3}	4.6×10^{-6}	3.6×10^{-3}
Oxy-Blown with RFG at ESP Outlet	2.2×10^{-4}	3.2×10^{-3}	0.043	1.1×10^{-3}	2.3×10^{-7}	0.01
Oxy-Blown with RFG at Scrubber Outlet	0.015	5.1×10^{-3}	0.069	1.9×10^{-3}	3.7×10^{-7}	9.6×10^{-3}

4.4.3 Conclusions

The pilot-scale combustion experiment showed that oxy-blown combustion with RFG generated a flue gas with less volume that contained HAPs at higher levels than that of air-blown combustion. The observed enrichment of HAPs is caused by the cumulative effect of the RFG and reduced flue gas volume generation with oxycombustion. However, since the majority of the flue gas was recycled back to the combustor during oxycombustion, the actual amount of flue gas released into the atmosphere was much less than that of air-blown combustion. Other than PM, the emission rates of most of the HAPs were lower than that of air-blown combustion, showing that oxycombustion is not only a solution to CO_2 capture, but can also provide overall better performance on HAP reductions.

Mercury sampling data indicate that both CMM and sorbent trap methods are capable of providing accurate mercury measurement in reducing syngas stream, while results of the wet-chemistry method such as EPA Method 29 show interference from reactions between syngas constituent and reagents used in wet-chemistry sampling.

4.5 Mercury Measurement and Control in Coal Gasification Applications

4.5.1 Experimental Approach

Mercury Measurement in a Coal Gasification System

Three main mercury-sampling methods have been used in coal gasification systems:

1. Wet-chemistry sampling: Method 29, Ontario Hydro, and 101A

2. Continuous mercury monitor: wet conversion and dry conversion

3. Sorbent trap: total Hg measurement (EPA Method 30B), speciated Hg measurement (FAMS [flue gas absorbent mercury speciation])

Unlike mercury sampling in combustion flue gas, strong oxidants, such as hydrogen peroxide and potassium permanganate used in wet-chemistry methods, not only capture Hg^0 but also react with most other reducing syngas constituents such as such as CO, H_2, and H_2S that are at much higher levels than mercury in syngas. As a result, a fast breakthrough of mercury across the wet-chemistry sampling train could take place and result in mercury measurement data in syngas that may not be valid. Similarly, concerns are raised for CMM and sorbent trap methods regarding their accuracy and consistency in coal syngas application. Therefore, CATM conducted a series of experiments to validate CMMs, sorbent traps, and a modified EPA Method 29 in a simulated syngas stream with a known amount of mercury.

Elemental mercury vapor from a Hg permeation source was carried by a N_2 stream and mixed with syngas constituents including H_2, CO, CH_4, CO_2, and H_2S. Two different syngas streams were generated for evaluation of the methods, with detailed syngas compositions listed in Table 4-10. The Hg-laden syngas was then heated to 400°F and pressurized to 600 psi, a typical operating condition for coal gasification. Mercury concentrations in the syngas stream were measured simultaneously with the three different mercury-sampling methods: a CMM (Horiba DM-6B), sorbent trap, and EPA Method 29. Note that an extra 500 mL 0.5M NaOH was added into the M29 impinger solution to remove H_2S, and possibly CO, through the following reactions:

$$2NaOH + H_2S \rightarrow Na_2S + 2H_2O$$
$$NaOH + CO \rightarrow NaCOOH \rightarrow NaCHO_2$$

The goal is to protect $KMnO_4$ from reacting with H_2S and CO. Standard protocols were applied to CMM and sorbent trap sampling.

In order to verify the accuracy of mercury measurement by directly sampling syngas, the same syngas was later combusted in a thermal oxidizer to convert to a combustion flue gas where the total mercury concentration was remeasured with the same three mercury sampling techniques. The derived mercury concentration in combustion flue gas served as a reference point and was compared to corresponding mercury measurement in syngas to determine the validity of mercury measurement in gasification applications.

Mercury Control in Syngas Conditions

Having established mercury-sampling protocols for syngas conditions, bench- and pilot-scale experiments were conducted to evaluate mercury capture with the EERC's proprietary sorbent in syngas streams. Over the years, the EERC has been developing metallic-based nanosorbents that are applicable to reducing syngas conditions at elevated temperatures conditions. The sorbents were initially tested in a bench-scale fixed-bed reactor through which mercury-laden simulated syngas stream flowed. Mercury emissions were monitored using a CMM to obtain mercury breakthrough data as a function of exposure time. The reactor was maintained at 400°F and 600 psi. The nominal gas flow rate was controlled at 5.3 scfh, which provided a space velocity of 1538 1/hr across the sorbent during the test. Syngas I, listed in Table 4-10, was selected for screening the sorbents to mimic a real coal gasification process, where most of the H_2S has been removed by desulfurization sorbents.

Table 4-10. Syngas Composition and Condition

	H_2, %	CO, %	CH_4, %	CO_2, %	N_2, %	H_2S, ppm
Syngas I	25	20	7.5	25	Balanced	0
Syngas II	25	20	7.5	25	Balanced	~625
Temperature	400°F					
Pressure	600 psi					

The most promising sorbent candidate identified by the bench-scale tests was then further evaluated in a real syngas environment. As shown in Figure 4-13, a subbituminous Powder River Basin coal was selected and gasified in a fluidized-bed reactor, and the resulting syngas passed through a warm-gas-cleanup system that included candle filters for PM capture, a fixed-bed reactor for sulfur removal, a water/gas catalyst (ShiftMax(R)120) reactor for CO reforming, and another fixed-bed reactor for sulfur polishing (Actisorb(R) S2). The cleaned syngas was then routed into a fixed-bed reactor for mercury capture. The syngas was maintained at ~500°F and ~220 psi. A CMM was also used to monitor mercury emissions at the outlet of the sorbent bed to obtain a mercury breakthrough curve as a function of time. The same syngas was also treated with a commercial sorbent for mercury capture, while sorbent trap sampling was conducted at the syngas exhaust to determine mercury emissions from the commercial sorbent. The derived results were compared with the mercury emission data for the EERC's sorbent.

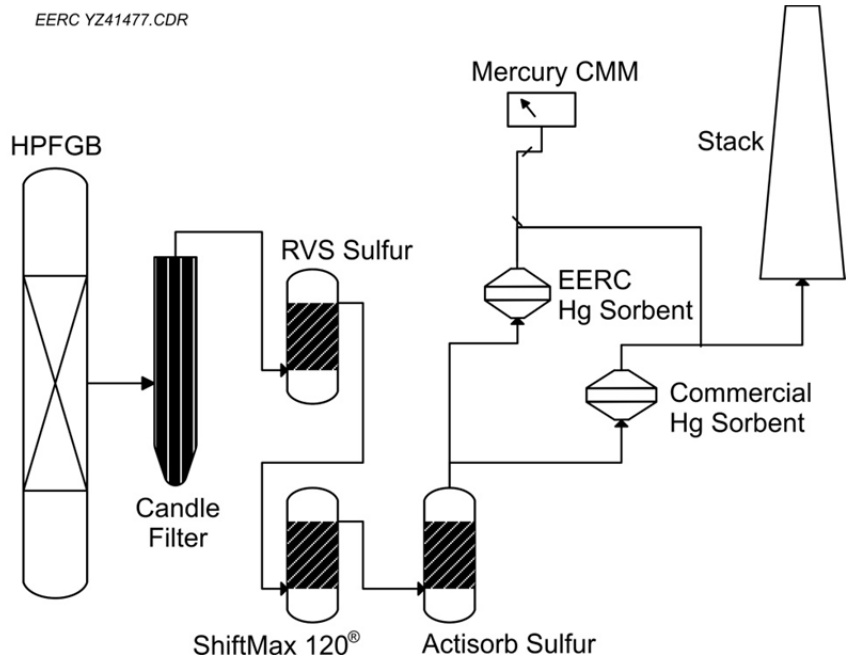

Figure 4-13. Schematic diagram of the pilot-scale test.

4.5.2 Results and Discussions

Evaluation of Mercury Measurement in Reducing Syngas Stream

Figure 4-14 summarizes the mercury measurement data with CMM, modified Method 29, and a sorbent trap. Syngas constituents, temperature, and pressure were selected and set to be representative to coal gasification applications. In addition to direct sampling syngas for mercury, the same syngas stream was fed into a thermal oxidizer to convert the syngas to a typical combustion flue gas oxidized state. The resulting combusted gas stream was also measured for mercury concentrations, and the derived results served as a reference and were compared with the sampling data from the syngas stream to determine if the three mercury-sampling techniques could provide valid results in syngas conditions.

Experimental data indicate that both CMMs and sorbent traps can provide consistent and accurate total mercury measurement in a syngas stream. Even with 625 ppm H_2S in the syngas, the measured mercury was approximately ±10% of its corresponding reference point. However, the modified Method 29 sampling data did not match its reference point very well. The relative difference is greater than ±10%. It is noted that Method 29 mercury data in syngas without H_2S was consistently lower than its reference point, while with H_2S in the syngas, the data were higher than the reference point. The interference is mainly caused by the unwanted reactions of $KMnO_4$ with reducing syngas constituents of CO and H_2S, possibly through the following pathways:

$$KMnO_4 + \frac{1}{2}CO \rightarrow MnO_2 + \frac{1}{2}K_2CO_3 + 0.5O_2$$

$$KMnO_4 + \frac{3}{2}H_2S \rightarrow MnO_2 + \frac{3}{2}S + KOH + H_2O$$

$$2KMnO_4 + H_2O + 6Hg \rightarrow 3Hg_2O + 2MnO_2 + 2KOH$$

As a result, $KMnO_4$ was overconsumed and could not capture Hg^0 efficiently.

Bench-Scale Sorbent Screening Test

The EERC has been developing various proprietary low-cost metallic nanosorbents for capturing Hg in syngas conditions. Figure 4-15 summarizes mercury removals within the first hour of syngas exposure for different metallic sorbents, including silica-based, iron-based, and copper-based composite sorbent. The copper-based composite sorbents were the research focus because of their low-cost and were synthesized through five different routes with different promoters.

Copper Composite 5 showed the highest mercury removal of 89% and was further investigated for its mercury adsorption kinetics by measuring mercury breakthrough curves as a function of syngas exposure time. The derived mercury breakthrough curves were plotted in Figure 4-16. Also included in Figure 4-16 is the mercury breakthrough curve when the same Copper Composite 5 sorbent was treated in situ with H_2 for 2 hr prior to syngas exposure. The overall mercury adsorption capacity of Cu Composite 5 sorbent was in the range of 137–

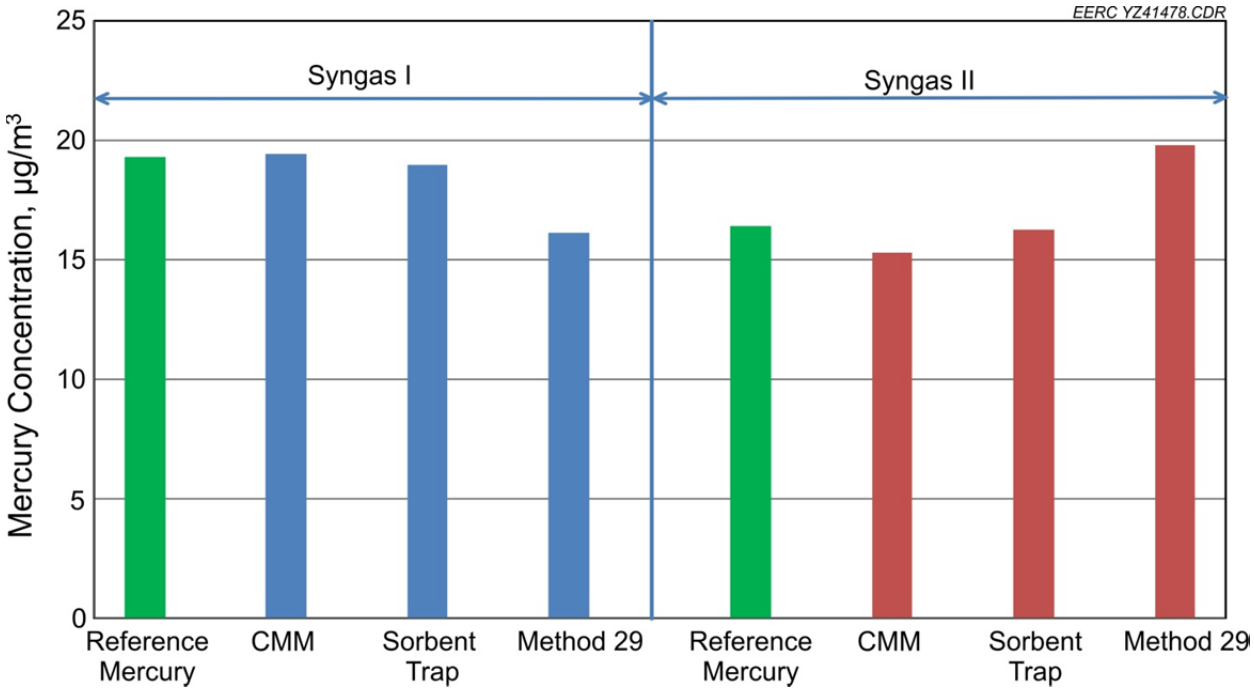

Figure 4-14. Comparison of mercury measurement in syngas.

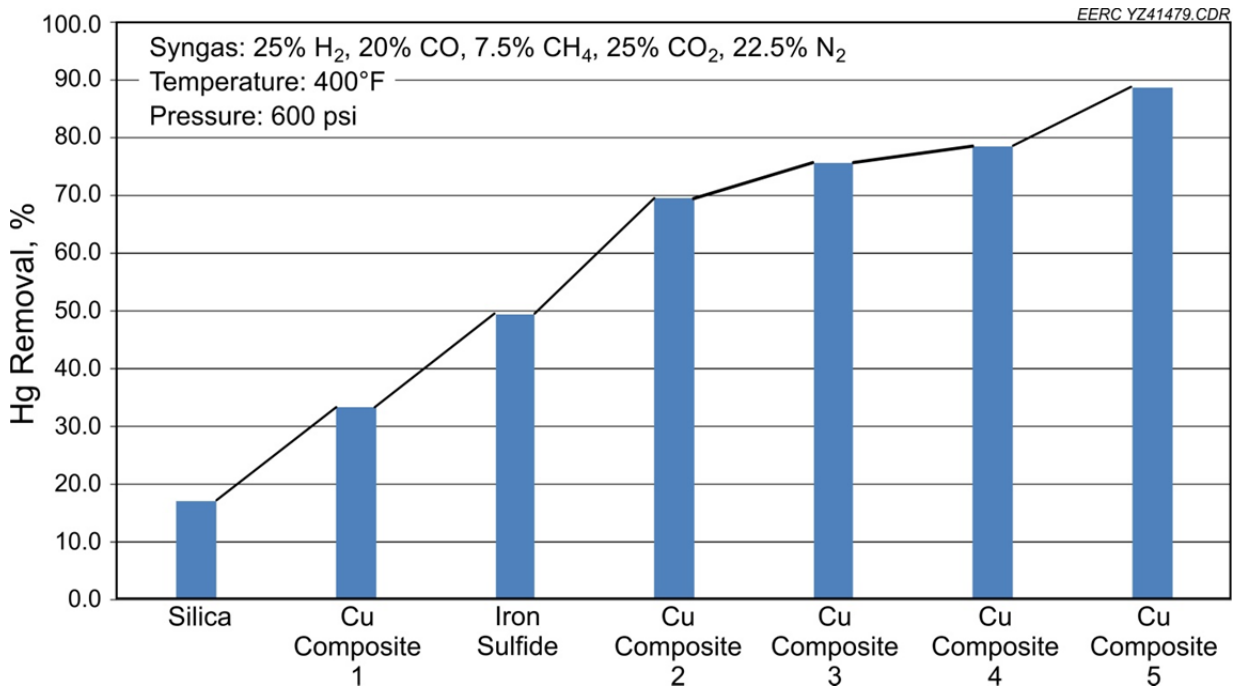

Figure 4-15. Sorbent screening test in Syngas I.

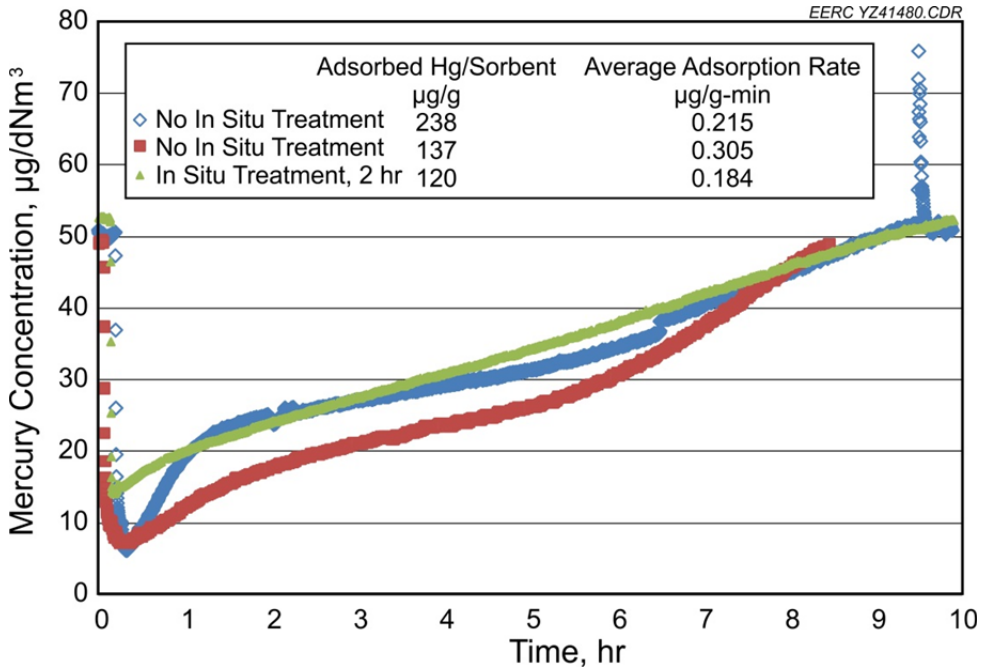

Figure 4-16. Mercury breakthrough curves for Cu-based sorbent in Syngas I, 400°F.

238 µg-Hg/g sorbent, with an averaged specific adsorption rate of 0.2–0.3 µg/g-min. The supplementary in situ H_2 treatment did not improve mercury capture. Since there was no H_2S and/or carbonyl sulfide (COS) in the simulated syngas stream, the observed mercury capture with the copper sorbent is mainly due to the formation amalgam where the mercury was bound within copper matrix through a small amount of charge transfer to provide a metallic type of bonding with delocalized electrons in conduction bands.

Pilot-Scale Mercury Sorbent Evaluation

The Copper Composite 5 sorbent was further evaluated in a real syngas stream from a fluidized-bed coal gasifier, as shown in Figure 4-13. Table 4-11 lists the proximate/ultimate analysis data of the coal tested, and Table 4-12 lists the syngas condition to which the mercury sorbent was exposed.

Mercury vapor concentration was initially measured with a CMM to establish mercury baseline, and the CMM data are plotted in Figure 4-17, showing mercury vapor concentration in the syngas stream varied from 10 up to 55 µg/m^3, with an average value of 26 µg/m^3. Note that, based on the mercury content in the coal (0.05 µg/g dry basis), the coal feed rate, and the volume of syngas produced, it is estimated that ~32 µg/m^3 mercury is in the syngas. The variation of the measured mercury concentration was mainly caused by gasifier operation.

Because the operating condition of the coal gasifier was changed later in the test, mercury concentration in the syngas was increased to ~50 µg/m^3 in comparison with 62 µg/m^3 mercury estimated based on the coal feed rate and volume of syngas generated. The syngas was then

Table 4-11. Proximate/Ultimate Analysis of the Tested PRB Coal*

	As-Det.	As-Rec'd.	Dry	Dry-/Ash-Free
Proximate Analysis, wt%				
Moisture	11.38	24.41	N/A	N/A
Volatile Matter	34.07	29.06	38.44	40.63
Fixed Carbon, ind.	49.77	42.45	56.16	59.37
Ash	4.79	4.08	5.40	N/A
Ultimate Analysis, wt%				
Hydrogen	5.44	6.28	4.70	4.97
Carbon	61.63	52.57	69.54	73.51
Nitrogen	4.79	4.08	5.40	5.71
Sulfur	0.35	0.30	0.39	0.42
Oxygen, ind.	23.01	32.69	14.57	15.40
Ash	4.79	4.08	5.40	N/A
Heating Value, Btu/lb	10,340	8820	11,668	12,334

* As-received hydrogen not including hydrogen from moisture 4.07%; as-received oxygen not including oxygen from moisture 15.09%.

Table 4-12. Syngas Composition and Condition of Pilot-Scale Test

	H_2, %	CO, %	CH_4, %	CO_2, %	N_2, %	H_2S, ppm
Syngas	32.6	8.3	3.0	48.0	2.5	0.175
Temperature	530°F					
Pressure	280 psi					

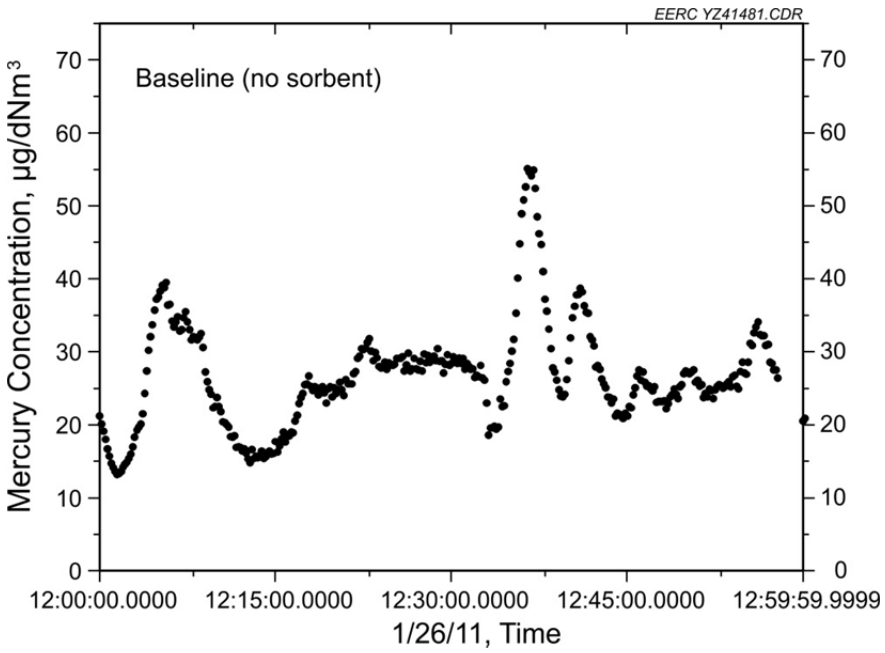

Figure 4-17. Mercury baseline in the test syngas.

introduced into the fixed-bed reactor where the sorbent was loaded. Mercury vapor concentration at the outlet was measured as a function of time, as shown in Figure 4-18. Also included in Figure 4-18 is the estimated mercury concentration of the syngas during the test. The CMM indicated that mercury emission was reduced from ~50 µg/ mercury vapor to less than 5 µg/m^3. For the approximately 2-hr testing period, the averaged mercury emission after the sorbent reactor was 2.83 µg/m^3. The same syngas was also treated with a commercial sorbent for mercury capture, and the resulting sorbent trap sampling data indicated mercury emission was reduced to ~3.33 µg/m^3.

4.5.3 Conclusions

Mercury-sampling data indicate that both CMM and sorbent trap methods were capable of providing accurate Hg measurement in a reducing syngas stream, while results of a wet-chemistry method, such as EPA Method 29, showed interference from reactions between syngas constituents and reagents used in the wet-chemistry sampling.

Copper-based nanocomposite sorbents were synthesized and tested in a bench-scale fixed-bed reactor, which was maintained at a temperature of 400°F with a pressure of 600 psi, in which simulated syngas containing H_2, CO, CO_2, CH_4, and N_2 flowed through. The mercury breakthrough curves indicated that overall mercury adsorption capacity of Copper Composite 5 sorbent was in the range of 137–238 µg Hg/g sorbent with an average specific adsorption rate of 0.2–0.3 µg/g min. The copper nanocomposite sorbent was further evaluated in a real syngas

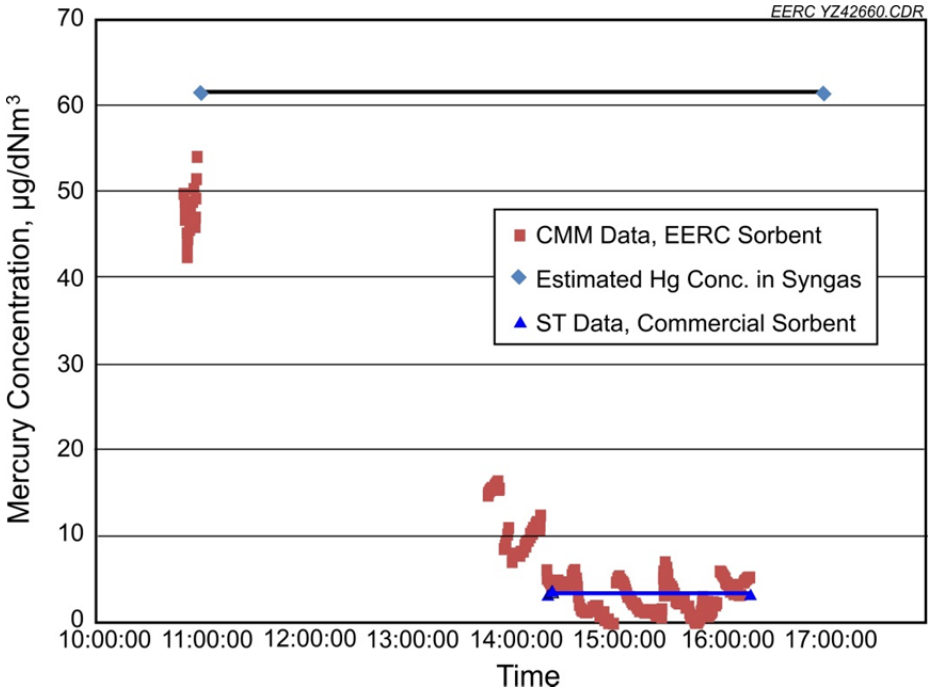

Figure 4-18. Mercury emission after copper-based sorbent treatment.

stream generated from coal gasification. For the approximately 2-hr testing period, the average mercury emission after the sorbent reactor was 2.83 μg/m^3, slightly better than a commercial sorbent for mercury capture that indicated ~3.33 μg/m^3 mercury emission during the test.

The pilot-scale evaluation data prove that the copper-based, low-cost nanosorbent can effectively scavenge mercury vapor in a real syngas condition, and the resulting mercury removal was similar to, or slightly better than, that of commercial sorbent.

4.6 Mercury Emissions from a CO_2 Amine Scrubber and Corrosion of Steels in a CO_2-Rich Post-Amine Stripper Atmosphere

4.6.1 Experimental Approach

Mercury Emission from a CO_2 Amine Scrubber

A pilot-scale amine scrubber was added to the EERC's pilot-scale combustion system. The configuration of the combustion system includes a pc-fired combustor followed by a FF for fly ash capture, a wet scrubber for SO_2 removal, and an amine scrubber and amine stripper for CO_2 capture. A low-sulfur subbituminous coal (Antelope) was burned in the combustor, and OH method sampling was carried out at the SO_2 scrubber outlet, amine scrubber outlet, and stripper outlet, respectively, to establish mercury transformation across the amine scrubber.

Corrosion of Steels in a CO_2-Rich Post-Amine Stripper Atmosphere

In order to characterize Hg-induced corrosion in an elevated CO_2 environment, a bench-scale experimental apparatus was structured to test the corrosion of common steels in a simulated environment downstream of an amine stripper prior to the carbon dioxide compression stage.

A simulated flue gas stream containing 85 ppmv amine vapor, 20 ppm mercury, 70.6% CO_2, and 29.3% water vapor was introduced into the reaction chamber, which was maintained at atmospheric pressure and a temperature of 60°C (140°F). For comparison, a similar flue gas stream without the presence of Hg^0 was also used as baseline condition. Figure 4-19 shows a schematic of the gas-handling system for the sample chambers. A standard commercial grade of Praxair carbon dioxide was obtained and used without further purification. The house nitrogen supply was used for purging as required. A permeation cell held at a temperature of −8°C (17.6 °F) was used to produce Hg^0 vapor. Water and amine vapor were introduced as a liquid solution into a preheater for vaporizing, with the subsequent vapor flow split between the two sample chambers (with and without Hg). Huntsman Petrochemical Corporation 85% MEA was diluted with deionized (DI) water to produce a 30% MEA solution.

The CO_2 or purge nitrogen supply was split between flowmeters to provide gas to Chamber 1 (no Hg) and to the Hg permeation tube. To achieve the desired Hg concentration and flow rate, the flow exiting the permeation tube was split between flowmeters to Chamber 2 and to a bypass line. Most of the flow exits through the bypass line. It was found that moisture condensing in the exit lines outside the heated sample box would force of all the gas flow

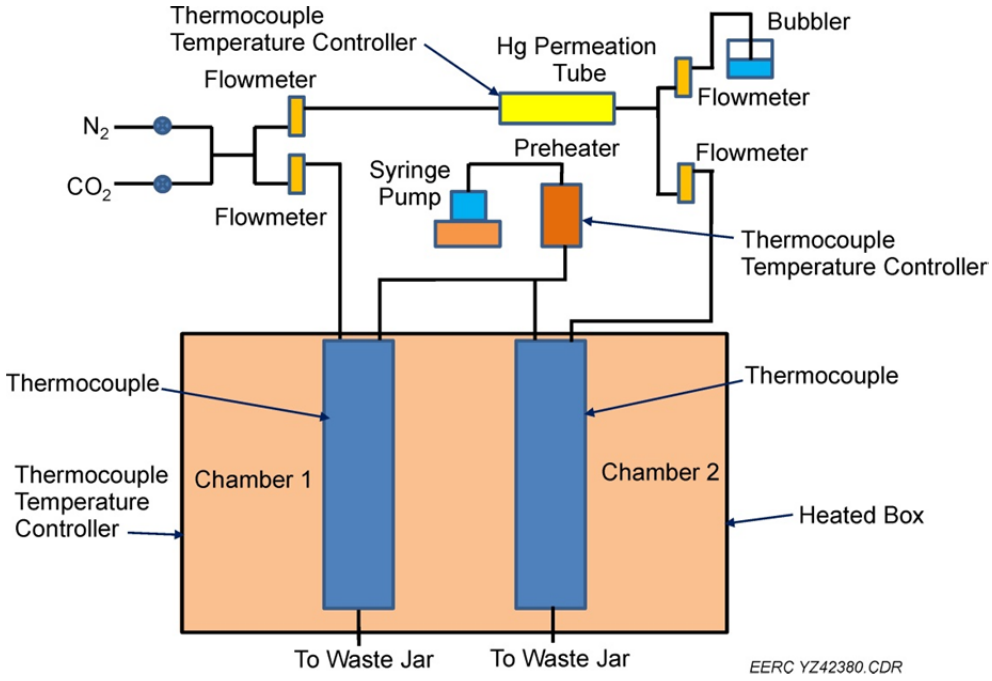

Figure 4-19. Schematic of the gas-handling system for the sample chambers.

through the bypass line. A water bubbler at the exit of the bypass line was used to provide sufficient back pressure to overcome this. An Instrument Specialties Co. Model 314 syringe pump (capacity 375 mL) was used to meter the water–amine solution into the sample chambers. The injection line first passes through a preheater to vaporize the solution, which is then split between the two sample chambers. It is assumed that equal amounts of vapor enter each chamber.

Coupons of 316L stainless steel, 304L stainless steel, and C1018 mild steel were selected for the corrosion test. Coupon dimensions were 7.62 cm (3”) in length, 1.27 cm (0.5”) in width, and 1.5875 mm (0.0625”) in thickness with a 4.7752 mm (0.188”) mounting hole drilled at one end. Chemical composition of the steel lots from which the coupons were fabricated are listed in Table 4-13. Sufficient coupons were purchased to provide triplicate samples of the three steels at three exposure times for the two different gas compositions (18 coupons of each steel type). Figure 4-20 shows the arrangement of the coupons on the holders, and Figure 4-21 shows the sample holder with coupons in place.

The coupons were cleaned by sonicating in 800 mL DI water with 1 mL of Cole-Parmer Micro 90 detergent for 10 minutes. They were then rinsed with DI water and sonicated in 800 mL DI water. They were then rinsed with 95% ethyl alcohol, placed on chemwipes on a metal tray, and dried at 105°C (192°F) for 0.5 hour before cooling and weighing.

The holders with mounted coupons were placed in the sample chambers. They were heated under a nitrogen purge with no MEA solution flow until the heated box was at a stable set point temperature of 60°C (140°F), with the preheater temperature at 75°C (167°F). The gas flow was

Table 4-13. Coupon Compositions (balance iron), wt%

	C	Mn	P	S	Si	Cu	Ni	Cr	Mo
316L Stainless Steel	0.0265	1.4585	0.0295	0.0010	0.2620	0.4300	10.1050	16.6960	2.0540
304L Stainless Steel	0.0202	1.7350	0.0300	0.0010	0.3570	0.6750	8.0100	18.1570	0.3300
C1018 Mild Steel	0.1900	0.6700	0.0030	0.0010	0.0200	0.0800	0.0400	0.0300	0.0200
	Sn	Al	V	Nb	N	Ti	Ba	Ca	Sn
316L Stainless Steel	0.0000	0.0000	0.0000	0.0000	0.0447	0.0000	0.0000	0.0000	0.0000
304L Stainless Steel	0.0000	0.0000	0.0000	0.0000	0.0609	0.0000	0.0000	0.0000	0.0000
C1018 Mild Steel	0.0080	0.0300	0.0030	0.0040	0.0070	0.0040	0.0000	0.0010	0.0080

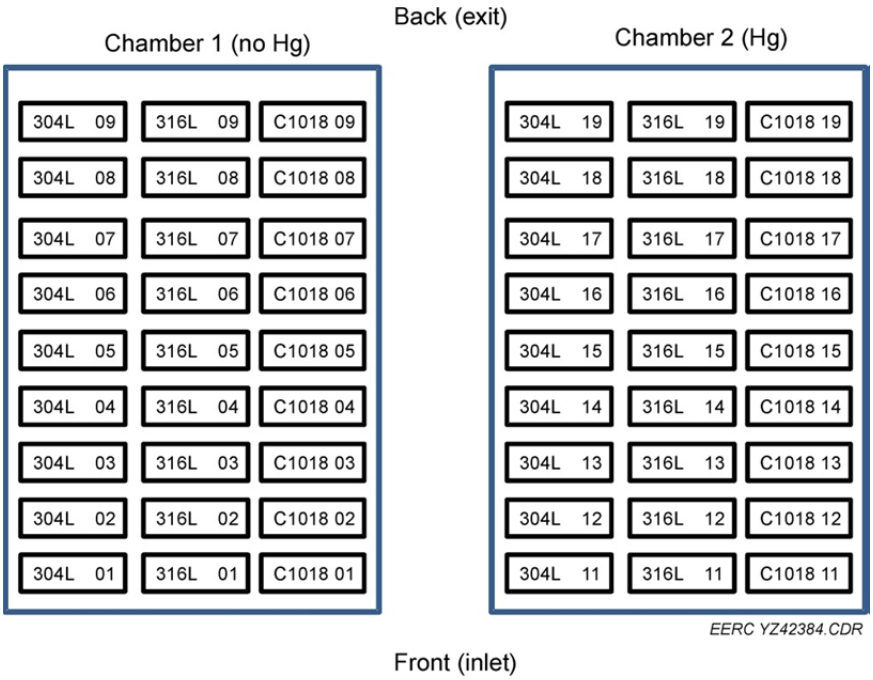

Figure 4-20. Coupon arrangement.

Figure 4-21. Coupon holder with spacers and coupons in place.

then switched to the simulated flue gas stream. After planned exposure times, the gas flow was switched from CO_2 to the nitrogen purge, the MEA mixed flow stopped with the pump flow reversed to remove any solution in the line to the preheater, and the heaters for the preheater and the box containing the chambers shut off. When the chambers had cooled to room temperature, they were opened and selected sets of coupons removed. The chambers were then resealed and the box heated back to operating temperature following the same start-up procedure. The removed coupons were weighed as soon as possible after removal.

4.6.2 Results and Discussions

Mercury Emission from a CO_2 Amine Scrubber

A pilot-scale combustion test has been performed to evaluate mercury speciation across the amine scrubber that was used to capture CO_2 from coal combustion flue gas. The system was configured so the flue gas passed through the SCR unit, ESP, FGD scrubber, direct contact cooling, liquid desiccant dehumidification system (LDDS), and amine scrubber before exiting through the stack. The average flue gas concentrations at the furnace exit and the stack for each sampling period are presented in Table 4-14, and the analysis for the PRB subbituminous coal used during these runs is presented in Table 4-15. The CO_2 in the flue gas was captured in the amine scrubber by MEA at a concentration of 30%–35% by weight with a balance of DI water. Mercury samples were collected at the inlet and outlet of the amine scrubber using the OH method and speciating sorbent traps.

Table 4-14. Flue Gas Concentrations Across the Combustion System

Run No.	AF-CTS-1103		AF-CTS-1104		AF-CTS-1121	
Date	01/28/10		02/01/10		03/17/10	
Sample Location	Furnace Exit	Stack	Furnace Exit	Stack	Furnace Exit	Stack
NO_x, ppm	674	39.6	520	40.3	206	14.1
SO_2, ppm	284	ND[1]	328	ND	194	29.3
CO_2, %	16.4	4.5	16.4	4.8	5.8	2.9
O_2, %	3.4	4.5	3.4	4.6	3.7	5.0
Temperature, °F	337	317	354	323	338	311

[1] Not detected.

Table 4-15. Antelope Valley Coal Analysis

	As Fired	Moisture-Free
Proximate Analysis, wt%		
Moisture	19.00	N/A
Volatile Matter	41.19	50.87
Fixed Carbon, ind.	34.31	42.34
Ash	5.5	6.79
Ultimate Analysis, wt%		
Hydrogen	6.09	4.91
Carbon	53.23	65.74
Nitrogen	0.53	0.66
Sulfur	0.32	0.39
Oxygen, ind.	34.33	21.51
Ash	5.5	6.79
Heating Value, Btu/lb	8693	10,736

Table 4-16 presents a summary of the mercury data collected during the combustion tests. The objective of the sampling was to determine if mercury was captured or oxidized in the amine scrubber. The results show there was less than 2.0 $\mu g/m^3$ of total mercury in the flue gas by the time it reached the amine scrubber. For the first two tests, the mercury was almost all elemental but greater than 70% oxidized for the third test. Regardless of the speciation, the data do not show that any mercury was captured across the amine scrubber or that the speciation was altered.

Corrosion of Steels in CO_2-Rich Post-Amine Stripper Atmospheres

The corrosion exposure test last approximately ~600 hours, while triplicate sets of coupons were removed at 208, 440, and 600 hours for weight measurement. The weight gain/loss of the coupons is plotted as a function of exposure time in Figure 4-22. There was effectively no change (either gain or loss) in coupon weight over the duration of the test. The greatest change

Table 4-16. Mercury Speciation Data Across Amine Scrubber

Date	Run No.	Sample Port	Sample Type	Hg^{2+}, $\mu g/m^3$	Hg^0, $\mu g/m^3$	$Hg_{(T)}$, $\mu g/m^3$	Hg^{2+}, %	Hg^0, %
1/28/10	AF-CTS-1103	Amine scrubber inlet	Sorbent trap	0.06	0.40	0.45	13	89
		Amine scrubber outlet	OH method	0.04	1.39	1.43	3	97
		Amine scrubber outlet	Sorbent trap	.000	1.04	1.04	0	100
2/01/10	AF-CTS-1104	Amine scrubber inlet	OH method	0.03	1.20	1.23	2	98
		Amine scrubber inlet	Sorbent trap	0.10	1.66	1.77	6	94
		Amine scrubber outlet	OH method	0.00	1.36	1.36	0	100
		Amine scrubber outlet	Sorbent trap	0.01	1.40	1.42	1	99
03/17/10	AF-CTS-1121	Amine scrubber inlet	OH method	0.73	0.29	1.02	71	29
		Amine scrubber inlet	Sorbent trap	1.31	0.33	1.64	80	20
		Amine scrubber outlet	OH method	1.34	0.58	1.92	70	30
		Amine scrubber outlet	Sorbent trap	0.91	0.46	1.37	66	34

was a gain of 0.4 mg for the 304L coupons after 440 hours. The 304L coupons are the only ones that show gains in weight, which may be statistically significant (greater than two standard deviations). However, because of the very small weight changes, this result may be suspect. No noticeable difference in weight change between the coupons with and without Hg in the gas stream was seen.

Visually, there was no apparent change in the coupons after 208 hours. After 440 hours, a few isolated small pitting (rust spots) were seen on the C1018 mild steel. After 602 hours, the pitting on the C1018 coupons was still isolated, but somewhat more extensive. Isolated dots,

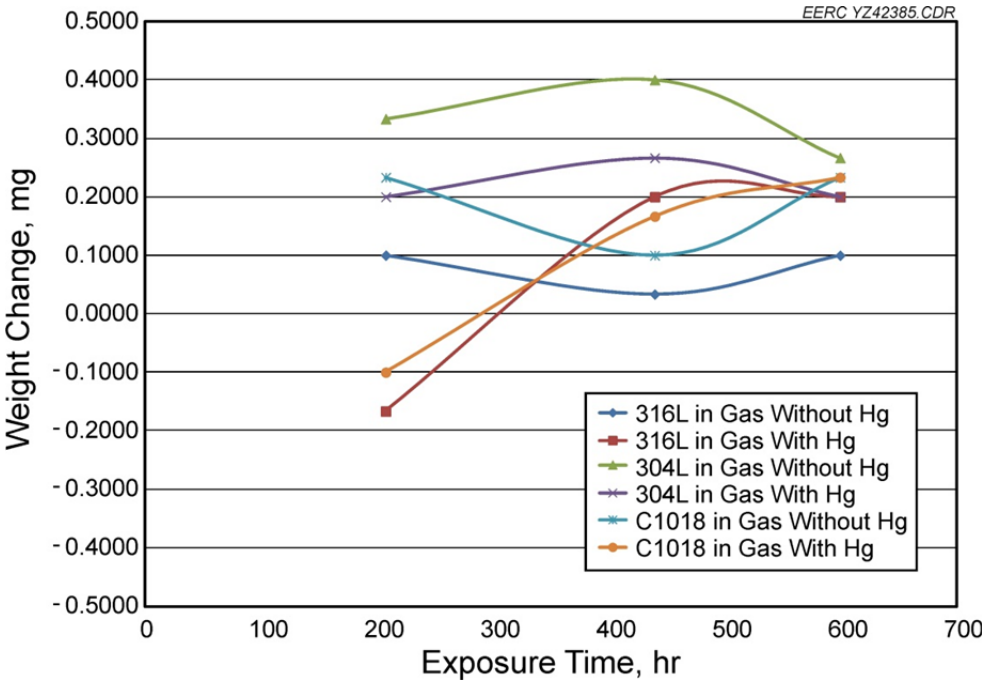

Figure 4-22. Weight gain/loss of coupons in post-amine flue gases with and without Hg.

unlike those on the mild steel were seen on the 304L coupons. No noticeable change was observed for the 316L steel. The surfaces of three coupons were examined by scanning electron microscopy (SEM) and chemical analyses performed at points along a line on the coupons. Coupons 316L 03, 304L 03, and C1018 04 (all in the gas atmosphere without Hg) were selected for examination.

Figures 4-23 and 4-24 show a line scan across the coupon of 316L, showing no visible evidence of corrosion or pitting. The major components of the steel are Fe and Cr. The Fe content shows decreases because of grains containing Si naturally in the steel. Other elements showed no discernible trend.

Isolated dots could visually be seen on the surface of the 304L coupon. Under SEM examination, these appear to be "exfoliated" corrosion areas. A line scan of one of these areas is shown in Figures 4-25 and 4-26. As in the 316L stainless steel, there are grains containing Si. These are not associated with the exfoliated area. The exfoliated corrosion area shows a dramatic decrease in Fe and Cr content, along with very high Na concentrations. The Na does not appear to be associated with elevated Cr levels. The origin of the Na is not known, possible sources being the amine solution or residual fingerprints on the chamber surfaces. As noted previously, the coupons themselves were cleaned and handled with gloves or tweezers. The tests do indicate that the presence of sodium or other alkali elements may be significant in producing corrosion of the 304L steel. It is hypothesized that sodium ion could possibly react with amine oxygen formed on the metal surface after the loss of Fe and Cr.

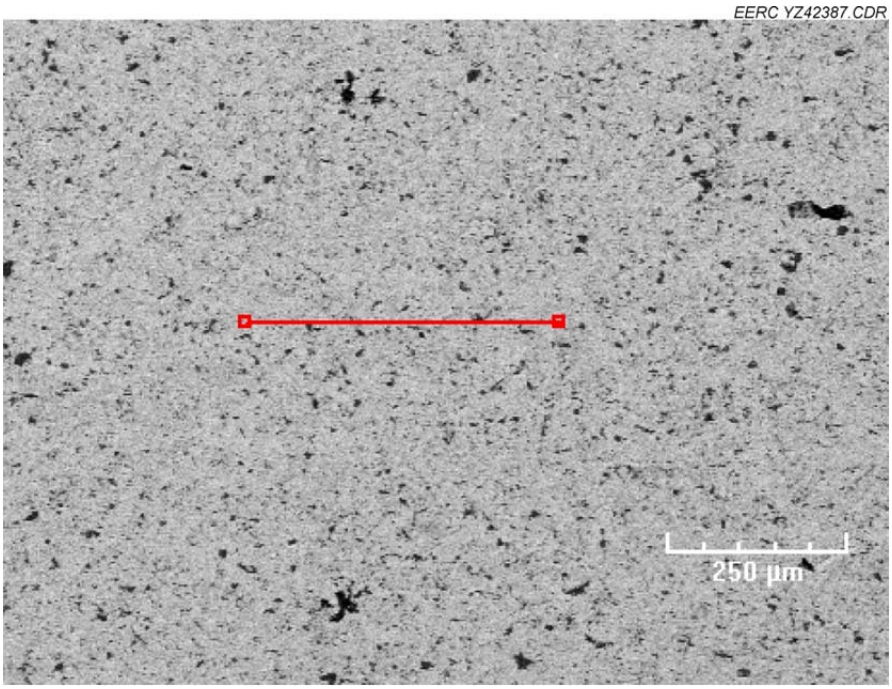

Figure 4-23. SEM image of 316L 03 coupon. Analysis was along the line from left to right.

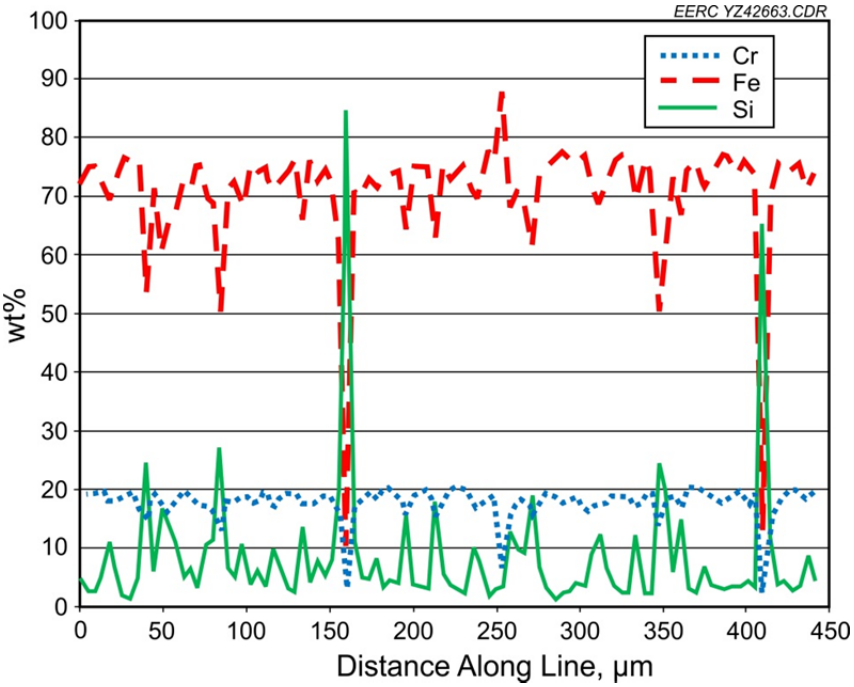

Figure 4-24. Analysis of 316L 03 coupon showing Fe, Cr, and Si concentrations.

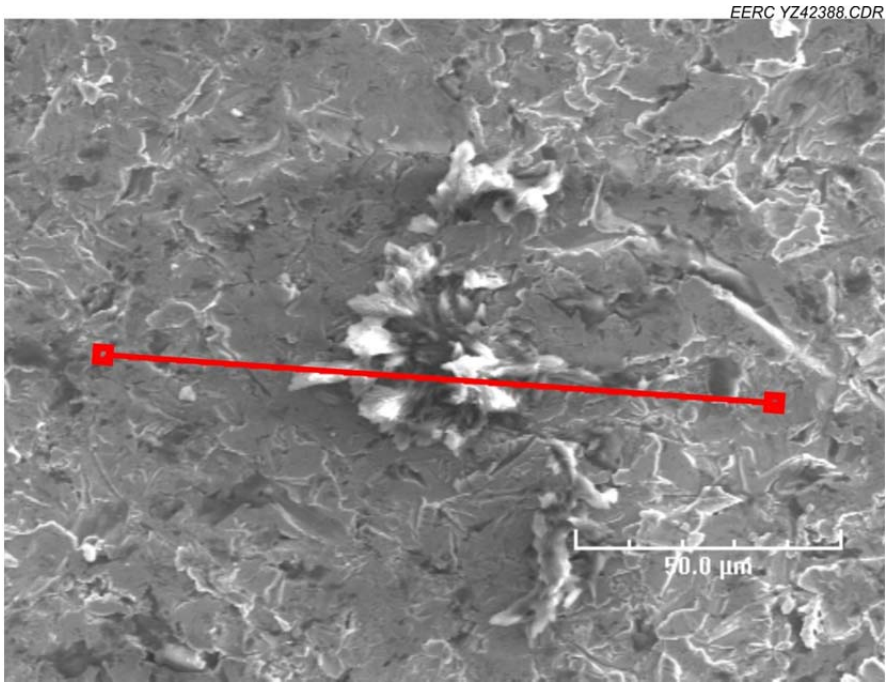

Figure 4-25. SEM image of 304L 03 coupon. Analysis was along the line from left to right.

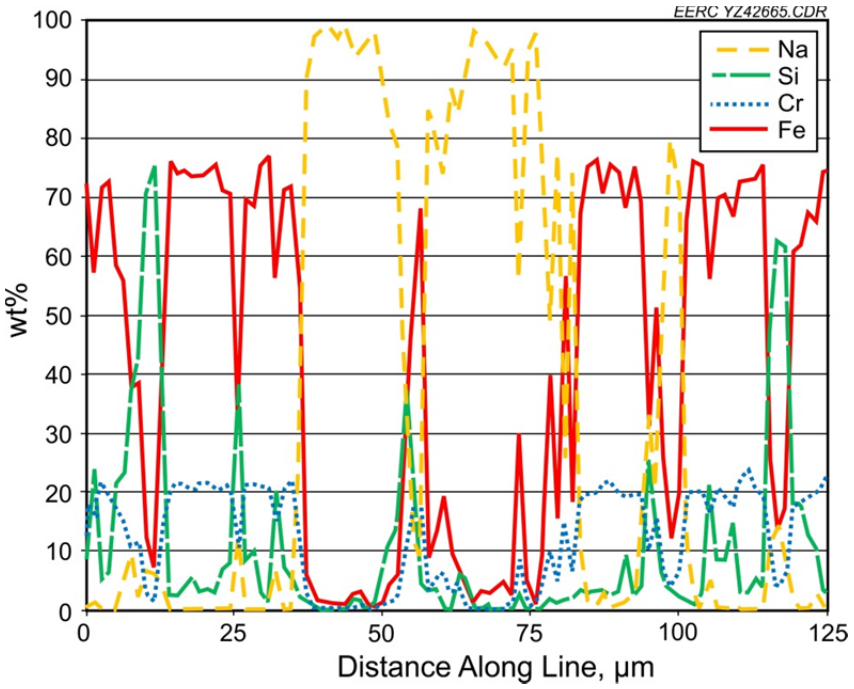

Figure 4-26. Analysis of 304L 03 coupon showing Fe, Cr, Si, and Na concentrations.

The C1018 coupons showed the greatest amount of corrosion, although this was still in the form of isolated dots. Figures 4-27 and 4-28 show a line scan across one of the corroded areas. The corroded area shows almost no change in Fe concentration and is not associated with either Na or Si. On the unaffected steel, there are some areas of elevated Si because of natural grains. The analysis is consistent with the formation of iron oxide (Fe_2O_3) on the surface. Since oxygen is not quantified by the analysis, the Fe concentration of iron and iron oxide remain effectively the same.

No mercury species were found on the testing coupons, mainly because Hg and its compounds are volatile and decompose under the SEM electron beam.

4.6.3 Conclusions

Mercury-sampling data indicated no mercury was captured across the amine scrubber or that the mercury speciation was altered.

Very little corrosion was observed for the three steels during the 600-hour testing at 60°C (140°F) in a CO_2–water vapor atmosphere with trace amounts of MEA and mercury present. There was no difference in corrosion due to the presence of mercury. No clearly statistically significant gain or loss of coupon mass was found.

The 316L stainless steel showed the least effect, with no clearly observable corrosion. The 304L stainless steel exhibited isolated dots of corrosion. These are associated with the depletion

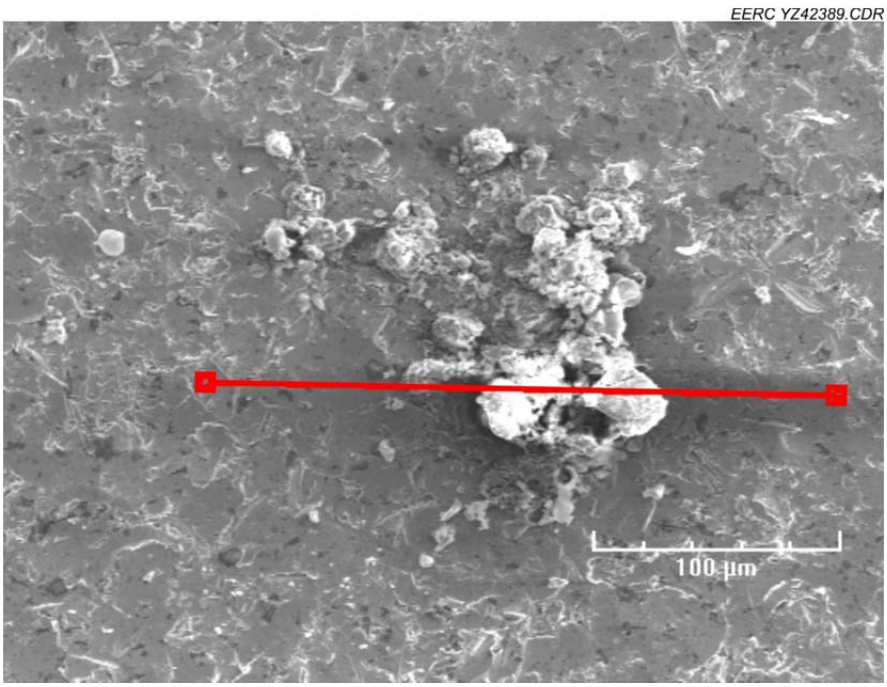

Figure 4-27. SEM image of C1018 04 coupon. Analysis was along the line from left to right.

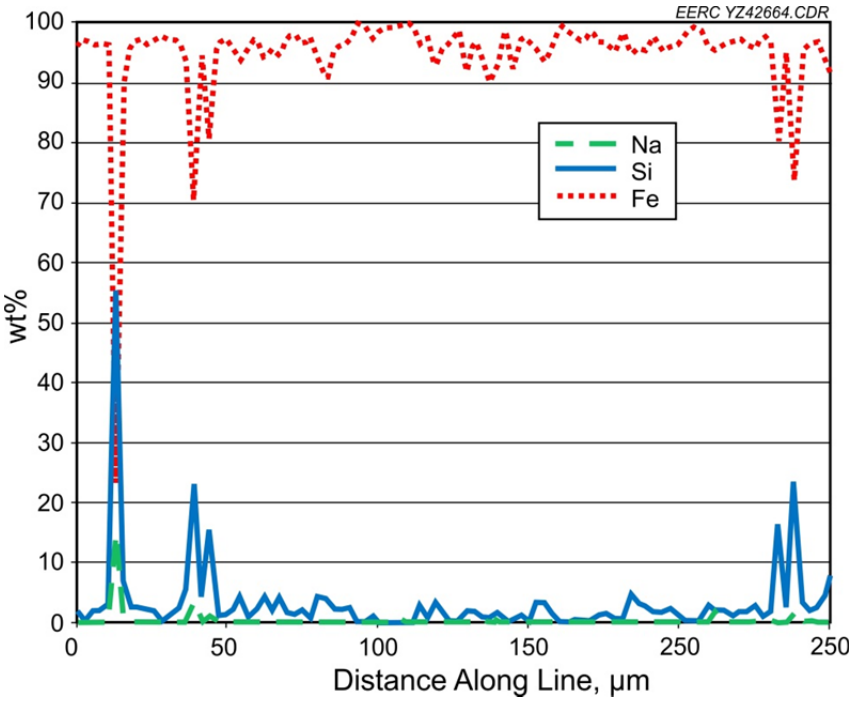

Figure 4-28. Analysis of C1018 04 coupon showing Fe, Si, and Na concentrations.

of Fe and Cr and the presence of elevated sodium concentrations. The presence of sodium in a system with CO_2, water vapor, and MEA presence may exacerbate corrosion of 304L steel. The C1018 mild steel showed the most corrosion, although this was confined to isolated dots on the surface. This corrosion appears to be simple rusting and not associated with sodium. However, it should be noted that the present exposure experiments were conducted under ambient pressure and at relatively low temperatures, whereas both temperature and pressure will increase as the Hg-laden flue gas goes through a compression stage. Although the data present here indicate no significant corrosion across the amine scrubber, additional research should be continued to further evaluate Hg-induced corrosion after the compression stage.

4.7 References

1. Intergovernmental Panel on Climate Change. *Climate Change 2001. The scientific basis;* 2001.

2. Wall, T.F. Combustion Processes for Carbon Capture. In *Proceedings of the Combustion Institute;* 2007.

3. Okawa, M. et al. Trial Design for a CO_2 Recovery Power Plant by Burning Pulverized Coal in O_2/CO_2. *Energy Convers. Manage*. **1997**, *38*.

4. Nsakala, N.Y. et al. Engineering Feasibility of CO_2 Capture using Existing U.S. Coal-Fired Power Plant. In *1st National Conference on Carbon Sequence*; Washington D.C., May 15–17, 2001.

5. Rathnam, R.K.; Elliott, L.; Moghtaderi, B.; Gupta, R.; Wall, T.F. Differences in Coal Reactivity in Air and Oxy-Fuel Conditions and Implications for Coal Burnout. In *The 31st International Technical Conference on Coal Utilization and Fuel Systems;* Clearwater, FL, 2006.

6. Shaddix, C.R.; Murphy, J.J. Coal Char Combustion Reactivity in Oxy-Fuel Applications. In *20th Pittsburgh Coal Conference*; Pittsburgh, PA, 2003.

7. McCauley, K.J.; Farzan, H.; Alexander, K.C.; McDonald, D.K.; Varagani, R.; Prabhakar, R.; Tranier, J.P.; Perrin, N. Commercialization of Oxy-Coal Combustion: Applying Results of Large 30-MWth Pilot Project. *Energy Procedia* **2009**, *1*, 439–446.

8. Nimmo, W.D., Daood, S.S.; Gibbs, B.M. The Effect of O_2 Enrichment on NO_x Formation in Biomass Co-Fired Pulverised Coal Combustion. *Fuel* **2010**, *89* (10), 2945–2952.

9. Croiset, E.; Thambimuthu, K.V. NO_x and SO_2 emissions from O_2/CO_2 Recycle Coal Combustion. *Fuel* **2001**, *80* (14), 2117–2121.

10. Hu, Y.Q.K.; Kobayashi, N.; Hasatani, M. The Reduction of Recycled-NO_x in Coal Combustion with O_2/Recycled Flue Gas under Low Recycling Ratio. *Fuel* **2001**, *80* (13), 1851–1855.

11. Okazaki, K.; Ando, T. NO_x Reduction Mechanism in Coal Combustion with Recycled CO_2. *Energy* **1997**, *23* (2/3), 207–215.

12. Hu, Y.N.; Naito, S.; Kobayashi, N.; Hasatani, M. CO_2, NO_x and SO_2 Emissions from the Combustion of Coal with High Oxygen Concentration Gases. *Fuel* **2000**, *79* (15), 1925–1932.

13. Fleig, D. et al. The Fate of Sulphur During Oxy-Fuel Combustion of Lignite. *Energy Procedia* **2009**, *1*, 383–390.

14. Santos, S. *Challenges in Understanding the Fate of Mercury during Oxyfuel Combustion*. In *MEC7 Workshop*; DLCS, Strathclyde University, Glasgow, Scotland, June 16–18, 2010.

15. Qiu, J.L.; Liu, H.; Wen, C.; Zeng, H.; Wu, H. Particulate Matter, Mercury and Trace Metals Emissions in Oxy-Coal Combustion. In *233rd ACS National Meeting*; Chicago, IL, March 25–29, 2007.

16. Ueno, S.-I.; Sato, N.; Kawata, H.; Yamada, T. The Behavior of Mercury in the Flue Gas of Oxy-Coal Combustion. *Sekitan Kagaku Kaigi Happyo Ronbunshu* **2008**, *45,* 82–83.

17. Sekine, Y. et al. Release Behavior of Trace Elements from Coal During High-Temperature Processing. *Powder Technology* **2008**, *180*, 210–215.

18. Sloss, L.L. *Mercury – Emissions and Control*; IEA Coal Research: London, 2002.

19. Frandsen, F.; Dam-Johansen, K.; Rasmussen, P. Trace Elements from Combustion and Gasification of Coal – An Equilibrium Approach. *Progress in Energy and Combustion Science* **1994**, *20*, 115.

20. Helble, J.J. et al. Trace Element Partitioning During Coal Gasification. *Fuel* **1996**, *75* (8), 931–939.

21. Bunt, J.R.; Waanders, F.B. Trace Element Behaviour in the Sasol–Lurgi MK IV FBDB Gasifier, Part 1 – The Volatile Elements: Hg, As, Se, Cd and Pb. *Fuel* **2008**, *87*, 2374–2387.

22. Reed, G.P. et al. Control of Gasifer Mercury Emissions in a Hot Gas Filter: The Effect of Temperature. *Fuel* **2001**, *80*, 623–634.

23. Lu, D.Y.; Granatstein, D.L.; Rose, D.J. Study of Mercury Speciation from Simulated Coal Gasification. *Industrial & Engineering Chemistry Research* **2004**, *43*, 5400–5404.

24. Meij, R. A Sampling Method Based on Activated Carbon for Gaseous Mercury in Ambient Air and Flue Gases. *Water Air Soil Pollut*. **1991**, *56*, 117.

25. U.S. Environmental Protection Agency. *Information Collection Request for Electric Utility Steam Generating Unit Mercury Emissions Information Collection Effort*; 1999; EPA ICR No. 1858.

26. Pflughoeft-Hassett, D.F. *IGCC and PFBC By-Products Generation, Characteristics, and Management Practices*; U.S. Environmental Protection Agency, 1997.

27. Ratafia-Brown, J. et al. *Major Environmental Aspects of Gasification-Based Power Generation Technologies;* Final Report for Gasification Technologies Program; National Energy Technology Laboratory, U.S. Department of Energy, Dec 2002.

28. Wagner, N.J.; Hlatshwayo, T.B.; Ginster, M. A Source Apportioned Mercury Mass Balance Across a Coal-Based Petrochemical Complex. *Fuel Processing Technology* **2008**, 1351–1357.

29. Rutkowski, M.D.; Klett, M.G.; Maxwell, R.C. The Cost of Mercury Removal in an IGCC Plant. In *Gasification Technologies 2002*; San Francisco, CA, 2002.

30. Eastman Chemical. In *Environmental Performance/Issues of Gasification-Based Power System*, McLean, VA, 2001.

31. Reed, G.P. et al. Trace Element Distribution in Sewage Sludge Gasification: Source and Temperature Effects. *Energy & Fuels* **2005**, *19* (1), 298.

32. Granite, E.J.; King; W.P. Pennline, H.W. Techniques for Mercury Control and Measurement in Gasification System. In *5th International Symposium on Gas Cleaning at High Temperature*; Morgantown, WV, 2002.

33. Musich, M.A. et al. Advanced Mercury and Trace Metal Control with Monolith Traps. In *24th Annual International Pittsburgh Coal Conference 2007;* Curran Associates, Inc.: Johannesburg, South Africa, 2007.

34. Steckel, J.A. Density Functional Theory Study of Mercury Adsorption on Metal Surfaces *Physical Review B: Condensed Matter and Materials Physics* **2008**, *77* (11), 115412/–115412/13.

35. Granite, E.J. et al. Sorbents for Mercury Capture from Fuel Gas with Application to Gasification Systems. *Industrial & Engineering Chemistry Research* **2006**, *45*, 4844–4848.

36. Poulston, S. et al. Metal Sorbents for High Temperature Mercury Capture from Fuel Gas. *Fuel* **2007**, *86,* 2201–2203.

37. Sugier, A.; La Villa, F. Process for Removing Mercury from a Gas or a Liquid by Absorption on a Copper Sulfide Containing Solid Mass. Institut Francais du Petrole France, 1976.

38. Rao, A.B.; Rubin, E.S. A Technical, Economic, and Environmental Assessment of Amine-Based CO_2 Capture Technology for Power Plant Greenhouse Gas Control. *Environmental Science & Technology* **2002**, *36*, 4467–4475.

39. Rennie, S. Corrosion and Materials Selection for Amine Service. *Materials Forum* **2006**, *30*, 126–130.

40. Goutier, F. et al. Oxidation of Stainless Steel 304L in Carbon Dioxide. *Corrosion Science* **2010**, *52*, 2403–2412.

41. Nengkoda, A. et al. Understanding of Mercury Corrosion Attack on Stainless Steel Material at Gas Well: Case Study. In *Society of Petroleum Engineers-International Petroleum Technology Conference 2009;* 2009, pp 958–965.

42. Miller, S.J. et al. Flue Gas Effects on a Carbon-Based Mercury Sorbent. *Fuel Processing Technology* **2000**, *65–66,* 343–363.

43. Laumb, J.D.; Benson, S.A.; Olson, E.A. X-Ray Photoelectron Spectroscopy Analysis of Mercury Sorbent Surface Chemistry. *Fuel Processing Technology* **2004**, *85* (6–7), 577–585.

44. Zhuang, Y. et al. Impact of Calcium Chloride Addition on Mercury Transformations and Control in Coal Flue Gas. *Fuel* **2007**, *86* (15), 2351–2359.

45. Tan, Y. et al. Combustion Characteristics of Coal in a Mixture of Oxygen and Recycled Flue Gas. *Fuel* **2006**, *85*, 507–512.

46. Banchero, J.T.; Verhoff, F.H. Evaluation and Interpretation of the Vapor Pressure Data for Sulphuric Acid Aqueous Solutions with Application to Flue Gas Dewpoints. *Inst. Fuel* **1975**, 76–80.

47. Zhuang, Y.P.; Martin, C.; Botha, F. Cobenefit of SO_3 Reduction on Mercury Capture with Activated Carbon in Coal Flue Gas. *Fuel* **2011**, *90*, 2998–3006.

5.0 FATE AND CONTROL OF MERCURY AND TRACE ELEMENTS IN POWER SYSTEMS WITH CONVENTIONAL AND MULTIPOLLUTANT CONTROL TECHNOLOGIES

5.1 Activity Objectives

The original goals of the proposed research under this activity were to:

- Create a predictive model for mercury control with AC, based on the fundamental CATM-developed model for mercury–carbon interactions.
- Develop effective, noncontaminating in-flight mercury sorbents using methods for preparing highly-dispersed, catalytically active materials.
- Develop structurally resilient ACs that have sufficient reactivity for mercury control and are strong enough to withstand multiple exposure–regeneration cycles.
- Identify surface-modified ACs that have improved mercury capacities in SO_2-containing flue gas by selectively slowing the oxidation of SO_2 to H_2SO_4 on the carbon surface.
- Identify promising additives and technologies that either oxidize elemental mercury or prevent its reemission across wet FGD systems.
- Develop a mechanistic understanding of mercury–slurry interactions to guide the development of new trace metal control technologies.
- Develop vapor-phase selenium control technologies based on understanding the chemical and thermophysical properties of flue gas selenium.

A number of individual approaches were taken to pursue each of the goals outlined above. These approaches are broadly grouped into the topics of mercury sorbent development, wet FGD mercury capture and retention, and selenium capture technology development. The rationale for each investigated approach and the obtained results are discussed according to these topic areas.

5.2 Mercury Sorbent Development

This topic area incorporates those approaches that are intended to either improve or develop new sorbent-based options for mercury control. AC injection is the most mature retrofit technology for mercury capture at existing coal-fired power plants. Despite this development, a number of improvements would facilitate mercury capture. Activity within this topic area includes investigation of the underlying mechanisms involved with AC sorbents such as modeling of in-flight mercury capture and fundamental measurements of reactivity. In addition, a number of approaches were pursued to develop novel sorbents that were intended to address specific shortcomings of conventional sorbents. Sorbent development activities included a composite sorbent, a class of inorganic sorbents, and improvements to carbon-based sorbents including the development of a durable AC and evaluation of surface modified carbons.

5.2.1 Modeling In-Flight Mercury Capture

AC is the most developed mercury control technology for coal-fired utilities, yet its removal efficiency varies greatly from plant to plant and from coal type to coal type. The EERC, under previous CATM-sponsored work (1), created a mechanistic model for mercury capture on AC. The model is comprehensive and provides a basis for interpreting the observed interactions between mercury and AC. The objective of this approach was to combine this interaction model with mass transfer calculations that represent the situation of in-flight mercury capture. This applied model of in-flight mercury capture could then be used to identify the factors that limit mercury capture and provide insight to optimize activated carbon injection (ACI) system performance.

To develop the applied model, a simplified reaction pathway was identified within the CATM mechanistic model that includes only those reactions that are relevant to in-flight capture. This central pathway was identified from the strongest sensitivities identified during previously performed, parametric, fixed-bed tests (1) to investigate the effects of specific flue gas constituents on the mercury capture process. The applied model was then substantiated with relative kinetic data and structural information about AC that was also collected from previous CATM work (2). Calculated mercury capture data generated by the applied model were compared to experimentally measured mercury removal data for a variety of coal types for a qualitative validation, and finally, the model was used to perform a sensitivity study to identify the limiting mechanisms for the in-flight capture of mercury on AC. Figure 5-1 diagrammatically shows the interactions that have been identified through this parametric testing.

The mechanistic model highlights many reactions that impact mercury capture under various flue gas chemistries, including, for example, active site promotion, elemental mercury oxidation, reemission of volatile mercury species, and competition from SO_2 and SO_3 for active sites on the carbon. During development of an applied model for in-flight mercury capture, a simplified version of the mechanistic model was implemented that incorporates only the reaction pathways relevant to in-flight capture. The simplified reaction pathway for the engineering model of in-flight capture consists of the following steps:

- Available oxidation sites on the carbon surface must be promoted by specific flue gas constituents, flue gas additives, or pretreatment before they can support Hg^0 oxidation or Hg^{2+} capture. HCl, SO_3, and SO_2 are key activation agents as identified from fixed-bed testing.

- Hg^{2+} can be captured directly on the carbon, but Hg^0 must undergo an oxidation step at an activated site for capture to occur at flue gas temperatures.

- Activated sites on the carbon can also be occupied by H_2SO_4 derived from a direct reaction with SO_3 vapor (and omnipresent moisture) or as the result of an oxidation reaction with SO_2. Once an activated site is occupied by H_2SO_4, it can no longer support mercury capture.

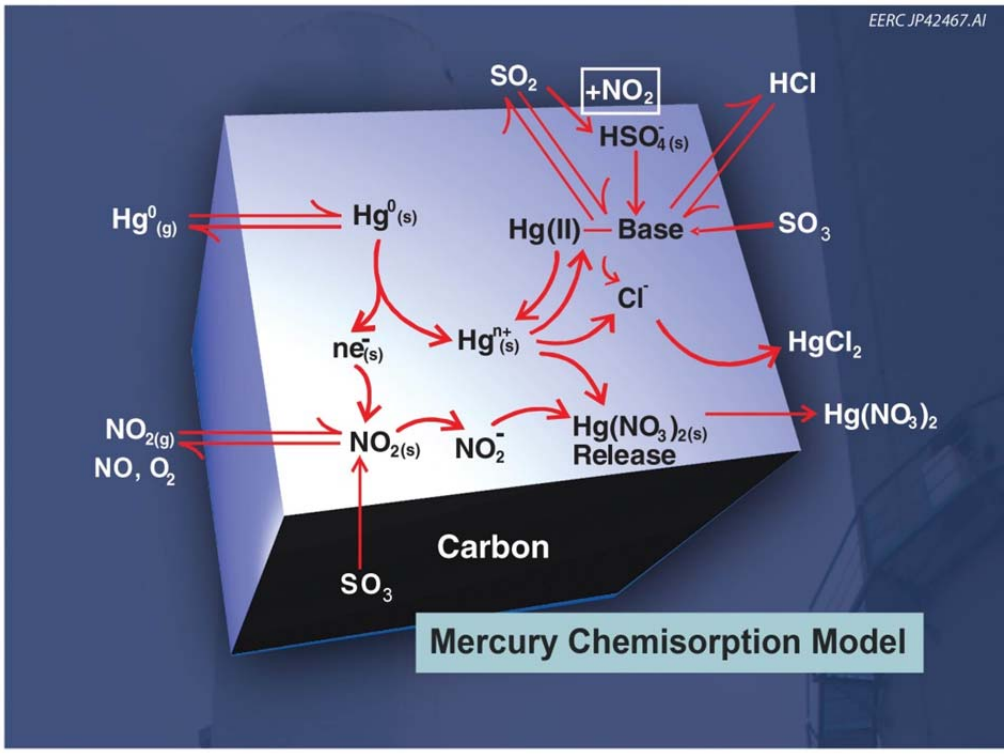

Figure 5-1. Mechanistic mercury–AC interaction model.

- Based on fixed-bed test results, NO_2 appears to be a primary oxidant for Hg^0 and SO_2 since it rapidly speeds mercury capture compared to other potential oxidants in flue gas (2).

The simplified, in-flight reaction pathway outlined above is implemented in the applied model as a series of elementary reactions involving flue gas species and sites on the carbon sorbent. The sites are modeled as being in one of three states that represent the sequence of site activation and occupation by H_2SO_4. Potential sites are considered to be inherent structures on the carbon that can support oxidation and chemisorption. Three pathways are considered for available site (AS) promotion:

$$HCl + AS \rightarrow \text{Promoted Site (PS)} \quad [1]$$
$$SO_2 + NO_2 + AS \rightarrow PS \quad [2]$$
$$SO_3 + AS \rightarrow PS \quad [3]$$

The acid gas components, HCl, SO_2, and SO_3, have been identified as site promoters from parametric, fixed-bed testing since they have a significant effect on reducing the induction period for untreated carbons (2). Once promoted sites exist on the carbon, they can be consumed by mercury or competing species as outlined in the following reactions.

$$Hg^0 + NO_2 + PS \rightarrow \text{Consumed Site (CS)} \quad [4]$$
$$Hg^{2+} + PS \rightarrow CS \quad [5]$$

$$H_2O + xSO_2 + NO_2 + PS \rightarrow CS \quad [6]$$

$$H_2O + SO_3 + AS \rightarrow CS \quad [7]$$

In the applied model of in-flight mercury capture, no further reactions are considered for the consumed sites on the carbon. However, fixed-bed testing clearly shows that reactions still occur at these sites; for example, mercury oxidation is still supported at the consumed sites, and volatile mercury salts can be displaced from the consumed sites by H_2SO_4 accumulation. While these reactions clearly occur, they have a minimal impact on in-flight mercury capture and are disregarded in this first-order engineering approximation.

Note that in Equation 6, a scale factor, x, is incorporated to account for the slower kinetics of SO_2 oxidation relative to the other reaction steps. This factor is defined and discussed further in a subsequent section.

The elementary reactions outlined in Equations 1–7 determine how species interact when they are brought together; the rate that species are brought together is determined by mass transfer between sorbent particles and the surrounding flue gas. Simplifying assumptions are used to speed calculation. For instance, bulk mass transfer of gas-phase species to the AC is based on a monodisperse particulate size distribution for the AC. Furthermore, it is assumed that the injected carbon is uniformly distributed throughout the flue gas and that the individual carbon particles are fully entrained with the flow of flue gas. Full entrainment assumes that there is zero relative velocity between the flue gas and the carbon particles; therefore, mass transfer is dominated by diffusion of species through the gas to the carbon surface.

The diffusion transport of flue gas constituents to the entrained sorbent can be described using Equation 8:

$$\frac{dC_i}{dt} = -k_g \frac{a}{V}\left(C_i - C_i^*\right) \quad [8]$$

Where C_i is the gas-phase concentration of species i; k_g is the mass transfer coefficient of gas phase species i to the entrained sorbent, a/V is the total surface area of sorbent per unit volume of flue gas, and C^*_i is the concentration of the adsorbed species i at the sorbent surface. Since experimental data suggest that the relevant reaction kinetics are much faster in comparison to the mass transfer time scale, the reactant concentration at the carbon surface was approximated by equating it to zero.

The mass transfer coefficient (k_g in Equation 8) for the gas-phase diffusion of a species i to the surface of a sorbent particle can be estimated using Equation 9:

$$k_g = \frac{2 \cdot D_i}{d_p} \quad [9]$$

Where D_i is the diffusivity of species *i* in flue gas and d_p is the diameter of the sorbent particle.

As for the carbon particles themselves, they are assumed to be uniform spheres with available sites distributed across the surface. Interparticle diffusion is assumed to have minimal effect for in-flight capture and is not considered in this approximation. To account for the evolution of available sites to promoted sites and eventually to consumed sites, the surface area term is modified by the ratio of specific site type to the total number of available sites. The modified form of Equation 8 that is used to calculate the transport of species to the sorbent particles is presented as Equation 10:

$$\text{Transport of Species i to Target Sites per Time Step} = -k_g \frac{a}{V}\left(\frac{\text{Target Sites}}{\text{Total Sites}}\right)(C_i)\Delta t \qquad [10]$$

Species that reach the surface and react according to one of the reaction steps in Equations 1–7 are deducted from the current time step flue gas concentration, and a new concentration, C_i, is calculated accordingly.

The mechanistic model is constructed around the concept that mercury reactions take place at distinct sites on the carbon. In the applied model, the number of sites is finite, and their depletion is central to explaining the macro-scale results for in-flight mercury capture. The estimate for the number of available sites on the carbon sorbent is based on the accumulated sulfates at the point of mercury breakthrough during a fixed-bed test. It is assumed that breakthrough represents the point at which essentially all of the sites that are able to support mercury capture have been occupied, primarily by H_2SO_4 formed from sulfur oxides in the flue gas. Previous work has measured the SO_2 oxidation rate on AC (3), and this rate was used to estimate sulfate concentration at breakthrough for a fixed-bed test. The resultant estimate for site density was 3.4 moles of available sites per kg of AC.

Differences between treated and untreated carbons are modeled by changing the initial fraction of promoted sites. For treated carbons, it was assumed that 100% of the available sites were promoted through the treatment process, while for the untreated carbon, a presumed fraction of 70% promoted sites seemed to give reasonable agreement over multiple sets of experimental data.

For the primary reaction pathway, the kinetics are assumed to be significantly faster than the time scale needed for mass transfer; therefore, the reactions are modeled to occur completely within the time steps used to calculate gas-phase species diffusion. The one exception is the SO_2 oxidation reaction, Equation 6, which is a competing reaction to mercury oxidation, Equation 4, in terms of NO_2 use and promoted site consumption. Given the relative abundance of SO_2 in flue gas compared to mercury, it is readily apparent that the mercury oxidation reaction is highly preferred to that of SO_2, otherwise significant mercury capture would not be possible. This relative preference or equivalent reaction rate ratio of SO_2 versus mercury oxidation is a key parameter for modeling in-flight mercury capture.

Previous fixed-bed measurements of SO_2 oxidation determined that 1.2 mg of sulfate accumulated per minute of exposure time for both treated and untreated carbons (3). For the specific conditions of those experiments, that rate equates to approximately 1 mole of SO_2 oxidizing on the carbon out of each 192 moles that reached the surface. This reaction rate

fraction is incorporated in the engineering model by introducing the factor x in Equation 6, to account for the 1/192 fraction of SO_2 molecules that oxidize. It is probable that this oxidation fraction is a function of flue gas composition and temperature and that the measured rate is only accurate for the specific test conditions (low acid gas). However, in the absence of a more complete data set, x was set to 1/192 for all modeling.

For the sake of calculation efficiency, the modeled particle-size distribution of the AC was assumed to be monodisperse, i.e., consisting of a single diameter particle. The diameter was chosen to provide an equivalent mass transfer rate as that from an actual AC sample on a unit mass basis. The measured AC particle-size distribution that was used to determine the monodisperse particle diameter is shown in Figure 5-2.

In the calculations, particle size is a factor in the mass transfer coefficient, k_g, and the ratio of sorbent surface area to flue gas volume, a/V, in Equation 10. When simplified, the net effect of particle-size distribution in Equation 10 is proportional to the product of particle diameter and the number of particles for each diameter. For a polydisperse size distribution, the combined term is approximated by the sum of the individual number and diameter products. Equation 11 equates this summation to the product of a monodisperse particle-size distribution, where n is the number of particles of a given diameter, d.

$$\sum_{j=d_{\min}}^{d_{\max}} (nd)_j = (nd)_{monodisperse} \qquad [11]$$

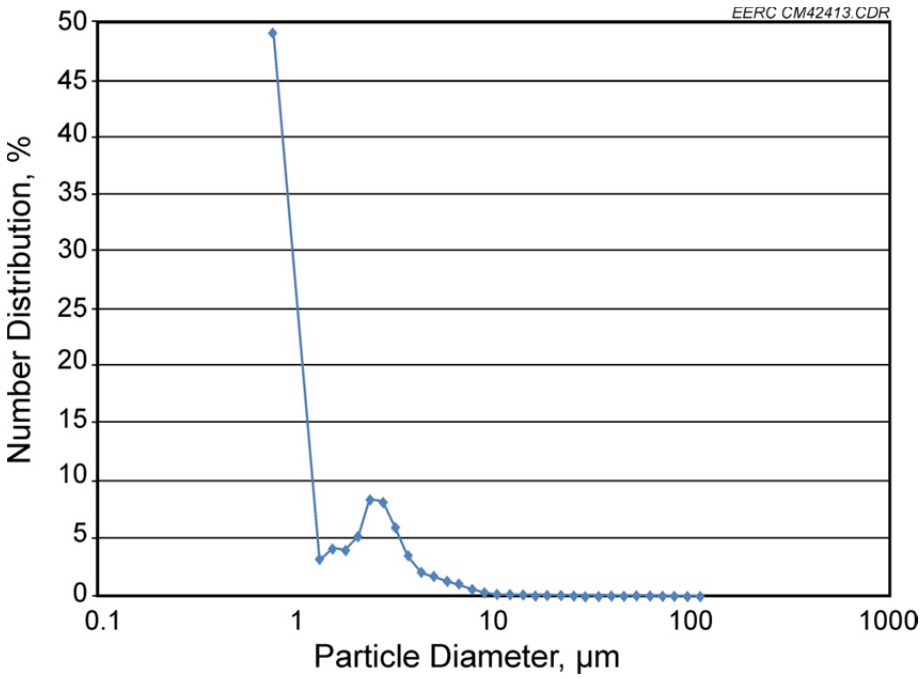

Figure 5-2. Measured particle-size distribution for the modeled AC.

By assuming spherical particles and a constant material density, the monodisperse particle diameter in Equation 11 can be determined; for the measured particle-size distribution of Figure 5-2, it was found to be 6.2 μm.

Results from the engineering model of in-flight mercury capture have been compared to experimental results measured on the EERC's particulate test combustor (PTC) for a variety of coals. The PTC is a good source for comparative data since its AC injection setup is well characterized and the small duct diameters ensure good mixing between the sorbent and flue gas. Comparative test data were selected from PTC test results collected within the last 5 years, 2005–2010.

During PTC operation, several model input parameters are recorded; for verification modeling, these measured parameters were used directly in the applied model calculations. These parameters included flue gas flow rate, temperature, and composition (SO_2 and Hg). Also used in the model were the ACI rate and type of carbon. If available, supplemental flue gas composition data were also used, including HCl, and SO_3. Unfortunately, NO_2, which is the required oxidant in the model, was not measured independently; therefore, NO_2 input values were adjusted based on reasonable NO_2 values expected in flue gas in good agreement with the experimental data. A summary of the model inputs is provided in Table 5-1.

Results of the validation modeling using the parameters in Table 5-1 are plotted in Figure 5-3, along with the experimentally measured PTC data. As shown in the figure, the modeling results reasonably reproduce the measured mercury removal data. For instance, the model calculates the distinctive capture "plateau" for the low- and medium-sulfur subbituminous coals owing to a depletion of oxidant. On the other hand, results with the high-sulfur eastern bituminous coal show the distinctive dampening due to a combination of SO_2 and SO_3 competition for sites on the carbon. The model also appears to reflect the slight advantage that a standard carbon has over a treated carbon in the high-sulfur flue gas. The higher initial reactivity of the treated carbon results in a slight penalty to mercury capture because SO_2 and SO_3 site consumption begins instantly.

Table 5-1. Modeling Inputs Based on Measured PTC Data

Flue Gas Conditions	Medium-S Subbituminous Treated AC	Low-S Subbituminous Treated AC	Low-S Subbituminous Standard AC	High-S Lignite Treated AC	High-S Bituminous Standard AC	High-S Bituminous Treated AC
Temp., °F	350	300	300	350	300	300
% Hg^0	84	75	75	69	22	22
SO_2, ppm	440	173	173	1200	3470	3470
HCl, ppm	N/A	N/A	1	N/A	9.1	9.1
SO_3, ppm	1.5	1	1	0	28	28
NO_2, ppm	3.5	0.9	0.9	0.5	50	50

Note: Shaded cells indicate estimated values, all other data from measured conditions.

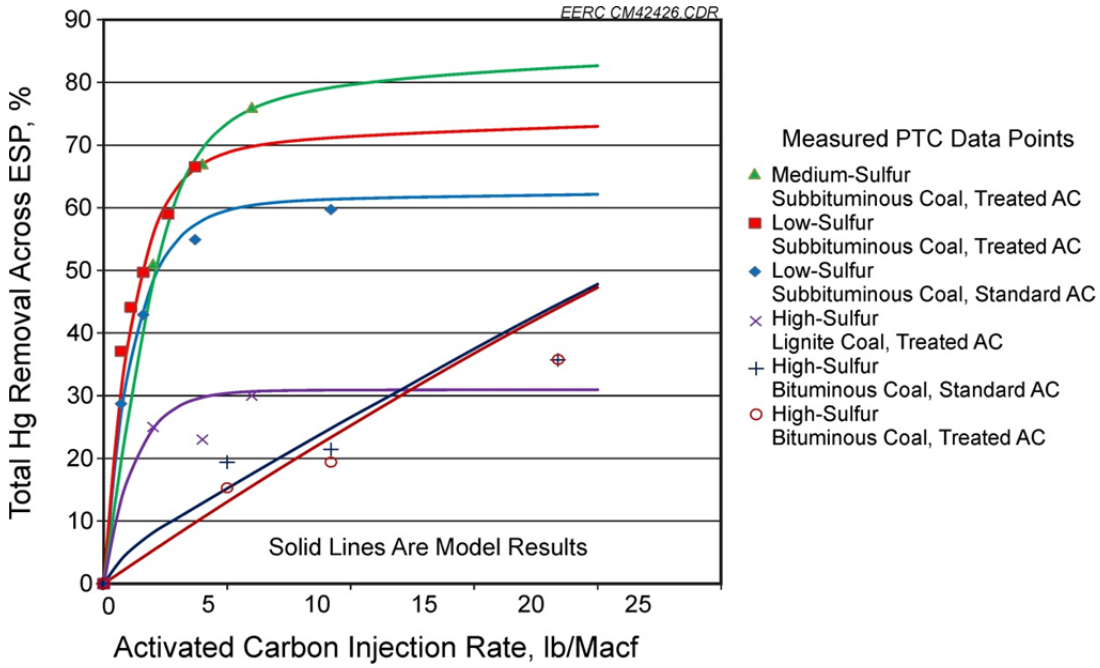

Figure 5-3. Comparison of model results to measured in-flight mercury capture data.

In addition to the qualitative validation of Figure 5-3, the model was also used to perform a sensitivity study of in-flight mercury capture. In practice, this case is encountered with AC injection into an ESP. Mercury capture across other air pollution control devices, e.g., a fabric filter or spray dryer, are quite different, and the identified trends will not necessarily apply.

The sensitivities explored have distinctive impacts to the overall mercury removal curve and can be grouped according to their resultant impact to mercury capture. Figure 5-4 is a generic mercury removal curve that could be expected from the in-flight capture of mercury. Three distinct regimes have been identified where distinct mechanisms can be associated with limiting mercury capture. These regimes include the extreme situations that are labeled "site-limited" and "reactant-limited" which are bridged by the third regime labeled "second-order effects."

In the site-limited regime, mercury capture is limited by the sites available to support oxidation and mercury capture. The fundamental limitation here is the site density available on the AC itself. For sorbents capable of supporting in-flight capture, the site density itself is usually not the limitation; more typical is limitation based on direct competition for activated sites from flue gas species that have similar mass transfer and reaction kinetics to mercury. SO_3 vapor has been shown to provide such competition (4). Common site-limited situations arise with native SO_3 produced during combustion of high-sulfur coals, when SO_3 is generated from SO_2 oxidation across SCR catalyst, and when SO_3 is injected for ash conditioning and improved particulate control. Sensitivity calculations for two of these situations are shown in Figure 5-5.

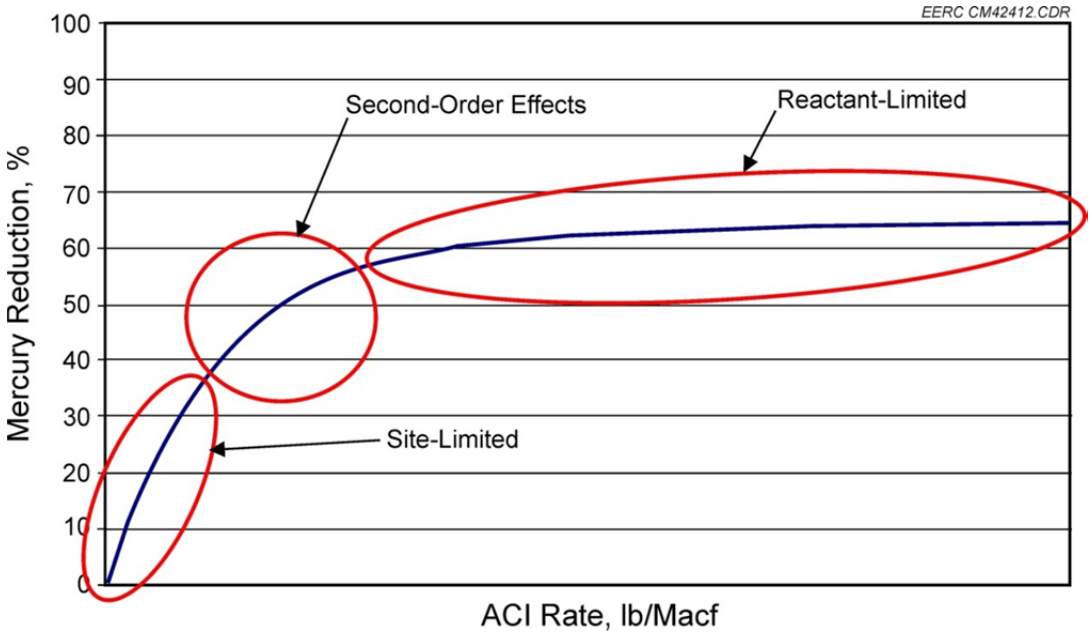

Figure 5-4. Generalized mercury removal performance curve highlighting distinct limiting regimes.

The reactant-limited regime falls at the opposite end of the mercury capture performance curve. According to the simplified engineering model for mercury capture, two additional flue gas constituents are typically needed to enable mercury capture in addition to mercury itself. HCl or other acid gases are required to promote sites, and NO_2 is required to oxidize elemental mercury. In the reactant-limited regime, one of these necessary species becomes depleted and the rapid mercury reaction pathway comes to a standstill. Figure 5-6 shows sensitivity calculations for depleted flue gas oxidant, in this case, NO_2. Reactant limitation results in the "plateau" typical of mercury removal data. In this region, more carbon injection simply consumes the limited reactant faster but without additional mercury capture.

Effective strategies to improve reactant-limited mercury capture are to reduce the limitations associated with activation reactant limitation, e.g., using treated carbons or adding a Sorbent Enhancement Additive™ (SEA™), an EERC-patented technology.

In-flight mercury capture between the endpoints of site- and reactant-depleted regimes is limited by a number of second-order effects that occur at rates relatively slower than the primary reaction pathway. One example of a second-order effect is site competition from SO_2, as shown in the sensitivity results of Figure 5-7. As mentioned previously, SO_2 undergoes oxidation to form H_2SO_4, which consumes promoted sites on the sorbent and oxidant species (e.g., NO_2) from the flue gas. However, compared to the analogous mercury reactions, SO_2 is oxidized at a slower rate and SO_2-induced second-order effects are typically only encountered at relatively high SO_2 concentrations.

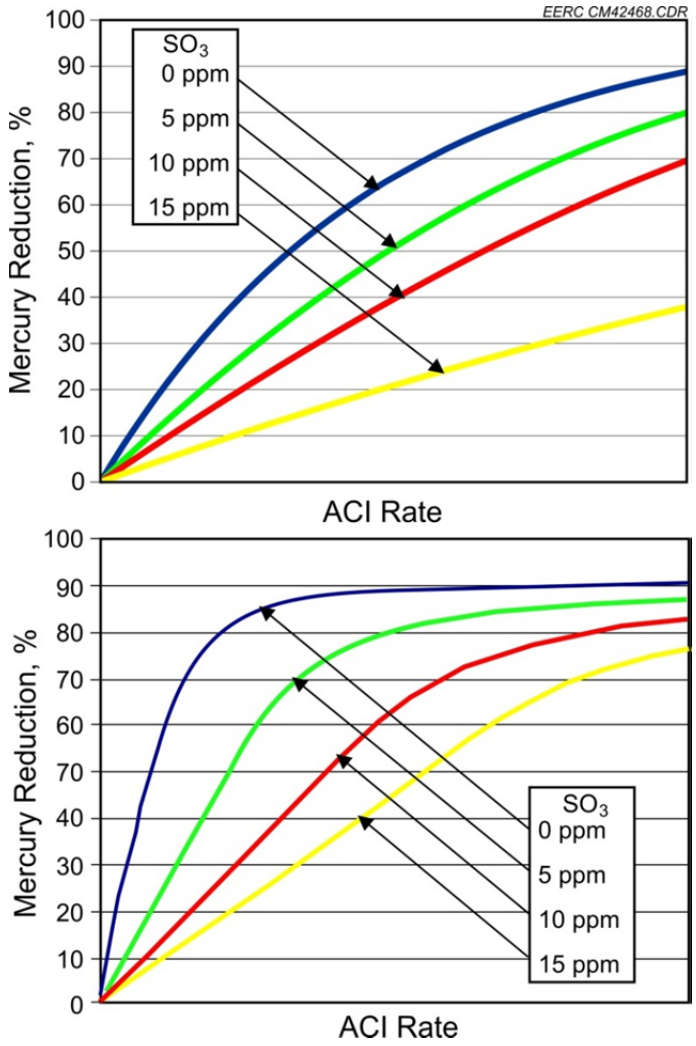

Figure 5-5. Sensitivity modeling for two instances of SO_3-induced, site-limited mercury capture: a high-sulfur coal with native SO_3 (top) and a low-sulfur coal with added SO_3 (bottom).

A universal second-order effect is caused by poor mass transfer of mercury and other species in the flue gas to the injected carbon. Good mixing or distribution of the sorbent in the flue gas is essential to minimize these limitations and achieve good mercury removal. This is typically a plant-specific issue that is best evaluated with modeling of flue gas flow within a particular duct geometry. However, assuming good sorbent distribution is present, the applied model of in-flight mercury capture can separate the distinct elements of residence time and sorbent particle size on overall mass transfer. The sensitivity of mercury removal to these effects is shown in Figures 5-8 and 5-9 for residence time and particle size, respectively. As demonstrated in the figures, longer residence times and smaller particle sizes enhance mass transfer and minimize the second-order limitation associated with poor mass transfer. However, it is important to note that even the most optimum conditions in Figures 5-8 and 5-9 do not alter the fundamental boundaries created by the site- and reactant-limited regimes. Micronizing the sorbent prior to injection may lead to a better utilization of the injected sorbent, but altering the particle size alone does not change its ultimate capture potential.

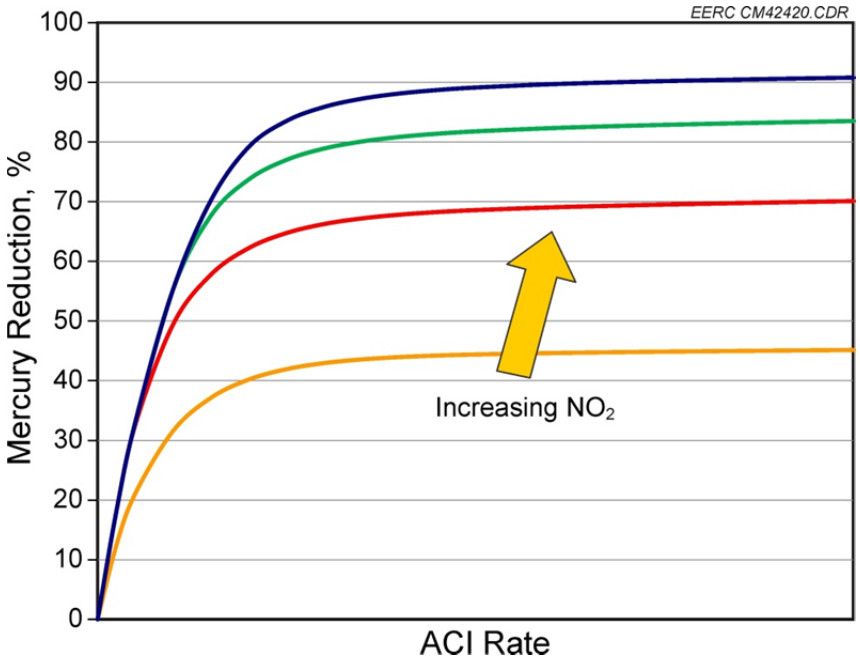

Figure 5-6. Sensitivity modeling highlighting the effect of NO_2 depletion.

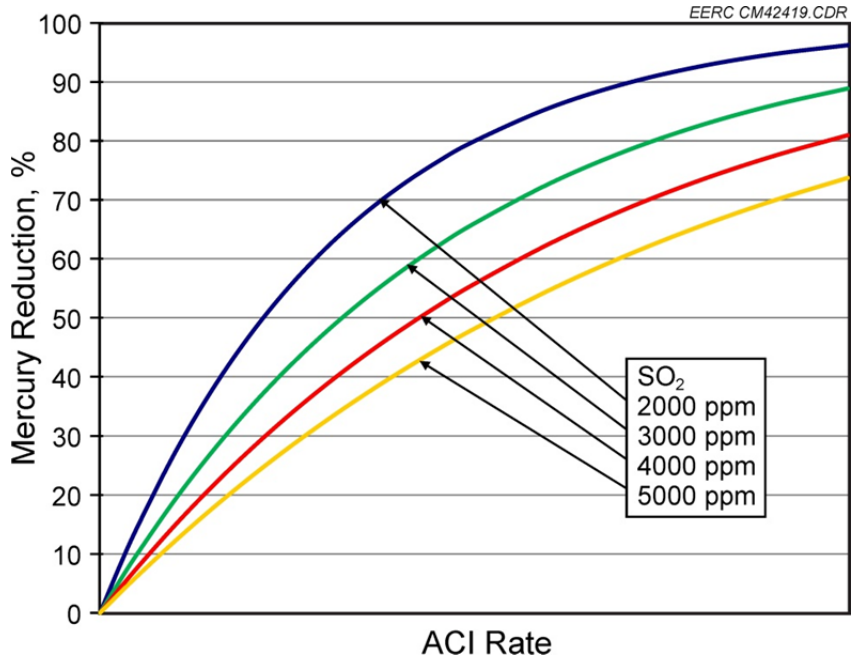

Figure 5-7. Sensitivity calculations highlighting the second-order effect of high SO_2 on mercury capture.

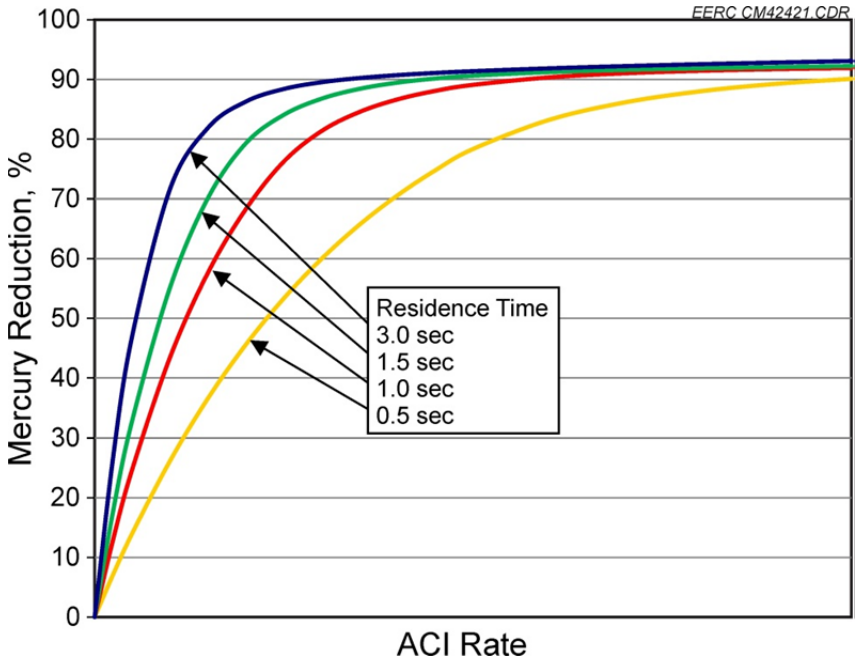

Figure 5-8. Effect of contact time between the sorbent and flue gas on overall mercury removal.

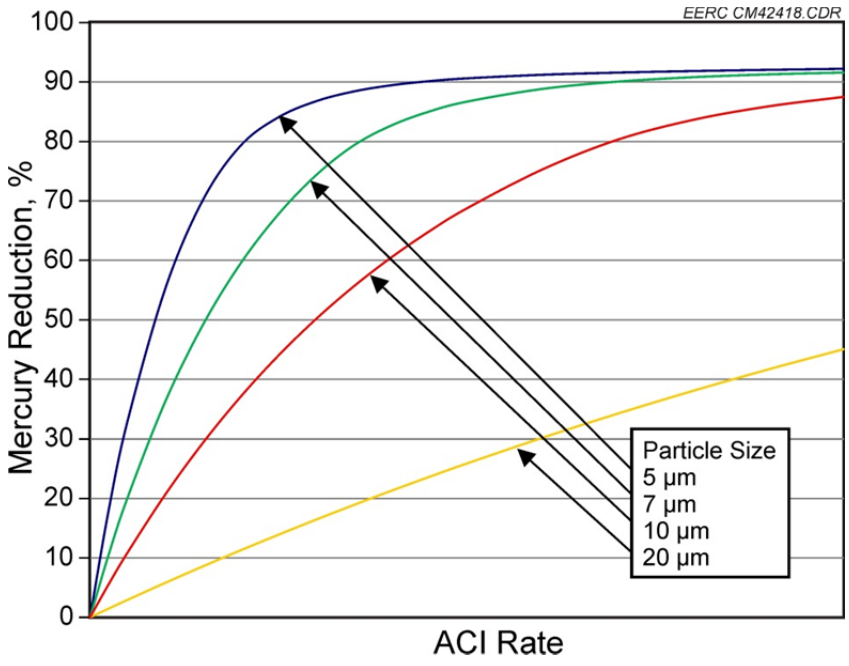

Figure 5-9. Effect of monodisperse sorbent particle size on mercury removal.

5.2.2 Inorganic Sorbent Investigation

Development and testing of inorganic sorbents under this activity used a high-temperature fixed-bed reactor obtained for this project to screen candidate materials. Testing with this reactor started with standard AC and low acid gas conditions at a temperature of 300°F in order to provide a direct comparison to the conventional fixed-bed apparatus used in previous CATM investigations. Multiple tests were performed to troubleshoot the sorbent loading method since some problems were encountered in obtaining a uniform layer of sorbent. Figure 5-10 shows results from a mercury capture test using the sorbent packing arrangement that gave the most consistent results. Approximately 40 mg of carbon was used to create a uniform sorbent layer as opposed to the 150 mg of sorbent that is typically used in fixed-bed testing. The lower sorbent mass was necessary to maintain a relatively thin bed and reduce the impacts of intrabed mass transfer.

As Figure 5-10 shows, 100% mercury capture was not observed, instead the maximum capture rate was in the range of 70%–75%. The less than 100% capture could be due to flow maldistribution (perhaps more flow passing around the outer edges of the quartz plug supporting the sorbent sample), or capture could be limited by mass transfer or reaction kinetics at the higher face velocity in the high temperature reactor. However, the in-flight performance characteristics of AC are known to be very good, so the maximum removal demonstrated in Figure 5-10 served as a reference point for evaluating the inorganic sorbents. Since only the maximum capture rate was needed for comparison to the other sorbents, the test in Figure 5-10 was ended before complete breakthrough occurred.

Two proprietary candidate inorganic sorbents were chosen for initial evaluation; H2AM and MAN-1. The simulated flue gas composition for these screenings was representative of a low acid flue gas. H2AM tests were performed at 300°F, and the results for three different sorbent mass sizes are summarized in Figure 5-11. For all of the tests in Figure 5-11, the total and elemental mercury readings suggest a brief and very modest capture of mercury (the near-zero total readings for the first and third tests are thought to be a result of the transition from inlet readings to the high temperature reactor). However, there is no significant effect as a result of increasing the sorbent mass, so the conclusion of mercury capture is called into question. Another observation regarding this sorbent is that it changed color after gas exposure from a pink/purple to a light tan, possibly suggesting a decomposition reaction took place.

Approximately 200 mg of MAN-1 was tested at temperatures of 735°, 450°, and 300°F under low acid gas conditions; these results are shown in Figures 5-12 and 5-13. The results indicate a sharp desorption peak of oxidized mercury for the 735° and 300°F tests; however, the diminished peak at 450°F suggests that the tests may have been clearing away contamination instead of showing a true temperature-induced effect (note that the tests were performed in the order 735°, 300°, then 450°F). Another observation was that the sorbent could be responsible for an initial period of mercury oxidation which is most clear in the 300° and 450°F testing of Figure 5-13. The 735°F also suggests some oxidation, but perhaps the duration was too short to obtain sufficient resolution.

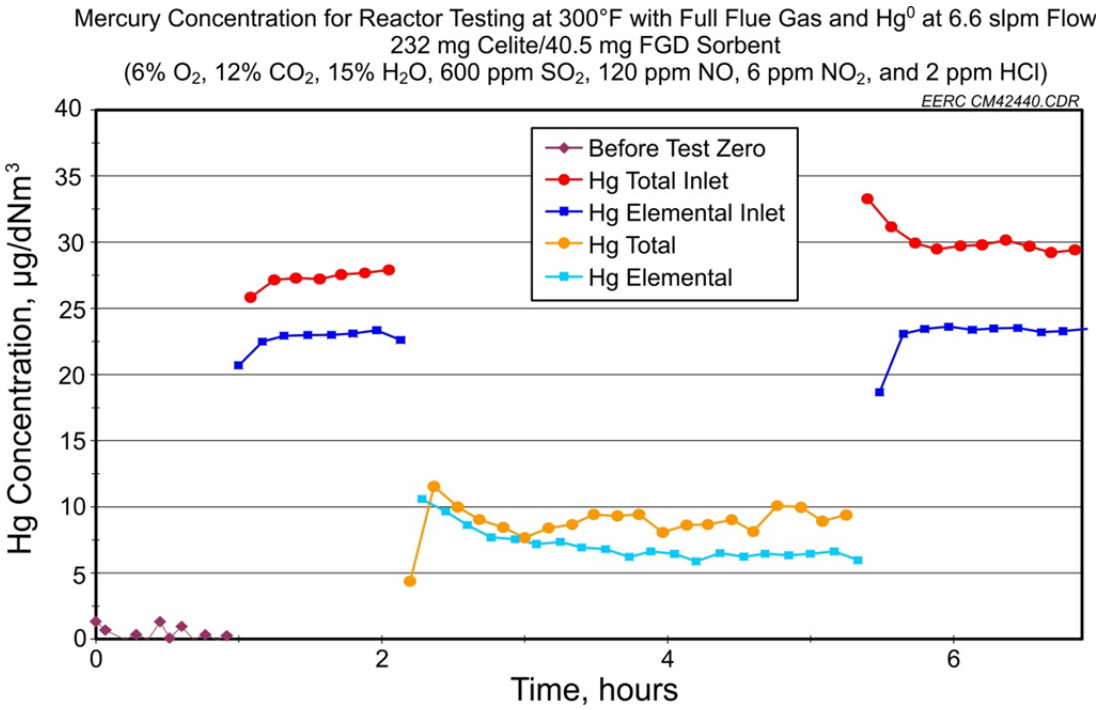

Figure 5-10. Standard AC breakthrough under LAG conditions at 300°F.

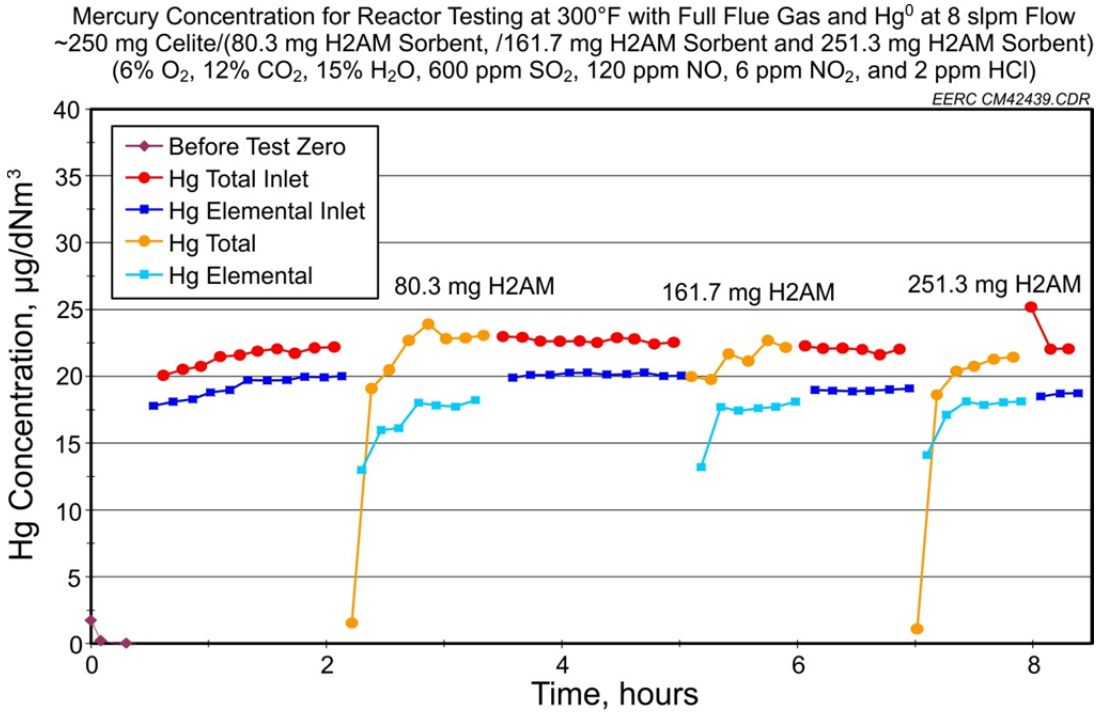

Figure 5-11. H2AM test results at 300°F and LAG composition.

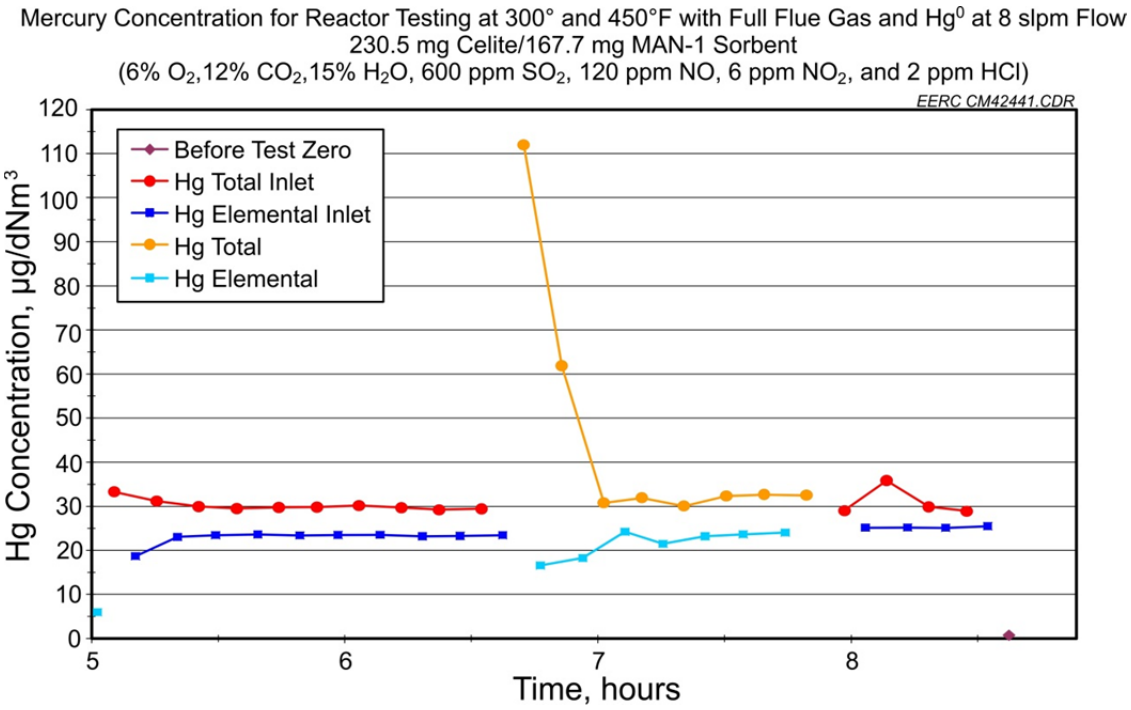

Figure 5-12. 735°F testing of MAN-1 under LAG composition.

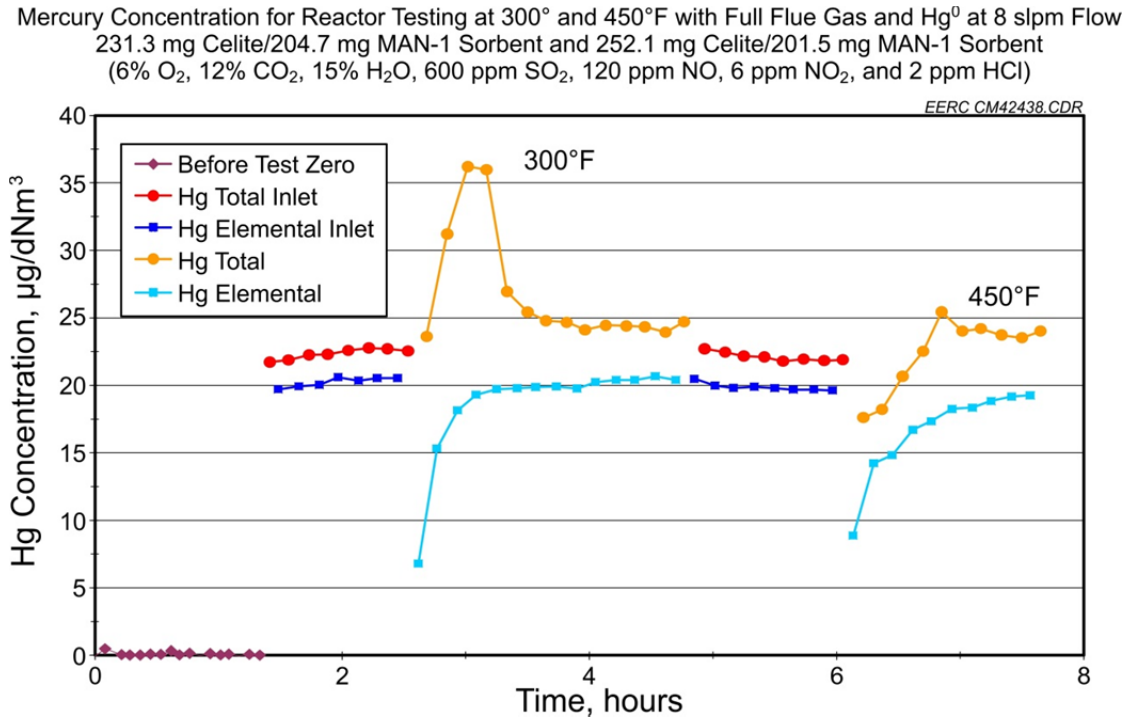

Figure 5-13. 300° and 450°F testing of MAN-1 under LAG composition.

The MAN-1 sorbent appeared to have a true period of mercury absorption and eventual breakthrough compared to the H2AM. Therefore, this sorbent was selected for further parametric study of mercury interactions to learn about the mechanism and perhaps optimize it for future sorbent development. A slightly modified form of MAN-1, MAN-2B, was tested in the high-temperature reactor, and the test matrix is presented in Table 5-2. Test parameters consisted of flue gas (either low-acid gas [LAG] or high-acid gas [HAG] composition), gas temperature, and on/off switching of selected flue gas components.

For each test, approximately 250 mg of MAN-2B was layered in the 0.5-inch-inside diameter tube on top of a 250-mg layer of Celite diatomaceous earth to prevent channeling of the gas flow. Additional disruption was prevented by sandwiching the powder layers between quartz wool plugs. A constant gas flow of 3.3 slpm was sent through the reactor for all tests. This meant that the actual volume flow rate increased with temperature, but the sorbent's mercury exposure was consistent on a per-unit-time basis since the mass flow of gas was fixed. The MAN-2B tests used a higher ratio of sorbent mass to gas flow rate compared to a standard AC breakthrough test that uses 150 mg of sorbent and 15 slpm gas flow.

Figures 5-14–5-19 summarize the key data in the form of normalized mercury breakthrough data. Figure 5-14 shows the results from LAG testing for the three temperatures. These data suggest that temperatures between 300° and 700°F may be less optimal since the 450°F results showed the shortest time to breakthrough. Under HAG conditions in Figure 5-15, no appreciable mercury capture appeared to occur, but a small amount of mercury oxidation continued for approximately 45 minutes.

Figures 5-16 and 5-17 compare the LAG and HAG results for the 450° and 700°F temperatures, respectively. These plots clearly show deteriorated performance under HAG conditions for both temperatures.

Table 5-2. MAN-2B Test Matrix

Gas Composition*	Reactor Temperature, °F
LAG	300
LAG	450
LAG (repeat)	450
LAG	700
HAG	450
HAG	700
HAG without NO_2	450
HAG without SO_2	450

* Either LAG or HAG conditions, where:
LAG = 6% O_2, 12% CO_2, 15% H_2O, 600 ppm SO_2, 120 ppm NO, 6 ppm NO_2, and 1 ppm HCl
HAG = 6% O_2, 12% CO_2, 8% H_2O, 1600 ppm SO_2, 400 ppm NO, 20 ppm NO_2, and 50 ppm HCl.

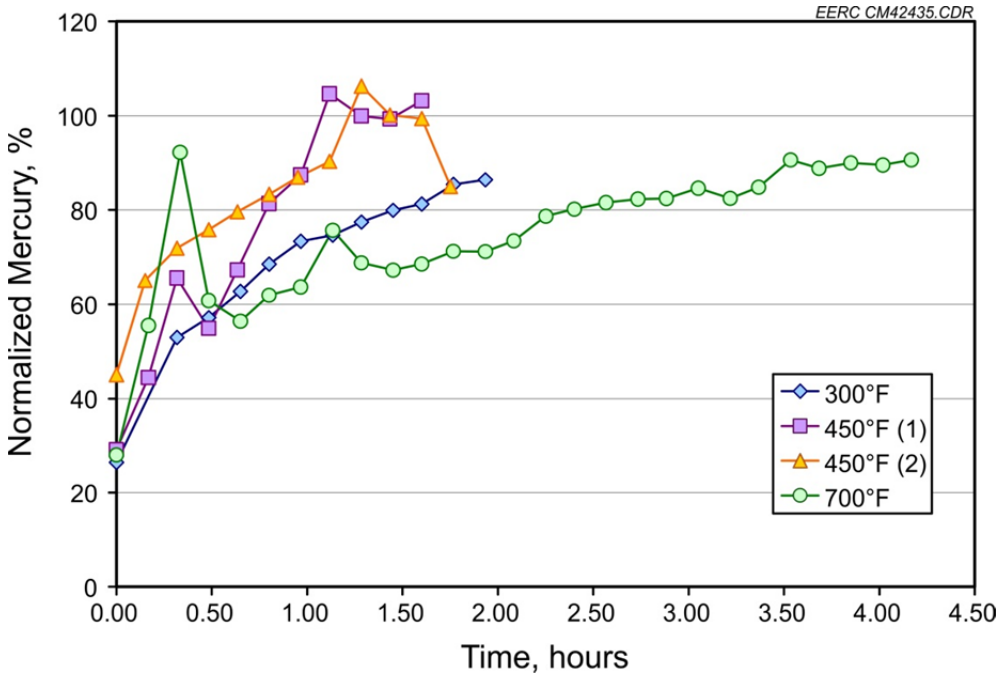

Figure 5-14. MAN-2B breakthrough under LAG conditions and multiple temperatures.

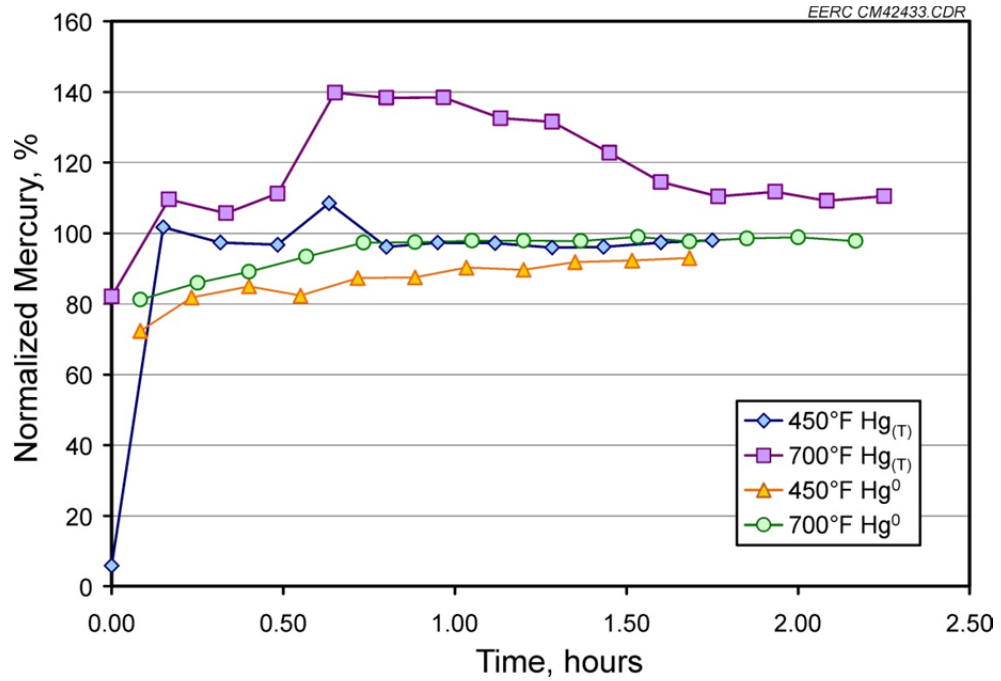

Figure 5-15. MAN-2B breakthrough under HAG conditions and multiple temperatures.

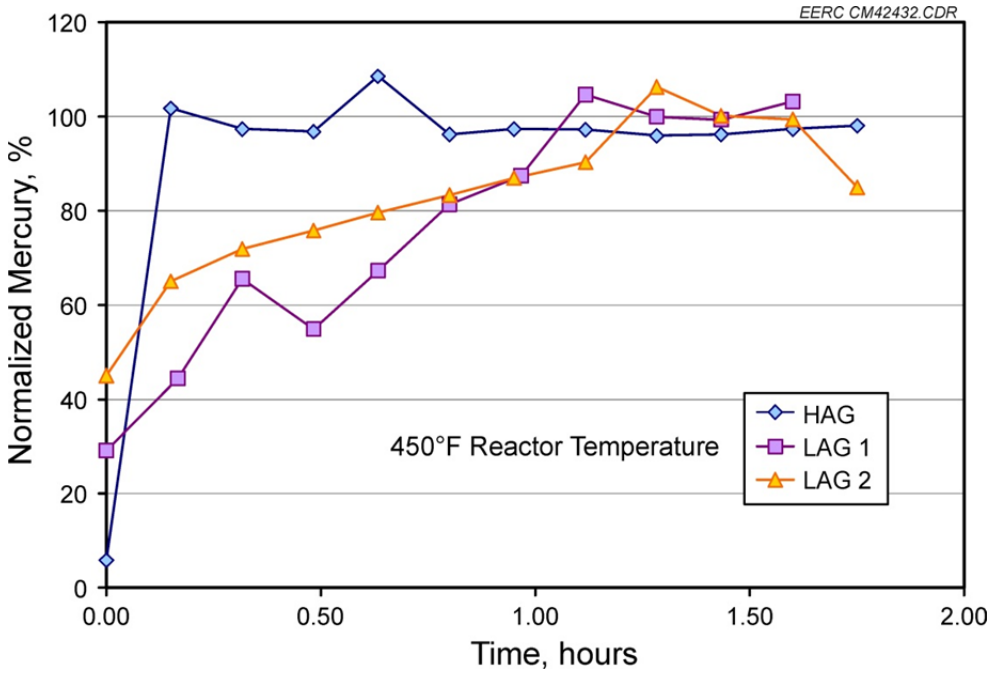

Figure 5-16. MAN-2B breakthroughs under LAG and HAG conditions at 450°F.

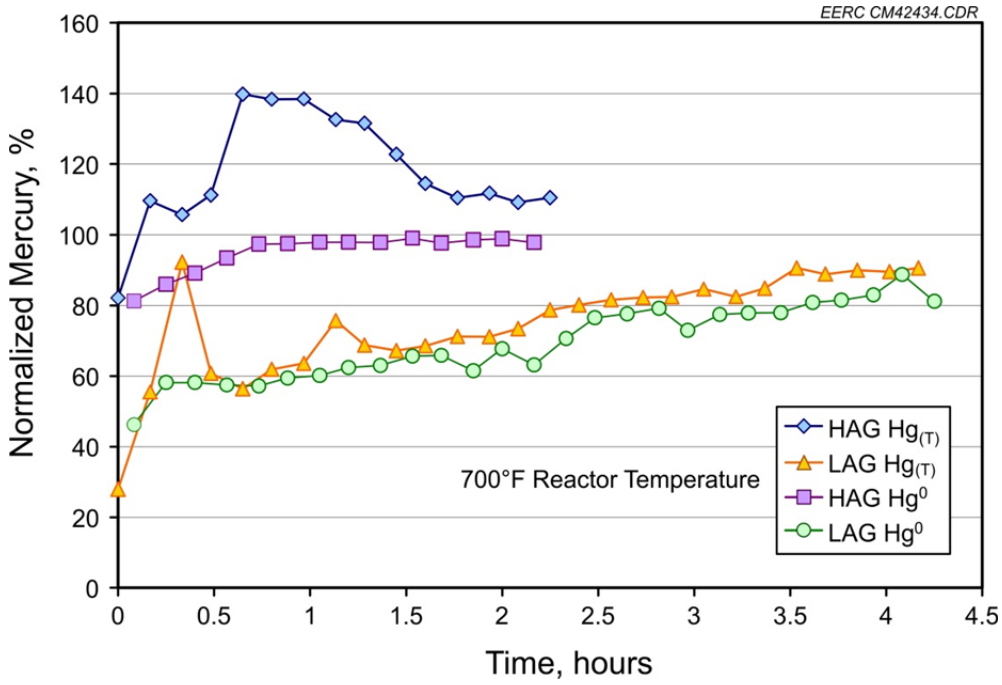

Figure 5-17. MAN-2B breakthroughs under LAG and HAG conditions at 700°F.

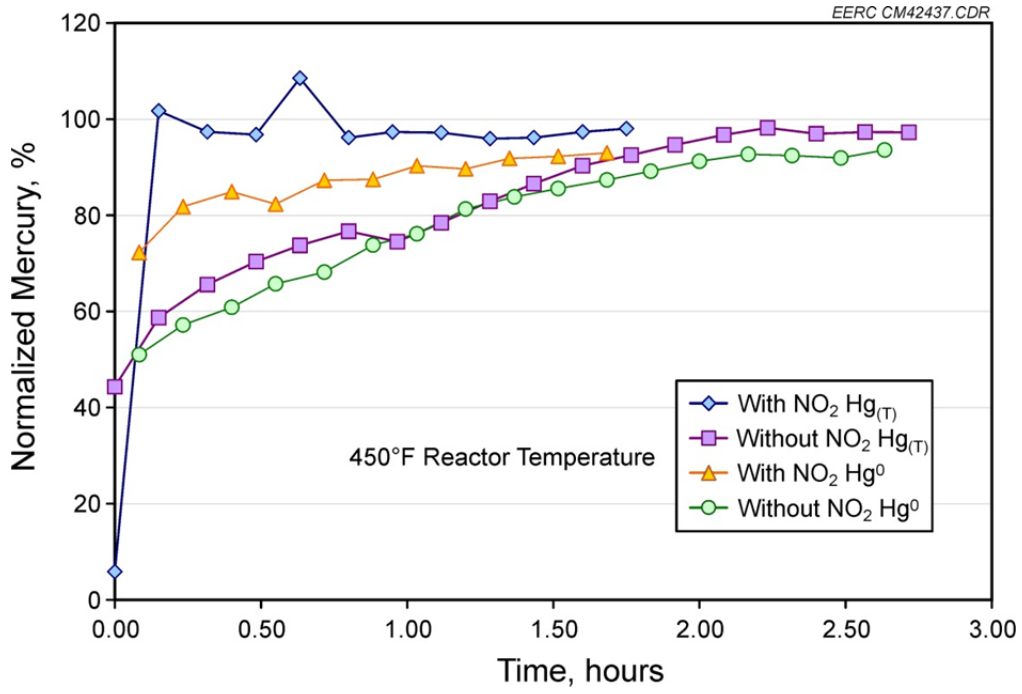

Figure 5-18. MAN-2B breakthrough under HAG conditions with and without NO_2.

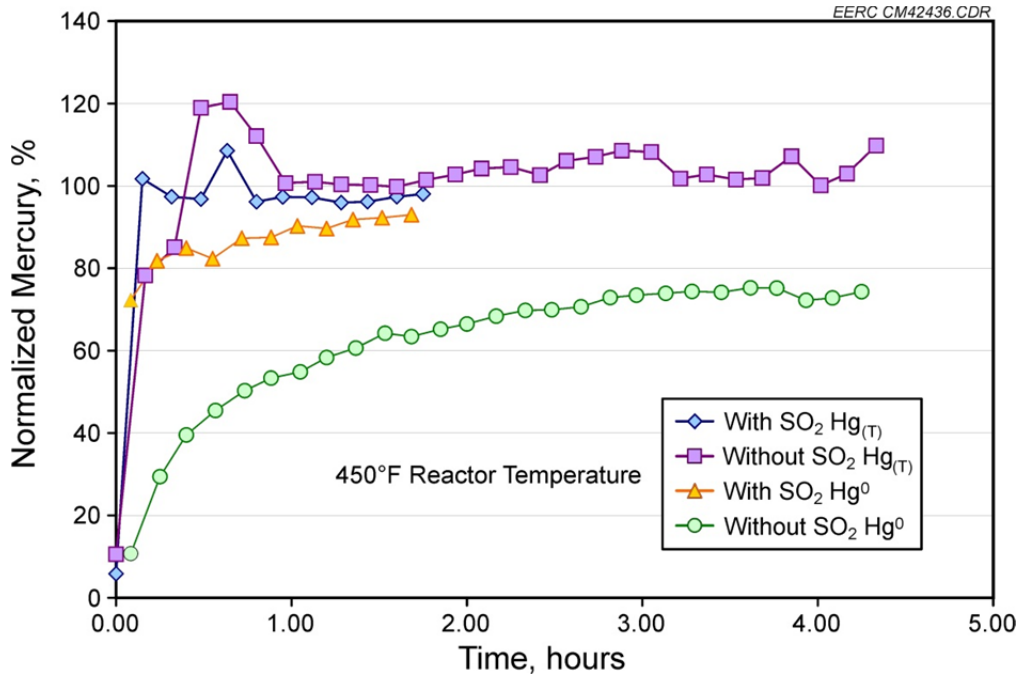

Figure 5-19. MAN-2B breakthrough under HAG conditions with and without SO_2.

Parametric studies continued by repeating tests with selected flue gas components switched off. Figure 5-18 is a comparison with and without NO_2 present, and Figure 5-19 presents the equivalent results for SO_2. These flue gas components were selected based on the mechanistic understanding of mercury capture on AC, where NO_2 is a needed oxidant and SO_2 is a key competitor for active sites on carbon sorbents. Figure 5-18 suggests a different role for NO_2 on MAN-2B. Mercury oxidation and capture are greatly improved without NO_2, so it seems that NO_2 may enable a competing or counteracting reaction instead of mercury oxidation on this particular sorbent. The results without SO_2 in Figure 5-19 show a slight improvement in mercury capture compared to those with SO_2, but there is a dramatic increase in the amount of mercury oxidation that takes place. Figure 5-19 suggests that SO_2 interferes with the mercury oxidation process, which is counter to the observations on AC. With AC, the mechanism for mercury oxidation appears quite robust since mercury continues to be oxidized even when its capacity to capture mercury has been exhausted. Furthermore, SO_2 does not appear to interfere with mercury oxidation on carbon.

By comparing the parametric results for MAN-2B to the partial carbon breakthrough test of Figure 5-10, it seems that the sorbent has far less capacity for mercury capture than carbon. While capacity is not usually a determining factor for in-flight capture, it is indicative of the number of sites available to support mercury capture. MAN-2B's faster breakthrough times suggest fewer total sites and a relatively limited ability to support in-flight capture. Perhaps equally as detrimental, it seems that the mercury oxidation mechanism is highly inhibited by SO_2. Assuming that mercury oxidation is a required first step for mercury capture (as it is on AC), then MAN-2B may be of even more limited use in high-sulfur flue gases.

5.2.3 Durable AC Evaluation

The highest cost associated with mercury control using AC injection is the ongoing expense for the consumable sorbent. Instead of disposal after a single use, regeneration of the AC is possible provided the sorbent can be separated from the fly ash after injection or contained in a packed-bed arrangement. Previous CATM research pioneered the regeneration of mercury sorbents, and in some cases, the physical strength of the sorbents limited their useful lifetime after several regeneration and exposure cycles. For applications requiring recycling of ACs in flue gas treatment, the subject carbons need to have the following qualities:

1. Abrasion resistance to permit handling of bed materials for a regeneration operation.

2. Oxidation resistance to permit longevity during exposure to oxidizing gases at flue gas temperatures.

3. Large numbers of Lewis basic sites that can be promoted for mercury oxidation by addition of Lewis acids.

Several samples of AC were prepared from a Souris lignite coal char using steam activation. Inspection and sizing of the resulting ACs demonstrated that they were extremely hard and resilient compared to more conventional lignite- and biomass-based carbons. Samples of the crushed and sieved carbons were screened for mercury capture potential using fixed-bed

mercury breakthrough tests under HAG and LAG simulated flue gas conditions. Details of the fixed-bed apparatus have been described previously (2). Quantitative measures of initial reactivity and the time needed for 50% breakthrough were determined from the resulting breakthrough curves as shown in the example of Figure 5-20 for a standard AC. These values provide concise measures about the number of sites available on the sorbent and their initial reactivity towards mercury.

Results from the fixed-bed screenings are summarized in Table 5-3. Overall, carbons prepared from the very hard Souris coal char exhibited poor capacities (i.e., short breakthrough) and mediocre reactivities. Comparative values for standard AC under HAG conditions are 2% initial reactivity and 1.10 hours to reach 50% breakthrough. Given the short breakthrough times for the Souris carbons, it is likely that they lack the large number of sites present on other ACs. Increasing the temperature and duration of activation resulted in an even lower capacity, suggesting that more severe activation actually destroys the sites present as the additional carbon surface burns off in the steam activation. Bromination did help promote the sites under LAG conditions; however, the longer breakthrough for this test may be due to the lower SO_2 deactivation rate under LAG conditions. The 50% breakthrough time for a standard AC under LAG conditions would be approximately 3.5 hours.

The results observed with the Souris carbons are consistent with the behavior of hard anthracitic carbons rather than lignite- and many bituminous-derived carbons. Although the hardness of the carbons may allow transport or movement of bed materials composed of the carbons, the capacities are still relatively low. Furthermore, after some exposure to flue gases, the ability to oxidize elemental Hg is depleted, as evidenced by the high percentage of Hg^0 in the bed effluent at the end of each test in Table 5-3.

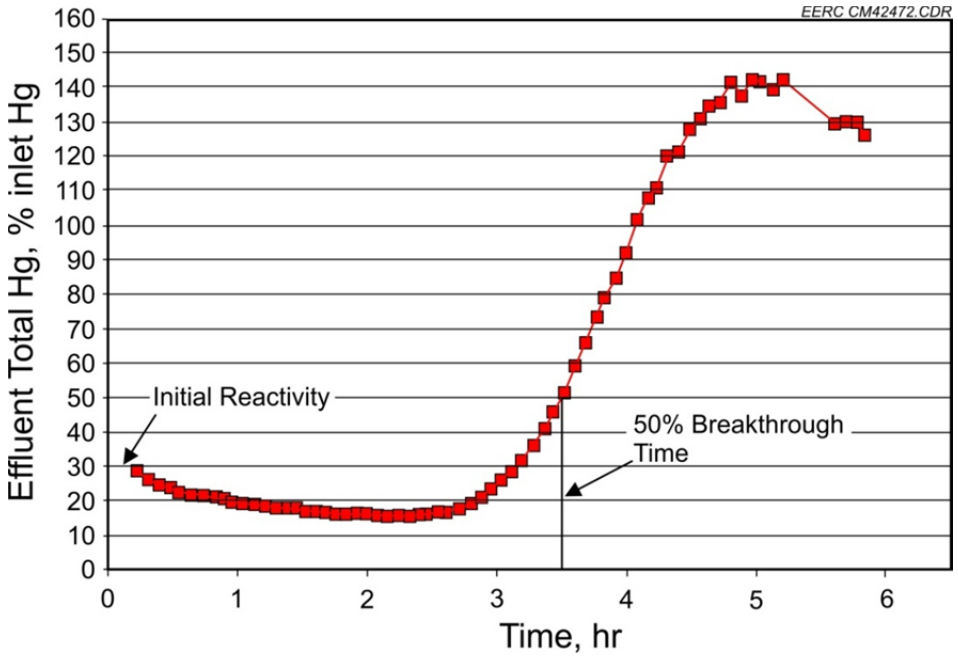

Figure 5-20. Baseline $Hg_{(T)}$ breakthrough curve for a standard AC under LAG conditions.

Table 5-3. Test Data for Steam-Activated Souris Char Carbons

Steam Activation Conditions	Test Flue Gas[a]	Initial Reactivity, % $Hg_{(T)}$ inlet	50 % Breakthrough Time, hr	Comments
850°C for 30 min	HAG	5	0.25	Fast breakthrough, poor oxidation (67% Hg^0 at end of test)
850°C for 30 min[b]	LAG	5	0.48	Improved breakthrough, very poor oxidation (95% Hg^0 at end of test)
900°C for 45 min	HAG	5	0.11	Very fast breakthrough, poor oxidation (75% Hg^0 at end of test)

[a] HAG: 6% O_2, 12% CO_2, 15% H_2O, 20 ppm NO_2, 400 ppm NO, 1600 ppm SO_2, and 50 ppm HCl
LAG: 6% O_2, 12% CO_2, 15% H_2O, 6 ppm NO_2, 120 ppm NO, 600 ppm SO_2, and 1 ppm HCl.
[b] Pretreated with 5% Br_2.

5.2.4 Surface-Modified ACs

The main factor limiting mercury capacity of AC sorbents is the buildup of H_2SO_4 on the carbon surface from the oxidation of SO_2 in the flue gas. While mercury capacity is not an issue for short residence time, in-flight capture with AC injection, it is the primary limitation for reusing carbon sorbents or for fixed beds in flue gas. The goal of this sorbent development approach was to identify surface modified ACs that have improved mercury capacities in SO_2-containing flue gas by selectively slowing the oxidation of SO_2 to H_2SO_4 on the carbon surface.

This work began by preparing a number of AC samples that received various chemical pretreatments. These samples were then screened using the EERC's fixed-bed apparatus with a simulated LAG consisting of 6% O_2, 12% CO_2, 15% H_2O, 6 ppm NO_2, 120 ppm NO, 600 ppm SO_2, and 1 ppm HCl. Further details of the fixed-bed apparatus have been described previously (2). Quantitative measures of initial reactivity and the time needed for 50% breakthrough were determined from the breakthrough curves, as shown in Figure 5-20.

Surface modification was performed by treatment of a standard AC with various halogenated Lewis acids. The LAG test results are presented in Table 5-4 and show improved initial reactivities for Hg oxidation compared to the parent carbon, as predicted, but they showed no improvement in capacity as demonstrated by the 50% breakthrough times. This means that the additional halogens at the active sites did not affect the oxidation rate of SO_2, since there was no change in the 50% breakthrough time. This is consistent with the theory that the loss of capacity is due entirely to the accumulation of sulfuric acid on the reaction sites (from SO_2 oxidation), that the reaction sites for Hg and SO_2 are the same, and that rates of reaction with Hg and with SO_2 were affected in the same direction and amount by surface modification. Furthermore, binding of the sulfuric acid product seemed to be unaffected. If the surface were more hydrophobic, owing to the halogenation, the sulfuric acid should have departed more easily, improving the capacity. It is, therefore, likely that the activated sites involved in binding reaction products are not hydrophobic, owing to the more ionic character of the phosphorus and boron halides attached to the carbon surface. The hypothesized progression at the carbon surface

Table 5-4. Test Data for Surface-Modified Carbons under LAG Conditions (samples diluted 1:3 with Celite, except as noted)

Carbon Treatment	Initial Reactivity, % $Hg_{(T)}$ inlet	50% Breakthrough Time, hr	Comments
BCl_3 imp*	27	2.72	
BCl_3-700	2	0.59	Very good reactivity
$POCl_3$ imp	5	0.15	Very poor capacity
$POCl_3$-700	1	0.50	Very good reactivity
PBr_3 imp	2	0.50	Very good reactivity
PBr_3-700	2	0.53	Very good reactivity
Parent AC	27	0.58	

* Not diluted with Celite.

is surface modification, Equation 12, followed by either mercury or SO_2 complexing, Equations 13 and 14, respectively:

$$\text{Carbene} + PBr_3 \rightarrow \text{Carbenium}^{(+)}\text{–}PBr_3^{(-)} \quad [12]$$

$$\text{Carbenium}^{(+)}\text{–}PBr_3^{(-)} + Hg \rightarrow Hg \text{ complex} \rightarrow \text{carbinylmercurybromide–}PBr_2 \quad [13]$$

$$\text{Carbenium}^{(+)}\text{–}PBr_3^{(-)} + SO_2 \rightarrow SO_2\text{–complex} \rightarrow H_2SO_4 \text{ (bound to active site)} \quad [14]$$

Additional halogen-modified sorbents were also tested under HAG conditions, which consisted of 6% O_2, 12% CO_2, 15% H_2O, 20 ppm NO_2, 400 ppm NO, 1600 ppm SO_2, and 50 ppm HCl. Celite dilution was not used for these tests. These results are summarized in Table 5-5 and show that unlike the LAG case, some differences in the initial reactivities were observed with the HAG conditions. The PBr_3-treated sorbent (800°C) exhibited superior reactivity, whereas the BCl_3-treated (800°C) sorbent and PBr_3-treated (900°C) sorbent were less reactive. The PBr_3-900 sample had lost Br in the treatment, which may have resulted in the lower reactivity. There were little differences in the capacities, however, indicating that the relative rates of SO_2 and mercury oxidation remained unaffected.

While the surface modifications evaluated proved ineffective at altering the relative kinetics between mercury and SO_2 oxidation, the experiments did substantiate the mechanistic understanding of SO_2 and mercury competition for promoted sites. Unfortunately, the experiments suggest that SO_2 and mercury oxidation are linked to the same sites on activated carbon and that entirely different site structures may be needed to differentiate their reaction kinetics.

Table 5-5. Test Data for Surface Modified Carbons under HAG Conditions

Carbon Treatment	Initial Reactivity, % $Hg_{(T)}$ inlet	50% Breakthrough Time, hr	Comments
BCl_3-800	5	1.22	Poor reactivity, better capacity
PBr_3-800	0	1.10	High reactivity
PBr_3-900	8	1.14	Poor reactivity (lost Br in activation)
Parent AC	2	1.10	

5.3 Wet FGD Mercury Capture and Retention

Novel mercury reemission additives were screened for their relative effectiveness in a manner similar to that used in a previous study (5). The additional aspect examined under this topic area was to consider the effect of reemission additives on mercury and selenium precipitation and separation from a wet FGD slurry. The most promising EERC additive, EERC-A, was evaluated, and two existing additives were also included in the precipitation study as reference technologies for comparison.

The general procedure for evaluating the effect on trace element precipitation and separation is diagrammed in Figure 5-21. Simulated scrubber slurry solutions were prepared and spiked with trace elements of interest and then mixed with the reemission additive under test. After a predetermined settling time, these solutions were filtered, and the filtrate was analyzed for what was assigned to be soluble mercury or selenium.

The mercury and selenium compounds evaluated were mercuric chloride ($HgCl_2$), selenite (as Na_2SeO_3), and selenate (as Na_2SeO_4). The additives utilized were a previously investigated EERC additive (denoted EERC-A), sodium hydrosulfide (NaHS), and sodium thiosulfate ($Na_2S_2O_3$). Baseline solutions without the reemission additives were also evaluated. The calcium-based reagents used in the experiments to represent solid-phase components of wet FGD slurry were calcium sulfate ($CaSO_4$), calcium sulfate dihydrate ($CaSO_4 \cdot 2H_2O$), and calcium hydroxide ($Ca(OH)_2$). Milli-Q distilled, DI water was used in the preparation of all standards and solutions.

The matrix of solutions prepared is shown in Table 5-6. In addition to the duplicate samples specified in the table, further duplicate analyses were performed on selected individual solutions. The baseline concentration was 0.0005 mM for both mercury and selenium (0.1 ppm

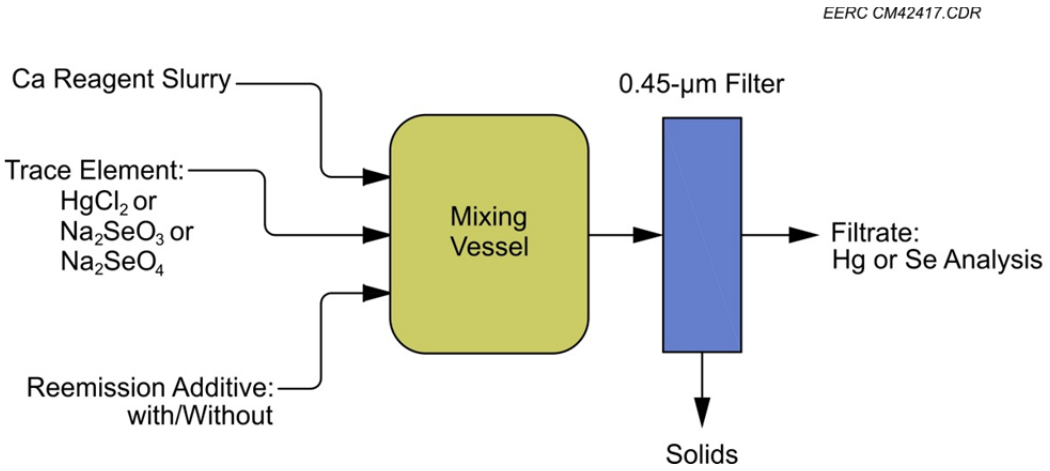

Figure 5-21. Test setup for precipitation study.

Table 5-6. Test Matrix for Quantitative Determination of Mercury and/or Selenium in the Clear Liquid Phase of Simulated Wet FGD Slurry Mixtures

Sample	Mixture	Analysis	Notes
IC-1	$HgCl_2$ parent	Hg, Se	Baseline components
IC-2	Na_2SeO_3 parent	Hg, Se	
IC-3	Na_2SeO_4 parent	Hg, Se	
IC-20	EERC-A parent	Hg, Se	
IC-21	$CaSO_4$ parent	Hg, Se	
IC-21a	$CaSO_4 \cdot 2H_2O$ parent	Hg, Se	
IC-22	$Ca(OH)_2$ parent	Hg, Se	
IC-24	Milli-Q water parent	Hg, Se	
IC-39	NaHS parent	Hg, Se	
IC-31	$Na_2S_2O_3$ parent	Hg	
IC-4	$HgCl_2 + CaSO_4$	Hg	Baseline mercury precipitation
IC-4a	$HgCl_2 + CaSO_4$	Hg	
IC-4b	$HgCl_2 + CaSO_4$	Hg	
IC-4f	$HgCl_2 + CaSO_4 \cdot 2H_2O$	Hg	
IC-4g	$HgCl_2 + CaSO_4 \cdot 2H_2O$	Hg	
IC-4h	$HgCl_2 + CaSO_4 \cdot 2H_2O$	Hg	
IC-4c1	$HgCl_2 + CaSO_4 \cdot 2H_2O$	Hg	1-hour kinetic baseline mercury precipitation
IC-4d4	$HgCl_2 + CaSO_4 \cdot 2H_2O$	Hg	4-hour kinetic baseline mercury precipitation
IC-4e24	$HgCl_2 + CaSO_4 \cdot 2H_2O$	Hg	24-hour kinetic baseline mercury precipitation
IC-4i24	$HgCl_2 + CaSO_4 \cdot 2H_2O$	Hg	
IC-4j24	$HgCl_2 + CaSO_4 \cdot 2H_2O$	Hg	
IC-10	EERC-A + $HgCl_2 + CaSO_4$	Hg	Mercury precipitation
IC-10a	EERC-A + $HgCl_2 + CaSO_4 \cdot 2H_2O$	Hg	
IC-10b	EERC-A + $HgCl_2 + CaSO_4 \cdot 2H_2O$	Hg	
IC-10f	EERC-A + $HgCl_2 + CaSO_4 \cdot 2H_2O$	Hg	
IC-10c1	EERC-A + $HgCl_2 + CaSO_4 \cdot 2H_2O$	Hg	1-hour kinetic mercury precipitation
IC-10d4	EERC-A + $HgCl_2 + CaSO_4 \cdot 2H_2O$	Hg	4-hour kinetic mercury precipitation
IC-10e24	EERC-A + $HgCl_2 + CaSO_4 \cdot 2H_2O$	Hg	24-hour kinetic mercury precipitation
IC-10g24	EERC-A + $HgCl_2 + CaSO_4 \cdot 2H_2O$	Hg	
IC-10h24	EERC-A + $HgCl_2 + CaSO_4 \cdot 2H_2O$	Hg	
IC-5	$HgCl_2 + Ca(OH)_2$	Hg	Baseline mercury precipitation
IC-11	EERC-A + $HgCl_2 + Ca(OH)_2$	Hg	Mercury precipitation
IC-29	NaHS + $HgCl_2 + CaSO_4 \cdot 2H_2O$	Hg	Mercury precipitation
IC-29a	NaHS + $HgCl_2 + CaSO_4 \cdot 2H_2O$	Hg	
IC-29b	NaHS + $HgCl_2 + CaSO_4 \cdot 2H_2O$	Hg	

Continued…

Table 5-6. Test Matrix for Quantitative Determination of Mercury and/or Selenium in the Clear Liquid Phase of Simulated Wet FGD Slurry Mixtures (continued)

Sample	Mixture	Analysis	Notes
IC-29c1	$NaHS + HgCl_2 + CaSO_4 \cdot 2H_2O$	Hg	1-hour kinetic mercury precipitation
IC-29d4	$NaHS + HgCl_2 + CaSO_4 \cdot 2H_2O$	Hg	4-hour kinetic mercury precipitation
IC-29e24	$NaHS + HgCl_2 + CaSO_4 \cdot 2H_2O$	Hg	24-hour kinetic mercury precipitation
IC-29f24	$NaHS + HgCl_2 + CaSO_4 \cdot 2H_2O$	Hg	
IC-29g24	$NaHS + HgCl_2 + CaSO_4 \cdot 2H_2O$	Hg	
IC-30	$Na_2S_2O_3 + HgCl_2 + CaSO_4 \cdot 2H_2O$	Hg	Mercury precipitation
IC-30a	$Na_2S_2O_3 + HgCl_2 + CaSO_4 \cdot 2H_2O$	Hg	
IC-30b	$Na_2S_2O_3 + HgCl_2 + CaSO_4 \cdot 2H_2O$	Hg	
IC-30c1	$Na_2S_2O_3 + HgCl_2 + CaSO_4 \cdot 2H_2O$	Hg	1-hour kinetic mercury precipitation
IC-30d4	$Na_2S_2O_3 + HgCl_2 + CaSO_4 \cdot 2H_2O$	Hg	4-hour kinetic mercury precipitation
IC-30e24	$Na_2S_2O_3 + HgCl_2 + CaSO_4 \cdot 2H_2O$	Hg	24-hour kinetic mercury precipitation
IC-30f24	$Na_2S_2O_3 + HgCl_2 + CaSO_4 \cdot 2H_2O$	Hg	
IC-30g24	$Na_2S_2O_3 + HgCl_2 + CaSO_4 \cdot 2H_2O$	Hg	
IC-6	$Na_2SeO_3 + CaSO_4$	Se	Baseline selenite precipitation
IC-6a	$Na_2SeO_3 + CaSO_4$	Se	
IC-6b	$Na_2SeO_3 + CaSO_4$	Se	
IC-6c	$Na_2SeO_3 + CaSO_4 \cdot 2H_2O$	Se	
IC-12	$EERC\text{-}A + Na_2SeO_3 + CaSO_4$	Se	Selenite precipitation
IC-12a	$EERC\text{-}A + Na_2SeO_3 + CaSO_4 \cdot 2H_2O$	Se	
IC-12b	$EERC\text{-}A + Na_2SeO_3 + CaSO_4 \cdot 2H_2O$	Se	
IC-25	$HgCl_2 + Na_2SeO_3 + CaSO_4$	Hg, Se	Mercury–selenite precipitation
IC-16	$EERC\text{-}A + HgCl_2 + Na_2SeO_3 + CaSO_4$	Hg, Se	
IC-7	$Na_2SeO_3 + Ca(OH)_2$	Se	Baseline selenite precipitation
IC-13	$EERC\text{-}A + Na_2SeO_3 + Ca(OH)_2$	Se	Selenite precipitation
IC-26	$HgCl_2 + Na_2SeO_3 + Ca(OH)_2$	Hg, Se	Mercury–selenite precipitation
IC-17	$EERC\text{-}A + HgCl_2 + Na_2SeO_3 + Ca(OH)_2$	Hg, Se	
IC-8	$Na_2SeO_4 + CaSO_4$	Se	Baseline selenate precipitation
IC-8a	$Na_2SeO_4 + CaSO_4$	Se	
IC-8b	$Na_2SeO_4 + CaSO_4$	Se	
IC-8c	$Na_2SeO_4 + CaSO_4 \cdot 2H_2O$	Se	

Continued…

Table 5-6. Test Matrix for Quantitative Determination of Mercury and/or Selenium in the Clear Liquid Phase of Simulated Wet FGD Slurry Mixtures (continued)

Sample	Mixture	Analysis	Notes
IC-14	EERC-A + Na_2SeO_4 + $CaSO_4$	Se	Selenate precipitation
IC-14a	EERC-A + Na_2SeO_4 + $CaSO_4 \cdot 2H_2O$	Se	
IC-14b	EERC-A + Na_2SeO_4 + $CaSO_4 \cdot 2H_2O$	Se	
IC-14c	EERC-A + Na_2SeO_4 + $CaSO_4 \cdot 2H_2O$	Se	
IC-27	$HgCl_2$ + Na_2SeO_4 + $CaSO_4$	Hg, Se	Mercury–selenate precipitation
IC-18	EERC-A + $HgCl_2$ + Na_2SeO_4 + $CaSO_4$	Hg, Se	
IC-9	Na_2SeO_4 + $Ca(OH)_2$	Se	Baseline selenate precipitation
IC-15	EERC-A + Na_2SeO_4 + $Ca(OH)_2$	Se	Selenate precipitation
IC-28	$HgCl_2$ + Na_2SeO_4 + $Ca(OH)_2$	Hg, Se	Mercury–selenate precipitation
IC-19	EERC-A + $HgCl_2$ + Na_2SeO_4 + $Ca(OH)_2$	Hg, Se	

for mercury and 0.04 ppm for selenium). The EERC-A, NaHS, or $Na_2S_2O_3$ were included at a 1:1 ratio with the mercury and/or selenium (0.0005 mM). The $CaSO_4$, $CaSO_4 \cdot 2H_2O$, or $Ca(OH)_2$ was included at about a 12% solid content.

Solutions containing a solid-phase component were prepared in the following order:

1. The $CaSO_4$, $CaSO_4 \cdot 2H_2O$, or $Ca(OH)_2$ was weighed and dissolved in Milli-Q water and brought up to one-half of the final solution volume.

2. The solid-containing solution was transferred to a sample container with the remaining one-half volume of Milli-Q water less the required volume for other sample constituents.

3. The remaining sample constituents were added to the sample container in the following order as needed per solution: additive, selenium compound, and $HgCl_2$.

Following preparation of a solution, the bottle was shaken three times and filtered immediately. Solutions included in the kinetic testing were rotated using end-over-end agitation at approximately 30 rpm for a 1-, 4-, or 24-hour duration prior to filtering. Separate solutions were prepared for each time period. For all prepared solutions, the solids were filtered from the solution through a 0.45-µm filter. The majority of solutions filtered within 1 minute, while some solutions, especially those containing $CaSO_4$, filtered more slowly but within 7 minutes.

An approximate pH of the resulting liquid was obtained using pH paper for each solution type. The filtered solutions were preserved with HCl for mercury determination or with nitric acid (HNO_3) for selenium determination. Mercury concentrations were determined using

CVAAS. Selenium was determined using inductively coupled plasma mass spectrometry (ICP–MS).

Results from the precipitation study tests in Table 5-6 were evaluated on the basis of mercury and/or selenium that could be separated by filtration. The calculation for mercury is shown as Equation 15; the selenium calculation is performed in the same manner:

$$Fraction\ of\ Hg\ Blocked\ by\ Filtration = 1 - \frac{Hg_{filtrate}}{Hg_{parent\ solution}} \quad [15]$$

It is assumed that the amount of mercury or selenium blocked by filtration represents the amount of the trace element that would become bound to the solid phase in an actual wet FGD slurry and ultimately removed in the solids separation process.

The first set of test results is the relative comparison of mercury precipitation in a $CaSO_4$ slurry among the three additives evaluated and the baseline condition with no additive. These results are summarized in Figure 5-22. The standard deviation is indicated in the figure for conditions where multiple measurements were collected. Significant variability was observed under some conditions, specifically the zero-hour conditions for NaHS and $Na_2S_2O_3$. The underlying reason for this variability was not determined.

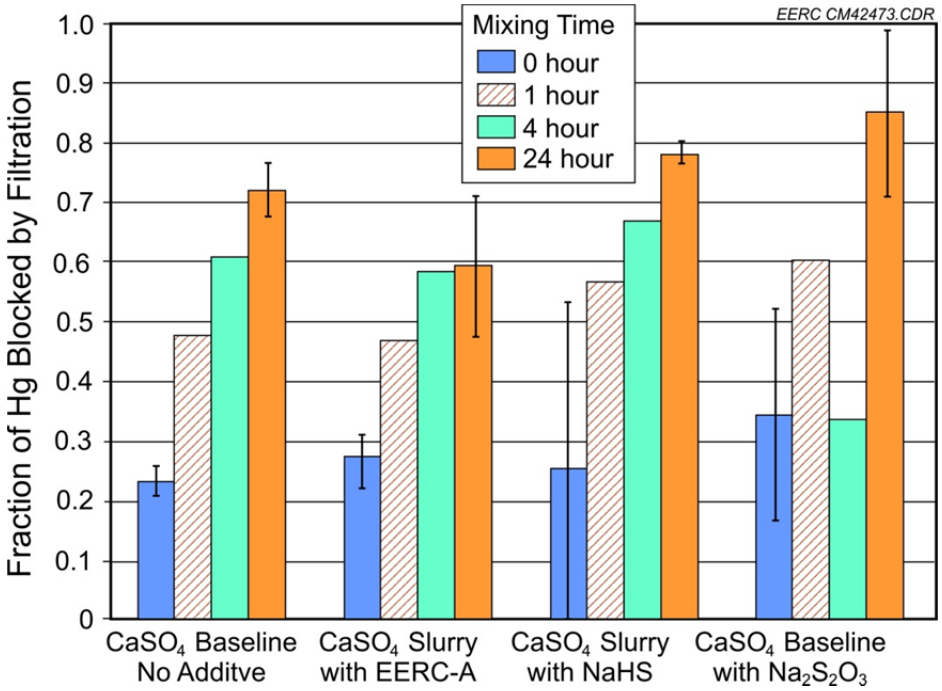

Figure 5-22. Mercury precipitation results with $CaSO_4$ slurry.

The general trend for all of the conditions in Figure 5-22 is an overall increase in blocked mercury with extended mixing time. Baseline data indicate that approximately 72% of the mercury became particulate bound after 24 hours of mixing. The reference additives of NaHS and $Na_2S_2O_3$ appear to increase the amount of blocked mercury, while the EERC-A additive appeared to slightly lower the amount of blocked mercury. Previous work has shown that EERC-A has a very strong affinity for mercury; it is possible that reaction of the additive and mercury rapidly forms insoluble precipitates that are too small to be effectively filtered. Regardless, it seems that EERC-A slightly interferes with the mercury precipitation process, where NaHS and sodium thiosulfate do not.

The effect of EERC-A was also investigated for its impact on selenium precipitation. In wet FGD wastewater treatment systems, selenium is more difficult to remove via precipitation than mercury. Additionally, the oxidized selenate form of selenium is more difficult to remove that the selenite that forms from SeO_2 absorption. Selenium precipitation results with EERC-A in $CaSO_4$ slurry are summarized in Figure 5-23. In relation to the mercury results of Figure 5-22, the selenium conditions would be considered zero hour; i.e., they were mixed and agitated briefly then filtered immediately.

The results in Figure 5-23 show that the selenite form was precipitated more effectively than the difficult-to-remove selenate form. Selenite was blocked by the filter in proportions that were comparable to the equivalent zero-hour mercury data in Figure 5-22. EERC-A appeared to have little effect on selenite precipitation. The selenate baseline had virtually zero precipitation, and the addition of EERC-A made only a slight improvement.

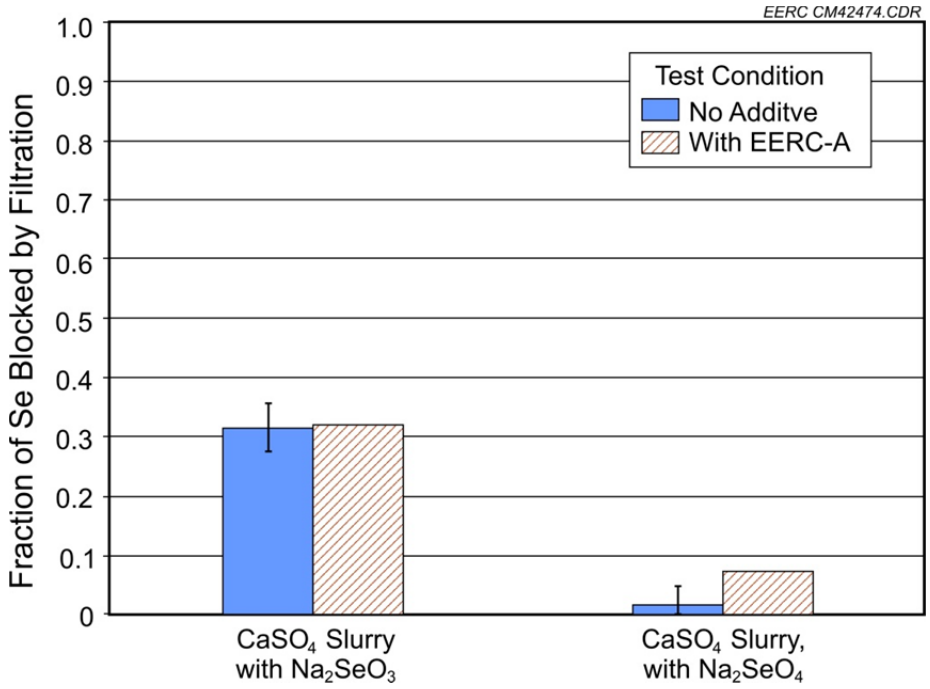

Figure 5-23. Selenite and selenate precipitation results with $CaSO_4$ slurry.

A further part of the precipitation study was designed to investigate interactions between mercury and selenium in the slurry and whether EERC-A could be used to enhance any interactions. Possible synergies between EERC-A, mercury, and selenium were not observed except at high pH conditions with the $Ca(OH)_2$ reagent. Compared to the $CaSO_4$ slurry, which had a pH range of 8.2–9.0, the $Ca(OH)_2$ slurry pH ranged over 13.2–13.6.

Figure 5-24 summarizes zero-hour mercury results from the $Ca(OH)_2$ slurry tests, and Figure 5-25 shows the corresponding selenium data. The effects were more dramatic for mercury under these conditions; the addition of selenite or selenate approximately doubled the amount of mercury blocked by filtration. The addition of EERC-A resulted in another approximate doubling compared to baseline conditions. Peak mercury removals with EERC-A and selenium were 85% and 89% for the selenite and selenate forms, respectively.

As Figure 5-25 indicates, the selenium blockage was greatly increased under the higher pH conditions with $Ca(OH)_2$ compared to the equivalent results with $CaSO_4$ in Figure 5-23. Selenite filter retention increased from 31% to 86%, and for selenate it went from 2% to 55%. However, the effects of interaction with mercury and the addition of EERC-A are much more moderate in terms of altering selenium precipitation compared to the same effects with mercury.

Since trace element removals were greatly improved with the high pH $Ca(OH)_2$ slurry, future work should focus on the validity of these tests in representing conditions that are achievable within FGD wastewater treatment systems. On the other hand, testing with the more representative $CaSO_4$ slurry indicates that addition of reemission additives will have little impact on trace element removal.

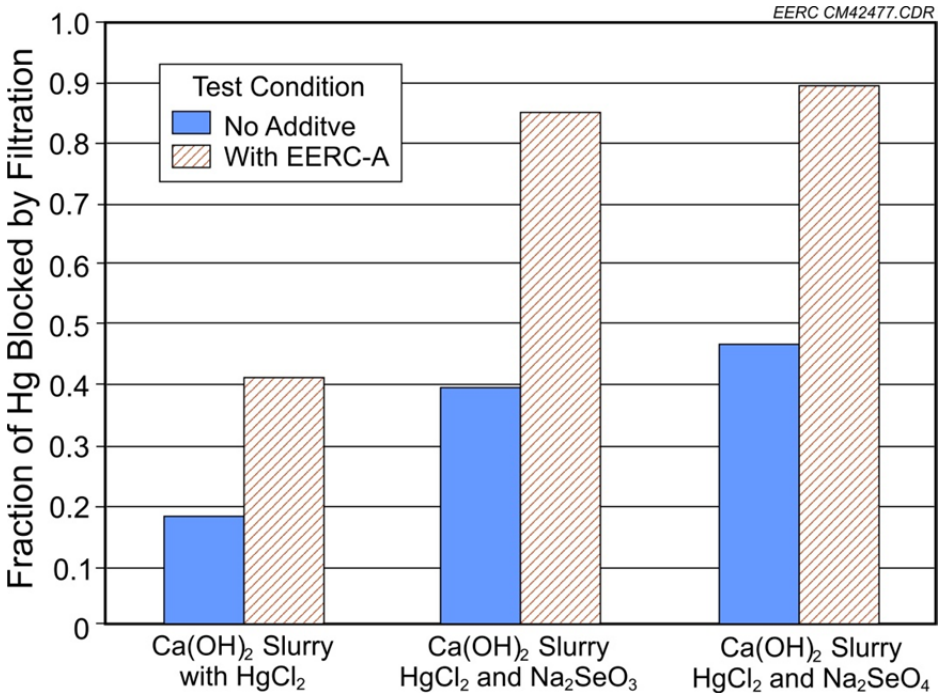

Figure 5-24. Mercury precipitation results with $Ca(OH)_2$ slurry.

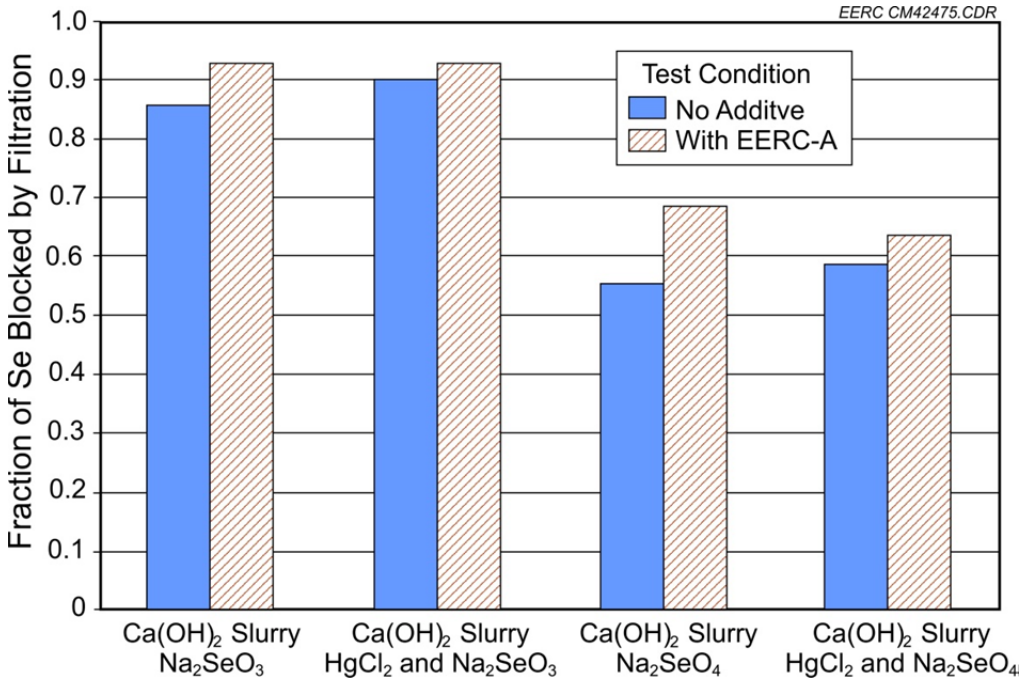

Figure 5-25. Selenium precipitation results with $Ca(OH)_2$ slurry.

5.4 Selenium Capture Technology Development

Selenium is the next most volatile trace element in coal following mercury, and while it is an essential micronutrient for life, selenium can be toxic at elevated concentrations, and its emission to the environment has come under review. The proposed EPA rule (6) for coal-fired utilities does not impose direct limits on stack emissions of selenium; instead, pilot-scale combustion data have been used by EPA to justify the conclusion that total particulate matter and/or HCl will serve as effective surrogates for regulating stack emissions (6). According to EPA, "Se will either fall in to the category of 'non-Hg metal HAP' and be effectively removed in a PM control device, or it will fall into the category of 'acid gas HAP' as gaseous SeO_2 and be effectively removed using FGD technologies" (6).

Two aspects of selenium vapor capture were investigated. In the first, the interactions of selenium and AC were parametrically investigated using the CATM-developed model of mercury and AC interactions as a guide for interpretation. Secondly, the thermophysical properties of flue gas selenium were evaluated to estimate their impact on vapor-phase selenium capture.

5.4.1 Selenium–AC Interactions

This approach was undertaken to evaluate selenium capture on AC within the context of what is mechanistically understood about mercury capture on AC. The underlying goals were to identify critical flue gas interactions important for flue gas selenium capture in order to hypothesize about the ultimate potential for AC-based selenium removal.

The general procedure that has been used successfully to investigate mercury–AC interactions was also used for selenium analysis. Fixed beds of sorbent samples were exposed to a SeO_2-containing mixture of flue gas constituents. $SeO_2$was introduced using a permeation source calibrated to provide representative levels of the vapor in flue gas. The overall experimental setup is shown in Figure 5-26 and consists of the SeO_2 permeation source, fixed-bed sample holder, and an exhaust impinger to capture the remaining vapor phase SeO_2. During evaluation, the AC sample was exposed to the synthetic flue gas mixture spiked with SeO_2 for specified periods of time. At the conclusion of each test, the AC sample was submitted for selenium content analysis; the exhaust line from the sample holder was rinsed with nitric acid into the exhaust impinger, and this solution was also submitted for selenium analysis.

These exposure tests were performed under representative HAG conditions since this flue gas mixture represents plants that are likely to have wet FGD units and that may be most interested in altering the selenium partitioning within the plant using sorbent injection.

Each test only yielded a single, cumulative data point regarding SeO_2 capture on the AC. A 0.5-hour exposure time was selected for this initial study based on the known kinetics of mercury capture under the same conditions. A representative mercury breakthrough curve under the same HAG conditions is shown in Figure 5-27, and it is clear that mercury capture continues for approximately 45 minutes under these gas conditions before the reaction kinetics are altered by a presumed shortage of sorbent active sites. The selenium tests were purposely selected to fall within this window in order to minimize the effects of site depletion from the results. Future experiments could investigate the time history of selenium capture with multiple tests under identical conditions for varying lengths of time.

The experimental matrix is shown in Table 5-7. SeO_2 capture was evaluated as a function of three different parameters with respect to the baseline condition: no SO_2 in the flue gas, no

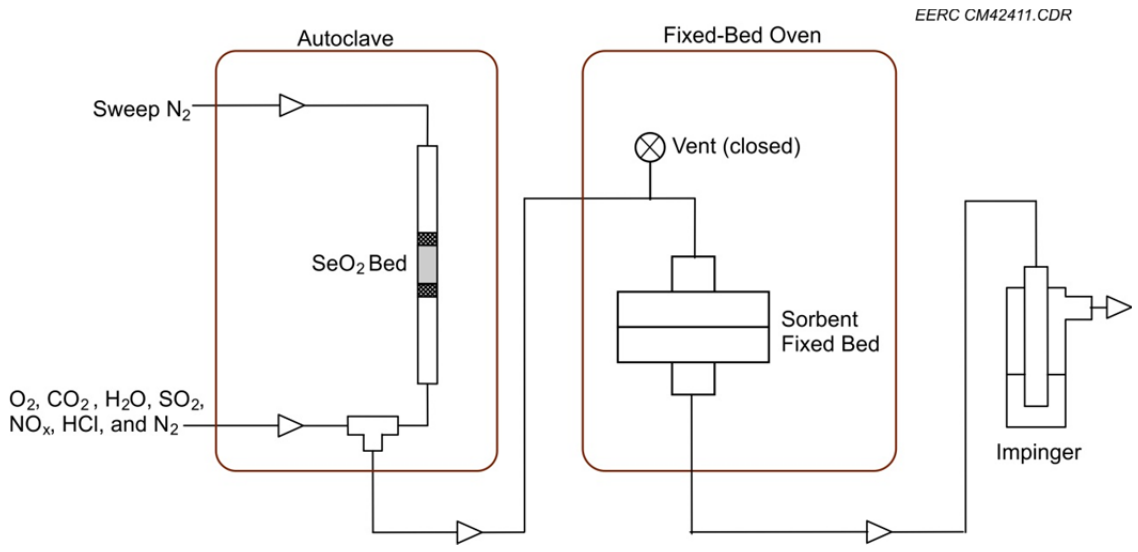

Figure 5-26. Setup for the selenium–sorbent interaction testing.

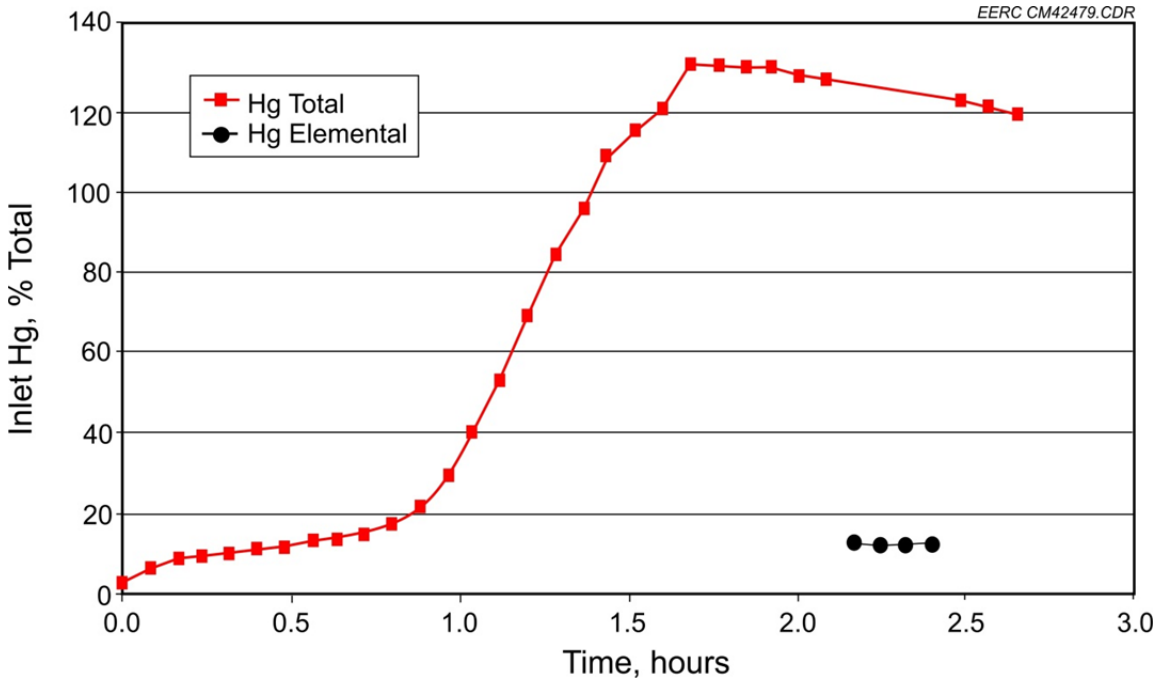

Figure 5-27. Mercury breakthrough curve highlighting the prebreakthrough capture period (elemental mercury capture on standard AC under high acid gas conditions).

Table 5-7. Selenium–AC Test Matrix

Test	Gas Composition	Sorbent	Exposure, hr
1	SeO_2 in high acid gas	None	0.5
2	SeO_2 in high acid gas	Standard AC	0.5
3	SeO_2 in high acid gas—no SO_2	Standard AC	0.5
4	SeO_2 in high acid gas—no NO_2	Standard AC	0.5
5	SeO_2 in high acid gas	Treated AC	0.5

NO_2, and treated versus untreated carbon performance. Again, the significance of these parameters was based on the most critical parameters that affect the mercury oxidation process. SO_2 is oxidized on AC in a competing reaction with mercury; NO_2 appears to be the primary oxidant for in-flight mercury capture; and a treated carbon can have different reaction kinetics for mercury capture. Test 1 was included to calculate a mass balance in order to verify that all selenium was being accounted for.

The average selenium capture for the 0.5-hr exposure was computed based on the difference between the selenium detected in the impinger and the input selenium that was determined during the permeation source calibration. A total mass balance of selenium was also performed for each test by measuring the selenium content on the carbon samples.

The 0.5-hour average selenium capture values for Tests 2–4 are shown in Figure 5-28. The baseline condition (standard carbon with complete high acid gas composition) resulted in approximately 50% selenium capture. Omitting SO_2 from the gas composition resulted in a higher average capture rate, 83%, and omitting NO_2 resulted in 98% capture.

The comparison of the effect of a treated AC is shown in Figure 5-29. The treated carbon has received a halogen pretreatment that is intended to eliminate the needed activation step using HCl from the flue gas. This treatment primarily provides the carbon with higher initial mercury reactivity under conditions where flue gas halogen content is low. As demonstrated by the mercury capture results, there is little benefit from the treatment under the HAG conditions. Selenium capture was mildly improved with the treated carbon compared to the standard.

Another interesting comparison in Figure 5-29 is between the capture rates for mercury and selenium. For both carbons, the average mercury capture is greater than 90%, while for selenium it is 50%–65%. Assuming that selenium breakthrough did not occur during the test period, these results would suggest that the overall kinetics for SeO_2 reaction are somewhat slower than for mercury; in other words, a higher percentage of the SeO_2 vapor is able to pass through the fixed bed of carbon without reacting. There is no direct correlation between fixed-bed performance and in-flight capture, but the results of Figure 5-29 suggest that selenium would be captured less effectively than mercury in HAG.

Selenium mass balance closures were also calculated for each test by measuring the selenium content of the exposed AC samples. These results are summarized in Table 5-8. The poor closure values obtained for Tests 3–5 obviously raise questions about the conclusions that can be drawn. Multiple calibration points provide confidence in the SeO_2 permeation source; other possible explanations for the variance include an incomplete detection of selenium on the carbon samples or the formation of selenium aerosols that travel through the exhaust impinger without being captured. The former appears more likely than the latter, and future work should focus on digestion and analysis methods for measuring selenium on ACs.

In spite of the poor closure values, one observation remains unchanged, specifically that there appears to be clear differences imparted to the selenium capture mechanism as a function of flue gas composition. The significant effect of NO_2 suggests that it may promote a competing set of reactions that interferes with selenium reaction. Also, the improved apparent capture of selenium in the absence of SO_2, Test 3, is in agreement with discussion earlier in the report and other works that have identified SO_2 as a reaction competitor with calcium-based sorbents, e.g., Agnihotri et al. (7).

5.4.2 Impact of Selenium Saturation on Capture Performance

A better understanding regarding selenium capture in wet FGD systems is sought since the amount of selenium that ends up in FGD wastewater can have a strong economic impact and because proposed environmental regulations are based on assumed FGD performance. Further understanding of the mechanisms involved with scrubber selenium capture will aid in evaluating the generalizations that are used in rulemaking and possibly lead to novel solutions for dealing with selenium stack emissions.

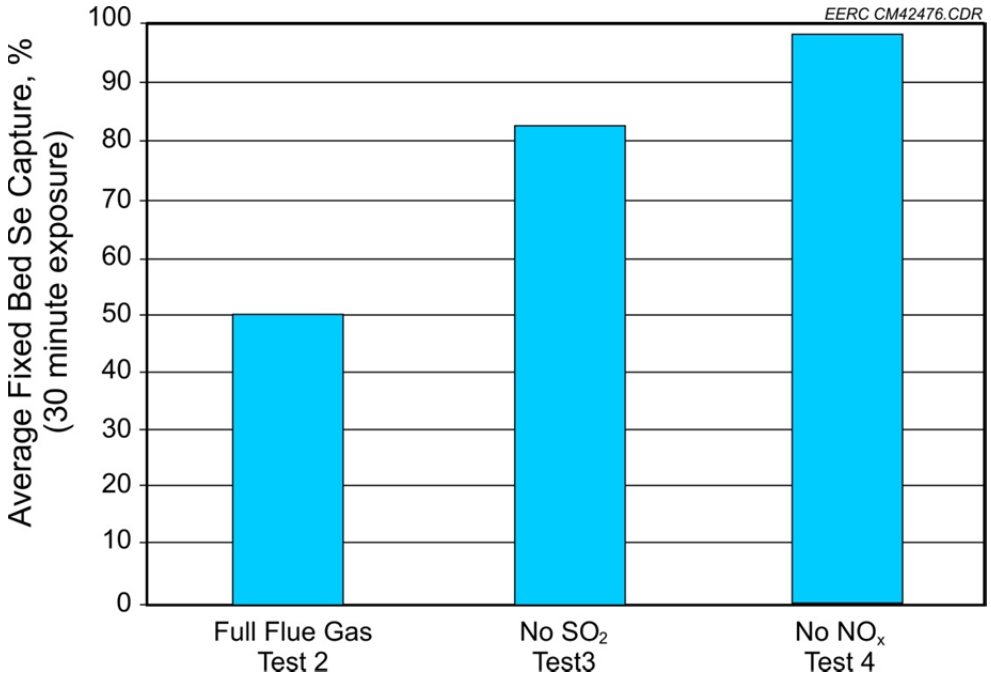

Figure 5-28. Average selenium capture rates for Tests 2–4.

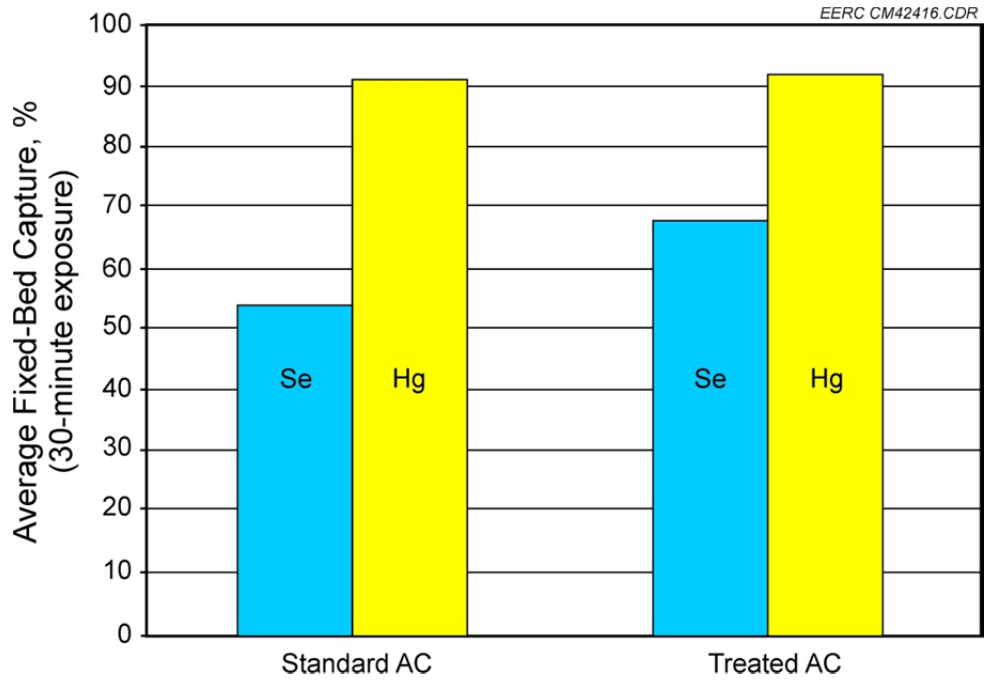

Figure 5-29. Comparison of average selenium and mercury capture rates for standard and treated AC samples.

Table 5-8. Selenium Mass Balance Data for the AC Testing

Test	Impinger Solution Se Content, µg	AC Se Content, µg	Calibrated Se Input, µg	Se Mass Closure, %
1	63.0	N/A	58.1	109
2	28.9	30.5	58.1	102
3	10.0	23.8	58.1	58
4	1.0	29.8	58.1	53
5	20.0	25.5	58.1	78

Selenium dioxide (SeO_2) is routinely identified as the model compound for gas-phase selenium in coal flue gas. A prior investigation into the speciation of selenium in coal flue gas by Yan et al. identified elemental selenium and SeO_2 as possible gas-phase forms (8). More recently, Senior et al. used experimentally derived SeO_2 reaction kinetics in a predictive model to reasonably estimate selenium partitioning on fly ash (9). SeO_2 is significantly more volatile than elemental selenium; it is also hygroscopic and will readily dissolve in water to form selenous acid (H_2SeO_3). The properties of SeO_2 suggests that wet FGD systems should be highly effective for its removal, yet selenium (presumably SeO_2) emissions seem to persist in excess of what would be expected for such a highly soluble compound. There is the possibility that an as-yet unidentified selenium speciation or reemission mechanism is responsible for the observed behavior, but the present work is focused on investigating the possible role of thermophysical properties in selenium capture, assuming SeO_2 to be the dominate constituent of vapor-phase selenium.

When SeO_2 phase changes are considered in flue gas, two mechanisms are possible. The first is sublimation between solid- and vapor-phase SeO_2, and the second is the vapor-to-liquid condensation of H_2SeO_3. The latter mechanism depends on the formation of H_2SeO_3 from the reaction between SeO_2 and moisture vapor:

$$SeO_2 + H_2O \leftrightarrow H_2SeO_3 \quad [16]$$

In moist flue gas, the saturation properties of both anhydrous SeO_2 and hydrated H_2SeO_3 must be considered. Under ambient pressure, H_2SeO_3 decomposes according to the reverse reaction in Equation 16 at 158°F. Above this temperature, only SeO_2 will exist, but below it, both SeO_2 and H_2SeO_3 can form. Compared to SeO_2, H_2SeO_3 has a much lower volatility, and its formation will have the effect of depressing the saturation concentration below that predicted for anhydrous SeO_2. An analogue would be the system of SO_3 and H_2SO_4, where the hydration of SO_3 vapor dramatically reduces its volatility and H_2SO_4 condensates form.

In a study of sampling methodology for selenium in ambient air, Oehm et al. (10) observed limited selenium volatility below the H_2SeO_3 decomposition temperature, but above it, they observed distinct periods of H_2SeO_3 decomposition and SeO_2 volatilization. Oehm et al. concluded that under the ambient air sampling conditions of interest in that work (10), SeO_2 vapor would react with atmospheric moisture and be found primarily as low-volatility, condensed H_2SeO_3. Given Oehm et al.'s conclusion, it seems that a transition must occur from vapor-phase SeO_2 that is dominate in flue gas to the condensed H_2SeO_3 end state in ambient air.

Estimating this point of transition in relation to conventional air pollution control equipment was the central focus of this approach.

During the investigation of SeO_2 saturation properties, three measurements were used; the first was emission rate measurement of SeO_2 vapor in dry nitrogen using a permeation source. Secondly, controlled condensation measurements were taken in flue gas that were analogous to those used for SO_3 sampling, but were instead analyzed for selenium content. Finally, impactor-based particulate measurements were taken across a pilot-scale wet FGD absorber, and each stage fraction was analyzed for selenium content.

To make the SeO_2 permeation source, SeO_2 powder was mixed with inert diatomaceous earth to reduce pressure drop, and the mixture was packed between quartz wool plugs inside of a 0.5-inch quartz tube. The packed bed was maintained at temperature inside of a tube furnace, and the entire assembly along with tubing connections was inserted into a heated cabinet to reduce the potential for cold spots and uncontrolled condensation. Preheated nitrogen sweep gas was passed through the permeation source from the top-down. This sweep stream approached equilibrium saturation conditions with the SeO_2 in the packed bed. Upon exiting the permeation source, the sweep flow was mixed with a preheated dilution flow of nitrogen to reduce the SeO_2 vapor pressure and avoid uncontrolled condensation. Both flows of nitrogen were regulated by calibrated mass flow controllers; the recorded mass flow controller flow rates were used to determine the total volume of sample flow. An overall schematic of the permeation source is shown in Figure 5-30.

The diluted flow left the heated cabinet and was sent through an ice-cooled impinger containing 2% nitric acid solution to capture the vapor-phase SeO_2. Sample recovery consisted of rinsing the transport umbilical into the impinger with 10% nitric acid solution and diluting the sample to a standard volume of 500 mL. Total selenium was analyzed using ICP–MS.

Controlled condensation measurements similar to those used for SO_3/H_2SO_4 sampling were also used to investigate the saturation properties of flue gas selenium vapor. Two simultaneous measurements were made on the EERC's PTC, both at the ESP outlet/wet FGD inlet, while combusting a low-sulfur bituminous coal. The sampling setup is shown in Figure 5-31 and consists of a standard EPA Method 5 particulate filter followed by a temperature-controlled condenser section, the impinger train from a Method 29, and finally a post-impinger-train filter. Both samples maintained the particulate filter at the flue gas temperature of 320°F; the condenser section for one of samples was also maintained at 320°F, while the other was cooled to 140°F in order to mimic a typical temperature drop across a wet FGD absorber. Following the condensers, each flue gas sample was then drawn through an umbilical to the ice-cooled impinger train and finally through a post-train particulate filter. Recovery for these samples consisted of weighing the filters and collecting separate rinses for each section of the sample including the nozzle, condenser, umbilical, H_2O_2 impingers, dry impinger, and the $KMnO_4$ impingers. Selenium analysis was performed separately for each filter and rinse solution.

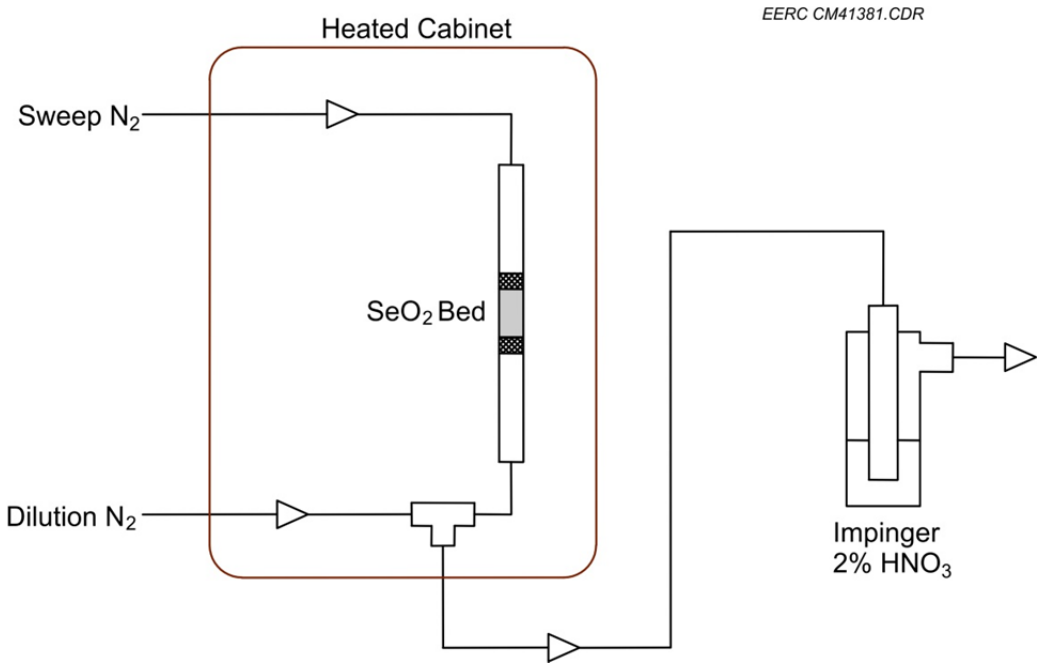

Figure 5-30. Schematic for SeO_2 permeation source.

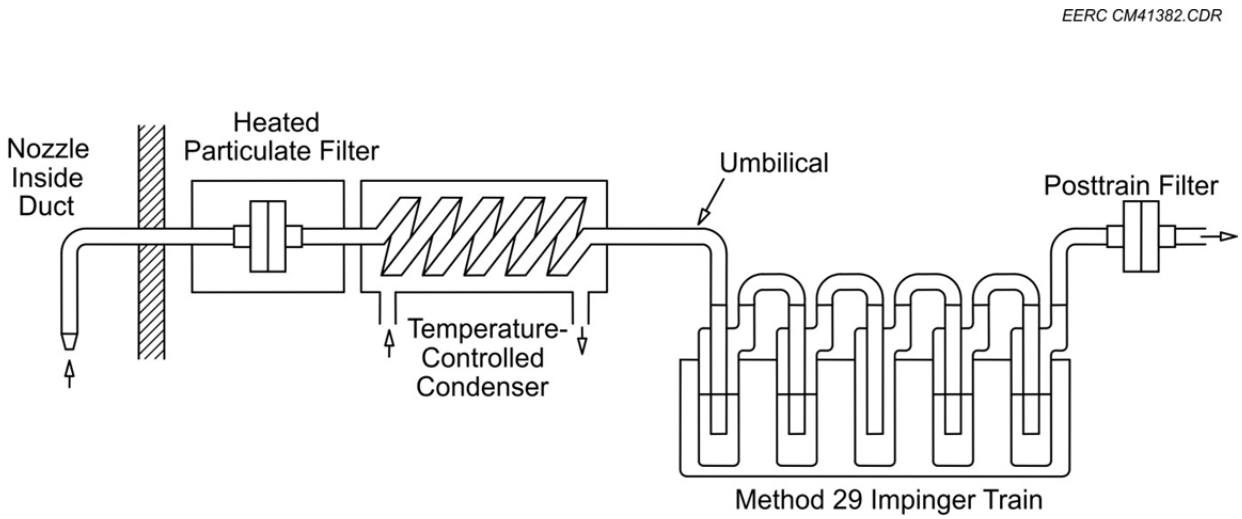

Figure 5-31. Sampling setup for the controlled condensation measurements.

Additional flue gas sampling was conducted across the PTC's wet FGD absorber using cascade impactor measurements. These measurements took place during a different PTC run than the controlled condensation measurements; the test coal for these samples was a low-sulfur subbituminous PRB. The general setup for these measurements is shown in Figure 5-32 and consists of a seven-stage Mark III cascade impactor followed by a heated particulate filter and a

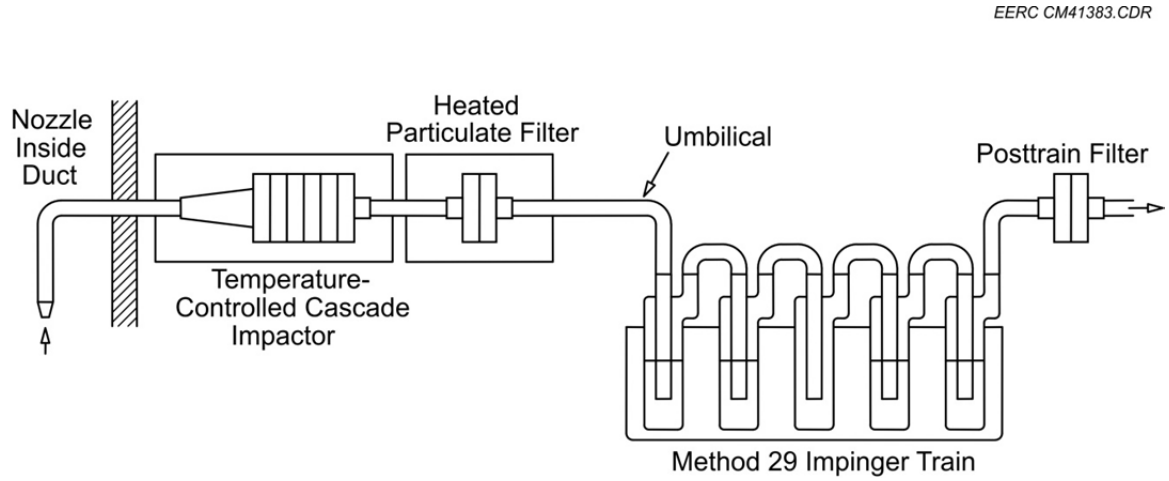

Figure 5-32. Sampling setup for the impactor measurements.

Method 29-based impinger train for vapor-phase trace element capture. Simultaneous measurements were made at the inlet and outlet of the PTC's wet FGD absorber. The impactors were maintained close to the corresponding flue gas temperatures (250° and 125°F at the FGD inlet and outlet, respectively) in order to minimize distortions to the particulate measurements from vaporization of volatile selenium. Sample recovery followed standard procedures except that, in addition to weight gain measurement, each impactor stage rinse was analyzed separately for total selenium.

The available handbook data for SeO_2 sublimation temperatures (11) have been augmented with measurements from the SeO_2 permeation source down to temperatures near the H_2SeO_3 decomposition point. Measurements of the dry vapor pressure of SeO_2 were relatively simple and in good agreement with the trend of the handbook data. However, saturation measurements with added moisture were not possible with the permeation source. When moisture vapor was added to the sweep flow in Figure 5-30, the SeO_2 deliquesced, and the packed bed arrangement was no longer feasible. Attempts were made to replace the permeation source with an equilibration chamber with sweep flow over a SeO_2 solution. This arrangement has been used with elemental mercury for various laboratory mercury vapor generators but was determined to be unsuitable for the SeO_2 evaluation based on poor agreement with duplicate dry condition measurements.

A better indication of the saturation point with moisture present came from the controlled condensation measurements of flue gas selenium. The detected selenium concentration as a function of sample breakdown is shown in Figure 5-33. As shown, the overall agreement in the total flue gas selenium content is quite good between the two measurements, but there is a dramatic shifting of where the selenium was detected based on condenser temperature. For the cooler 140°F condenser, the bulk of the selenium was condensed and remained in the condenser itself, while for the 320°F condenser, most of the selenium passed through and was detected in the unheated umbilical section.

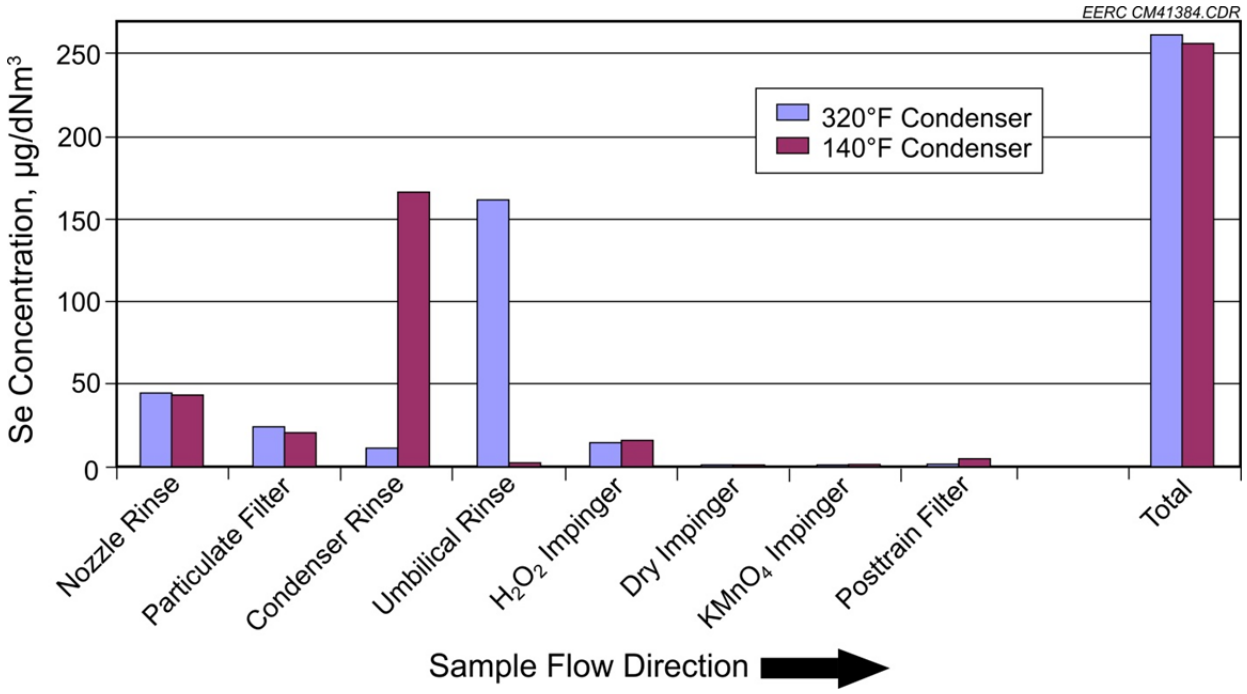

Figure 5-33. Selenium content as a function of the controlled condensation sample breakdown for a low-sulfur bituminous coal flue gas.

To estimate the impact of moisture content in the flue gas on selenium saturation, an assumption was made that the gas exiting the 140°F condenser was at or very near saturation conditions. In that case, the selenium detected downstream of the condenser, 18.9 µg/dNm^3, is a measure of the saturation concentration at 140°F and the measured flue gas moisture content of 5.3%.

The summary data for SeO_2/H_2SeO_3 saturation is shown in Figure 5-34, which is a plot of the vapor-phase selenium concentration (as elemental selenium) as a function of temperature. Selenium vapor concentrations that fall above the saturation lines for a given temperature exceed the concentration present at equilibrium, and condensate formation will be favored. The SeO_2 sublimation boundary is supported by a combination of existing handbook data points and those measured with the SeO_2 permeation source. This curve ends at the H_2SeO_3 decomposition temperature of 158°F, from which a tentative H_2SeO_3 condensation boundary has been extended through the controlled condensation data point at 140°F. There are too few data to support the actual H_2SeO_3 condensation boundary in Figure 5-34; the approximate boundary is shown only to indicate the impact of H_2SeO_3 formation, which is to dramatically decrease selenium volatility compared to that predicted by simple extension of the SeO_2 sublimation boundary.

To relate the saturation data to conditions encountered in coal flue gas, typical temperatures and selenium concentrations encountered in flue gas overlay the data in Figure 5-34. As inspection of the figure shows, the SeO_2 sublimation boundary could only be crossed with high selenium concentrations and temperatures below approximately 180°F. The

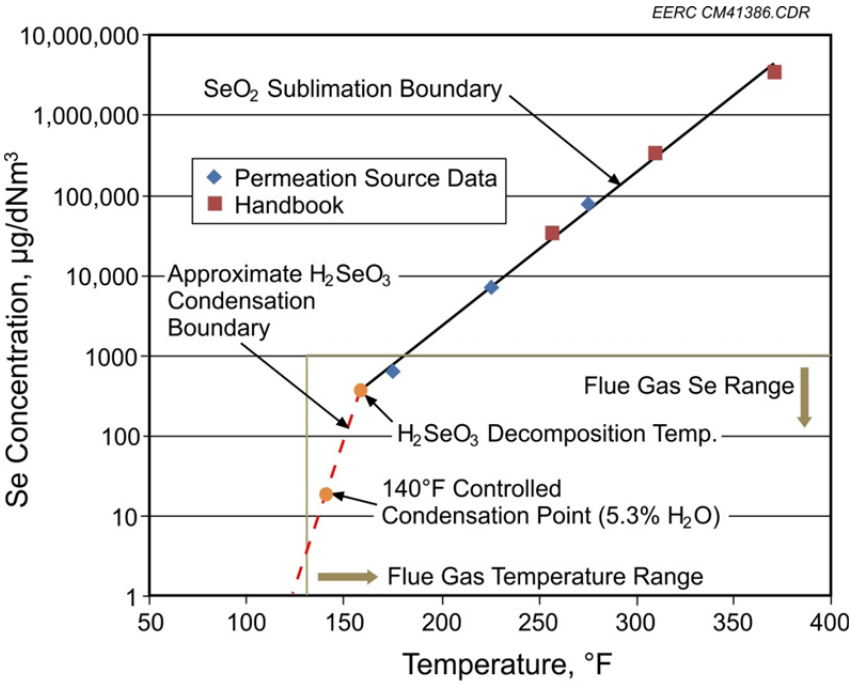

Figure 5-34. Approximate SeO_2/H_2SeO_3 saturation curve.

SeO_2 saturation limit rises rapidly with temperature and is in excess of 10,000 µg/dNm^3 at 300°F, meaning that SeO_2 saturation is not a consideration for analyzing selenium interactions within air pollution control equipment over this temperature range. This has been previously identified by the modeling effort of Senior et al. (9).

However, cooling to temperatures below 180°F is often a part of FGD systems, the most extreme of which would be in wet scrubbers where the flue gas can be cooled to very near its dew point. At temperatures below the H_2SeO_3 decomposition temperature, Figure 5-34 suggests that the saturation boundary decreases dramatically; at 130°F the saturated selenium vapor concentration is estimated to be only 4 µg/dNm^3. At temperatures below 130°F, the saturated selenium vapor concentration is expected to be even lower, which would be consistent with Oehm's conclusion that H_2SeO_3 is primarily present during ambient air selenium sampling (10).

Selenium saturation conditions may also have an effect on accurately measuring its partitioning between vapor and solid phases. The key place for this to be a concern is at the wet FGD outlet, since it is common practice at these sampling locations to reheat the flue gas sample from its moisture-saturated temperature to approximately 250°F in order to prevent moisture condensation on the particulate filter. However, as the data of Figure 5-34 suggest, a change in temperature from approximately 140° to 250°F is enough to decompose any H_2SeO_3 present and increase the selenium saturation concentration by a factor of approximately 1000. Any condensed selenium originally captured on the particulate filter could be volatilized, passed through the filter, and then be detected in the impinger solution and counted as being in the vapor phase. This sampling bias may contribute to interpretation errors regarding selenium capture across wet scrubbers using existing selenium measurement data.

While the combined data from the permeation source and controlled condensation measurements suggest that selenium condensation is favored at conditions across wet scrubbing systems, they do not demonstrate that it actually does occur in quenched flue gas. A set of impactor-based measurements was made in an attempt to directly measure particulate selenium changes across the PTC's wet FGD absorber. Unfortunately, the testing opportunity occurred with a low-sulfur PRB coal that produced flue gas selenium concentrations at the FGD inlet far below the estimated saturation levels. In fact, because of the high calcium content of the ash, the speciation of selenium was shifted toward the particulate phase, and the resulting vapor phase selenium concentrations were below detection limits for these measurements. Therefore, any opportunity for condensation and aerosol formation was small and impossible to ascertain.

It was possible to measure particulate selenium across the FGD absorber; the particle-size distribution data are summarized in Figure 5-35, which is a plot of the total dust stage weight distribution and the selenium stage weight distribution, both as a function of the calculated aerodynamic particle size. Total selenium summations are in fair agreement across the FGD, 0.15 µg/dNm^3 (3% O_2) at the inlet versus 0.17 µg/dNm^3 (3% O_2) at the outlet. This suggests that the particulate selenium detected at the inlet was carried through without capture to the outlet. However, the particle-size distribution did undergo changes. The particle-size distribution data show a general coalescing of inlet particulates into a larger average particle size and the reduction of submicrometer particles. Selenium concentration data confirm this particle-size shift since selenium was detected in the 2–10-µm particle-size range at the outlet, but it was not detected in this size range at the inlet. While these changes appear distinctive, repeat particle-size distribution measurements will be needed with a higher selenium content coal in order to form useful conclusions. The current impactor measurements are limited to only supporting a hypothesis that selenium-containing particulates can pass through a wet FGD absorber.

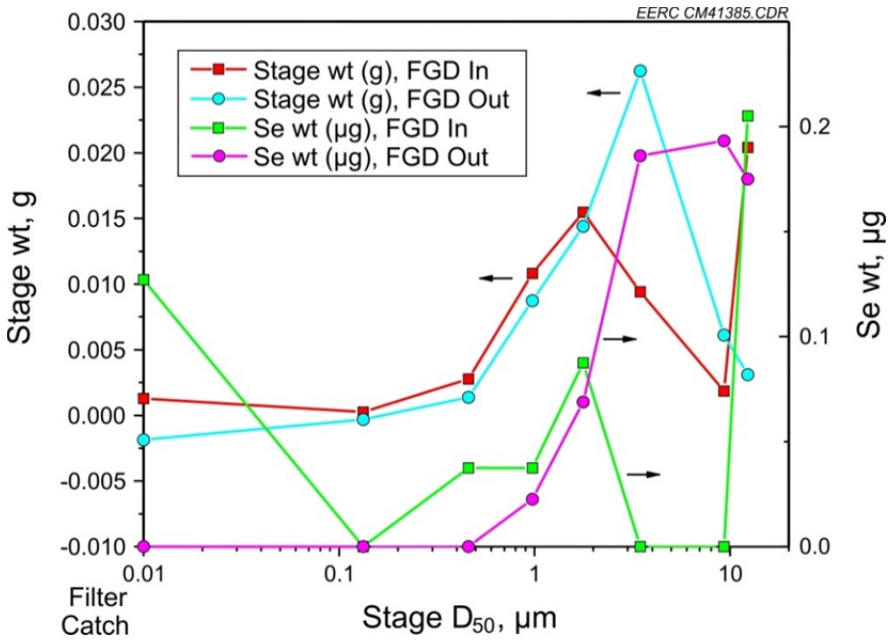

Figure 5-35. Particle-size distribution and selenium content across the PTC's FGD absorber for a low-sulfur PRB coal flue gas.

5.5 Conclusions

A number of conclusions can be drawn based on the pursuits of this CATM activity. These summary conclusions are outlined below:

- The applied model for calculating in-flight mercury capture with AC was shown to qualitatively predict the limiting factors for mercury capture with a variety of coal flue gases. Furthermore, the insights provided by the sensitivity study of mercury capture result in optimization recommendations that are in agreement with those gained from field experience.

- The most promising inorganic sorbent that was investigated appeared to have reasonable reaction kinetics, but far less capacity for mercury capture than AC. While capacity is not usually a determining factor for in-flight capture, it is indicative of the number of sites available to support mercury capture. The inorganic sorbent's shorter breakthrough times suggest fewer total sites and a relatively limited ability to support in-flight capture compared to AC. Activation methods could be pursued in future work to increase the number of active sites on the sorbent; however, the inorganic sorbent's reaction mechanism needs more research. It seems that the mercury oxidation mechanism on the inorganic sorbent was highly inhibited by SO_2. Assuming that mercury oxidation is a required first step for mercury capture (as it is on AC), then the inorganic sorbent may be of even more limited use in high-sulfur flue gases than AC.

- Testing of durable ACs suggest that their extreme physical toughness may have come at the cost of reactivity or, more specifically, the absolute number of active sites. These carbons perhaps may serve as novel catalyst supports but do not appear to be suitable mercury sorbents.

- The surface modifications performed on ACs proved ineffective at altering the relative kinetics between mercury and SO_2 oxidation. The experiments did, however, substantiate the mechanistic understanding of SO_2 and mercury competition for active sites on the carbon.

- The EERC mercury reemission additive candidate was shown to have a slightly detrimental effect on mercury precipitation in simulated $CaSO_4$ slurry solutions. This was in contrast to the reference additives, NaHS and $Na_2S_2O_3$, which resulted in slight improvements to mercury precipitation. The EERC additive had little to no effect on selenium precipitation in the $CaSO_4$ solutions, but selenium and mercury precipitation appeared to be dramatically better under the high pH slurry that used a $Ca(OH)_2$ reagent. Under these conditions, the EERC reemission additive approximately doubled the amount of mercury that was blocked by filtration. Future work should focus on the validity of these tests in representing conditions within a FGD wastewater treatment system so that these findings can be extrapolated and perhaps used to improve trace element removal.

- Measurements regarding selenium vapor interactions in flue gas suggest that the vapor-phase control of selenium may be more difficult than for mercury. Selenium can be captured on AC; however, AC is not as efficient for selenium capture as it is for mercury. Furthermore, sensitivities were identified between selenium capture and specific components of the flue gas, suggesting that selenium capture on AC will vary among coal types and plant configurations.

- Measurements of the SeO_2 saturation boundary show that the saturation limits for H_2SeO_3 can be exceeded in FGD systems that quench the flue gas to temperatures below 180°F. This indicates that the saturation properties of SeO_2/H_2SeO_3 should be considered when selenium vapor capture is investigated across these devices. Future research should consider additional selenium partitioning measurements across FGD absorbers to determine if H_2SeO_3 condensation does occur and to what degree it may affect scrubber selenium capture.

5.6 References

1. Olson, E.S.; Mibeck, B.A.; Benson, S.A.; Laumb, J.D.; Crocker, C.R.; Dunham, G.E.; Sharma, R.K.; Miller, S.J.; Pavlish, J.H. Mechanistic Model for Flue Gas–Mercury Interactions on Activated Carbons: The Oxidation Site. *Prepr. Pap.—Am. Chem. Soc., Div. Fuel Chem.* **2004,** *49* (1).

2. Center for Air Toxic Metals. *Center for Air Toxic Metals Final Technical Report;* Environmental Protection Agency Agreement No. CR 830929-01; May 1, 2003, to September 30, 2009 Vol. V Part I.

3. Olson, E.S.; Crocker, C.R.; Sun, J.; Brandt, K.H.; Dunham, G.E.; Pavlish, J.H. The Interactions of SO_2 and SO_3 on a Carbon Sorbent and Their Impact on Mercury Capture. In *Proceedings of the EPA-DOE-EPRI-AWMA Power Plant Air Pollutant Control Mega Symposium;* 2006; Vol. 2, pp 711–721.

4. Zhuang, Y.; Martin, C.; Pavlish, J.; Botha, F. Cobenefit of SO_3 Reduction on Mercury Capture with Activated Carbon in Coal Flue Gas. *Fuel* **2011**, *90*, (10), 2998–3005.

5. Martin, C.L.; Zhuang, Y.; Pavlish, J.H.; Botha, F. Pilot-Scale Study of Mercury Capture Enhancement Across Wet FGD Systems. In *Proceedings of Air Quality VII*; October 26–29, Arlington, VA, 2009.

6. U.S. Environmental Protection Agency. National Emission Standards for Hazardous Air Pollutants from Coal- and Oil-Fired Electric Utility Steam Generating Units and Standards of Performance for Fossil-Fuel-Fired Electric Utility, Industrial-Commercial-Institutional, and Small Industrial-Commercial-Institutional Steam Generating Units. Proposed Rule. *Federal Register* **2011** *76* (85).

7. Agnihotri, R.; Chauk, S.; Mahuli, S.; Fan, L.-S. Selenium Removal Using Ca-Based Sorbents: Reaction Kinetics. *Environmental Science & Technology* **1998**, *32* (12), 1841–1846.

8. Yan, R.; Gauthier, D.; Flamant, G.; Wang, Y. Behavior of Selenium in the Combustion Of Coal or Coke Spiked with Se. *Combustion and Flame* **2004**, *138*, 20–29.

9. Senior, C.; Van Otten, B.; Wendt, J.O.L.; Sarofim, A. Modeling the Behavior of Selenium in Pulverized-Coal Combustion Systems. *Combustion and Flame* **2010**, *157*, 2095–2105.

10. Oehm, G.J.; Crisp, P.T.; Ellis, J. The Recovery of Selenious Acid Aerosols on Glass Fiber Filters. J. Air & Waste Mgmt. Assoc. Chemical Rubber Company. 1978. *CRC Handbook of Chemistry and Physics,* 58th ed; CRC Press: Cleveland, OH, 1991; Vol. 41, No. 2, pp 190–194.

6.0 DEVELOPMENT AND TESTING OF SAMPLING AND ANALYTICAL METHODS FOR MERCURY AND TRACE ELEMENTS

6.1 Activity Objectives

To support the research activities proposed in this activity and to further the development of analytical measurement in the energy industry, the EERC evaluated and further developed measurement techniques with an emphasis on mercury and trace elements, reactions within scrubbers, and CO_2 capture technologies, as well as addressing challenges of current wet-chemistry EPA-approved flue gas-sampling procedures by providing a possible sorbent-based strategy to obtain valid and reliable trace metal data; this method, to be most effective, must be flexible, relatively easy to use, economical, and robust, as well as being able to pass scrutiny as an alternative sampling method to currently approved methods.

The goals of the proposed research under this activity were to:

- Assist CATM researchers in other areas in their need for nonroutine analytical measurements. A dry sorbent trap-based method was, therefore, developed that is an economical, fast, and robust method as a possible alternative to EPA Method 29 (M29) for trace metals and M26A for halogens. Initial evaluations were performed in actual flue gas environments.

- Use the speed, sensitivity, and selectivity of liquid chromatography (LC)–MS to identify the speciated forms of As, Se, Hg, and halogens present in a wet scrubber, including samples that were collected during pilot-scale runs (combustion and oxy-fired modes) and full-scale testing programs.

- Evaluate a variety of coal combustion product (CCP) samples with tests from the leaching framework, with synthentic groundwater leaching procedure (SGLP), and with 30-day long-term leaching (LTL). Using these data, interpret the results of samples within the leaching tests, compare and contrast mercury emission control CCPs with corresponding standard CCPs, and compare and contrast the leaching methods.

6.2 Development of a Multielement Sorbent Trap Method

6.2.1 Introduction

On March 16, 2011, EPA proposed the first national standard to reduce mercury, nonmercury metals, and HCl emissions from coal-fired power plants (1). This standard imposes significant emission reductions for existing and new units across the entire utility field. After implementation, EPA estimates that the standard will prevent serious illnesses and health problems for thousands of Americans, including up to 17,000 premature deaths, 11,000 heart attacks, 120,000 asthma attacks, 12,200 hospital and emergency room visits, 4500 cases of chronic bronchitis, and 5.1 million restricted activity days (1).

Power plants are estimated to be the largest emitters of mercury (50%), acid gases (over 50%), and toxic metals (over 25%) in the United States, as shown in Table 6-1. From 1990 to 2010, all of the emissions exhibited a slight increase even though there was a significant increase in the number of utilities in operation across the United States. This shows that the entire fleet has made some progress in reducing emissions through system upgrades, as well as state and federal regulations.

Additionally, as shown in Table 6-2, EPA notes that coal- and oil-fired electric utility steam-generating units (EGUs) contribute a large proportion of metal emissions compared to the total estimated anthropogenic metal emissions for some of the metals. For other metals, the anthropogenic emissions are far more substantial that the emissions from EGUs.

Under the proposed rule, EPA is establishing national emission standards for HAPs (National Emission Standards for Hazardous Air Pollutants [NESHAP]) from EGUs under Section 112 (d) of the Clean Air Act and proposing revised New Source Performance Standards (NSPS) under Section 111(b). More specifically, the proposed rule sets limits on mercury, nonmercury metals, and acid gas emissions from coal-fired plants. For nonmercury metals (as shown in Table 6-3), the rule proposes several alternative standards, as follows:

1. Limits on metal emission using particulate matter as a surrogate
2. Individual nonmercury metals (shown in Table 6-3)
3. Total nonmercury metals (shown in Table 6-3)

Owner and operators of EGUs may select from any of the above three alternatives but must demonstrate compliance with these limits either using continuous emission monitors (CEMs) or frequent sampling using EPA-approved methods, such as EPA M29 and M26A. For units that elect to use CEMs, the CEMs must be certified and validated using EPA-approved methods (e.g., M29, M26a). For units that elect to comply with the total or individual nonmercury metal emissions, the unit must conduct metal emission testing every 2 months using EPA M29. Sampling with M29 can be timely and expensive and require highly trained personnel.

Table 6-1. Nationwide Emissions for Six Priority HAPs, tpy (1)

	Coal		Oil		Natural Gas	
	1990	2010	1990	2010	1990	2010
HAP						
Arsenic	61	71	5	3	0.15	0.25
Chromium	73	87	4.7	2.4	–	–
Mercury	46	60	0.25	0.13	0.0015	0.024
Nickel	58	69	390	200	2.2	3.5
HCl	143,000	155,000	2900	1500	NM*	NM
HF	20,000	26,000	140	73	NM	NM

* Not measured.

Table 6-2. Summary of Metal Emissions from EGU Sources (1) 2005 Metal HAP Emissions from the Inventory Used for the National Air Toxics Assessment (NATA), tpy

	U.S. EGU Emissions	Non-EGU Emissions	Total U.S. Anthropogenic Emissions in 2005, %
Antimony	19	83	0
Arsenic	200	120	62
Beryllium	10	13	44
Cadmium	25	38	39
Chromium	120	430	22
Cobalt	54	60	47
Manganese	270	1800	13
Nickel	320	840	28
Selenium	580	120	83

An example of the complexity of M29 is provided in Figure 6-1, which represents only the field sample recovery scheme for M29. This scheme does not include any of the solution preparation or impinger preparation that must be performed in the field. There is also a lot of laboratory glassware such as volumetric flasks that are required to accurately dilute the samples to specific volumes. Since these recovery steps are done in the field and not in a clean laboratory, each step is a possible source for sample bias or contamination from the environment surrounding the recovery area as well as due to human error. The field recovery scheme also requires acetone, 0.1 N HNO_3, DI water, permanganate reagent, and 8 N HCl. All of these chemicals have to be shipped or transported to the field site, and typically solutions have to be made from more concentrated solvents to ensure fresh, stable solutions.

Even though M29 is a cumbersome method, it traditionally has provided sufficient detection limits for HAP metal analysis. The current EPA utility MACT rule poses significant challenges for M29 though, and many of the elements fall below the method detection limits. Table 6-4 also displays the HAP metal emission limits for existing coal-fired units converted to $\mu g/dNm^3$ at 3% O_2 values so that they can be directly compared to the published detection limits present in M29. The detection limits are based on a flue gas volume of 1.25 m^3 as stated in M29. As seen from the table, the Sb and Ni emission limits are at or below the published M29 detection limits. These detection limits are also for analysis by ICP or graphite furnace atomic absorption (GFAA) and not AA. The detection limits for AA are much higher than ICP or GFAA and would not be sufficient even at long sampling times for most of the HAP metals. The MACT rules mandate a flue gas volume minimum of 4 dscm, which will improve the detection limits by a factor of 3.2. Although this improves the detection limit, it also results in an extremely long sampling time of 4–6+ hours for most units. These long sampling times may degrade the solvents and will dramatically increase the amount of ice used during the sampling process. This is especially important when sampling at outdoor stacks in hot environments with limited space around the sampling areas. The amount of ice consumed during a 6-hour test on a 90°F day will be much higher than a 2-hour test.

Table 6-3. Alternative Emission Limitations for Existing Coal- and Oil-Fired EGUs (1)

Subcategory	Coal-Fired Unit Designed for Coal ≥ 8300 Btu/lb	Coal-Fired Unit Designed for Coal < 8300 Btu/lb	IGCC lb/TBtu (lb/GWh)	Liquid Oil, lb/TBtu (lb/GWh)	Solid Oil-Derived
SO_2	0.20lb/MMBtu (2.0 lb/MWh)	0.20 lb/MMBtu (2.0 lb/MWh)	NA	NA	0.40 lb/MMBtu (5.0 lb/MWh)
Total Non-Hg Metals	0.000040 lb/MMBtu (0.00040 lb/MWh)	0.000040 lb/MMBtu (0.00040 lb/MWh)	5.0 (0.050)	NA	0.000050 lb/MMBtu (0.00040 lb/MWh)
Antimony, Sb	0.60 lb/TBtu (0.0060 lb/GWh)	0.60 lb/TBtu (0.0060 lb/GWh)	0.40 (0.0040)	0.20 (0.0030)	0.40 lb/TBtu (0.0070 lb/GWh)
Arsenic, As	2.0 lb/TBtu (0.020 lb/GWh)	2.0 lb/TBtu (0.020 lb/GWh)	2.0 (0.020)	0.60 (0.0070)	0.40 lb/TBtu (0.0040 lb/GWh)
Beryllium, Be	0.20 lb/TBtu (0.0020 lb/GWh)	0.20 lb/TBtu (0.0020 lb/GWh)	0.030 (0.0030)	0.060 (0.00070)	0.070 lb/TBtu (0.00070 lb/GWh)
Cadmium, Cd	0.30 lb/TBtu (0.0030 lb/GWh)	0.30 lb/TBtu (0.0030 lb/GWh)	0.020 (0.0020)	0.10 (0.0020)	0.40 lb/TBtu (0.0040 lb/GWh)
Chromium, Cr	3.0 lb/TBtu (0.030 lb/GWh)	3.0 lb/TBtu (0.030 lb/GWh)	3.0 (0.020)	2.0 (0.020)	2.0 lb/TBtu (0.020 lb/GWh)
Cobalt, Co	0.80 lb/TBtu (0.0080 lb/GWh)	0.80 lb/TBtu (0.0080 lb/GWh)	0.60 (0.0040)	3.0 (0.020)	2.0 lb/TBtu (0.020 lb/GWh)
Lead, Pb	2.0 lb/TBtu (0.020 lb/GWh)	2.0 lb/TBtu (0.020 lb/GWh)	29.0 lb/MMBtu (0.30 lb/MWh)	2.0 (0.030)	11.0 lb/TBtu (0.020 lb/GWh)
Manganese, Mn	5.0 lb/TBtu (0.050 lb/GWh)	5.0 lb/TBtu (0.050 lb/GWh)	3.0 (0.020)	5.0 (0.050)	3.0 lb/TBtu (0.040 lb/GWh)
Mercury, Hg	NA	NA	NA	0.050 lb/TBtu (0.000780 lb/GWh)	NA
Nickel, Ni	4.0 lb/TBtu (0.040 lb/GWh)	4.0 lb/TBtu (0.040 lb/GWh)	5.0 (0.050)	8.0 (0.080)	9.0 lb/TBtu (0.090 lb/GWh)
Selenium, Se	6.0 lb/TBtu (0.060 lb/GWh)	6.0 lb/TBtu (0.060 lb/GWh)	22.0 lb/TBtu (0.20)	2.0 (0.20)	2.0 lb/TBtu (0.020 lb/GWh)

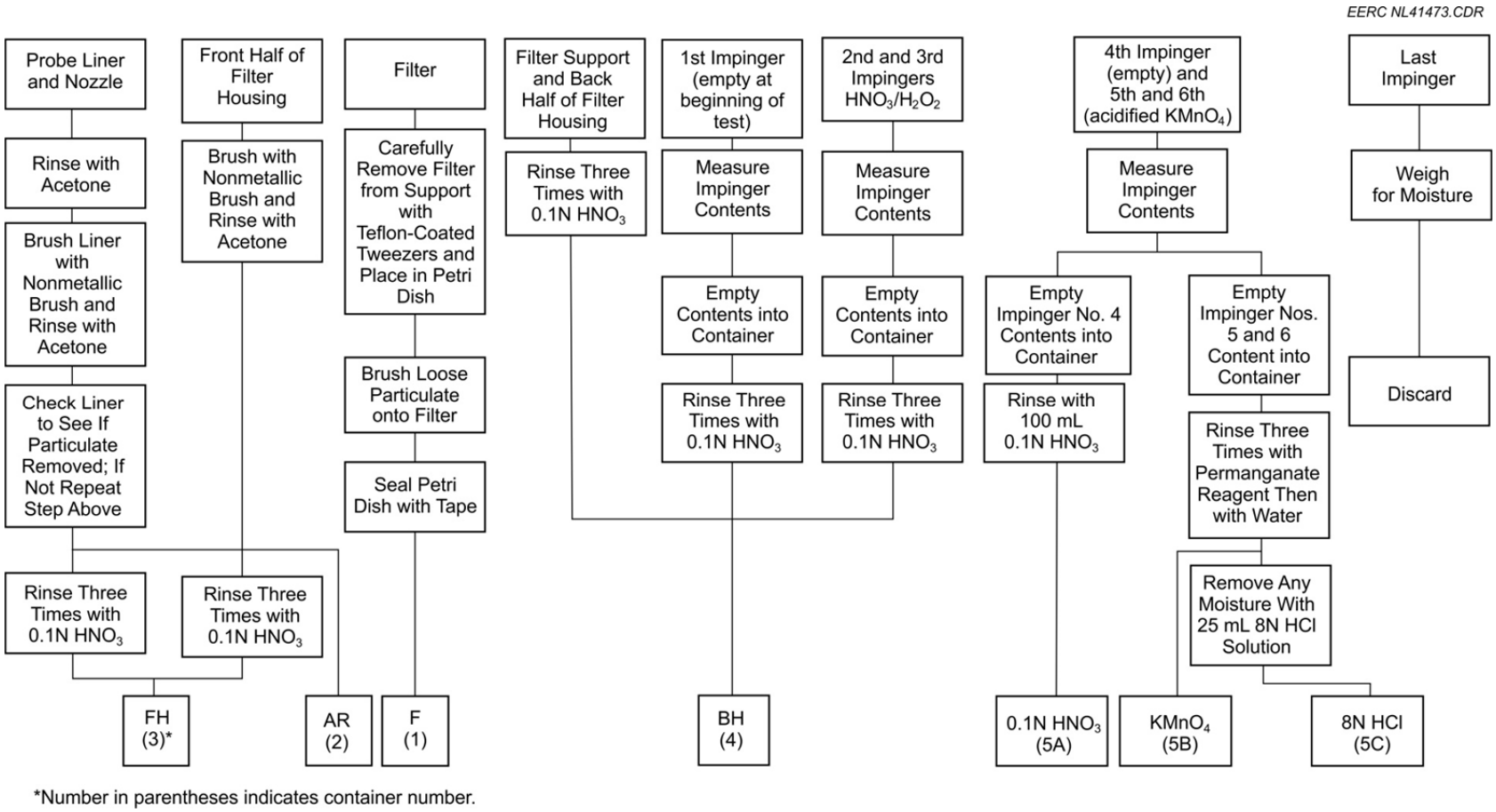

Figure 6-1. M29 field sample recovery scheme (2).

Table 6-4. Individual Non-Hg HAP Metal Emissions for Existing Coal-Fired Units

	Utility Boiler Published Units[a]	dppmv at 3% O_2	µg/dNm^3 at 3% O_2	M29 detection limit, µg/dNm^3 at 3% O_2
Total Non-Hg Metals	0.000040 lb/MMBtu (0.00040 lb/MWh)	–	55.16	
Antimony, Sb	0.60 lb/TBtu (0.0060 lb/GWh)	0.00016	0.82	1.1
Arsenic, As	2.0 lb/TBtu (0.020 lb/GWh)	0.00088	2.74	0.4
Beryllium, Be	0.20 lb/TBtu (0.0020 lb/GWh)	0.00073	0.27	0.08
Cadmium, Cd	0.30 lb/TBtu (0.0030 lb/GWh)	0.00009	0.41	0.03
Chromium, Cr	3.0 lb/TBtu (0.030 lb/GWh)	0.00190	4.10	0.3
Cobalt, Co	0.80 lb/TBtu (0.0080 lb/GWh)	0.00045	1.09	0.3
Lead, Pb	2.0 lb/TBtu (0.020 lb/GWh)	0.00032	2.74	0.3
Manganese, Mn	5.0 lb/TBtu (0.050 lb/GWh)	0.00300	6.84	0.3
Mercury, Hg	–	–	–	
Nickel, Ni	4.0 lb/TBtu (0.040 lb/GWh)	0.00224	5.47	5.4
Selenium, Se	6.0 lb/TBtu (0.060 lb/GWh)	0.00250	8.21	0.8

[a] Calculated values based on a PRB coal and a heat rate of 10,000 Btu/kWh.

For new coal-fired units, M29 does not provide sufficient detection limits even with the 4-dscm collection volume. Six of the ten HAP metal emission values are below the M29 detection limit with the 4-dscm collection volume. This prevents new units from measuring trace metal emissions to demonstrate PM compliance.

Similar detection limit issues arise with HCl sampling and M26A. The MACT HCl emission limits for existing coal-fired units, major boilers, and cement kilns are presented in Table 6-5. The units have also been converted to dppmv values so that they can be directly compared to the published M26A detection limits. Even though the M26A published detection limit for HCl is 0.04 dppmv, a practical detection limit is in the 1–5-dppmv range. The MACT emission limits are in the detection limit range, which means that they are possible with a trained

Table 6-5. HCl Emission Limits for Existing Sources

MACT Rules	Published Units	dppmv at 3% O_2	µg/dNm^3 at 3% O_2
Utilities ≥ 8300 Btu/lb[a]	0.0020 lb/MMBtu (0.020 lb/MWh)	1.85	2732
Utilities < 8300 Btu/lb[b]	0.0020 lb/MMBtu (0.020 lb/MWh)	1.92	2824
Major Boilers			
Coal Stoker[a]	0.035 lb/MMBtu	32.5	47,842
Coal Fluidized Bed[a]	0.035 lb/MMBtu	32.5	47,842
Pulverized Coal[a]	0.035 lb/MMBtu	32.5	47,842
Biomass Stoker/other	0.035 lb/MMBtu	35.5	52,328
Biomass Fluidized Bed	0.035 lb/MMBtu	35.5	52,328
Biomass Dutch Oven/Suspension Burner	0.035 lb/MMBtu	35.5	52,328
Biomass Fuel Cells	0.035 lb/MMBtu	35.5	52,328
Biomass Suspension/Grate	0.035 lb/MMBtu	35.5	52,328
Cement	3 dppmv at 7% O_2	3.86	–

[a] Calculated values based on a PRB coal and a heat rate of 10,000 Btu/kWh.
[b] Calculated balues based on a ND lignite coal and a heat rate of 10,000 Btu/kWh.

sampling crew. This is not the case for new coal-fired units, even though the HCl emission limits are approximately 0.03 dppmv. This value is below the stated method detection limit of M26A and clearly shows that the method is unable to precisely and accurately measure HCl emissions for new coal-fired units.

As an alternative to both M29 and M26A, the EERC has developed a novel sorbent trap-based method that can sample for trace elements and/or halogens. This method is designed to be a simpler and more cost-effective alternative to M29 and M26A. The simplicity of the multielement sorbent trap (ME-ST) method in the field is shown in Figure 6-2, which displays the ME-ST field sample recovery scheme. The ME-ST field sample recovery process only involves two simple steps. No solvents or other glassware are involved in the process, and there is very little preparation prior to sampling. The reduction in steps also significantly reduces the chances for the introduction of biases and sample contamination from the surrounding environment. Since the sorbent trap is not composed of hazardous substances, it can be shipped via an overnight courier to a laboratory for analysis. This allows the results to become available much faster than M29 or M26A, which often cannot be shipped because of the hazardous chemicals (M29) or volume restrictions (M26A).

This method can easily be deployed in the field without the use of strong acids, bases, or solvents. In fact, no solvents are required to be in the field for the whole ME-ST sampling process, which significantly reduces the complexity of the method. In addition, this method is safer and more flexible than the approved M29 method for multimetal sampling; the resulting sorbent trap can easily be sent for analysis since no hazardous materials are involved.

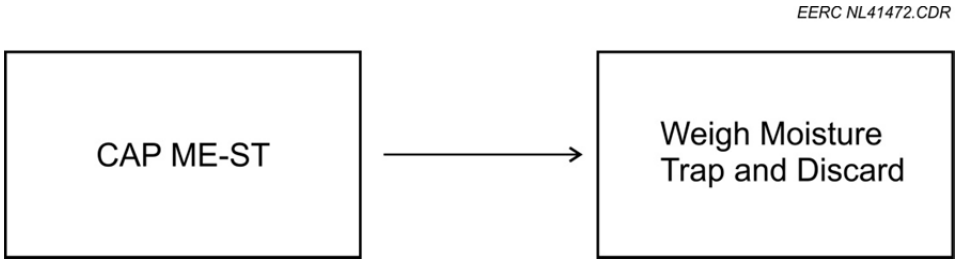

Figure 6-2. ME-ST field sample recovery scheme.

6.2.2 Experimental

Combustion

To evaluate the ME-ST method, data were collected on the EERC's PTC. The PTC is a 550,000-Btu/hr pc-fired unit designed to generate fly ash representative of that produced in a full-scale utility boiler. The combustor is oriented vertically to minimize wall deposits. A refractory lining helps to ensure adequate flame temperature for complete combustion and prevents rapid quenching of the coalescing or condensing fly ash. Based on the superficial gas velocity, the mean residence time of a particle in the combustor is approximately 3 seconds. The coal nozzle of the PTC fires axially upward from the bottom of the combustor, and secondary air is introduced concentrically to the primary air with turbulent mixing. Coal is introduced to the primary air stream via a screw feeder and eductor. An electric air preheater is used for precise control of the combustion air temperature.

The PTC instrumentation permits system temperatures, pressures, flow rates, flue gas constituent concentrations, and particulate control device (baghouse, advanced hybrid particle collector [AHPC], and/or ESP) operating data to be monitored continuously and recorded on a data logger.

Flue gas samples can be taken at any combination of two of three available system sample points: the furnace exit, the particulate control device inlet, and the particulate control device outlet. After passing through sample conditioners to remove the moisture, the flue gas is typically analyzed for O_2, CO, CO_2, SO_2, and NO_x. Except for CO and CO_2, each constituent is normally analyzed at both the furnace exit and the outlet of the particulate control device simultaneously, using two analyzers. The concentration values from all of the instruments are recorded continuously using circular charts. In addition, data are manually recorded at set time intervals. NO_x is determined using two Thermoelectron chemiluminescent NO_x analyzers. The O_2 and CO_2 analyzers are made by Beckman, and the SO_2 analyzers are manufactured by DuPont. Each of these analyzers is regularly calibrated and maintained to provide accurate flue gas concentration measurements.

The two test coals were a Knight Hawk (Illinois 6) bituminous coal and an Absaloka subbituminous coal. The sample location was at the ESP outlet for the halogen and trace metal data.

Oxycombustion

The oxycombustion sampling was performed on the EERC's combustion test facility (CTF) furnace in conjunction with another test program. The pilot-scale CTF furnace was previously modified under the Partnership for CO_2 Capture Program to be able to run in either normal combustion mode or oxycombustion mode. The system was fired with a Knight Hawk bituminous coal. ME-ST and EPA M29 samples were collected at the ESP out sampling location.

Gasification

The gasification data were collected on the EERC's high-pressure fluidized-bed gasifier (HPFBG). The gasifier was operated with a warm-gas cleanup system that removed halogens, sulfur, select metals, and Hg from the syngas. The warm-gas cleanup system also included two water–gas shift catalyst beds to increase syngas hydrogen concentrations. The test coal was a PRB coal. The ME-ST sampling point was just after the warm-gas cleanup system and before the quench pots.

6.2.3 Results and Discussion

Baseline ME-ST sorbent samples were analyzed to determine the trace element blank levels and detection limits. Table 6-6 displays the blank analysis of six trace element ME-STs. The blank levels are very low except for Cr, Mn, and Ni. Of these three elements, Mn has the highest blank levels. The majority of the elements have blank concentrations below 1 ng/g. With the exception of Mn, the standard deviations are also fairly consistent which shows that the sorbent has consistent blank levels.

The blank levels from Table 6-6 were used to determine ME-ST method detection limits on a $\mu g/m^3$ basis so that the method detection limits can be directly compared to EPA M29-published detection limits. Table 6-7 displays the EPA M29 and ME-ST detection limits for the

Table 6-6. ME-ST Sorbent Blank Levels*

Element	Average, ng/g	Standard Deviation
Hg	0.18	0.24
As	0.66	0.30
Be	0.41	0.10
Cd	0.31	0.21
Co	2.98	0.73
Cr	11.16	3.32
Mn	187.75	76.50
Ni	12.33	5.26
Pb	0.96	0.69
Sb	0.42	0.14
Se	0.74	0.30

* n = six samples.

Table 6-7. EPA M29 and ME-ST Trace Element Detection Limits

Element	Front Half: Probe and Filter, µg/m^3	Back Half: Impingers 1–3, µg/m^3	Back Half: Impingers 4–6, µg/m^3	Total M29 Train, µg/m^3	ME-ST, µg/m^3
Antimony	0.7	0.4		1.1	0.0084
Arsenic	0.3	0.1		0.4	0.0132
Barium	0.5	0.3		0.8	
Beryllium	0.05	0.03		0.08	0.0082
Cadmium	0.02	0.01		0.03	0.0062
Chromium	0.2	0.1		0.3	0.2232
Cobalt	0.2	0.1		0.3	0.0596
Copper	1.4	0.7		2.1	
Lead	0.2	0.1		0.3	0.0192
Manganese	0.2	0.1		0.3	3.575
Mercury	0.06	0.3	0.2	0.56	0.0036
Nickel	3.6	1.8		5.4	0.2466
Phosphorus	18	9		27	
Selenium	0.5	0.3		0.8	0.0148
Silver	1.7	0.7		2.4	
Thallium	0.2	0.1		0.3	
Zinc	0.5	0.3		0.8	

trace elements of interest. The EPA M29 detection limits are based on sampling 1.25 m^3 of flue gas, so the same flue gas volume was used for the ME-ST detection limit calculations. With the exception of Mn, all of the ME-ST detection limits are below the EPA M29 detection limits, with many of the detection limits significantly below the M29 detection limits. This demonstrates that the ME-ST method is theoretically able to measure trace elements at or below the levels in M29.

Figure 6-3 displays the trace element ME-ST data collected during a CATM-sponsored project on the PTC while Absaloka and Knight Hawk coals were fired on different test days. The results on the left were obtained while the Absaloka coal was fired, and the results on the right were obtained while the Knight Hawk coal was fired. Each individual test run was collected under a different condition so the data cannot be directly compared to the other data sets. Two ME-ST samples were collected at the same time and location as the EPA M29 sample. This allowed for a side-by-side comparison of the ME-STs as well as a comparison to M29. The plots show that the "A" and "B" ME-STs demonstrated consistent values for all elements and for both of the test coals. This shows that the traps are able to perform similarly and generate precise data. The results show that the ME-ST data are generally in good agreement with the M29 data and demonstrate the feasibility of the method in a combustion setting.

During a follow-up test run, additional M29 and ME-ST samples were collected on the PTC when once again firing an Absaloka coal. Figure 6-4 presents the data from the additional

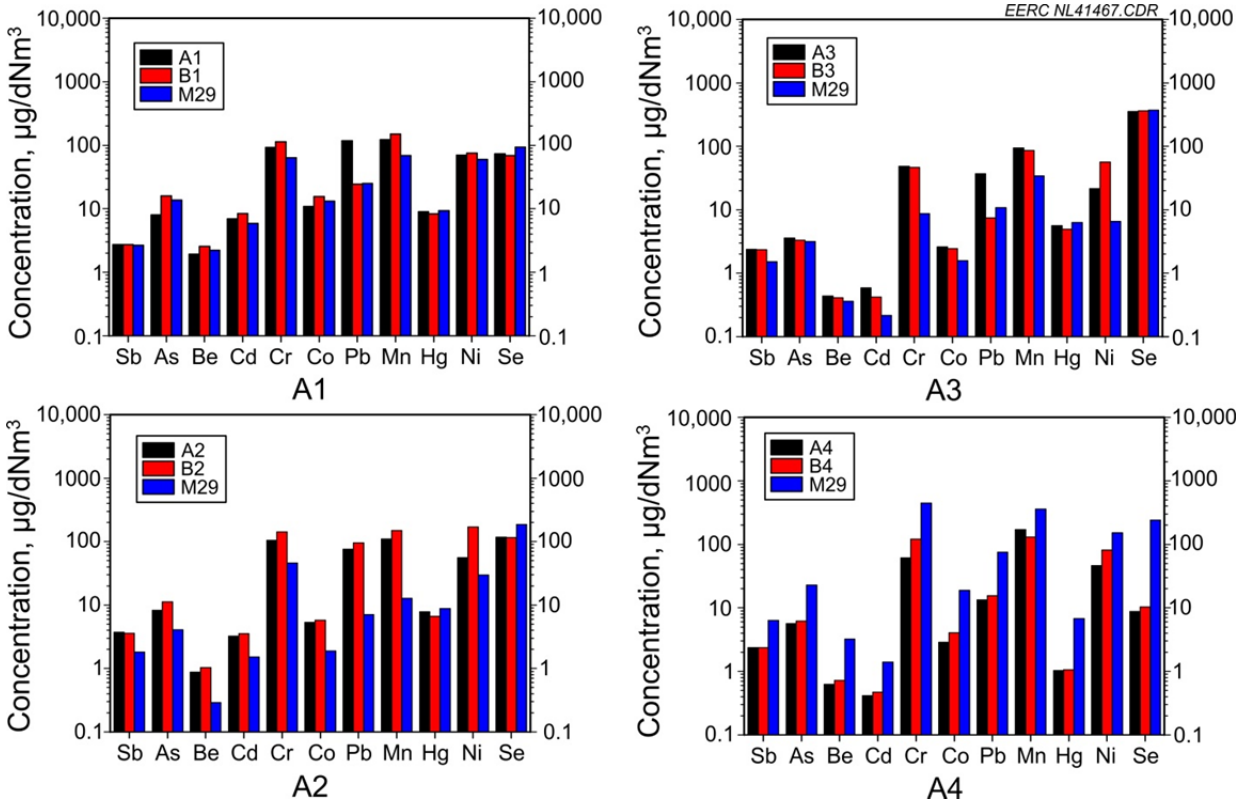

Figure 6-3. Comparison of ME-ST (A and B data) and M29 data collected during a pilot-scale test run.

PTC run on Absaloka coal. As with the previous test run, the sample point was the ESP out location. The samples were collected at significantly different conditions than the previous test run, so the data sets cannot be directly compared. Once again, the A and B ME-ST traps are fairly consistent for the three data sets and have values that are similar to the EPA M29 trace metal data. Cr, Mn, and Ni had the poorest correlations, which is likely due to the higher background concentrations of these elements in the ME-ST sorbent.

In addition to the trace element data, halogen ME-ST and M26a samples were collected during the PTC test run while firing the Absaloka coal. The halogen ME-ST is a slightly different trap than the trace element trap, but the sampling procedure is identical. Analysis of blank samples yielded theoretical method detection limits below 0.01 dppmv. It would be possible to run a dual probe and have one halogen and one trace metal ME-ST sample collected at the same time. Figure 6-5 presents the HCl and HBr ME-ST data as well as the EPA M26A data collected at the same time. The samples were collected at the ESP out sampling location. The ME-ST and EPA M26A HCl data are similar in concentration for two of the three data sets, with relative differences of <18%. The concentrations that were measured were below 1 dppmv, a level at which M26a has decreased precision and accuracy which could factor into the variability between the two methods.

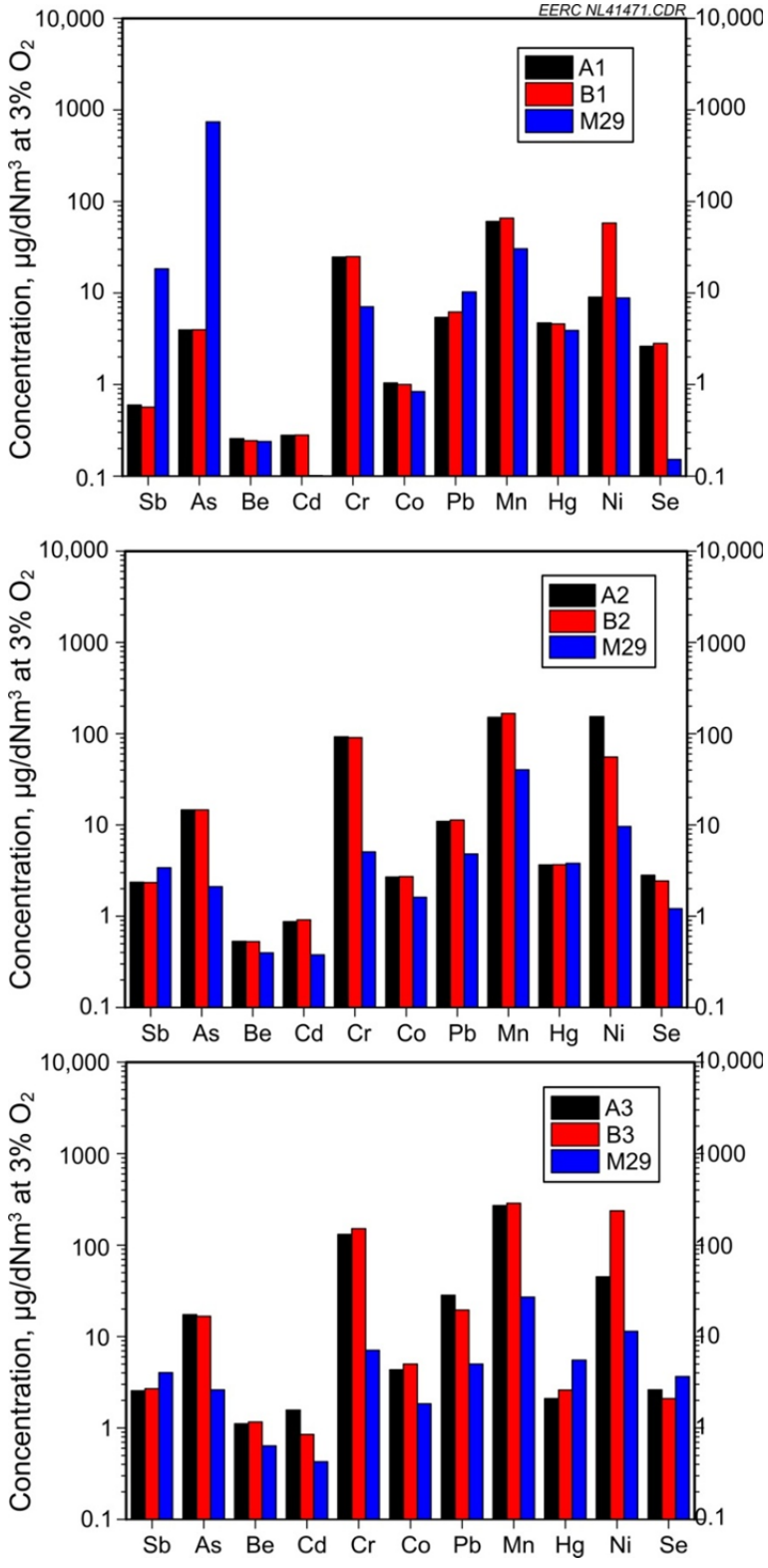

Figure 6-4. M29 and ME-ST trace element data comparison during a second pilot-scale test run.

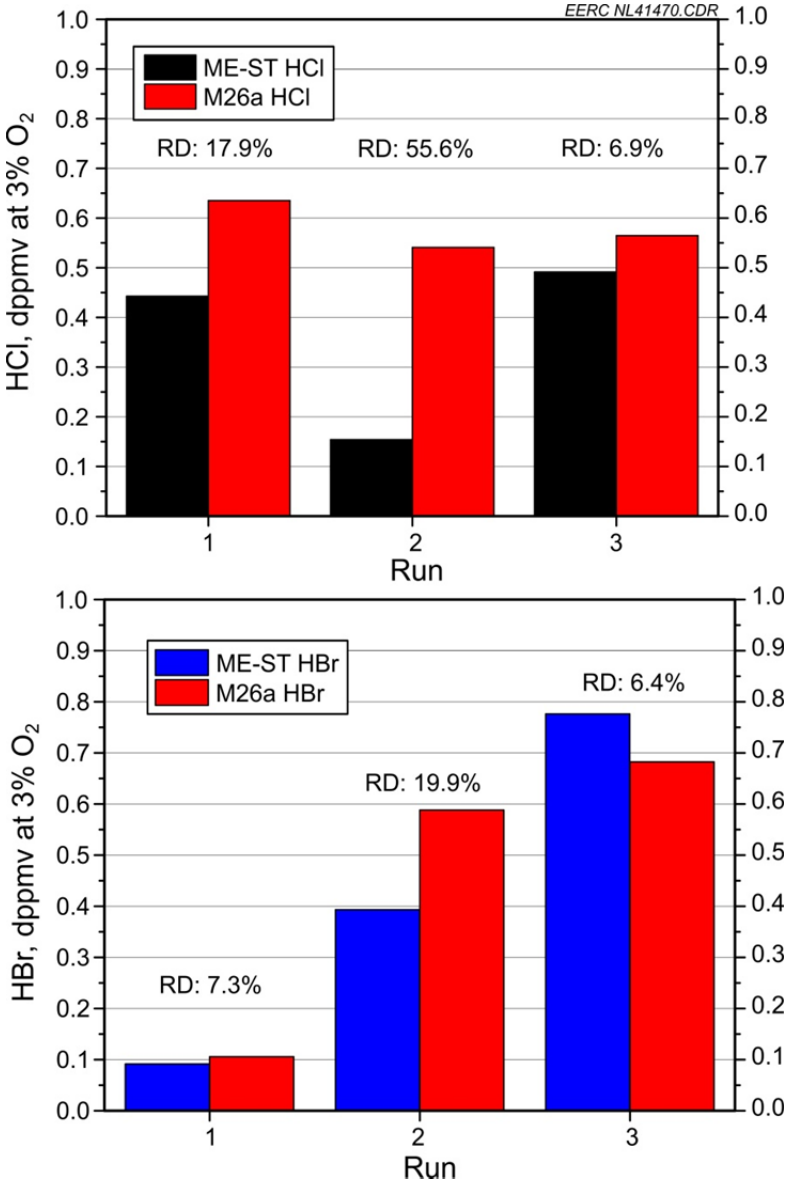

Figure 6-5. HCl and HBr ME-ST and EPA M26A data collected during a PTC pilot-scale test run while firing Absaloka coal.

The HBr data show excellent agreement for all three sets of samples. The relative differences for all three data sets are <20%, with two of the data sets having relative differences of <8%. This shows that the two methods agree very well for the HBr data. All of the HBr measurements were below 1 dppmv, which also demonstrates that the ME-ST method is able to accurately measure low levels of HBr.

During an oxycombustion test run, EPA M29 and ME-ST data were able to be collected to determine the efficacy of the method in an oxycombustion environment. Figure 6-6 displays the ME-ST and M29 test data collected during the oxycombustion test run. The sampling point was

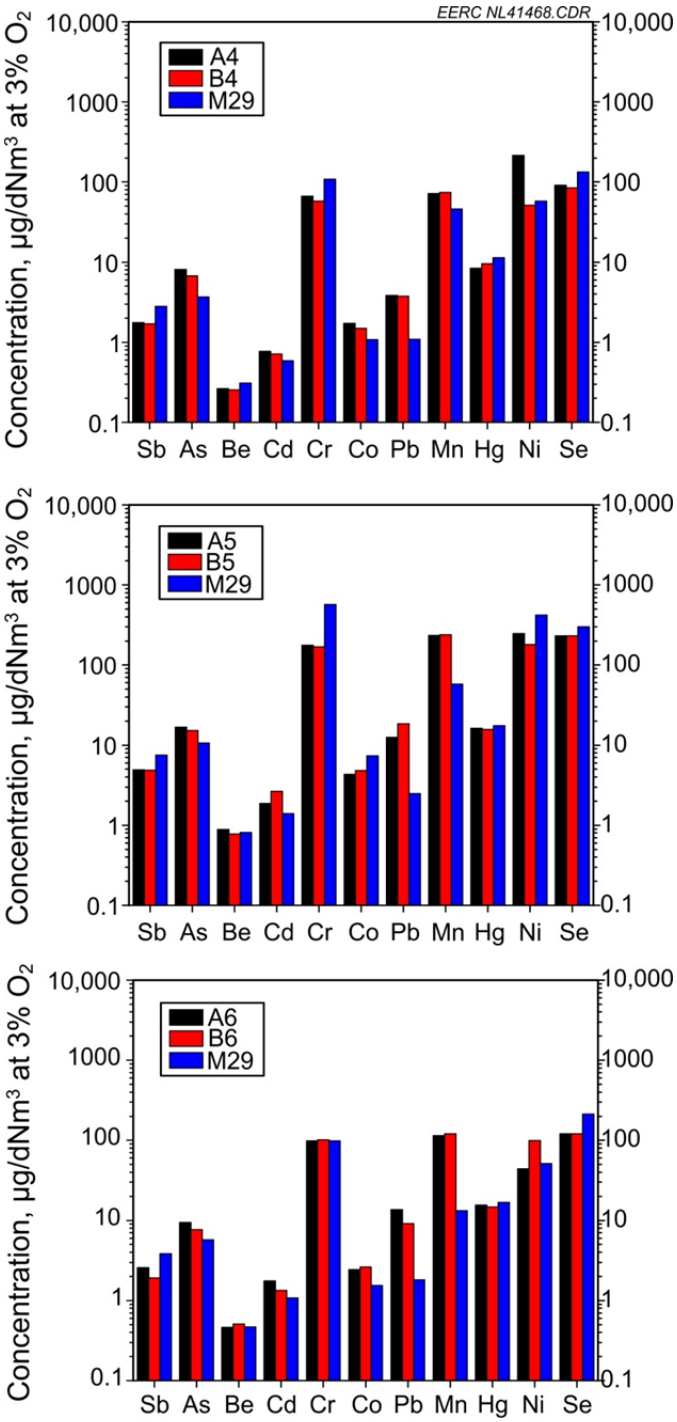

Figure 6-6. EPA M29 and ME-ST data collected during an oxycombustion test run.

at the ESP outlet. During flue gas sampling in the oxycombustion environment, no additional complications were experienced for either test method. The ME-ST A and B traps showed excellent agreement, with relative differences <20% for the majority of the data. This data set demonstrated the best agreement. The ME-ST data also closely matched the M29 data for all three data sets which demonstrates that the ME-ST method can be used for trace element testing during oxycombustion.

In addition to combustion data, to demonstrate robustness of the method, a limited ME-ST data set was collected on the EERC's HPFBG while gasifying a PRB coal. Traditionally, solution-based sampling methods have not performed well in the reducing environments of a gasifier. The reducing environments significantly affect the ability of the impinger chemicals to absorb the trace metals in solution and often display data that is biased low. The data presented in Figure 6-7 display the ME-ST trace element data for six samples. All of the samples were collected under similar operational conditions. The data were fairly consistent for the majority of the trace elements for all six samples, with the exception of Ni. The trace metals without any data points had values below the method detection limit.

6.2.4 Conclusions

The feasibility of the ME-ST method to measure trace elements and halogens has been established at the pilot-scale level. The detection limits are as good or better than the currently used methods, which is important because of the low detection limits required for trace metals and halogens in the draft utility MACT rule. The ME-ST method has proven to provide comparable data in a wide variety of settings, including normal combustion, oxycombustion, and gasification systems on different types of coal. The ease of sampling and reduced personnel hours to obtain a sample will yield substantial cost savings for emission sources required to perform trace metal and HCl sampling.

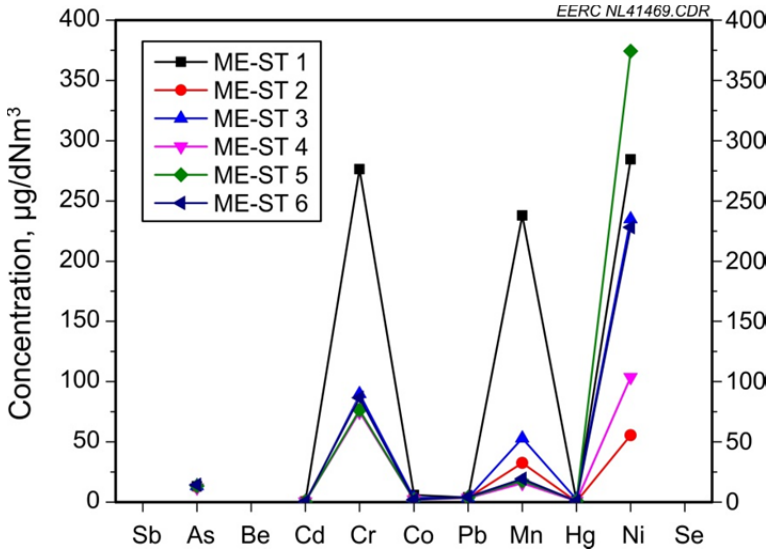

Figure 6-7. ME-ST data collected during the gasification of a PRB coal.

Future directions include conducting full-scale test campaigns so that a statistical comparison can be made between the ME-ST and EPA methods. In addition, future testing on the larger data set will include different coal ranks and pollution control devices. A validation test using EPA M301 is also anticipated in the near future so that the ME-ST can mature into an approved method.

6.2.5 References

1. U.S. Environmental Protection Agency. Draft Rule – National Emission Standards for Hazardous Air Pollutants from Coal- and Oil-Fired Electric Utility Steam Generating Units and Standards of Performance for Fossil Fuel-Fired Electric Utility, Industrial-Commercial-Institutional, and Small Industrial-Commercial-Institutional Steam Generating Units. 40 CFR, Parts 60 and 63. Draft released March 16, 2011.

2. U.S. Environmental Protection Agency. Method 29 – Determination of Metals Emissions from Stationary Sources. 40 CFR Part 60 Appendix A-8, Meth29, Issued June 25, 1996.

6.3 ESI–MS Analysis of Scrubber Slurry Solutions

6.3.1 Introduction

Mercury reemission remains an issue for utilities equipped with WFGD scrubbers and can result in much lower mercury removals. Hg reemission can play a significant role in hindering units from achieving their target emission limits proposed under the MACT regulations. Mercury reemission occurs because of oxidized mercury being converted back to elemental mercury in the scrubber. The elemental mercury then leaves the scrubber and is not retained in the slurry solution. Mercury reemission can be determined by measuring the scrubber inlet and outlet elemental mercury concentrations. If the outlet Hg^0 concentration is higher than the inlet Hg^0 concentration, Hg reemission is likely occurring. Mercury reemission is typically on the order of 1–5 μg/dNm^3 at 3% O_2 but can be higher depending on the fuel type and unit configuration.

This work sought to collect electrospray ionization (ESI)–MS spectra of scrubber samples to determine the major and trace species present in the scrubber samples and to determine if any of these species play a role in mercury reemission in scrubbers. A "fingerprint" mass spectrum was collected, and the ions present were identified using ESI–MS.

6.3.2 Experimental

ESI–MS spectra were collected on an Applied Biosystems API2000 instrument. The instrument is a triple quadrupole instrument equipped with a curtain gas interface. The instrument has a mass range of 5–1800 m/z. The samples were directly infused to the ESI source via the instrument syringe pump at a flow rate of 10 μL/min. Spectra were collected in both positive and negative ion mode. Collision-induced dissociation (CID) spectra were collected at a collision gas nominal rate of 1–3 units. Figure 6-8 shows a picture of the instrument used in the study.

Figure 6-8. API2000 ESI–MS instrument.

The wet FGD samples were collected during various pilot- and full-scale test runs. The samples were stored in I-Chem bottles until the samples were analyzed.

6.3.3 Results and Discussion

The wet FGD "fingerprint" study seeks to identify the small molecules present in wet FGD systems to see if a pattern of small molecules exists in scrubbers that do and do not reemit Hg. ESI–MS spectra were collected as an initial tool to identify some of the small molecules present in wet FGD samples. Figures 6-9 and 6-10 show negative and positive ion mode spectra collected from a wet FGD sample collected on one of the EERC's pilot-scale combustors. In Figure 6-9, a cluster ion distribution is present starting at mass to charge (m/z) 103.3 and continues every 70 m/z and includes m/z 173.2, 243.1, 312.8, and 382.8. These ions are due to the scrubber slurry reaction with SO_2 in the flue gas and are the main small molecules expected in solution. In Figure 6-10, there are three main ions present at m/z 38.1, 47.1, and 57.1. Based on the isotope distributions, these ions are singly charged and not trace metals.

In order to gain more information from the ions present in the negative ion mode spectrum, CID spectra were collected. CID spectra provide fragmentation information which helps to determine the functional groups present on the ion. Figure 6-11 shows the negative ion mode CID mass spectrum of m/z 103.3. The presence of ions at m/z higher than the parent ion show that there are multiply charged ions present at m/z 103.3 along with singly charged ions. This complicates the singly charged isotope distribution at m/z 103.3 because the ion abundances from the doubly charged ions are overlapping some of the peaks from the singly charged ions.

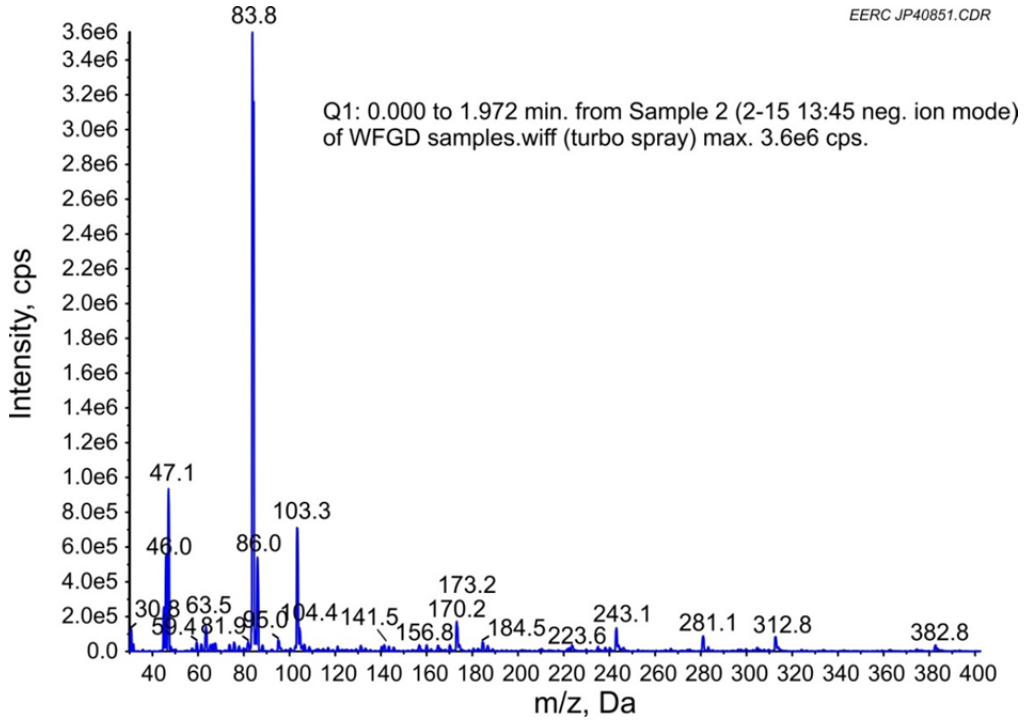

Figure 6-9. Wet FGD spectrum collected in negative ion mode.

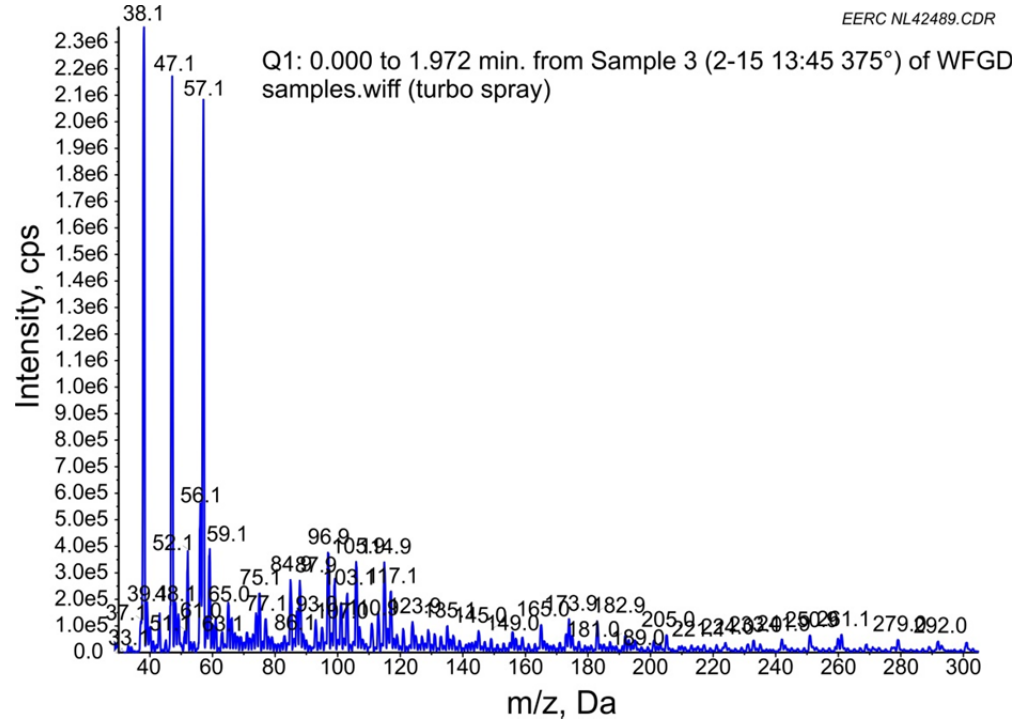

Figure 6-10. Wet FGD spectrum collected in positive ion mode.

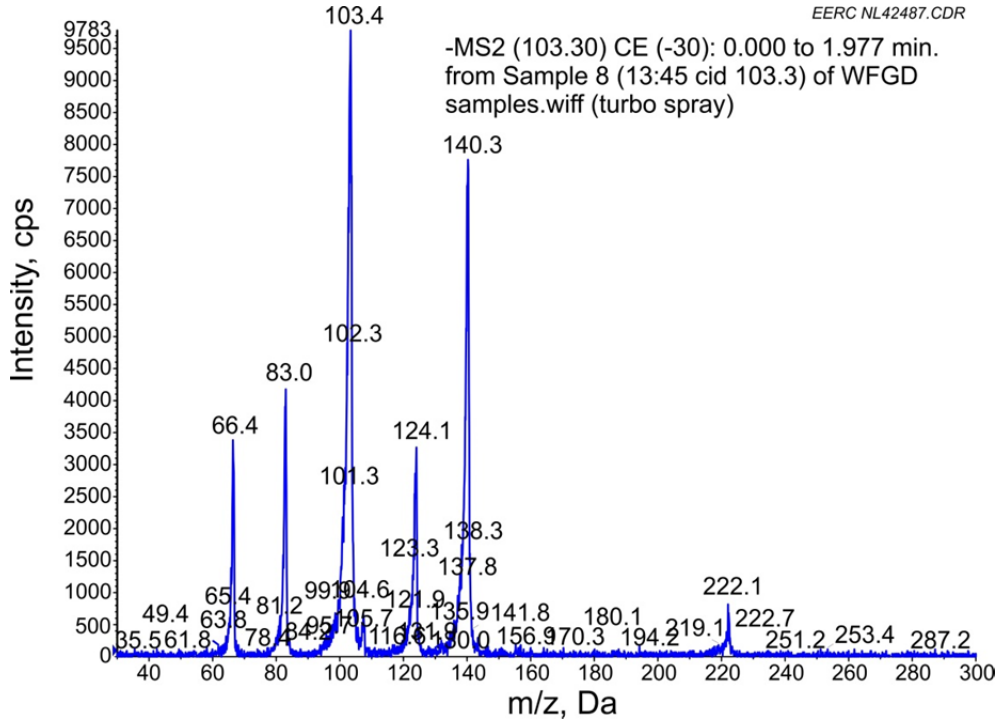

Figure 6-11. Negative ion mode CID mass spectrum of m/z 103.3.

The CID spectrum of m/z 83.8 in Figure 6-12 shows that the parent ion loses a water molecule and the ion at m/z 66.5 remains. After a sulfur is accounted for (present based on isotopic distribution), an additional m/z of 34 remains unaccounted for. The remaining m/z of 34 is currently still not identified, but it is likely two hydroxide ions. This would yield a possible molecule of $HSO_2 \cdot H_2O$.

6.3.4 Conclusions

ESI–MS spectra were collected from scrubber samples collected during a pilot-scale test run. The major species present in the spectrum were predominantly sulfur-based molecules due to SO_2 being captured from the flue gas. CID spectra showed that there were both singly and double-charged ions present at the same m/z. Future testing will expand the data set and include additional analyses such as ion chromatography (IC) to look at the anions present in the wet FGD samples.

6.4 Comparison of Select Leaching Methods for Coal Combustion Product Samples (CCPS)

6.4.1 Introduction

CCP samples from mercury emission control technology demonstrations and corresponding standard CCPs were evaluated for the leachability of select constituents. The

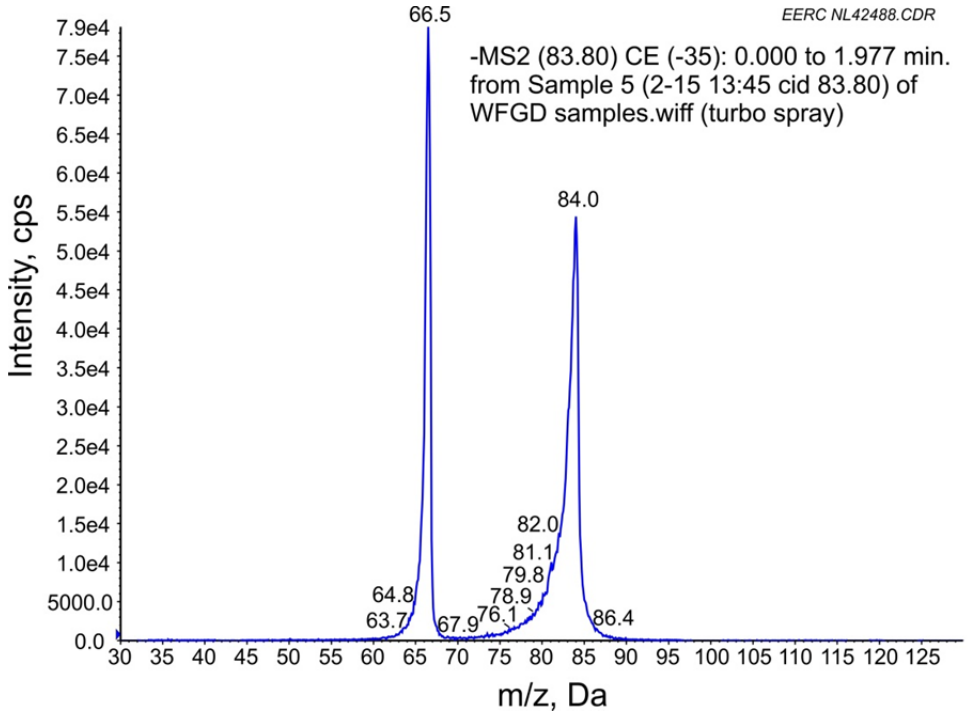

Figure 6-12. Negative ion mode CID mass spectrum of m/z 83.8.

leaching tests used included the SGLP (1) and select tests from a leaching framework described by Kosson and others (2). The leaching framework has since been revised and named the Leaching Environmental Assessment Framework (LEAF). The EERC had not utilized the LEAF methods previously and chose to evaluate a number of CCPs using SGLP and select tests from LEAF to compare and contrast the results from the methods. One sample with a slurry pH > 11 was chosen for evaluation under an extended leaching duration of 30 days applied to all tests to assess potential changes in pH and elemental leachate concentrations. The resulting leachate samples were evaluated for six trace elements (arsenic, cadmium, chromium, mercury, nickel, and selenium), three halogens (bromide, chloride, and fluoride), and sulfur compounds as sulfates.

A wide variety of leaching procedures have been utilized to assess CCPs and have generated much discussion among CCP researchers, marketers, users, and regulators (3–5). A great amount of leaching performed on CCPs at the EERC has utilized the SGLP with LTL. The EPA National Risk Management Research Laboratory has implemented the use of select procedures from the leaching framework for the evaluation of CCPs. Two of the methods (SR002.1 [Solubility and Release as a Function of pH] and SR003.1 [Solubility and Release as a Function of LS ratio]) were considered near-routine methodology in a 2006 report by EPA (6). The two methods are now part of LEAF.

SGLP and LTL

The EERC developed a leaching method to allow the use of synthetic groundwater and longer leaching times. These tests came to be known as the procedure SGLP and LTL (1, 7–9). The SGLP usually employs a leaching solution consisting of water from the site, water which has been prepared in the lab similar to water likely to contact the ash, or distilled DI water (1). Multiple leaching bottles are set up and analyzed at different time intervals for the long-term component of the procedure. A typical SGLP and LTL test might consist of 18-hour, 30-day, and 60-day equilibration times.

For a leaching test to be used to determine the potential for environmental impact of coal combustion products and stand up to legal and scientific scrutiny, a series of criteria must be met:

1. The test must take into account any reactivity or unusual properties of the material being leached.

2. The test must as closely as possible utilize a leaching solution that mimics the leaching solution most likely to contact the material in a natural disposal setting.

3. If the ash is reactive with water, the test must take this into account by allowing the hydration reactions to occur during the course of the leaching test. This necessitates the use of LTL (10).

Over 30 years ago, EERC researchers were performing two research efforts simultaneously. One was an effort to identify an appropriate leaching methodology focused on high-calcium alkaline CCPs, and the second was research on ash hydration reactions. The two studies intersected suddenly with the realization that the mineral ettringite was the primary hydration phase that was always seen during the reaction of alkaline ash with water (11, 12). At times, this mineral may exhibit poor crystallinity, but it always forms. Ettringite, which is a calcium aluminate sulfate hydroxide hydrate with the nominal composition $Ca_6Al_2(SO_4)_3(OH)_{12}{\cdot}26\ H_2O$, can substitute other oxyanions for sulfate during formation (12–14). Ettringite requires sources of calcium, aluminum, sulfate, excess water, and high pH (>11) in order to form. Variations in these requirements may play a role in the level of crystallinity of the ettringite formed. Oxyanions shown to participate in the ettringite formation include those of arsenic, boron, chromium, molybdenum, selenium, and vanadium. As a result of incorporating these elements into the ettringite structure, decreases in solution concentration of these elements can be observed in what the EERC refers to as anomalous leaching behavior.

When deciding if LTL should be performed on a CCP sample, the bulk pH of the CCP is determined by measuring the pH in slurry after 10–15 minutes of stirring. Recently at the EERC, the stirring has continued to 24 hours, since the pH may change with time and short-term leaching tests are typically run 18–48 hours. Measurements of pH levels after 24 hours in previous leaching studies have shown a change in pH of more than 4 pH units between the 10–15-minute and 24-hour measurements. The range of pH change in samples that exhibited the greatest change in pH was from a decrease of 1.5 pH units to an increase of 4.3 units. At times,

the pH increased from acidic to alkaline. These changes in pH may be associated with the AC present in some samples, hydration reactions, or solubility of surface coatings or specific phases in the sample. The decreases could also be due to uptake of CO_2 from the atmosphere. In some cases, the 24-hour pH provided a pH value closer to that observed in the leachate samples (15, 16). If the bulk pH of the CCP is greater than 10.5, LTL is performed because the CCP is determined to be reactive. Although a pH of 10.5 is not likely to cause the formation of ettringite, pH levels on a microscale within the CCP may have pH > 11 and cause ettringite formation on a smaller level.

Results have indicated that LTL provides significant added data only for reactive CCPs (7). Short-term leaching is adequate for evaluating CCPs with pH < 9 because ettringite formation occurs at much higher pH levels. It is well known that concrete can take up to years to reach its maximum strength. Some of the same hydration reactions responsible for concrete strength development are also responsible for the reduced leaching of some CCP constituents. A leaching duration of years is impractical for most purposes. LTL experiments at the EERC include a time series of up to 2 or 3 months with the resulting data interpreted relative to the short-term leaching (18 hours) and at least two long-term data points. Although 60 or 90 days is often not long enough to have achieved complete equilibrium, it is generally long enough to determine the concentration evolution of individual parameters. The most important factor when performing LTL is to have at least three equilibration times to determine a true trend, which is part of the data interpretation. Direct evidence of ettringite formation is only achieved by using x-ray diffraction techniques to compare the initial solid sample to the hydrated solid sample after leaching. Field evaluation of high-calcium CCPs shows ettringite present in disposed masses for up to 10 years following placement (17, 18).

Leaching Framework (now LEAF)

LEAF consists of four leaching test methods. The protocols are derived from published leaching methods (2) contained within LEAF, an integrated set of testing methods, data management tools, and report support utilities that can be used to support a wide range of environmental management decisions. Contained within LEAF are batch, column, and tank leaching tests, which can be interpreted individually or integrated to assess leaching behavior of a solid material over a range of potential release scenarios. The U.S. EPA Office of Resource Conservation and Recovery has initiated the review and validation process for four leaching tests based on LEAF under consideration for inclusion into SW-846. The method identification numbers are subject to change. Preliminary versions of the methods are available publicly (19, 20):

- Method 1313: Liquid–Solid Partitioning as a Function of Extract pH for Constituents in Solid Materials using a Parallel Batch Extraction Procedure

- Method 1314: Liquid–Solid Partitioning as a Function of Liquid-Solid Ratio for Constituents in Solid Materials using an Up-Flow Percolation Column Procedure

- Method 1315: Mass Transfer Rates of Constituents in Monolithic or Compacted Granular Materials using a Semi-Dynamic Tank Leaching Procedure

- Method 1316: Liquid–Solid Partitioning as a Function of Liquid–Solid Ratio for Constituents in Solid Materials using a Parallel Batch Extraction Procedure

LEAF is considered a tiered-testing approach of leachability. Tier 1 tests provide data for screening purposes. Tier 2 consists of tests to characterize a material over a broad range of plausible management conditions as a function of pH and liquid-to-solid ratio. Proposed Methods 1313, 1314, and 1316 fit within the Tier 2 testing. Tier 3 uses mass transfer rate testing in proposed Method 1315 for detailed characterization, compliance testing, and quality control. Interpretation protocols are provided.

The EPA Science Advisory Board (SAB) and the National Academy of Sciences (NAS) raised concerns over the use of single-point pH tests such as the toxicity characteristic leaching procedure (TCLP) that are not representative of actual CCP management conditions. EPA Office of Research and Development (ORD) worked closely with EPA's Office of Solid Waste and Emergency Response (OSWER) to identify the leaching framework as an appropriate leaching protocol for evaluating CCPs. The leaching framework methods have been used by EPA to evaluate the range of field conditions that CCPs are exposed to in response to the concerns raised by the EPA SAB and NAS. The following attributes of the leaching framework were considered as part of the selection process:

- The leaching framework will permit development of data that are comparable across U.S. coal and CCP types.

- The leaching framework will permit comparison with existing laboratory and field leaching data on CCPs.

- The leaching framework was published in the peer-reviewed scientific literature.

- On consultation with EPA's OSWER, it was recommended as the appropriate protocol based on review of the range of available test methods and assessment approaches.

- On consultation with the Environmental Engineering Committee of the Science Advisory Board, the committee considered the leaching framework methods responsive to earlier SAB criticisms of EPA's approach to leaching evaluation, and it also was considered broadly applicable and appropriate for the EPA studies (21).

EPA stated that it chose the leaching framework methods because it considers the waste form, buffering capacity, and field conditions through a more detailed analysis. The leaching framework includes a suite of different test methods that account for 1) pH and liquid-to-solid ratio-dependent leaching, 2) percolation-based release using column leaching, and 3) diffusion-limited release from monoliths and compacted granular materials that behave as monoliths after placement. The results have been considered to be more representative of actual field conditions than single-point pH tests that have been used in the past (19).

Previous Leaching Studies

In previous testing at the EERC, eight sample sets consisting of lignite and subbituminous CCPs from mercury emission control technology demonstrations using halogens and corresponding standard CCPs were evaluated using SGLP and LTL (on some samples). The halogens added during the demonstration were more mobile than the other elements evaluated and remained similar across all leaching durations. The CCPs from the mercury emission control technology demonstrations generally leached higher concentrations of arsenic and selenium than the standard CCPs. However, the percent of total amount of each element leached varied inconsistently as a comparison between the demonstration CCP and standard CCP. Anomalous leaching, a decrease in leachate concentration over time, was noted in all but one of the samples that had LTL performed for arsenic and selenium. A summary of a number of previous leaching studies of mercury emission control demonstration CCPs is included with that study. The referenced studies noted 1) changes in the leachability of constituents between standard CCPs and CCPs from mercury emission control demonstrations and 2) decreases in leachate concentrations of elements such as arsenic and selenium with long-term leaching (15).

An extensive report from EPA included data on 73 CCPs (34 fly ashes, 20 FGD gypsums, seven "other" FGD residues [e.g., scrubbers without oxidation or with inhibited oxidation], and eight blended CCPs "as managed" [e.g., scrubber sludge mixed with fly ash and lime prior to disposal]). Leachate testing included pH- and liquid-to-solid ratio-dependent leaching derived from the leaching framework methods. The major conclusions reported from the research included:

- "There is great variability in both the range of total constituent concentration values and in leaching values (orders of magnitude). In comparing these results to health indicator values such as the maximum concentration limit or toxicity characteristic, there are multiple COPCs [constituents of potential concern] of potential concern.

- "Distinctive patterns in leaching behavior have been identified over a range of pH values that would plausibly be encountered for CCR [coal combustion residue] management.

- "Total constituent content is not a good indicator of leaching which has been found to be a function of the characteristics of the material (pH) and field conditions in which the material is managed.

- "The maximum eluate concentration from leaching test results varies over a wide range in pH and is different for different CCR types and elements. This indicates that there is not a single pH for which testing is likely to provide confidence in release estimates over a wide range of disposal and beneficial use options, emphasizing the benefit of multi-pH testing. Furthermore, for CCRs, the rate of constituent release to the environment is affected by leaching conditions (in some cases dramatically so), and that leaching evaluation under a single set of conditions will, in many cases, lead to inaccurate conclusions about expected leaching in the field" (21).

Following the completion of this project, the question of appropriate leaching tests surfaced within the federal regulatory arena. EPA released a proposed rule to regulate the disposal of CCPs in 2010 and solicited comments on the use of LEAF methods or other leaching methods on CCPs not only for disposal management scenarios but also for beneficial use management scenarios (22). A Notice of Data Availability (NODA) was signed on September 30, 2011, announcing and inviting comment on additional information obtained by EPA in conjunction with the June 21, 2010 proposed rule. Included in the NODA was leachate data. A prepublication version of the NODA was available on EPA's Web site at the time of this report.

6.4.2 Experimental

Ten CCP samples were evaluated for this effort. Three CCP samples generated during mercury emission control technology demonstrations were selected from the EERC Coal Ash Properties Database (CAPD). These samples had been evaluated using SGLP and LTL under previous projects, and the limited data were incorporated with the data generated in this project as a means of expanding the characterization and interpretations. The other seven CCP samples were generated at two plants during recent mercury emission control technology demonstrations and had not been previously characterized.

Available sample identification information is provided in Table 6-8. These samples were generated at five separate coal-fired power plants. Four categories of mercury emission control technology strategy demonstrations were performed during the generation of these samples, labeled A–D. One sample was obtained from Plants 1–3 each: either a standard CCP or mercury emission control test sample. Three composite samples were prepared in the laboratory from material obtained from Plant 4, consisting of two mercury emission control test samples and a corresponding standard CCP. The mercury control sorbent injection rate differed for Samples 5 and 6 from Plant 4. Four samples were obtained from Plant 5, consisting of two mercury emission control test sample/corresponding standard CCP sample sets; Samples 7 and 8 were collected from different hoppers on the same day, and a few days later, Samples 9 and 10 were each collected. Sample 9 was collected from the same hopper as Sample 7, but Samples 8 and 10 were collected from different hoppers. The samples in Table 6-9 are not representative of a broad range of CCPs.

The collection location of each sample is noted in Table 6-9; all samples were collected from ESP or FF hoppers. Obtaining a CCP sample that is representative of the testing conditions is very difficult for reasons such as hopper emptying time or frequency variations, difficulty in defining hopper collection rates for a composite, and maldistributions of ash in hoppers. Additionally, some samples were obtained from a portion of the hopper for use in the main mercury emission control test study or the test duration was short. Therefore, it should not be assumed that the samples in this study are completely indicative of the stated test conditions. To best understand the effect of mercury emission reductions on the CCPs generated at a specific power plant, it is essential to characterize the as-managed CCPs that will be beneficially reused or placed in a disposal setting.

Table 6-8. Sample Identification

Sample	Plant	Sample Type	Mercury Emission Control Technology[1]	Collection Location, Hopper	Coal Type	Particulate Collection	SO_2 Control	NO_x Control
1	1	Fly ash + A[2]	A	ESP	Lignite	ESP-CS[3]	None	LNB[4] w/ OFA[5]
2	2	FGD–SDA[6] + B[2]	B	FF	Lignite	2 FF in parallel	SDA	None
3	3	Fly ash	None	ESP	Subbit[7]	ESP-CS & COHPAC FF	None	LNB
4	4	Fly ash	None	ESP (lab composite)	Subbit	2 ESP-CS in series	Wet FGD	LNB w/ CCOFA[8] and SOFA[9]
5	4	Fly ash + C[2]	C	ESP (lab composite)	Subbit	2 ESP-CS in series	Wet FGD	LNB w/ CCOFA and SOFA
6	4	Fly ash + C[2]	C	ESP (lab composite)	Subbit	2 ESP-CS in series	Wet FGD	LNB w/ CCOFA and SOFA
7	5	Fly ash + C[2]	C	ESP	Subbit	ESP-CS	None	
8	5	Fly ash	None	ESP	Subbit	ESP-CS	None	
9	5	Fly ash + D[2]	D	ESP	Subbit	ESP-CS	None	
10	5	Fly ash	None	ESP	Subbit	ESP-CS	None	

[1] The mercury emission control technologies are coded for anonymity.
[2] Consists of fly ash plus mercury emission control additives/sorbents.
[3] Cold-side electrostatic precipitator.
[4] Low-NO_x burner.
[5] Overfire air.
[6] FGD–spray dryer absorber (SDA) material that contains fly ash.
[7] Subbituminous.
[8] Close-coupled overfire air.
[9] Separated overfire air.

Chemical characterization techniques were utilized to provide an interpretation tool for the leachate results. The samples had multiple leaching tests performed, which included some or all of the following: SGLP, 30-day LTL, and select leaching framework tests. Additionally, previous SGLP and 30- and/or 60-day LTL results were incorporated into the results. Based on work performed by the EPA (6) the procedures performed on the CCPs in this project were the Tier 1 titration pretest and the pH-dependent and liquid-to-solid ratio-dependent parallel batch leaching (Leachability A and B tests from Tier 2 in the original framework). The methods used for each of the leaching procedures are described in the sections below.

A separate leaching bottle was used for each leaching test on each sample. For samples with a long-term component applied, multiple bottles were set up and analyzed at the different time intervals. For all leaching procedures, the solids were centrifuged if needed for separation from the leaching solution and filtered through a 0.45-µm filter. The pH of the resulting leachate

Table 6-9. Analysis Methods

Analyte	Method	Title	Solids Reporting Limit, µg/g[1]	Leachate Reporting Limit, mg/L
Antimony	EPA SW-846 Method 6020A	Inductively Coupled Plasma Mass Spectrometry	0.5	0.001
Arsenic	EPA SW846 Method 7010	Graphite Furnace Atomic Absorption Spectrometry	2.0	0.004
Beryllium	EPA SW-846 Method 6020A	Inductively Coupled Plasma Mass Spectrometry	0.05	0.0001
Bromide	ASTM D5987	Standard Test Method for Total Fluorine[2] in Coal and Coke by Pyrohydrolytic Extraction and Ion Selective Electrode or Ion Chromatograph Methods	5	NA
	EPA Method 300.0	Determination of Inorganic Anions by Ion Chromatography	NA[3]	1.0
Cadmium	EPA SW-846 Method 6020A	Inductively Coupled Plasma Mass Spectrometry	0.25	0.0005
Chromium	EPA SW-846 Method 6020A	Inductively Coupled Plasma Mass Spectrometry	0.5	0.001
Chloride	ASTM D6721	Standard Test Method for Determination of Chlorine in Coal by Oxidative Hydrolysis Microcoulometry	5	NA
	EPA Method 300.0	Determination of Inorganic Anions by Ion Chromatography	NA	1.0
Cobalt	EPA SW-846 Method 6020A	Inductively Coupled Plasma Mass Spectrometry	0.1	0.0002
Fluoride	Modified ASTM D5987[4]	Standard Test Method for Total Fluorine in Coal and Coke by Pyrohydrolytic Extraction and Ion Selective Electrode or Ion Chromatograph Methods	30	NA
	EPA Method 300.0	Determination of Inorganic Anions by Ion Chromatography	NA	1.0
Lead	EPA SW-846 Method 6020A	Inductively Coupled Plasma Mass Spectrometry	0.1	0.0002
Manganese	EPA SW-846 Method 6020A	Inductively Coupled Plasma Mass Spectrometry	2.5	0.005
Mercury	Modified EPA Method 245.1	Cold Vapor Atomic Absorption Spectrometry	0.025	0.00005
Nickel	EPA SW-846 Method 6020A	Inductively Coupled Plasma Mass Spectrometry	0.5	0.001
Selenium	EPA SW-846 Method 6020A	Inductively Coupled Plasma Mass Spectrometry	1.0	0.002
Sulfate	EPA Method 300.0	Determination of Inorganic Anions by Ion Chromatography	NA	1.0
Sulfur	ASTM D5373	Standard Test Methods for Instrumental Determination of Carbon, Hydrogen, and Nitrogen in Laboratory Samples of Coal	0.01%[5]	NA

[1] A higher reporting limit was necessary for some samples.
[2] Analyzed for Br on IC instead of F.
[3] Not applicable.
[4] The sample size was reduced, and the heating time was increased.
[5] Determined using a LECO Corporation sulfur analyzer and reported on a wt% basis.

was measured, and the leachate was preserved in separate aliquots as needed for analysis. Preservation methods included HNO_3 to pH < 2 for determination of trace elements, HCl to pH < 2 for determination of mercury, and no preservation for determination of halogens and sulfate.

Chemical Characterization

The moisture content and LOI of the CCP samples was determined using ASTM International (ASTM) C311-04 (Standard Test Methods for Sampling and Testing Fly Ash or Natural Pozzolans for Use in Portland-Cement Concrete).

Table 6-9 provides the primary analysis methods used for each of the analytes. Prior to determination of the total air toxic element content, the CCPs were digested as per ASTM Method D6357 (Standard Test Methods for Determination of Trace Elements in Coal, Coke, and Combustion Residues from Coal Utilization Processes by Inductively Coupled Plasma Atomic Emission Spectrometry, Inductively Coupled Plasma Mass Spectrometry and Graphite Furnace Atomic Absorption Spectrometry).

Alternate analysis methods for previous results for Samples 1 and 2 are noted here. The digestion prior to the determination of trace elements consisted of a hydrofluoric acid (HF) digestion followed by EPA 3050 (Acid Digestion of Sediments, Sludges, and Soils) using HCl and HNO_3 except Se for which an HCl/HNO_3 microwave digestion was used. The total mercury content of the CCPs was determined using a DMA-80 (direct mercury analyzer) by EPA Method 7473 (Mercury in Solids and Solutions by Thermal Decomposition, Amalgamation, and Atomic Absorption Spectrophotometry). The selected halogen contents were determined using standard x-ray fluorescence (XRF) spectrometry techniques on these two samples.

SGLP and LTL

The SGLP batch-leaching procedure is a relatively simple test that follows many of the conditions of ASTM D3987 Standard Test Method for Shake Extraction of Solid Waste with Water. The test utilizes a 20:1 liquid-to-solid ratio, end-over-end agitation at approximately 30 rpm, an 18-hour equilibration time, and usually a leaching solution consisting of water from the disposal or utilization site, water that has been prepared in the lab similar to water likely to contact the CCP, or distilled DI water (1). Distilled DI water was used as the leaching solution in this effort.

Prior to leaching, the bulk pH of the samples was determined in slurry using distilled water. The slurry was made on a volume basis of approximately 20 mL CCP diluted to 80 mL with distilled water. The pH was initially measured after 10–15 minutes of stirring. The sample slurry was then covered and stirring continued. A final pH value was obtained after 24 hours of stirring. A typical SGLP and LTL test consists of 18-hour, 30-day, and 60-day equilibration times on samples with a 24-hour pH >10; SGLP but not LTL is typically performed on samples with a 24-hour pH <10. Nonetheless, in this project, LTL was not applied to all qualifying samples because that was not a project objective.

pH-Dependent Parallel Batch Leaching

The generation of a pretest titration curve was necessary to determine the amount of acid or base solution needed to alter the natural pH of each CCP over a pH range of 2 to 12. The natural pH of each CCP was determined at a 100:1 liquid-to-solid ratio. To this solution, aliquots of 1N KOH were added sequentially to increase the pH of the solution to pH 12, with the pH monitored and recorded after each addition with a 5-minute settling time. In a separate flask, the pH was decreased in the same manner using aliquots of 2N HNO_3. Based on the acid and base aliquots and the corresponding pH values, a titration curve was plotted to generate a table of acid or base addition rates for the pH-dependent leaching. Exceptions to determination the minimum pH value are noted in the results section.

This leaching procedure (within the interpretation of the original leaching framework) consisted of separate leachate samples at eleven target pH levels of pH 2–12 at a liquid-to-solid ratio of 10:1 using distilled DI water plus the calculated amount of 1N KOH or 2N HNO_3 from the titration pretest. The eleven target pH levels were to be at pH = 2, 3, 4, etc., with one of the target levels used for the natural pH without acid or base addition. For this project, twelve parallel leaching tests were performed with the eleven target pH levels plus the natural pH sample. Each sample was rotated over a 48-hour period with end-over-end agitation at approximately 30 rpm. The 48-hour extraction period was chosen because the samples met the base case situation of particle size <2 mm; the actual particle size range was not evaluated. Exceptions to target pH tests performed are noted in the results.

Liquid-to-Solid Ratio-Dependent Parallel Batch Leaching

Five liquid-to-solid ratios including 10:1, 5:1, 2:1, 1:1, and 0.5:1 are to be employed within the liquid-to-solid ratio-dependent parallel batch leaching method. Each sample was rotated over a 48-hour period with end-over-end agitation at approximately 30 rpm. The 1:1 and 0.5:1 liquid-to-solid ratios were not evaluated in this effort. Additional exceptions to the liquid-to-solid ratios evaluated performed are noted in the results.

6.4.3 Results and Discussion

Chemical Characterization

The moisture content and LOI are given in Table 6-10. All samples were dry, with <1% moisture content. The LOI ranged from 0.3% to 7.9%. The LOI results confirm that, for the Plant 4 samples, although the same type of mercury emission control technology was used for the generation of Samples 5 and 6, the laboratory composite samples represent different injection rates of the sorbents used. Sample 10 was darker than the other three samples from Plant 5 and appeared to contain significant amounts of unburned carbon. Although Samples 8 and 10 were each collected as standard fly ash samples from the sample plant, the CCPs collected from the different hoppers on different days appear greatly different with a 0.10% increase in moisture content and almost 6.2% increase in LOI. This is an example of the potential difficulties encountered in collecting CCP samples during demonstration tests.

Table 6-10. Moisture Content and LOI, %

Sample	Plant	Sample Type + Mercury Control	Coal Type	Moisture Content	LOI
1	1	Fly ash + A	Lignite	0.07	2.48
2	2	FGD–SDA + B	Lignite	0.67	1.40
3	3	Fly ash	Subbit.	0.07	0.48
4	4	Fly ash	Subbit.	0.31	1.11
5	4	Fly ash + C	Subbit.	0.06	2.57
6	4	Fly ash + C	Subbit.	0.05	0.30
7	5	Fly ash + C	Subbit.	0.01	1.30
8	5	Fly ash	Subbit.	0.02	1.66
9	5	Fly ash + D	Subbit.	0.02	1.56
10	5	Fly ash	Subbit.	0.12	7.85

The total elemental concentrations of the CCPs were evaluated to be used as an interpretation tool for the leachate results. The results for the samples from Plants 4 and 5 can provide an indication of how the mercury emission control technologies are affecting the resulting CCPs as compared to the standard CCPs. The primary trace elements analyzed on all samples were As, Cd, Cr, Hg, Ni, Se, and S, shown in Table 6-11. The %S values were converted to ppm values in the table. As shown in Table 6-12, the samples were analyzed for the halogens of Br, Cl, and F. The Plant 4 samples also were analyzed for the trace elements of Sb, Be, Co, Pb, and Mn, as provided in Table 6-13.

Samples 1–3 cannot be directly compared to the other samples on a plant performance basis. The total S content is higher in Sample 2 than in the other samples because it contains material from the SDA, which is used for sulfur emission control.

Table 6-11. Total Trace Elemental Concentrations, ppm

Sample	Plant	Sample Type	As	Cd	Cr	Hg	Ni	Se	S
1	1	Fly ash + A	44.8	0.46	48.8	0.29	23.5	10.4	10,700
2	2	FGD–SDA + B	28.6	0.76	45.5	0.56	25.7	5.1	47,150
3	3	Fly ash	21.6	0.89	55.5	0.11	52.8	1.4	8500
4	4	Fly ash	39.0	1.5	69.7	0.33	69.9	29.1	15,700
5	4	Fly ash + C	19.2	1.7	61.2	8.16	56.4	22.3	14,900
6	4	Fly ash + C	22.2	1.3	65.3	0.02	58.1	23.1	13,600
7	5	Fly ash + C	13.4	0.74	33.2	0.38	28.1	3.8	1300
8	5	Fly ash	13.7	0.77	32.5	0.26	27.9	2.8	1800
9	5	Fly ash + D	17.7	0.78	36.1	0.38	27.9	3.5	1300
10	5	Fly ash	4.83	0.38	21.8	0.088	17.5	1.5	800

Table 6-12. Total Halogen Concentrations, ppm

Sample	Plant	Sample Type	Br	Cl	F
1	1	Fly ash + A	<5	844	270
2	2	FGD–SDA + B	39	336	360
3	3	Fly ash	<5	<5	550
4	4	Fly ash	<10	28	1800
5	4	Fly ash + C	194	46	780
6	4	Fly ash + C	<10	50	1160
7	5	Fly ash + C	30	6	380
8	5	Fly ash	11	11	440
9	5	Fly ash + D	33	6.5	280
10	5	Fly ash	9	7	230

Table 6-13. Additional Total Trace Elemental Concentrations on Plant 4 Samples, ppm

Sample	Plant	Sample Type	Sb	Be	Co	Pb	Mn
4	4	Fly ash	3.2	3.71	24.8	48.3	270
5	4	Fly ash + C	3.2	2.60	22.7	29.9	580
6	4	Fly ash + C	3.0	2.68	24.7	35.8	630

For Plant 4, slight variations are noted in some of the elements. A decrease in As, Ni, F, Be, and Pb levels in the samples from mercury emission control testing is noted. To a lesser extent, a decrease in Cr and Se is seen. An increase in Mn concentration is noted. The Hg and Br results show, as the LOI results did, that the laboratory composite samples represent different injection rates of the sorbents used between Samples 5 and 6.

The total elemental concentration results (beyond the noted increases in moisture content and LOI) in the sample set from Plant 5 emphasize the need for the analysis of as-managed CCP samples instead of individual hopper or composite samples to provide a realistic view of the effects of emission controls on changes to CCPs. As noted above, Samples 8 and 10 were collected as standard fly ash samples on different days from different hoppers with Sample 10 exhibiting a darker color and an appearance of significant amounts of unburned carbon. The concentrations of the tested elements in Sample 10 are well below those from Samples 7–9 from the same plant and will not be used as a comparison/contrast point. Mercury Emission Control Technology D appeared to alter the As, Cr, and F concentrations from the standard fly ash more than Technology C did. The Hg, Se, S, Br, and Cl concentrations were similar for both mercury emission control CCPs. The Cd and Ni concentrations remained relatively unchanged between Samples 7, 8, and 9.

Leaching Results

The results from all leaching tests are presented in this section. The pH of the leachates is examined first. Each element evaluated is discussed individually.

pH

The titration pretest curves generated for each of the samples using a 100:1 liquid-to-solid ratio and adding small aliquots of acid or base every 5 minutes, specified in the original leaching framework, are shown in Figure 6-13. Each chart is a plot of the measured pH as a function of the equivalents of acid or base (assigned a negative value for plotting) added per dry gram of material. With these charts, the material response to acid or base addition at a liquid-to-solid ratio of 10:1 can be interpreted. The pretest was repeated for some samples to the pH 4–6 range in order to capture the rapid change from pH 9 or 10 to pH 5 or 6.

These curves illustrate several points about the CCP samples. The pH value at 0 mEq/g represents the natural pH of the CCP at the evaluated 100:1 liquid-to-solid ratio, which is shown in Table 6-14. The curves are represented on the same x-axis to directly compare/contrast the mEq/g volume of acid or base addition to the samples. Samples 7–10, from Plant 5, required much less acid than the other six samples to reduce the pH of the sample from approximately pH 11.5 to near pH 2; <4 mEq/g acid was required. Up to 20 mEq/g of acid was added to the samples in this project to achieve a pH level of 4 or less. This portrays the variability in buffering capacity between samples. A volume of 20 mEq/g of acid in the titration pretest is equivalent to 400 mL of 2N HNO_3, which was the total amount of leaching solution utilized to prepare the 10:1 liquid-to-solid ratio leachate samples. The greatest change in pH with acid addition occurred from approximately the pH 9–10 range to pH 5 for most samples. The buffering capacity of the CCPs is evident below approximately pH 4 or 5 since larger equivalents of acid addition resulted in minimal changes in pH, particularly for Samples 1–6.

Although pH 3 and pH 2 acid equivalents were determined for most samples, it was chosen to not perform leaching at this level for some of the CCP samples because of the high volumes of 2N HNO_3 required and the limited budget. The filtered pH value of all leachate samples was measured. Figure 6-14 is a combination of two charts showing the effect of acid or base addition to the tested CCPs. The top chart shows the calculated amount of 2N HNO_3 needed to decrease or 1N KOH to increase the pH of the leachate to each of the target pH values based on the pretest titration curve generated. Leaching was not performed on samples requiring a calculated aliquot of 2N HNO_3 >200 mL (half of the 400-mL leaching solution amount), as indicated in the gray box in Figure 6-14. The bottom chart depicts the final leachate pH compared to the amount of acid or base added to the leaching solution. A comparison of the two charts shows that although the titration pretest provided a calculated amount of acid or base needed, the pH of the CCP samples had a strong influence on the final leachate pH. Most leachate pH values were within a range of 8–12 rather than the target pH range of 4–11, indicating that 5-minute intervals of acid addition in the pretest titration curve generation cannot adequately predict the response of the CCP with the acid addition. The addition of 1N KOH in the leaching solution increased the pH of the leachate to 12.5 to 13 instead of the desired pH of 12. This discrepancy in target pH to leachate pH was noted in another leaching method comparison study (5).

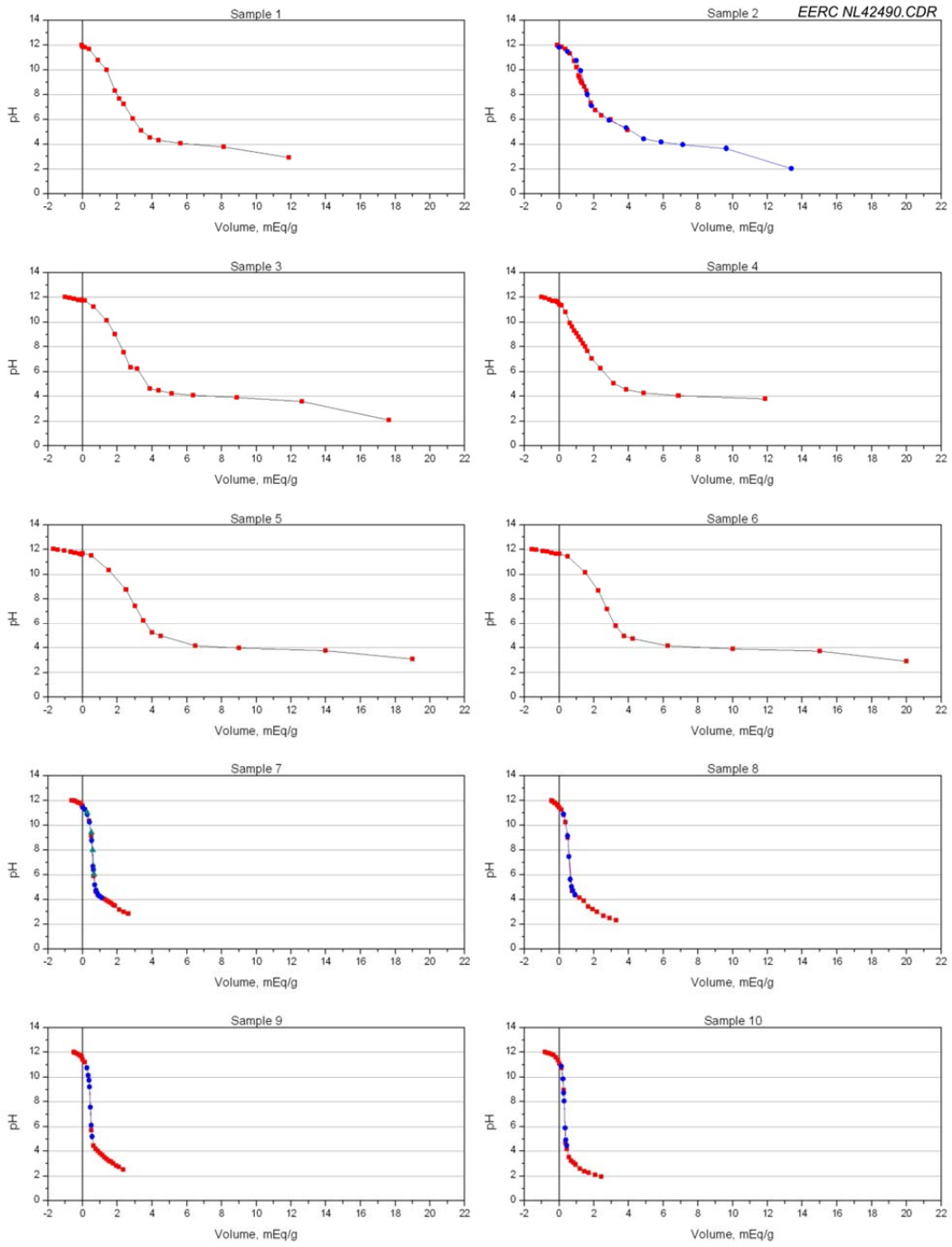

Figure 6-13. Pretest pH titration curves.

Table 6-14. Natural pH Determined in Pretest

Sample	Plant	Sample Type	Natural pH
1	1	Fly ash + A	11.86
2	2	FGD–SDA + B	11.82
3	3	Fly ash	11.73
4	4	Fly ash	11.43
5	4	Fly ash + C	11.74
6	4	Fly ash + C	11.68
7	5	Fly ash + C	11.42
8	5	Fly ash	11.42
9	5	Fly ash + D	11.42
10	5	Fly ash	11.42

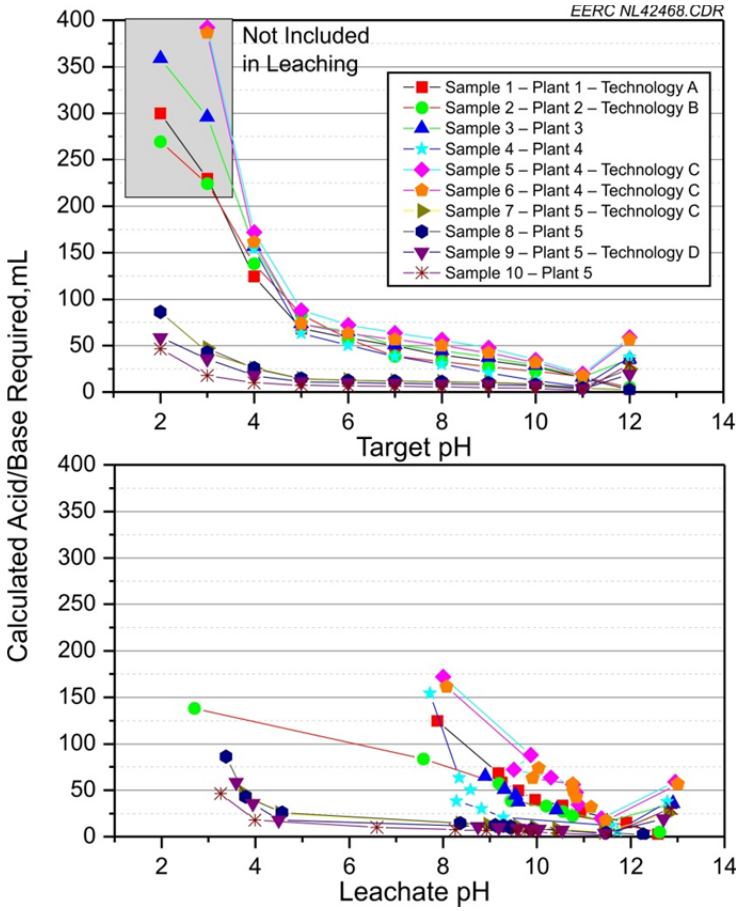

Figure 6-14. Target pH and leachate pH comparison as related to calculated acid or base requirement.

A comparison of the target pH to the final leachate pH is shown in Figure 6-15 for all pH-dependent leaching samples. This chart shows that in all but two cases, the leachate pH was higher than the target pH, which was up to 5 pH units higher than the target pH particularly at target pH 5. Figure 6-16 focuses on the Plant 4 target and leachate pH values. It shows that the CCPs from the mercury emission control testing behave similarly over all target pH levels, but these pH profiles vary by approximately 2 pH units from the pH profile of the standard CCP (Sample 4) between the target pH values of 5–9. Figure 6-17 shows the Plant 5 target and leachate pH values. Most of the Plant 5 pH profiles are similar at all target pH levels with a slight deviation of Sample 8 (a standard CCP) with the initial acid and base additions and more dramatically at the target pH of 4. Although the natural pH or all four samples was 11.42, the standard CCP Sample 8 responded to the addition of acid or base more effectively than the other samples at the lowest and highest pH levels. The leachate pH values were similar for Sample 9 after 48 hours of rotation (the standard test time) and an extension to 30 days of rotation except at the target pH level of 4.

A plot of the leachate pH values from the liquid-to-solid ratio leaching tests at 2:1, 5:1, and 10:1 (duration 48 hours) and the SGLP at 20:1 (duration 18 hours) is provided in Figure 6-18. This shows that at a 2:1 liquid-to-solid ratio, the pH of the tested CCPs is typically higher than measured for other tests, generally with a decrease in pH as the liquid portion increased. The two lignite CCPs (Samples 1 and 2) had the highest pH values. All leachate pH values were between 11.5 and 13.0. For Plant 4, at all liquid-to-solid ratios, the mercury emission control technology CCPs had a higher pH than the standard CCP. The Plant 5 samples maintained fairly similar profiles across the range of liquid-to-solid ratios.

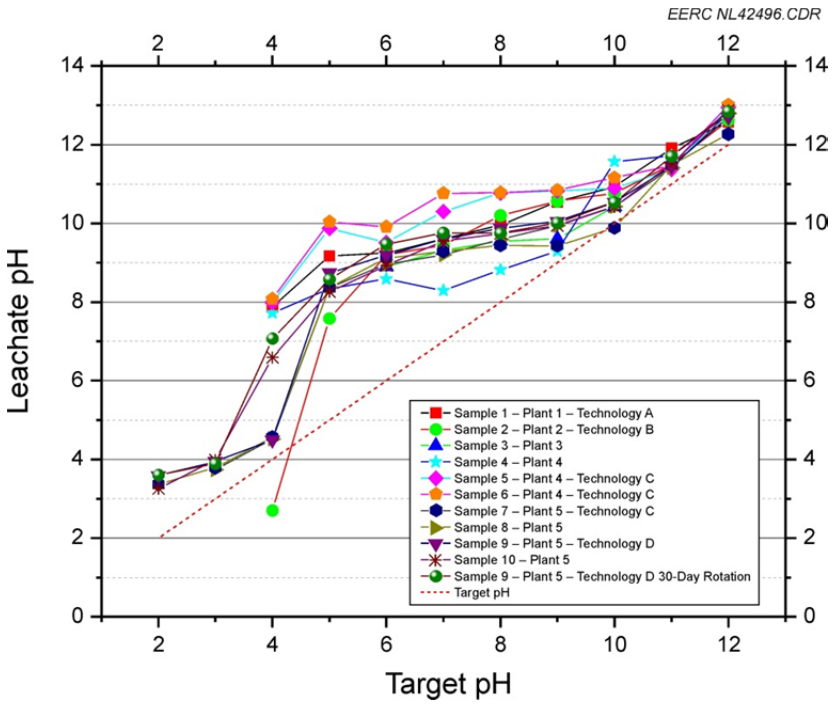

Figure 6-15. Target pH versus leachate pH for all pH-dependent leaching samples.

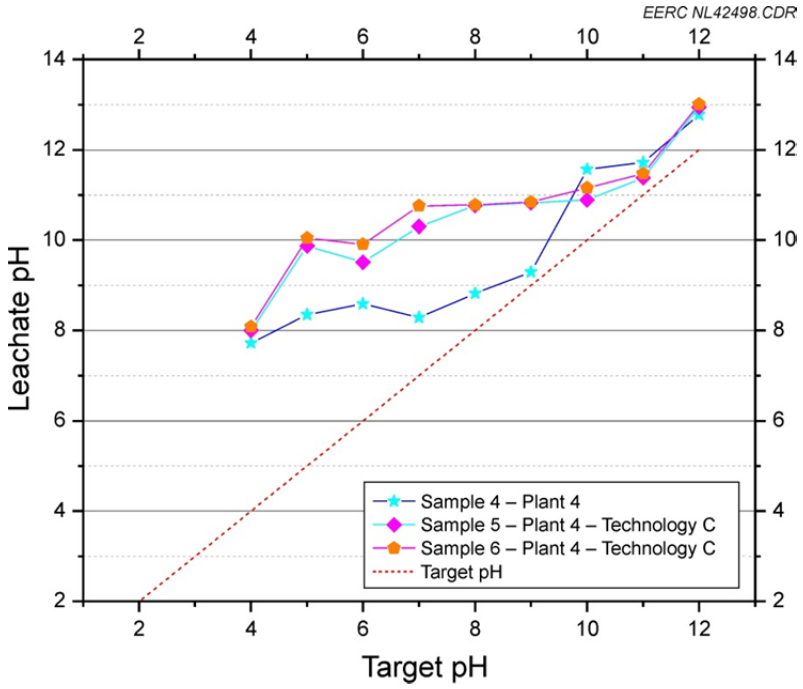

Figure 6-16. Target pH versus leachate pH for Plant 4 pH-dependent leaching samples.

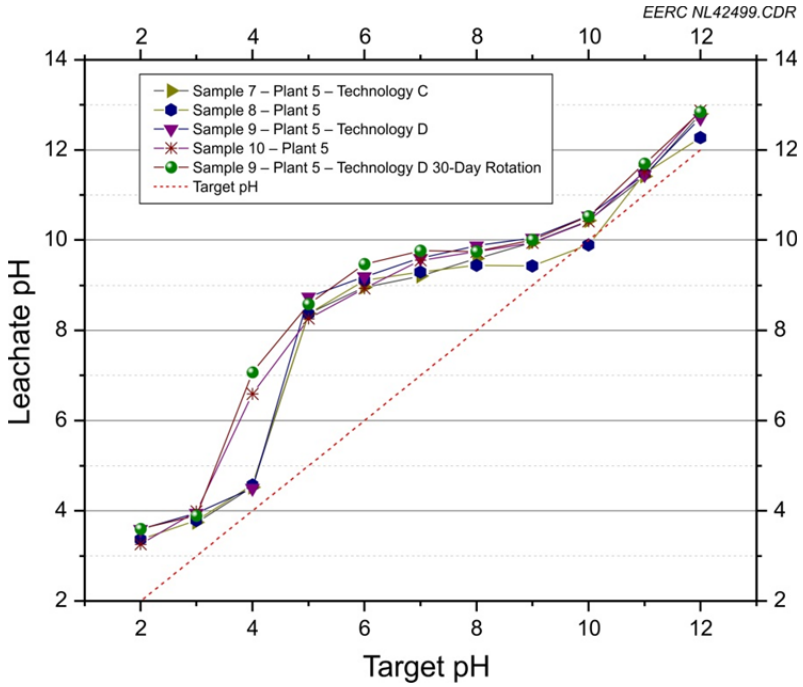

Figure 6-17. Target pH versus leachate pH for Plant 5 pH-dependent leaching samples.

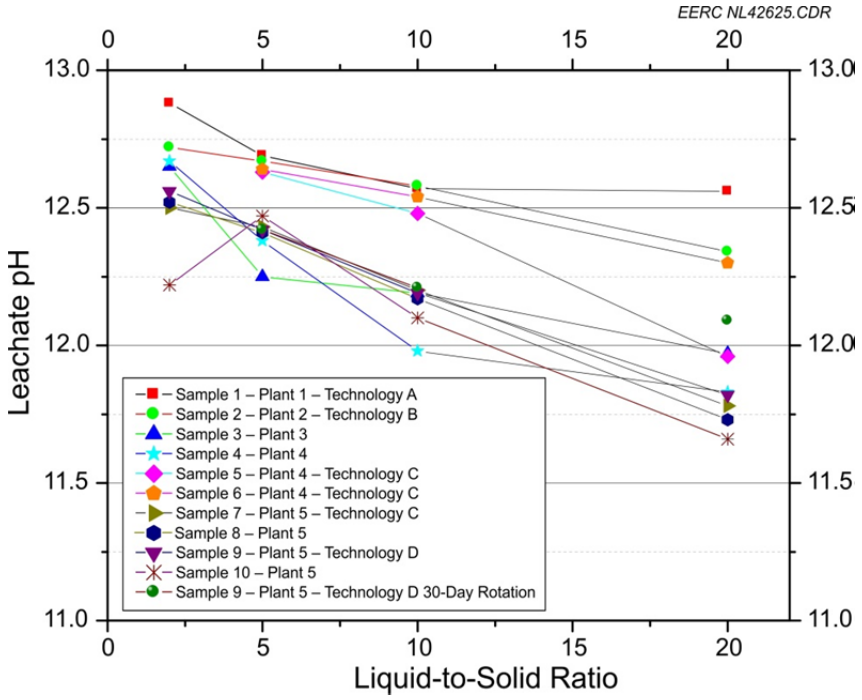

Figure 6-18. Liquid-to-solid ratio leaching pH values.

In previous work at the EERC, LTL with 30- and 60-day rotation at a 20:1 liquid-to-solid ratio was performed on Samples 1 and 2. In this current study, the leaching tests for Sample 9 were extended to 30 days at 10:1 and 20:1 liquid-to-solid ratios. The leachate pH values for all previous studies and the current effort are given in Table 6-15. Little change in pH was noted for Sample 1 at all leaching durations. Samples 2 and 9 show an increase in leachate pH with test duration with a higher pH at a 10:1 liquid-to-solid ratio.

Table 6-15. Short- and Long-Term Leaching pH Values

Sample	Plant	Technology	Test Duration	Liquid-to-Solid Ratio	Leachate pH
1	1	A	18 hours	20:1	12.56 ± 0.02
1	1	A	48 hours	10:1	12.57
1	1	A	30 days	20:1	12.61
1	1	A	60 days	20:1	12.59
2	2	B	18 hours	20:1	12.33 ± 0.02
2	2	B	48 hours	10:1	12.58
2	2	B	30 days	20:1	12.39
2	2	B	60 days	20:1	12.49 ± 0.01
9	5	D	18 hours	20:1	11.82
9	5	D	30 days	20:1	12.09
9	5	D	48 hours	10:1	12.19
9	5	D	30 days	10:1	12.21

Trace Element Leaching Results

All leachates from all tests were analyzed for arsenic, cadmium, chromium, mercury, nickel, selenium, and sulfur compounds as sulfate. Samples 4–6, from Plant 4, were also analyzed for antimony, beryllium, cobalt, lead, and manganese in the leachates. Neither antimony nor lead was detected in the leachate samples and, therefore, are not included in the discussion below. All leachate concentrations reported as less than the detection limit for the element have been changed to one-half of the provided detection limit for purposes of these evaluations. In some cases, the detection limit was not consistent for all leachate samples for a given element because of the sample matrix variabilities. The total concentration of the element in the solid sample, the leachate concentration, and the liquid-to-solid ratio used in the leaching test all contribute to the calculation of the amount of element leached, as a percentage, for each leaching test result. Because of these factors, the plotted amount of element leached as a percentage may vary for equivalent leachate concentrations.

Arsenic Leaching Results

Plots of the arsenic leachate concentrations as a percentage of the maximum leachable amount for each sample can be found in Appendix A. All samples leached less than 3% of the total As in the solid sample, with many leaching less than the detection limit in the liquid leachate. In the rare instances where As was detected in the leachate from Samples 1–6 from Plants 1–4, the amount of As leached was near the detection limit and was below 0.6% in all cases. The samples from Plant 5, Samples 7–10, leached up to 2.5% of the amount of As in the solid samples. For each of these samples from Plant 5, the maximum leached amount of As occurred near pH 9 in the leachate and generally decreased as the pH increased. The plot for Sample 7 is shown in Figure 6-19 as an example. The plots indicate an oxyanionic behavior with the maximum leachate values in the neutral to slightly alkaline range. Arsenic was noted in two instances under leachate pH 4.

Extending the leaching duration for Sample 9 to 30 days resulted in a slight decrease in the percentage of As leached over most of the pH range. In previous studies, all short- and long-term (30 and 60 days) As values for Sample 1 were less than the detection limit, which is similar to most results from the current study. Sample 2 short- and long-term leaching values at a 20:1 liquid-to-solid ratio were approximately 0.5% of the available As in previous studies.

An evaluation of the impact of mercury emission control demonstrations on the As leaching from the CCPs as compared to the standard CCPs is futile. The Plant 4 samples were below or near the detection limit. The mercury emission control CCPs yielded a percentage of As leached generally within ±1% of the standard CCP Sample 8.

Cadmium Leaching Results

Individual plots of the cadmium leachate concentrations as a percentage of the maximum leachable amount for each sample can be found in Appendix A. Samples 1–6 from Plants 1–4 leached less than 4% of the amount of Cd in the solid samples. The target pH 2 and 3 tests were

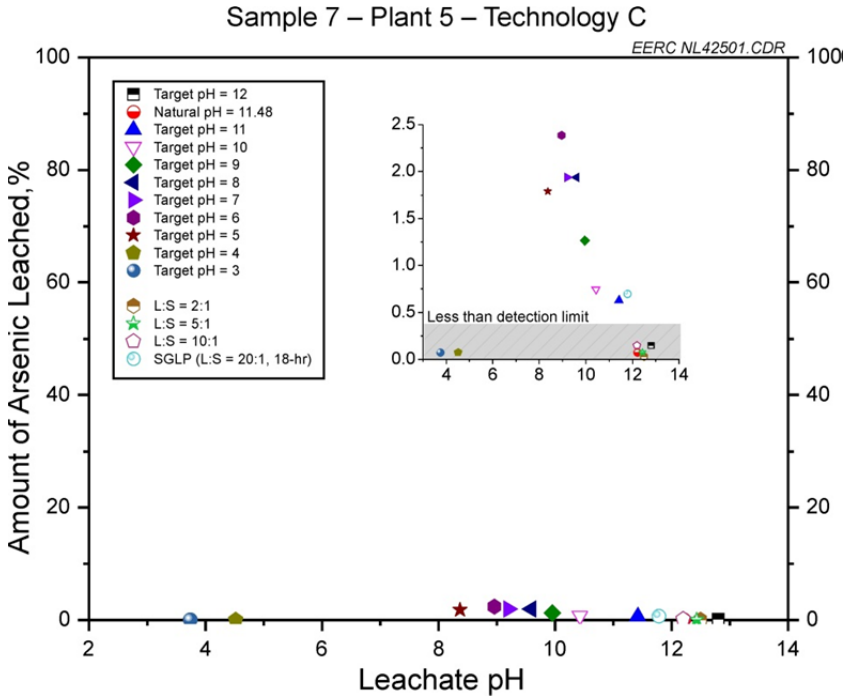

Figure 6-19. Percentage of total arsenic leached from Sample 7, Plant 5, Technology C.

not performed for these samples; the leachate pH values were in the 7–13 range with the exception of pH 2.7 for Sample 2 at the target pH 4. Similarly, the Plant 5 CCPs (Samples 7–10) leached up to 3% over the leachate pH range of 8–13. The lower target pH tests were performed on these samples, where the results showed that up to 21% of the amount of Cd in the solid samples leached over the leachate pH range of 3–7. An example is shown in Figure 6-20.

A slight decrease in the percent Cd leached was noted in most leachates with the extension of the leaching duration for Sample 9 to 30 days. In previous studies of short- and long-term (30 and 60 days) leaching of Samples 1 and 2, both samples exhibited a decrease from slightly above the detection limit from the 18-hour SGLP to the 30-day leaching.

Cadmium leachate concentrations that were above the detection limit for Plant 4 Samples 4–6 were all less than 0.4% of the maximum leachable concentration so any changes between the standard and mercury emission control CCP samples were well within the error of analyses. The change in percent cadmium leached from the two samples from mercury emission control demonstrations (Samples 7 and 9) for Plant 5 are compared to the standard CCP Sample 8 in Figure 6-21. As noted above, the lowest amount of Cd leached over the leachate pH range of 8–13, with a variation of change of ±2% from the standard CCP. The mercury emission control CCPs generally leached more Cd than the standard CCP except at the higher pH levels. Sample 9 leached up to 13% more Cd than the standard CCP over the leachate pH range of 3–5.

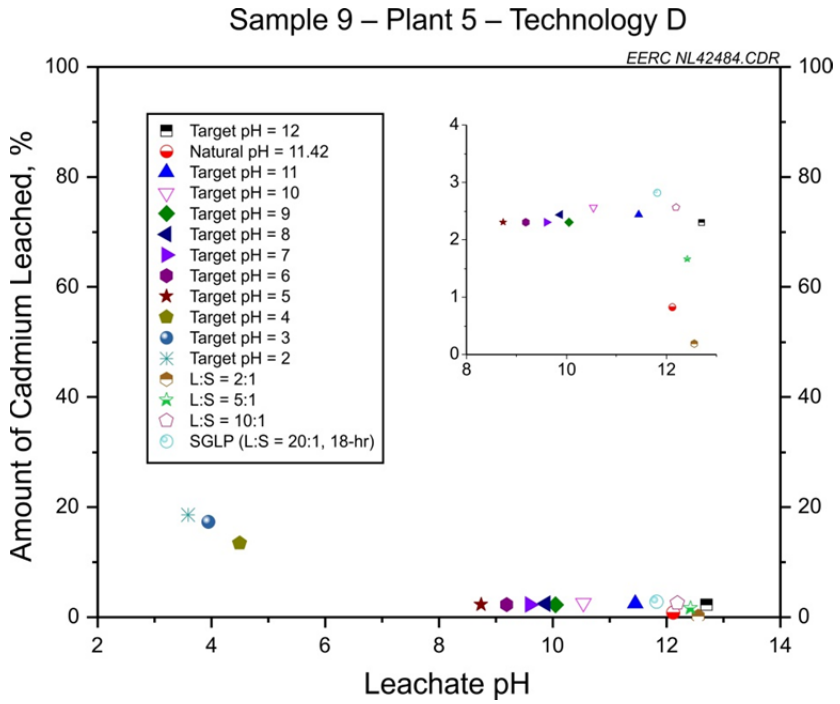

Figure 6-20. Percent of total cadmium leached from Sample 9, Plant 5, Technology D. The inset contains only values less than 4% and over the pH range of 8–13.

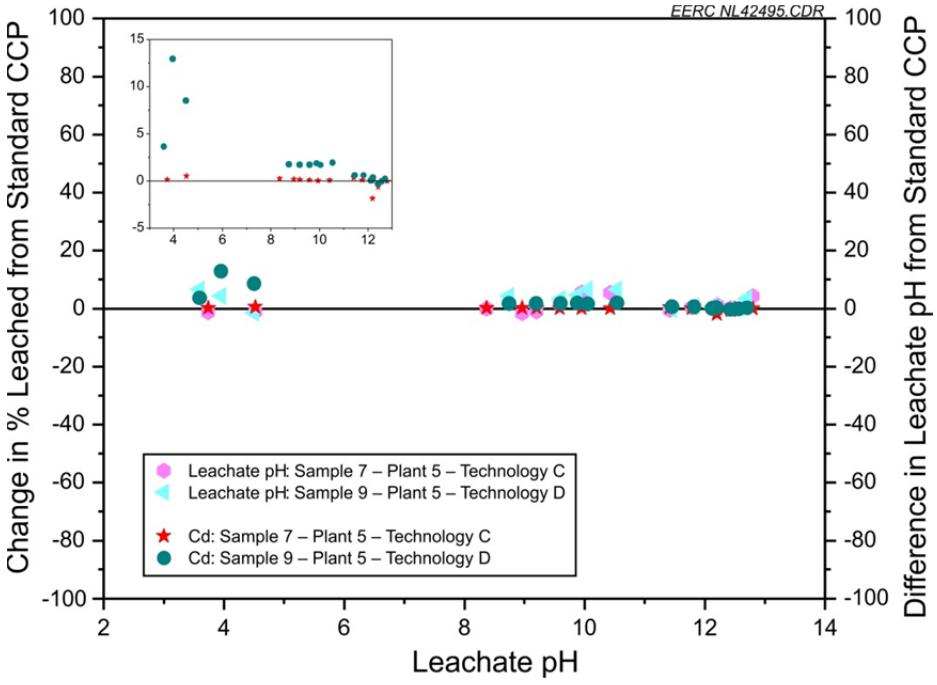

Figure 6-21. Change in percentage of cadmium leached and in leachate pH for Samples 7 and 9 from standard CCP Sample 8 (Plant 5). The inset is focused on a change in the percentage of cadmium leached.

Chromium Leaching Results

Plots of the chromium leachate concentrations as a percentage of the maximum leachable amount for each sample can be found in Appendix A. Samples 1–6 from Plants 1–4 leached less than 7% of the amount of Cr in the solid samples. Samples 7–10 from Plant 5 leached up to 15% over the leachate pH range of 4–13 but leached up to 34% of the amount of Cr in the solid samples at near pH 3.

A number of the samples exhibited a curve indicative of amphoteric species leaching where the minimum Cr concentrations were noted in the near-neutral pH range and showed an increase with increasing pH; nonetheless, these same samples displayed decreasing concentrations above pH 12 which is indicative of the presence of oxyanionic species. This curve is emphasized when the Sample 9 short-term and 30-day LTL results are compared. From approximately pH 8 to near pH 12, the 30-day LTL samples leached slightly more Cr than the short-term tests up to 4% and then leached less Cr than the short-term, up to 4%, above approximately pH 12.

In previous studies, Sample 1 decreased from approximately 2.7% Cr leached from the sample with the 18-hour SGLP to less than 0.1% at 30 and 60 days. Unlike Samples 1 and 9, Sample 2 indicated an increase in the amount of Cr leached from 18 hours to 30 days and then remained steady at 60 days.

The Plant 4 samples were more oxyanionic over the neutral-to-alkaline range than many of the other samples. For comparison purposes, the mercury emission control CCPs from Plant 4 leached a lower percentage of Cr, in most instances, than the standard CCP leached, with all changes within ±5%.

The apparent combination of amphoteric and oxyanionic species behavior is also emphasized when the mercury emission control demonstrations (Samples 7 and 9) are compared to the standard CCP Sample 8. In the 8–12 pH range, the mercury emission control CCPs showed 5% more of the available Cr leached than the standard CCP, while above approximately pH 12, these samples leached up to about 6% less Cr than the standard CCP.

Mercury Leaching Results

Appendix A contains the plots for the mercury leachate concentrations as a percentage of the maximum leachable amount for each sample. The majority of the mercury leachate concentrations were below the detection limit. Measureable Hg was analyzed in Samples 1–3 and the Sample 9 30-day leachates. The highest percent mercury leached (4.3%) was noted in Sample 2 for the target pH 4 sample which resulted in a leachate pH of 2.70 (the lowest pH of all sample leachates).

In previous studies, all short- and long-term Sample 1 mercury concentrations were below the detection limit, and the percent mercury leached varied from less than the detection limit to 0.22% for Sample 2.

Nickel Leaching Results

Appendix A contains plots of the nickel leachate concentrations as a percentage of the maximum leachable amount for each sample. With few exceptions, the Ni leachate results exhibited a decreasing trend in percentage of total Ni leached as the leachate pH increased, which is typical of cationic species. An example is displayed in Figure 6-22. The leachate samples with a pH below 4 leached up to approximately 30% of the total Ni while many leachate samples with highly alkaline pH had no detectable Ni leached. Above leachate pH = 6, all Ni leachate concentrations were equivalent to less than 6% of the total nickel in the CCP.

The greatest change in the Ni leaching from the short-term tests to 30-day leaching occurred in leachate samples with pH < 4 where the changes in percent leached were within ±4%. Otherwise, the leachate values were within ±1%. In previous studies, Samples 1 and 2 behaved differently from each other. Sample 1 showed an increase from less than 0.1% nickel leached from the sample with the 18-hour SGLP to 0.5%–0.7% at 30 and 60 days. Sample 2 leached close to 2% of the total Ni with the 18-hour SGLP and decreased to less than the detection limit at 30 and 60 days of leaching.

The mercury emission control demonstration CCP samples from Plant 4 leached a greater percentage of Ni than the standard CCP in all leaching tests by up to 1%. The percentage

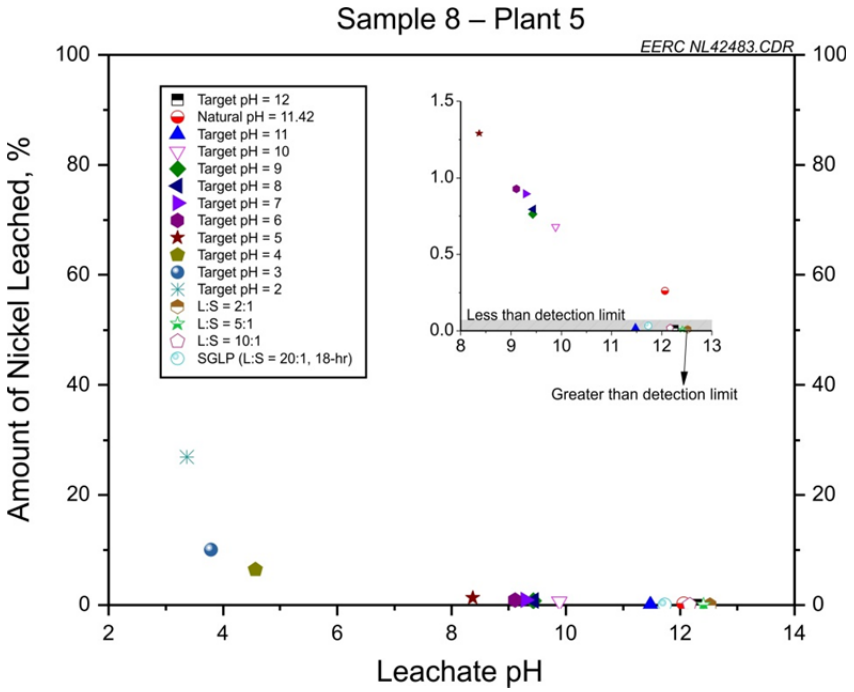

Figure 6-22. Percentage of total nickel leached from Sample 8, Plant 5. The inset contains only values less than 1.5% and over the pH range of 8–13. The 2:1 liquid-to-solid ratio leaching sample had a leachate concentration above the detection limit; however, the low liquid-to-solid ratio resulted in a percentage of nickel leached lower than the other liquid-to-solid ratios.

decreased as the leachate pH increased. The Plant 5 CCPs leached Ni at similar percentages of the total for each sample. Sample 9 leached up to 5.6% less Ni than the standard CCP, particularly at low pH levels.

Selenium Leaching Results

Plots of the selenium leachate concentrations as a percentage of the maximum leachable amount for each sample can be found in Appendix A. The Se results are unlike the majority of results from the other elements because up to 60% of the total Se leached from the CCP samples and few leachate concentrations were below the detection limit.

The Se plots are primarily indicative of an oxyanionic species curve. The formation of secondary hydrated phases such as ettringite can play a role in reducing the amount of oxyanions such as Se that leach from CCPs, but the samples were not analyzed for the presence of these phases. For some samples, the percentage of Se leached from the target pH 12 leaching test (with the addition of 1N KOH) was notably higher than the percentage of Se leached at many of the other pH levels. This provides indirect evidence that the 1N KOH added to the leachate solution for the target pH 12 leaching tests may be contributing to a delay in ettringite formation. An example of this is provided in Figure 6-23.

Figure 6-24 shows that with an extension of the leaching duration to 30 days for Sample 9, an increase in the percent Se leached was generally noted between pH 8 and pH 11 while a decrease in the percentage leached occurred at leachate pH levels below and above this. The decrease in the percentage of Se leached above pH 11 was significant with up to a 17% decrease measured between the 18-hour SGLP to 30-day LTL tests. In previous studies, Sample 1 decreased from approximately 4% Se leached from the sample with the 18-hour SGLP to less than the detection limit at 30 and 60 days. The Sample 2 leachates did not vary significantly for the short- and long-term leaching tests.

A comparison of the Plant 4 samples indicates that, in most instances, the mercury emission control CCPs leached a slightly lower percentage of Se than the standard CCP leached, with typical variations within ±2%. Of particular note is the target pH 12 point for the samples, where 1N KOH was added as part of the leaching solution. The concentration for each of the samples at this point increased over that of the other solutions in the leachate pH 10–13 range. The Se leachate concentrations at the target pH 12 point were higher in the mercury emission control CCPs than the standard CCP, corresponding to a 17%–25% increase over the standard CCP in the percentage of Se leached. These results imply that while many of the samples exhibited potential ettringite formation delay with the addition of 1N KOH, some samples were affected more dramatically than others.

While the mercury emission control CCP samples from Plant 4 generally leached a slightly lower percentage of Se than the standard CCP leached, the Plant 5 mercury emission control CCP samples leached more Se than the standard CCP in most cases. The change in the percentage of total Se in the solid that leached ranged from −1.4% to 24%, as shown in Figure 6-25. Sample 9 with Mercury Emission Control Technology D showed a higher percentage of Se leached than Sample 7 with Mercury Emission Control Technology C.

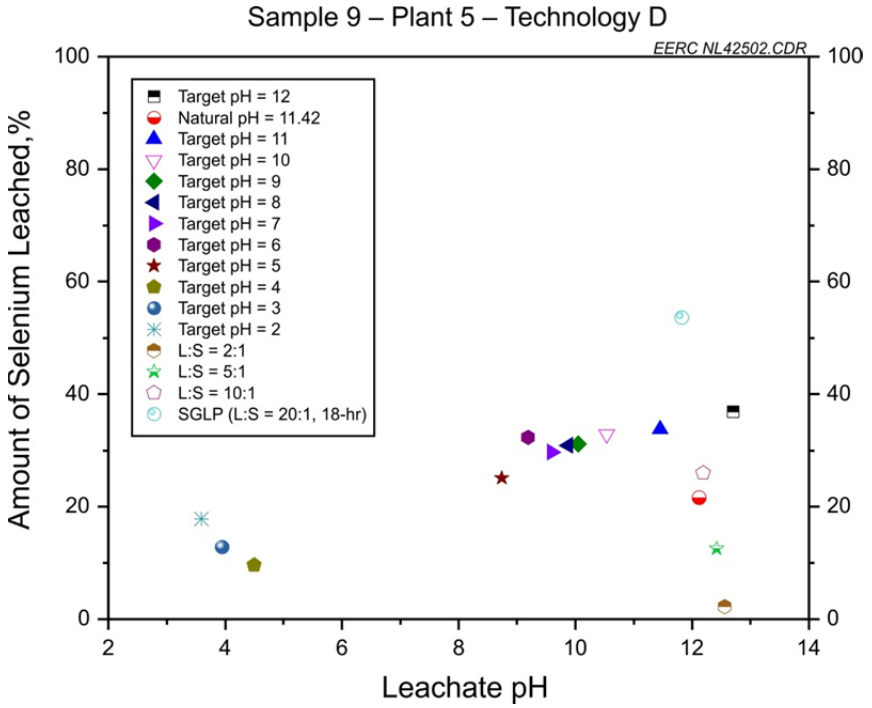

Figure 6-23. Percentage of total selenium leached from Sample 9, Plant 5, Technology D.

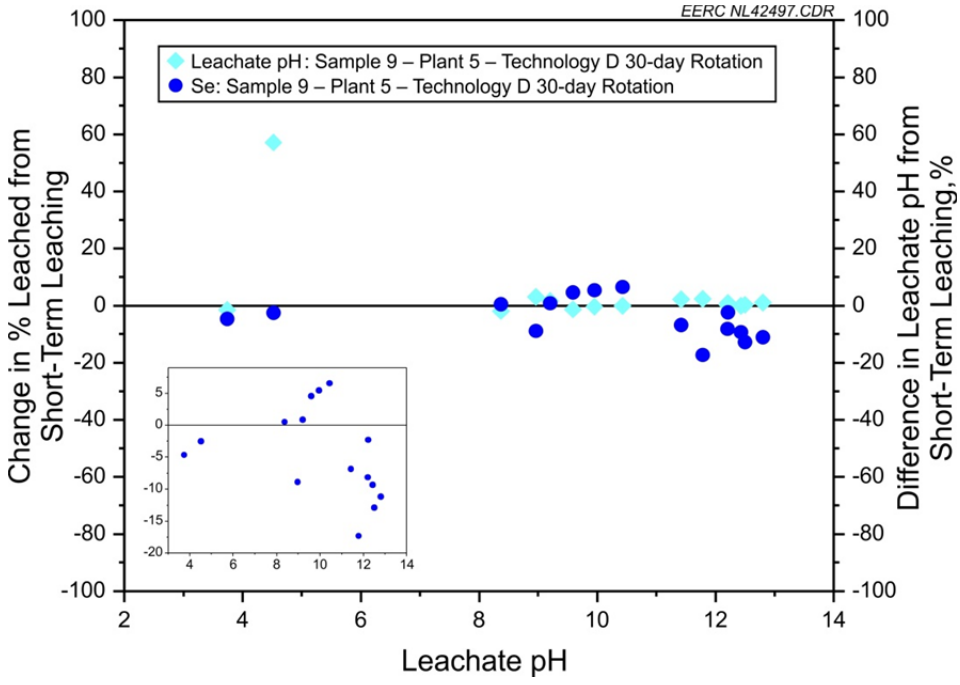

Figure 6-24. Change in percentage of selenium leached and in leachate pH for Sample 9 with a test duration extension to 30 days from short-term leaching of 18 or 48 hours (Plant 5). The inset is focused on change in percentage of selenium leached.

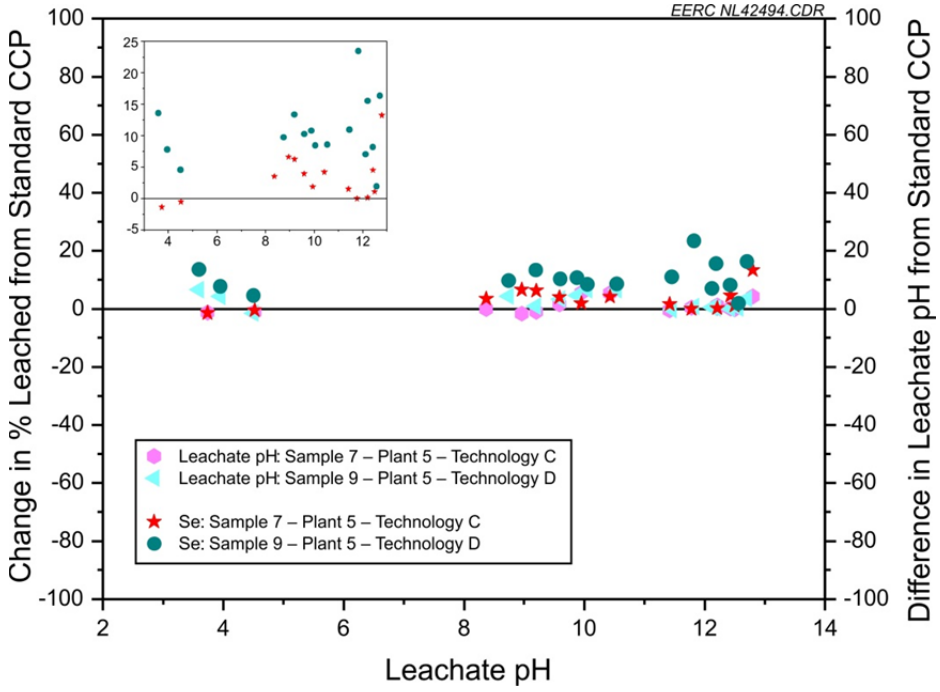

Figure 6-25. Change in percentage of selenium leached and in leachate pH for Samples 7 and 9 from standard CCP Sample 8 (Plant 5). The inset is focused on change in percent Se leached.

Sulfur Compounds as Sulfate Leaching Results

The sulfur compounds analyzed as sulfate in the leachates are plotted as a percentage of the maximum leachable amount for each sample in Appendix A. The leachate results analyzed for sulfate indicate leaching of a higher percentage of the available sulfur in the solid sample than most of the elements, which makes these results similar to the selenium results. Up to 60% of the total sulfur analyzed as sulfate leached from the CCP samples, and few leachate concentrations were below the detection limit.

The sulfate leaching results were, in many ways, similar to the Se results. The general trend of the sulfate plots indicates an oxyanionic species curve. The amounts of sulfur as sulfate leached from the target pH 12 leaching test, with the addition of 1N KOH, were often notably higher than the results of the other leaching tests for some samples. This is particularly evident for samples that exhibit a low percentage release of sulfur as sulfate in a general range in leachate pH of 11.5–13 and then an obvious increase for the target pH 12 leachate. This provides indirect evidence that the 1N KOH added to the leachate solution for the target pH 12 leach tests contributed to a delay in ettringite formation, as was also seen for Se.

The change in the leaching of sulfur as sulfate from 18 or 48 hours to 30 days was similar to the Se pattern. Over the range of approximately pH 6 to 11, little change to a slight increase in the percentage of sulfur as sulfate leached was observed in the pH-dependent leachates. Similar to the Se pattern, a decrease in the percentage of sulfur as sulfate leached occurred at leachate pH levels below 6 and above 11. The decrease in the percentage of sulfur as sulfate leached above

pH 11 was significant, with up to a 27% decrease measured for the 18-hour SGLP to 30-day LTL tests. In previous studies, Samples 1 and 2 each exhibited a significant decrease in the percentage of sulfur as sulfate leached from the sample between the 18-hour SGLP and the 30-day LTL test. Each then remained relatively steady at the lower concentration from the 30- to 60-day LTL tests. Sample 1 decreased from 32% to 0.05%, and Sample 2 decreased from 10.4% to 1.6% from the short-term to the long-term leaching tests.

As shown in Figure 6-26, Samples 5 and 6 from mercury emission control demonstrations leached a lower percentage of sulfur as sulfate as compared to the percentage leached for the Plant 4 standard CCP, Sample 4. Although the inset is focused on the changes within the range of 0% to −6%, changes in the percentage leached from the standard CCP to the mercury emission control demonstration CCPs were as much as −30% to −50%. In contrast to the Se results, the percentage of sulfur as sulfate leached decreased with the addition of 1N KOH in the target pH 12 mercury emission control CCPs, by −32% and −39% less than the standard CCP.

For Plant 5, the mercury emission control CCP samples leached less sulfur as sulfate than the standard CCP in most cases. The change in the percentage of total sulfur as sulfate in the solid that leached ranged from −21% to 0.05%, with the majority between −21% and −8%.

Beryllium Leaching Results

Plots of the Plant 4 beryllium leachate concentrations as a percentage of the maximum leachable amount for each sample can be found in Appendix A. All three samples leached less

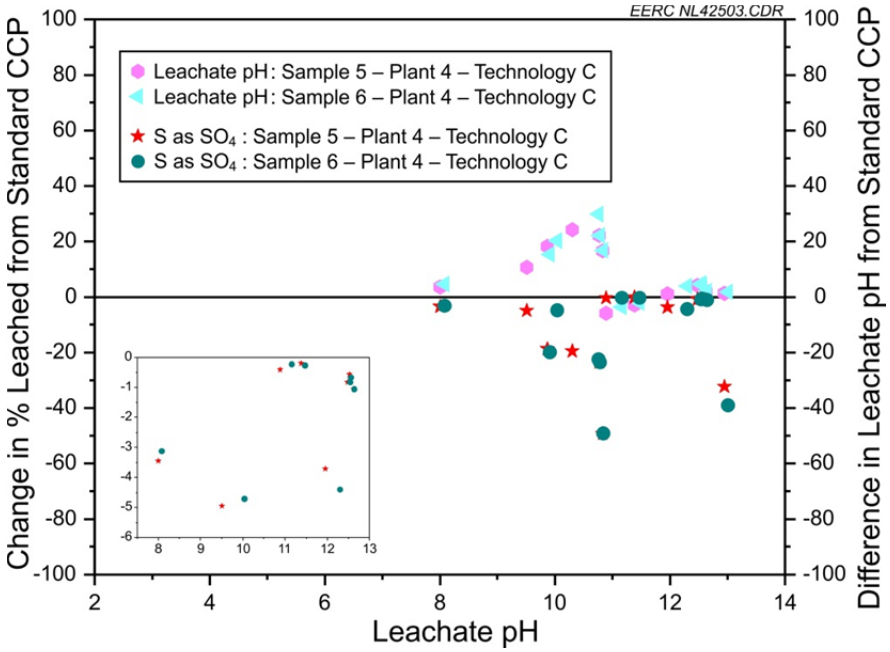

Figure 6-26. Change in percentage sulfur as sulfate leached and in leachate pH for Samples 5 and 6 from standard CCP Sample 4 (Plant 4). The inset is focused on a change in the percentage of sulfur as sulfate leached. The inset contains only values between 0% and −6%.

than 1% of the amount of beryllium in the solid samples. The Be leachate concentrations were similar for all samples; however, since the standard CCP Sample 4 contained a higher total Be content, the two mercury emission control CCPs can be seen as leaching a higher percentage of the total Be than the standard CCP.

Cobalt Leaching Results

Appendix A also contains the plots of the Plant 4 cobalt leachate concentrations as a percentage of the maximum leachable amount for each sample. Less than 0.6% of the amount of Co in the solid samples leached. The results were variable.

Manganese Leaching Results

Plots of the Plant 4 manganese leachate concentrations as a percentage of the maximum leachable amount for each sample can also be found in Appendix A. For all three samples, all leachate results were less than the detection limit with the exception of the target pH 4 leachate concentrations. The leachate pH of the target pH 4 samples was near pH 8. The standard CCP, Sample 4, leached approximately 5% of the available Mn, while the mercury emission control technology demonstration samples leached closer to 0.6% of the available Mn.

Halogen Leaching Results

Leachate samples were analyzed for the halogens bromide, chloride, and fluoride. Bromide results were not reported by the laboratory for the samples from the pH-dependent leaching tests where the pH was reduced using 2N HNO_3 in the leaching solution because the laboratory reported an interference between the bromide and nitrate peaks on the IC.

The halogen leachate results are not interpreted on the same basis as the trace elements (i.e., percentage of total leached) because the correlation between the total concentration of halogen in the CCP and leachate concentration of the halogen frequently indicated that greater than 100% of the total concentration of the halogen leached from the CCP sample. Funding was not available to determine the cause of this.

Bromide Leaching Results

Bromide leachate concentration plots are shown for the individual CCP samples in Appendix A. As mentioned above, Br was not analyzed in the pH-dependent leachate samples that contained 2N HNO_3 in the leachant solution; therefore, results were obtained for the natural pH, target pH 12 (with KOH addition), and liquid-to-solid ratio-dependent leachate samples. Sample 1 from Plant 1 and Sample 3 from Plant 3 did not exhibit any results above the detection limit of 1 mg/L Br. The concentrations measured for Sample 2 from Plant 2 generally indicated a dilution factor response to the change in the liquid-to-solid ratio.

Figure 6-27 provides a comparison of the bromide leachate concentrations for the samples from Plant 4. The standard CCP (Sample 4) had one bromide leachate result at, and all others less, than the detection limit. Although Samples 5 and 6 were each obtained from demonstrations

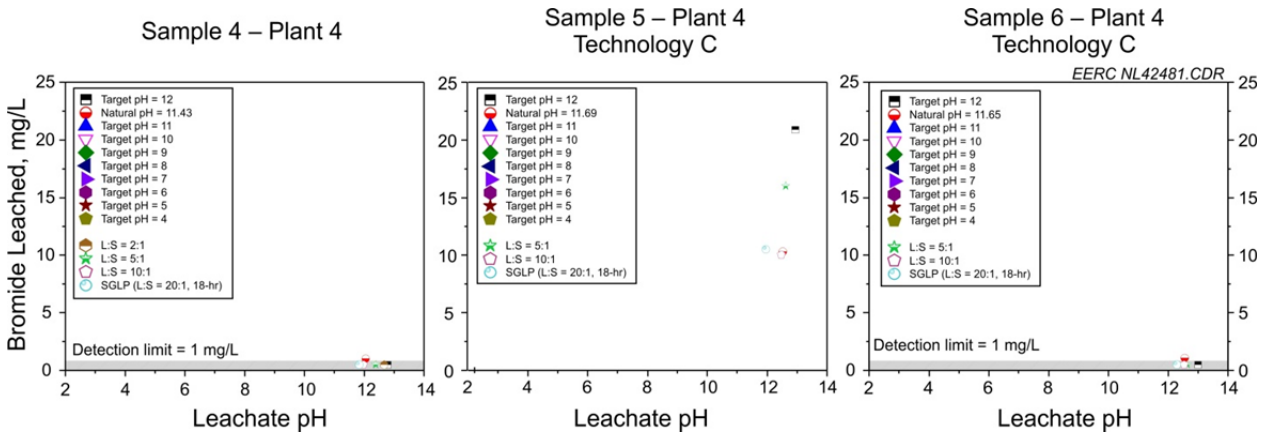

Figure 6-27. Bromide concentrations measured in leachates for standard CCP Sample 4 and mercury emission control demonstration CCP Samples 5 and 6 (Plant 4).

of the same type of mercury emission control technology, the results of bromide leachate concentrations were contrasting. Sample 6 exhibited similar results to the standard CCP, with one leachate value slightly above and all others less than the detection limit. Sample 5 showed detectable concentrations for all samples measured and generally exhibited a change in concentration based on the liquid-to-solid ratio of the leaching test.

For Plant 5, the standard CCP Sample 8 leached Br from the sample following the general trend noted for the change in liquid-to-solid ratio. The mercury emission control technology CCPs leached more Br than the standard CCP with similar leaching values.

Chloride Leaching Results

Chloride leachate concentration plots are shown for the individual CCP samples in Appendix A. The highest concentrations were noted in Sample 1 from Plant 1 and Sample 2 from Plant 2.

A comparison of the chloride leachate concentrations for the samples from Plant 4 indicates minor variations, within error, in the data. The leaching of Cl does not seem to be significantly altered by the application of the mercury emission control technologies. The liquid-to-solid ratio-dependent leaching results generally indicated a dilution factor response to the change in ratio for most of the samples with detectable chloride concentrations.

Figure 6-28 contains the plots for Samples 7–9 from Plant 5, which all show Cl leaching at less than 3 mg/L. Much of the data may be considered within instrumental error, but a subtle trend in the pH-dependent leaching data is noted in Samples 7 and 9, the mercury emission control CCPs. The Sample 9 concentrations decreased from the short-term to long-term 30-day tests.

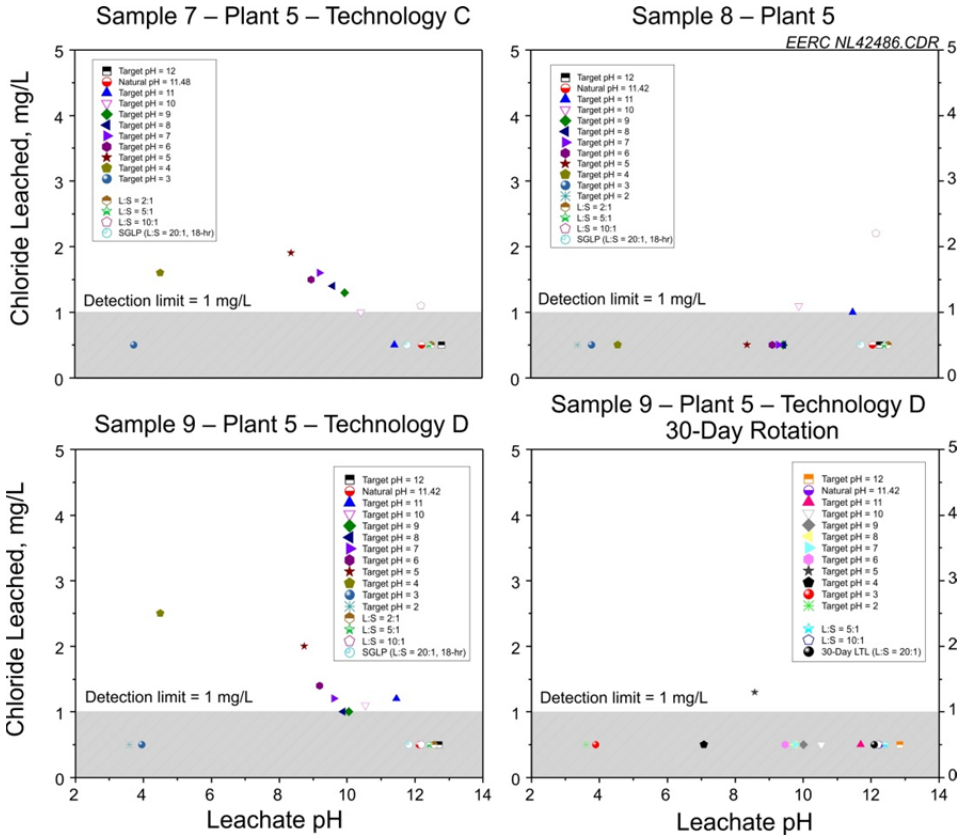

Figure 6-28. Chloride concentrations measured in leachates for standard CCP Sample 8 and mercury emission control demonstration CCP Samples 8 and 9 short-term and 30-day extension (Plant 5).

Fluoride Leaching Results

Fluoride leachate concentration plots are shown for the individual CCP samples in Appendix A. Most F leachate concentrations were above the detection limit and appear more pH-dependent than liquid-to-solid ratio-dependent.

A comparison of the F leachate concentrations for the samples from Plant 4 is provided in Figure 6-29. The standard CCP, Sample 4, results were variable for the pH-dependent leachates while the mercury emission control demonstration CCPs generally showed an oxyanionic species trend of a maximum concentration at a slightly alkaline pH with reduced leaching as the leachate pH increased. As for the liquid-to-solid ratio-dependent leachates, Sample 4 exhibited a muted stepped trend with a change in ratio whereas the leachate fluoride concentration remained relatively unchanged for Samples 5 and 6.

All of the Plant 5 samples generally show an oxyanionic species trend. The target pH 12 and liquid-to-solid ratio-dependent leachates generally showed an increase in concentration with an increase in leachate pH. The F concentrations remained similar between the Sample 9 short-term and long-term leachates.

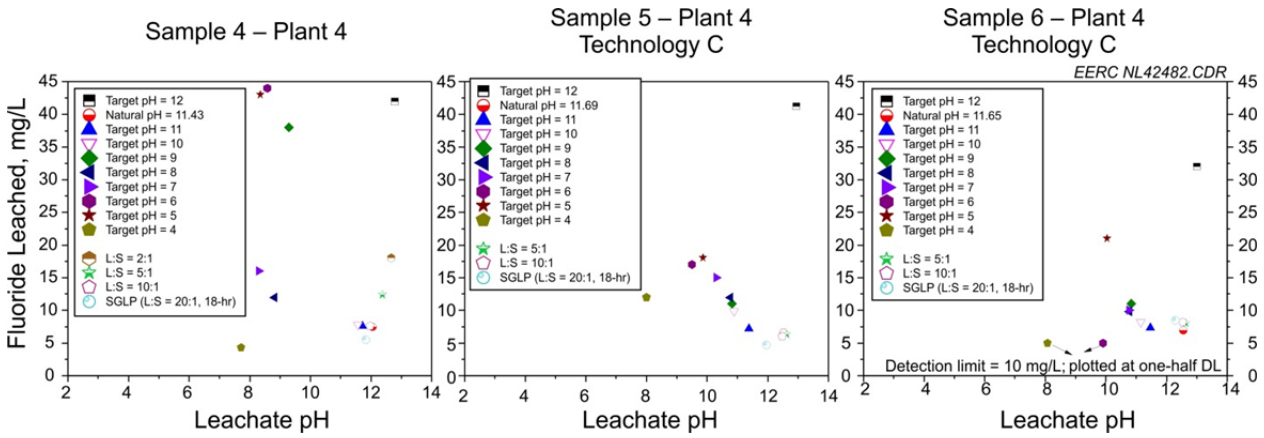

Figure 6-29. Fluoride concentrations measured in leachates for standard CCP Sample 4 and mercury emission control demonstration CCP Samples 5 and 6 (Plant 4).

6.4.5 Observations and Evaluation of Leaching Methods

A limited variety of CCP samples were evaluated with SGLP, with tests from the leaching framework, and with 30-day long-term leaching. The samples were limited to samples in the EERC sample bank that were from mercury emission control technology demonstrations with sufficient quantity to perform the desired chemical characterization and leaching tests. The samples turned out to all be alkaline CCP samples, which do not provide a group of samples representative of the broad range of CCPs produced in the United States. The observations below are based on the experience obtained through evaluating the limited set of CCPs in this study and on no previous experience with the tests within the leaching framework.

Following completion of this study, changes to the leaching framework used in this study have been made. The LeachXS Lite™ expert leaching system software program is available on the Vanderbilt University Web site LEAF pages to assist researchers with the implementation of all of the preliminary LEAF methods. The most notable changes were noted in the pH-dependent parallel leaching method, Preliminary Method 1313 (20) as follows:

- Nine target pH values are in the range of pH 2–13 instead of 11 target pH values in the range of pH 2–12. The natural pH is still included in the list. Instead of targeting each value of 2, 3, 4, etc., the target pH points are ±0.5 pH units of 2.0, 4.0, 5.5, 7.0, 8.0, 9.0, 10.5, 12.0, 13.0 and the natural pH (unless it falls within the range of one of the other targets, in which case the natural pH sample will replace that target pH value).

- The titration pretest method has been altered. Initially, the researcher determines if the solid would be characterized as having low, moderate, or high alkalinity. A five-point extraction test with 10-g samples over a 24–72-hour period, depending on particle size, is performed. This is done using a suggested acid or base schedule based on the alkalinity of the sample, which is expected to cover the pH 2–13 range fairly well. Additional extractions can be performed if a higher resolution of the titration curve is desired in order to determine intermediate acid/base additions. The leachate of any of

these may be used in the pH-dependent testing portion for analysis of analytes if the pH of the leachate falls within any of the target pH values ±0.5 pH units. Otherwise, the leachate is used only for pH determination.

- This is markedly changed from using a 100-g aliquot to determine the natural pH of the sample and adding aliquots of acid or base over 5-min periods with the expectation of calculating acid and base aliquots needed to alter the pH of the sample over a 24–72-hour leaching test.

As it was laid out in the 2002 leaching framework and performed in this study, the titration pretest to determine the acid or base equivalents required to achieve the target pH levels for the pH-dependent leaching was a time-consuming task. For the CCPs evaluated in this effort, the natural pH was generally near 11.5, and the acid additions necessary to lower the pH to near 2 required a full work day with personnel time overlap for a lunch break. In some instances, a full work day was needed to lower the pH to only 3 or 4. In these instances, lowering the pH of the sample closer to 2 was not attempted because it was not known how much additional time would be required and the calculation of acid required in the leaching solution had exceeded to total volume of leaching solution required for the pH-dependent test. The pretest was repeated for some samples to a pH of 4–6 in order to capture the rapid change from pH 9 or 10 to pH 5 or 6.

As pointed out in the pH results, the titration curves generated for the alkaline CCPs in this study portrayed the variability in buffering capacity between samples. The high buffering capacity of alkaline CCPs had been noted in EERC studies and elsewhere in the literature previously (16, 24–26). For the samples with pH-dependent leaching tests performed over the target pH range of 4–12 (explained in the results section), most leachate pH values were within a range of 8–13. This increase in pH over time can also be attributed, at least in part, to the buffering capacity of the CCPs and the formation of secondary hydrated phases. As described earlier, this knowledge of changes in pH over time are a reason that LTL is used with the SGLP for alkaline CCPs. In this study, the leachate pH values were clustered, and the information gained from the leachate results was limited to this narrow range of leachate pH values.

This effort shows that the pH-dependent leaching tests from the leaching framework can provide information over a range of pH values. However, as the methods state, the data must be interpreted in respect to the management of the CCP. For example, a reduction in the pH level of a number of the CCPs in this study may not be encountered in most management scenarios because of the amount of dilute acid required to achieve this in the laboratory. Therefore, the pH-dependent leaching results are only valid if the pH of the CCP is expected to change in the management of the CCP. The SGLP leaching results occasionally added to the trend of data obtained in the liquid-to-solid ratio tests from the leaching framework. The long-term leaching of 30 days performed on Sample 9 in this study and of 30 and 60 days on Samples 1 and 2 in previous studies highlights the need for LTL to determine the evolution of leaching of certain elements in reactive, alkaline CCPs. Although only one additional long-term leaching data point was obtained per test, which did not allow for a true determination of leaching trend requiring three data points, the additional data was used to determine if a dramatic change may occur with time, which cannot be determined by short-term leaching tests alone for reactive CCPs. Long-term leaching of CCPs such as Samples 1–6 may yield different leachate pH values than short-

term leaching and thus different elemental leachate concentrations given the greater pH buffering capacity as compared to Samples 7–10. The changes in leaching over long periods, especially in alkaline CCPs, cannot be ignored. This adds to the interpretations needed for an overall management scenario of a CCP where the CCP may be placed in a monofill with near-neutral-pH rainfall as the only liquid introduced and the water is incorporated within the CCP through hydration reactions. If leachate does occur from the CCP, the leaching conditions are different from that of the fresh CCP in a laboratory setting.

The leaching framework-derived testing performed during this effort was costly. Multiple elements were analyzed in 12–15 leachates per sample, depending on the CCP sample. In order to attempt to gain information on a variety of samples, duplicate leaching was abandoned to work with the available budget. Immediately following completion of this study, it was the opinion of the author that instead of performing all pH-dependent, liquid-to-solid ratio-dependent, and long-term leaching tests for each CCP, it would be beneficial to know the potential management scenario(s) and to assess the pH behavior in slurry and using the titration pretest (maybe in a modified form) to determine a limited number of steps within the tests that may provide the best information with the given budget for analyses. The modifications to the pH-dependent leaching and, particularly, the titration pretest now in Preliminary Method 1313 is seen by the EERC researchers as a marked improvement to the previous version, as it should resolve many pH issues noted in this project.

A 48-hour leaching was used for the leaching framework short-term tests; the SGLP has an 18-hour leaching designation. The leaching framework specified that the leaching duration should be 18 hours for samples with a maximum particle size of 0.3 mm and 48 hours for samples with a maximum particle size of 2.0 mm (2). It is noted in Preliminary Method 1313 that the recommended contact time based on particle size is designed to enhance the approach toward liquid-solid equilibrium (20). The 48-hour period was chosen because determination of the particle size of the samples was not achievable within the available budget and it was used by others in a leachate test comparison study (5). However, the EPA used 24-hour duration for the leaching reported in several reports (6, 21, 27), which is now the suggested leaching time for samples with a maximum particle size of 0.3 mm in Preliminary Method 1313. Since the CCP samples in this study differed from those in the EPA reports, it is unknown if a 24-hour difference in the short-term tests played a role in the leaching of any of the elements. Comparing the SGLP results to the liquid-to-solid ratio-dependent leaching results in this study shows that the answer may depend on the element. In some cases, the elemental concentration was relatively consistent across the various ratios. Other times, the concentration seemed to change with the ratio. And occasionally, it appeared that the concentration of an element from the SGLP test may have been attributed to the leaching time more than to the liquid-to-solid ratio.

As recommended in the leaching framework, 1N KOH was the base used to increase the pH of the CCP samples in this study. Preliminary Method 1313 also recommends the use of KOH unless potassium is an element of interest, in which case NaOH is recommended. However, within the report text of Garrabrants et al. (20), NaOH is recommended as the first choice of base unless sodium is an element of interest. It appears that this is a detail yet to be determined by the method's authors. The result of this study showed that, for Se and S compounds analyzed as sulfate in particular, the use of 1N KOH appeared to have an effect by

showing increased leaching of these elements at higher pH values. This is believed to be a result of delayed ettringite formation. However, as discussed in the introduction, long-term leaching, which may result in an increase in pH, shows a decrease in elements such as Se and S. Studies indicate that potassium hydroxide and sulfur are factors in delayed ettringite formation in concrete (28–30). EERC researchers believe that this must be taken into account when interpreting the leaching framework pH-dependent leaching results when attempting to increase the pH of alkaline CCPs using dilute potassium hydroxide. Dilute sodium hydroxide was not evaluated in this study.

6.4.6 Conclusions

Laboratory experiments included chemical characterization and leaching. The chemical characterization consisted of determining the moisture content, LOI, and total elemental concentrations of the selected constituents. A titration pretest was performed prior to the leaching framework pH-dependent leaching test to determine the amount of acid or base solution needed to alter the natural pH of the CCP over a pH range of 2 to 12. SGLP, pH-dependent parallel leaching, and liquid-to-solid ratio-dependent parallel leaching were performed on all samples. Thirty-day LTL was applied to all tests for one sample.

Results of the laboratory evaluations indicated that:

- The mercury emission control strategies demonstrated in the generation of the samples in this study can alter the total element concentrations of some elements, specifically, arsenic, beryllium, fluoride, lead, manganese, mercury, and selenium. The halogen concentrations are largely dependent on the mercury emission control strategy.

- The generation of titration pretest pH curves was a labor-intensive process that commonly did not accurately predict the leachate pH behavior of the reactive CCPs in this study. The modified method in Preliminary Method 1313 should help with this problem.

- Many of the elements leached less than 5% of the total amount in the CCP. Several elements were not detected in any of the leaching tests performed on individual CCPs.

- The greatest percentage of Cd, Cr, and Mn leached occurred in the pH range of 3–7 for some CCP samples.

- Up to 60% of the total Se and S (measured as sulfate in the leachates) leached from the CCPs. The highest percentage of Se or S leached occurred in the pH range of 8–9 in the SGLP leachate (where the liquid-to-solid ratio contributed to the percent of total), or in the target pH = 12 test (which used 1N KOH in the leaching solution).

- The most consistent change in leaching between the standard CCPs and the mercury emission control demonstration CCPs was for S as sulfate. Over all pH levels there was generally a significantly lower percentage of S as sulfate leached from the mercury emission control demonstration CCPs than the standard CCPs, of up to 50%.

- Long-term leaching was evaluated for all tests in Sample 9. The percentage of As, Cd, Cr, Se, and S as sulfate leached generally decreased at leachate pH levels above 11 or 12 by up to 20% and 30% for Se and S as sulfate. The percentage for all elements of change was small and did not significantly increase or decrease at pH levels below 11 or 12.

- The use of 1N KOH in the leaching solution appears to potentially inhibit ettringite formation in these reactive CCPs, even at a short leaching duration of 48 hours.

- This effort shows that the pH-dependent leaching tests from the leaching framework can provide information over a range of pH values. However, the data must be interpreted in respect to the management of the CCP.

- LTL of reactive, alkaline CCPs is essential in determining the evolution of leaching of certain elements in certain management scenarios.

- The leaching framework-derived testing performed during this effort was costly. When determining which leaching tests to perform, it would be beneficial to know the potential management scenario(s) and to assess the pH behavior in slurry and use the titration pretest (maybe in a modified form) to determine a limited number of steps within the tests that may provide the best information with the given budget for analyses.

The approach to the pH-dependent leaching in Preliminary Method 1313 appears to be an improvement on the leaching framework method. The EERC researchers would like to evaluate high pH-buffering capacity alkaline CCPs, such as Samples 1–6 in this study, using the new method to determine the effect on pH. An aspect of interest would be a determination of the amount of acid required to reduce the pH of these materials to 2. That would determine if leachate pH values below those measured in the current study are achievable, which would be extreme management conditions for those samples.

6.4.7 References

1. Hassett, D.J. The Synthetic Groundwater Leaching Procedure. In *Encyclopedia of Environmental Analysis and Remediation*; Meyers, R.A., Ed.; John Wiley and Sons, 1998; pp 4797–4803.

2. Kosson, D.S.; van der Sloot, H.A.; Sanchez, F.; Garrabrants, A.C. An Integrated Framework for Evaluating Leaching in Waste Management and Utilization of Secondary Materials. *Environ. Eng. Sci*. **2002**, *19* (3), 159–203.

3. Kim, A.G. CCB Leaching Summary: Survey of Methods and Results, In *Proceedings of Coal Combustion By-Products and Western Coal Mines: A Technical Interactive Forum*. Denver Marriott West Hotel, Golden, CO, April 16–18, 2002, Vories, K.C.;Throgmorton, D., Eds.; sponsored by U.S. Department of the Interior Office of Surface Mining, U.S.

Department of Energy National Energy Technology Center, and Coal Research Center, Southern Illinois University at Carbondale; 2002; pp 179–195.

4. Zandi, M.; Russell, N.V. Design of a Leaching Test Framework for Coal Fly Ash Accounting for Environmental Conditions. *Environ. Monit. Assess*. **2007**, *131*, 509–526.

5. Kim, A.G.; Hesbach, P. Composition of Fly Ash Leaching Methods. *Fuel* **2009**, *88*, 926–937.

6. Sanchez, F.; Keeney, R.; Kosson, D.; Delapp, R. *Characterization of Mercury-Enriched Coal Combustion Residues from Electric Utilities Using Enhanced Sorbents for Mercury Control*; U.S. Environmental Protection Agency EPA-600/R-06/008, Feb 2006.

7. Hassett, D.J. A Generic Test of Leachability: The Synthetic Groundwater Leaching Procedure. In *Proceedings of the Waste Management for the Energy Industries Conference;* University of North Dakota, April 29 – May 1, 1987; pp 31–39.

8. Hassett, D.J. *Evaluation of Leaching Potential of Solid Coal Combustion Wastes*; Final Report for Indiana Coal Council; Energy & Environmental Research Center: Grand Forks, ND, 1991.

9. Hassett, D.J. Scientifically Valid Leaching of Coal Conversion Solid Residues to Predict Environmental Impact. In *Proceedings of the Trace Element Transformations in Coal-Fired Power Systems Workshop;* Scottsdale, AZ, April 19–22, 1993; *Special Issue of Fuel Process. Technol*. **1994**, *39* (1–3), 445–459.

10. Hassett, D.J.; Pflughoeft-Hassett, D.F.; Heebink, L.V. Leaching of CCBs: Observations from over 25 Years of Research. *Fuel* **2005**, *84*, 1378–1383.

11. Hassett, D.J.; McCarthy, G.J.; Henke, K.R.; Korynta, E.D. Characterization of a Lignite Ash from the METC Gasifier III: Correlations with Leaching Behavior and Mineralogy. In *Fly Ash and Coal Conversion By-Products: Characterization, Utilization, and Disposal I;* McCarthy G.J.; Lauf, R.J., Eds.; Materials Research Society: Pittsburgh, PA, 1985.

12. Hassett, D.J.; Pflughoeft-Hassett, D.F.; McCarthy, G.J. Ettringite Formation in Coal Ash as a Mechanism for Stabilization of Hazardous Trace Elements. In *Stabilization and Aquatic Uses, Proceedings of the 9th International Ash Use Symposium*; Orlando, FL, Jan. 22–25, 1991; EPRI Report GS-7162, Project 3176, 1991; Vol. 2, pp 31–1 to 31–17.

13. Hassett, D.J.; Thompson, J.S. *Ettringite Formation as a Fixation Technology for Immobilizing Trace Elements;* Final Report to GRI; GRI-96/0322. Feb 1997, 41.

14. McCarthy, G.J.; Hassett, D.J.; Bender, J.A. Synthesis, Crystal Chemistry and Stability of Ettringite, a Material with Potential Applications in Hazardous Waste Immobilization. In *Proceedings of the Materials Research Society Symposium;* 1992; Vol. 245.

15. Heebink, L.V.; Pflughoeft-Hassett, D.F; Hassett, D.J. Effects of Mercury Emission Control Technologies Using Halogens on Coal Combustion Product Chemical Properties. *J. Environ. Monit*. **2010**, *12*, 608–613.

16. Hassett, D.J.; Heebink, L.V.; Pflughoeft-Hassett, D.F.; Buckley, T.D.; Zacher, E.J.; Xin, M.; Gustin, M.S.; Jung, R. *Mercury and Air Toxic Element Impacts of Coal Combustion By-Product Disposal and Utilization*; Final Report (Jan 23, 2003 – Dec 31, 2006) for U.S. Department of Energy National Energy Technology Laboratory Cooperative Agreement No. DE-FC26-02NT41727, North Dakota Industrial Commission Agreement No. FY03-XLVIII-117, Duke Energy, Great River Energy, Utility Solid Waste Activities Group, and Electric Power Research Institute; EERC Publication 2007-EERC-10-03; Energy & Environmental Research Center: Grand Forks, ND, Oct 2007.

17. McCarthy, G.J.; Butler, R.D.; Brekke, D.W.; Adamek, S.D.; Parks, J.A.; Foster, H.J.; Solc, J. Mineralogical Transformations and Microstructure after Disposal of Cementitious Advanced Coal Technology By-Products. In *Materials Research Society Proceedings;* **1995** Vol. 370, p 179–190.

18. McCarthy, G.J.; Butler, R.D.; Grier, D.G.; Adamek, Parks, J.A.; Foster, H.J. Long-Term Stability of Landfilled Coal Combustion By-Products. *Fuel* **1997**, *76* (8), 697–703.

19. Thorneloe, S.A.; Kosson, D.; Helms, G.; Garrabrants, A.C. Improved Leaching Test Methods for Environmental Assessment of Coal Ash and Recycled Materials Used in Construction. In *Proceedings of Sardinia 2009, Twelfth International Waste Management and Landfill Symposium*; S. Margherita di Pula, Cagliari, Italy, Oct 5–9, 2009.

20. Garrabrants, A.C.; Kosson, D.S.; van der Sloot, H.A.; Sanchez, F.; Hjelmar, O. *Background Information for the Leaching Environmental Assessment Framework (LEAF) Test Methods*; U.S. Environmental Protection Agency, Nov 2010, EPA-600/R-10/170.

21. Kosson, D.; Sanchez, F.; Kariher, P.; Turner, L.H.; Delapp, R.; Seignette, P. *Characterization of Coal Combustion Residues from Electric Utilities – Leaching and Characterization Data;* U.S. Environmental Protection Agency EPA-600/R-09/151, Dec 2009.

22. Hazardous and Solid Waste Management System; Identification and Listing of Special Wastes; Disposal of Coal Combustion Residuals from Electric Utilities; Proposed Rule. *Fed. Regist*. **2010**, *75* (118), 35128–35264.

23. Electric Power Research Institute. *Status of Mercury Control Technologies: Activated Carbon Injection and Boiler Chemical Additives*; Palo Alto, CA; 2006; 1010349.

24. Ward, C.R.; French, D.; Riley, K.; Li, Z.; Stephenson, L. Variation in Element Mobility from Fly Ashes Stored in Different Environments. In *Proceedings of the 2009 World of Coal Ash (WOCA) Conference*; Lexington, KY, May 4–7, 2009.

25. Kukier, U.; Ishak, C.F.; Sumner, M.E.; Miller, W.P. Composition and Element Solubility of Magnetic and Non-Magnetic Fly Ash Fractions. *Environmental Pollution* **2003**, *123*, 255–266.

26. Karapanagioti, H.K.; Atalay, AS. Laboratory Evaluation of Ash Materials as Acid-Disturbed Land Amendments. *Global NEST: the International Journal* **2001**, *3*, 11–21.

27. Sanchez, F.; Kosson, D.; Keeney, R.; Delapp, R.; Turner, L.; Kariher, P. *Characterization of Coal Combustion Residues from Electric Utilities Using Wet Scrubbers for Multi-Pollutant Control*; U.S. Environmental Protection Agency, July 2008, EPA-600/R-08/077.

28. Sahu, S.; Thaulow, N. Delayed Ettringite Formation in Swedish Concrete Railroad Ties. *Cement and Concrete Research* **2004**, *34* (9), 1675–1681.

29. Macías, A.; Goñi, S. Acid Attack on High-Alkali Cement Paste: Another Cause for Delayed Ettringite Formation. *J. Am. Ceram. Soc*. **1998**, *81* (11), 2894–2900.

30. Diamond, S. The Relevance of Laboratory Studies on Delayed Ettringite Formation to DEF in Field Concretes. *Cement and Concrete Research* **2000**, *30* (12), 1987–1991.

7.0 FATE OF MERCURY AND TRACE ELEMENTS IN THE ENVIRONMENT

7.1 Activity Objectives

The goals of the proposed research under this activity were to:

- Examine the chemical and physiological relationships between organic and inorganic Hg with organic/inorganic forms of Selenium (Se) and sulfur and evaluate kinetic, thermodynamic, and physiological effects on their binding behaviors.

- Determine the influence of Se on Hg bioavailability/bioaccumulation in freshwater fish, and evaluate correlations between their respective concentrations and other factors.

- Examine and establish Selenium-Health Benefit Values (SeHBV's) that correlate risks of Hg exposure vs. benefits from Se intake associated with fish consumption.

7.2 Experimental Methods

7.2.1 Molecular Basis of Mercury–Selenium Binding Interactions

Methylmercury (MeHg) is an irreversible inhibitor of Se-dependent enzymes (1). Inorganic Hg's affinity for inorganic Se is a million times greater than its affinity for inorganic sulfur, and similar relationships are expected to be observed for their organic forms. The chalcogen amino acid forms are molecularly identical (see Figure 7-1) other than having oxygen, sulfur, or Se moieties covalently bound to the β–carbon of their respective side chains. The influence of these side chains on their binding behaviors are significant. As indicated by the pK_a's (See footnote) shown in Figure 7-1, the hydroxyl of serine (Ser) and the thiol of cysteine (Cys) are mostly uncharged because they are predominantly protonated at intracellular physiological pH (7.4).

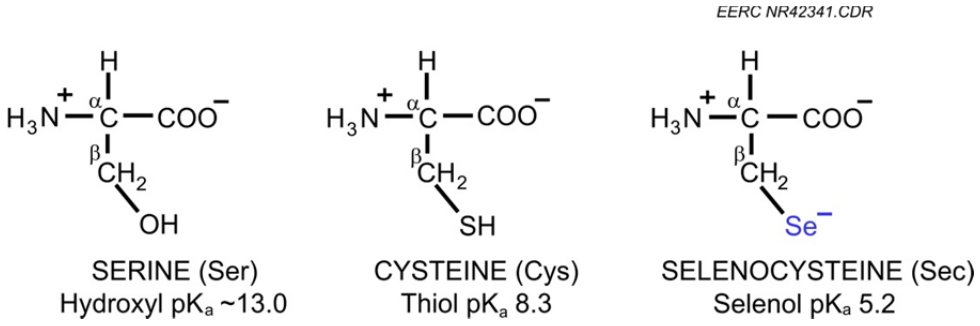

Figure 7-1. The chalcogen amino acid series.

Footnote: The pK_a of a molecule is the negative $\log_{10}$ of it's acid dissociation constant (K_a). In simple terms, it defines the pH where protons in association with the molecule are at equilibrium

with those free in solution. At physiological pH (~7.4), serine would be completely protonated, but selenocysteine would be almost completely ionized as shown in Figure 7-1.

The amino acids shown in Figure 7-1 are depicted in their zwitterionic forms, but in proteins and peptides, the charge at the amino terminus will be neutralized by the peptide bond. In natural peptides and proteins, Ser and Cys occur at various locations within the linear sequence of amino acid residues. In contrast, most selenoproteins other than selenoprotein P (which contains 10 Sec residues) generally express Sec exclusively at the carboxyl terminus of that comprise the protein/peptide.

The binding affinities of inorganic and organic Hg for these chalcogens are in the rank order oxygen<<<sulfur<<selenium. The differences between the Hg binding affinities of sulfur and Se appear to be sufficient to ensure that the reactions that form insoluble HgSe products will be unidirectional. Based on these considerations, thermodynamic, kinetic, and physiological influences of MeHg exposures on selenoenzyme activity and synthesis have been evaluated.

7.2.2 Selenium Influences on Mercury Bioaccumulation in Freshwater Fish

Previous work leading to this study had been performed in collaboration with Dr. Spencer Peterson (U.S.E.P.A.; retired). Although that work had examined the Hg:Se molar ratios in fish collected from across the Western U.S. (Peterson et al., 2009a; 2009b), it had not examined the effects of environmental Se on bioaccumulation of Hg in fish. This study continued that collaboration and also included Dr. Bruce Monson of the Minnesota Pollution Control Agency (MPCA). Fish samples from lakes in various regions of Minnesota that have already been analyzed for Hg contents by the MPCA were selected for Se analysis in this study. Lakes from areas of Minnesota expected to have notable distinctions in Se contents were identified and samples were shipped from the MPCA to the EERC. Using the previously acquired data for Hg contents in northern pike from Minnesota lakes and Se analyses performed on the same fish, relationships between Se and MeHg bioaccumulation has been assessed.

The soils of igneous origin that predominate in northern Minnesota are known to generally be lower in Se than soils from central and southern Minnesota which have greater proportions of Se-rich sedimentary parent materials. Since Se leaching from soils is the source of the Se in lake ecosystems, the hypothesis of this project is that the Se present in lakes, rivers, and streams decreases the amount of MeHg that bioaccumulates in fish from those aquatic ecosystems and diminishes the risk of toxicity associated with MeHg exposure from consuming those fish.

Homogenized northern pike fillet samples that had previously been analyzed for Hg contents were obtained from Dr. Bruce Monson of the MPCA. Aliquots of each sample (~5 g) were placed in prelabeled and preweighed trace metal-free plastic bags and lyophilized for 3 days until the samples had reached constant weights. The dry weights of the fish fillet samples averaged 20% ± 1% of their initial wet weights. No statistically significant differences between the groups were observed. Dry fish samples were crushed in the bag and mixed to homogenize before removing representative samples (~0.100 g) that were weighed into single-use, trace element-free, 50-mL digestion tubes (Environmental Express, Mount Pleasant, South Carolina). Every tenth sample was prepared in duplicate. Elemental spike recovery samples were analyzed

as part of each digestion batch. Each digestion/analysis batch also included blanks and certified reference materials (dogfish muscle certified reference material DORM-2, National Research Council of Canada, Ottawa, Ontario, Canada).

Samples were treated with 5 mL of HNO_3 (Fisher trace metal-grade, Fisher Scientific, www.fishersci.com) and heated at 85°C in deep cell hot blocks (Environmental Express) for 24 hours in capped tubes to preserve samples from trace element contamination. Samples were cooled, 1.5 mL of 30% H_2O_2 (Fisher Certified A.C.S., Fisher Scientific) was added, and samples were recapped and returned to heating in the dry block at 85°C for 8 hours. Samples were cooled once more, and 15 mL of 12N HCl (Fisher trace metal-grade) was added. Samples were heated at 90°C for 90 minutes to reduce Se(VI) to Se(IV) prior to analysis. Samples were cooled and diluted to 50 mL with double-distilled water. Samples were diluted as needed to bring their concentrations into instrumental calibration ranges and analyzed for Se contents by hydride generation atomic fluorescence spectroscopy using a P S Analytical Dual Millennium Excalibur (P S Analytical, Deerfield Beach, Florida). Before data from sample analysis runs were entered into the database, Se concentrations in sample digestion blanks were subtracted, and elemental recoveries in samples of certified reference materials were evaluated to qualify the analysis batch data as acceptable for inclusion.

In preparation for the study of northern pike Se effects on Hg bioaccumulation in lake fish, a broader evaluation of various types of fish from rivers and streams across the western United States was performed. Fish of various feeding guilds: piscivores (predators), herbivores/detritivores (primarily plant and bottom feeding), and insectivores (all fish consume insects during early life stages, but these species remain primary insect consumers throughout their life cycle). Based on prior research, the expectation of this study was that Hg bioaccumulation in piscivores would be inversely related to Se availability, but that the other two feeding guilds would not be influenced by environmental Se.

This task also assessed data from primary sources and publications that reported the concentrations of Hg and Se in studies of mammals, waterfowl, and invertebrates that participate in aquatic food webs. In all cases, data for Hg and Se were converted to a molar basis and compared to assess actual Hg risks. Environmental risk assessments based on observed Hg:Se molar ratio values were compared with risk assessments based on Hg concentrations alone and prepared in articles for publication in scientific journals.

7.3 Results and Discussions

7.3.1 Biochemical and Thermodynamics of the Hg–Se Reaction

Previous investigations of MeHg toxicity have assumed pseudo-first order reaction kinetics were involved in MeHg binding to thiol ligands that occur in saturating concentrations and could thus be considered as essentially constant. Since intracellular concentration of thiol ligands far exceed that of MeHg, a pseudo-first order approximation is valid for those reactions. However, now that the molecular mechanism of MeHg is known to involve irreversible inhibition of Se-dependent brain enzymes (selenoenzymes) that are required to prevent and reverse oxidative damage, the validity of the first-order approximation in estimations of MeHg toxicity must be

reconsidered. Because the intracellular concentrations of Se and its biologically active form Sec are ~5 orders of magnitude lower than intracellular thiols, high MeHg exposures can result in MeHg accumulating in intracellular concentrations that equal (~1 μM) or exceed those of Sec.

Therefore, for risk assessment evaluations, pseudo-first order approximations will not be uniformly appropriate. Furthermore, since incidence of MeHg toxicity is known to be inversely related to dietary Se status, it is clear that risks related to MeHg exposures will vary nonlinearly in relation to intracellular MeHg:Sec molar stoichiometries in the vulnerable target tissues such as the brain. The intracellular concentration of Se present in the brain and endocrine tissues are homeostatically controlled and are, therefore, maintained at levels close to optimal physiological concentrations. However, the total body reservoir of Se in kidney, liver, muscle, and other body tissues can vary dramatically in direct proportion to dietary Se intakes.

The MeHg that is present in fish meat is primarily bound to the thiol of Cys. This form (MeHg-Cys) is digestively absorbed and enters the cells of the body as a molecular mimic of methionine. The MeHg-Cys conjugate resembles the amino acid methionine on a molecular level (similar size and charge distributions) that may enter the cell's biochemical pathways of protein synthesis and undergo repeated cycles of insertion into cellular proteins in place of methionine. However, MeHg does not remain in association with the thiol of any one Cys molecule for long. It readily exchanges its current thiol-conjugate to form a similar partnership with a different thiol or a stronger bond with a selenol partner. It does not appear that molecular mimicry is associated with any pathological consequences itself, but understanding the kinetics, thermodynamics, and biochemistry of the formation of Hg–Se bonds eliminates mysteries regarding MeHg toxicity.

In brief, the mysteries about MeHg toxicity that become readily understandable when considered in relation to Se physiology include all the unique features of MeHg and its toxicity:

- The long residence of MeHg in tissues.
- The distribution of MeHg from blood into the hair, skin, and nails of exposed subjects.
- The extended latency period between toxic exposures and the appearance of symptoms.
- The specific tissues afflicted by MeHg toxicity.
- The nature of the biochemical consequences of toxicity.
- The Se-dependent protective effect against onset of toxicity.

Blood MeHg concentrations are typically reflective of recent exposures while the ~250-fold higher concentrations present in hair (similar relationships exist for nails and skin) reflect the long-term deposition of MeHg-Cys being inserted into keratin. A major pathway of MeHg elimination from the body occurs through its deposition into the keratin of hair, skin, and nails which effectively remove it from any further participation in physiological cycles in the body. Keratin comprises 85% of the cellular protein of epidermal skin cells, 65%–95% of the total hair fiber, and similar proportions of nail protein. Because Cys is the most abundant amino

acid in keratin (~18% of the total amino acids), the sulfur content of these tissues is remarkably high. For example, hair composition is ~5% sulfur by weight. The abundance of Cys in keratin enables formation of intra- and intermolecular disulfide bonds between keratin molecules that provide resilient tensile strength in flexible bundles of these molecules. Since no selenoproteins are encoded in keratin, the amount of selenium that is present in hair may represent nonspecific incorporation of selenomethionine in place of methionine. Since the methyl group would prevent approach and binding of MeHg, it is unlikely that selenium status would influence hair Hg.

Once MeHg-Cys in proteins of the blood supply enters the cells of tissues forming skin, hair, or nails, redistribution of MeHg to the abundant Cys moieties of newly synthesized keratin proteins will naturally proceed as a result of mass action. Therefore, the shedding of MeHg through these keratin-rich compartments is a fortuitous, but highly effective, means of removing MeHg from the body. In tissues, the distributions of MeHg resemble those of methionine. Since MeHg's association with these thiols are unregulated, high dietary MeHg intakes result in rapid increases in intracellular concentrations of MeHg-Cys in association with cellular proteins.

At the low nM blood levels typically present in regular seafood consumers, there is little likelihood of MeHg causing any serious interference with selenoenzyme synthesis and activities, particularly in adults. However, since fetal brain formation is far more sensitive to maternal MeHg exposures, there remains a need for further research to increase understanding of no observed adverse effect levels (NOAEL) and lowest observed adverse effect levels (LOAEL) in relation to current understanding of the Hg–Se interaction.

Catastrophic poisoning episodes involve MeHg exposures that cause blood and tissue Hg concentrations to rise to levels that approach/exceed normal intracellular Se concentrations (~1 μM). When MeHg rises to such high levels, a proper description of the kinetics of the reaction between MeHg and Sec requires that knowledge of both MeHg and Se be applied using bimolecular rate law equations. The derivation of the required equations is presented below, and the biochemical parameters that will need to be determined experimentally for validation purposes are described in the next section.

Consider the following bimolecular reaction:

$$\mathrm{MeHg} + \mathrm{Sec} \rightarrow \mathrm{MeHgSec} \quad [1]$$

The rate of Reaction 1 can be written as:

$$rate = -\frac{d[\mathrm{MeHg}]}{dt} = -\frac{d[\mathrm{Sec}]}{dt} = \frac{d[\mathrm{MeHgSec}]}{dt} \quad [2]$$

The rate law for Reaction 1 is given by:

$$rate = k[\mathrm{MeHg}]^x[\mathrm{Sec}]^y \quad [3]$$

Where k is the rate constant (mol^{-1} s^{-1}), [MeHg] is the concentration of MeHg (mol/L), [Sec] is the concentration of Sec (mol/L), x is the reaction order with respect to MeHg, and y is the reaction order with respect to Sec.

The overall order of Reaction 1 is obtained by summing x and y. Experimentally, the overall rate of reaction can be determined by monitoring the change in any of the reactants or product with time as given in Equation 2. In addition, the amount of unbound MeHg and "free" Se left in the system at any given time in the experiment is also measured. Equation 3 thus contains three unknown parameters: *k*, *x,* and *y*, which can be obtained using the experimentally determined data by using multiple linear regression methods.

The linearized Equation 3 is given by:

$$\mathrm{Ln}(rate) = \mathrm{Ln}(k) + x\mathrm{Ln}([\mathrm{MeHg}]) + y\mathrm{Ln}([\mathrm{Sec}]). \quad [4]$$

By using Equation 3, derived from Reaction 1, to describe the kinetics of MeHg's reaction with Sec three main scenarios of the reaction can be captured as shown in Figure 7-2.

Scenario 1: Low MeHg Exposures (large intracellular excess of Sec over MeHg)

Under normal circumstances, the intracellular concentration of Sec is in large excess relative to traces of MeHg that are present due to typically low exposures arising from fish consumption. In these circumstances, Reaction 1 will be pseudo-first order in relation to MeHg concentration, with *y* expected to have a value of 1.0 (similar to what obtains when MeHg reacts with thiol ligands). Therefore, Equation 2 reduces to:

$$rate = k[\mathrm{MeHg}] \quad [5]$$

and *k* and *y* can be determined by linear regression analysis.

Scenario 2: Toxic MeHg Exposures (MeHg present in ~ equimolar stoichiometry with Sec)

As MeHg exposures cause intracellular concentrations to rise to levels that approach or exceed equimolar stoichiometries, toxic effects (loss of selenoenzyme activities) become increasingly apparent in a dose- and time-dependent fashion. However, it is important to note that Se is abundant in ocean fish, the predominant source of MeHg exposure. Therefore, increasing MeHg exposures are typically accompanied by increasing dietary Se intakes. Since the varieties of ocean fish that are typically consumed tend to contain far more Se than MeHg, the only scenarios where MeHg exposures result in intracellular MeHg:Sec molar ratios that approach or exceed 1:1 will, of necessity, involve consumption of foods with MeHg in molar excess of Se.

In MeHg exposures where the concentrations of MeHg and Sec are similar, bimolecular reaction rates are required to adequately describe the dependence of the concentrations of MeHg and/or Sec on the toxicity outcomes. In this case (reverting to Equation 3), the values of x and y in the exponents of Equation 3 approach and eventually reach 1.

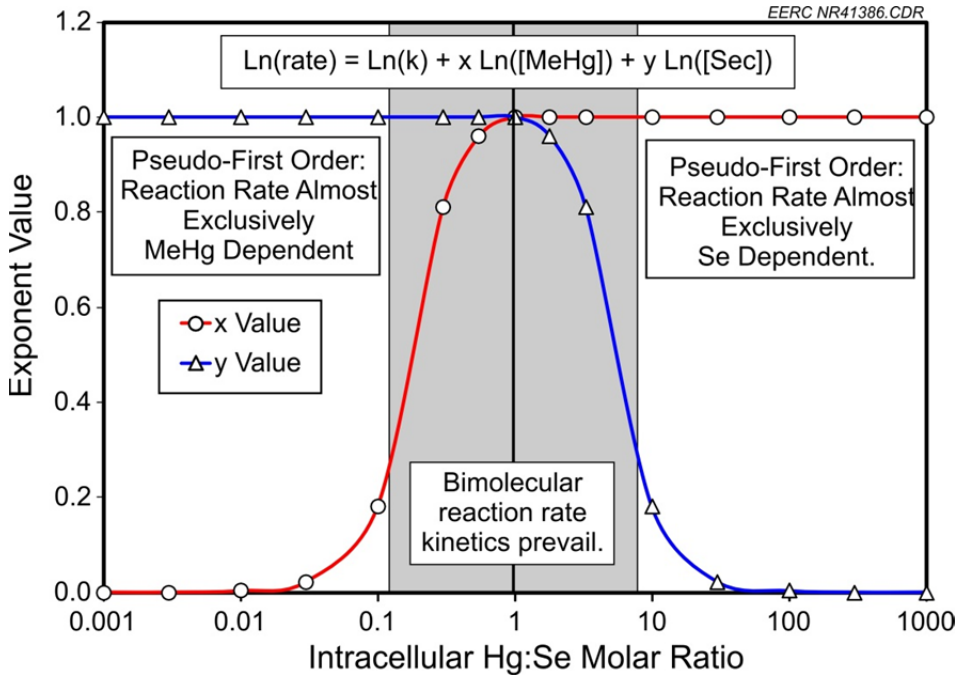

Figure 7-2. Depiction of approximated relationships between molar stoichiometries of reactants and the values of x and y exponents in reaction rate equations.

Scenario 3: Severely Toxic MeHg Exposures (molar excess of MeHg over Sec)

When the concentration of MeHg is present in large excess compared to that of Sec, the value of *x* in Equation 3 is extremely small and approaches zero. Hence, Reaction 1 becomes a pseudo-first order reaction, and Equation 3 becomes:

$$rate = k[\text{Sec}] \quad [6]$$

To verify this experimentally, Equation 6 can be parameterized as:

$$rate = k[\text{Sec}]^{y} \quad [7]$$

and *k* and *y* can then be determined by linear regression analysis.

Since toxic MeHg concentrations are saturating, the value of *y* would have a value of 1.0. Equation 7 can be experimentally verified following the same procedures as outlined above. Until linear regression analyses have been performed, we can only approximate the relationships between MeHg:Sec molar ratios and the values of the x and y exponents. Although convenient for purposes of calculation and discussion, the 1:1 molar ratio shown in Figures 7-1 and 7-2 does not necessarily define any "bright line" related to risk. Although adults are known to be relatively resistant to adverse effects of MeHg exposures and appear capable of surviving high MeHg exposures that undoubtedly go well beyond the 1:1 molar ratio, maternal exposures that are well below 1:1 may result in observable harms to their unborn offspring. To capture these

factors, it is clear that MeHg becomes increasingly toxic as molar ratios approach, and especially as they exceed, the 1:1 molar ratio.

7.3.2 Molecular Mechanisms of Mercury Toxicity

Based on the mutually confirmatory study results of CATM scientists and the findings of research groups from around the world, five biochemical reactions between MeHg and Se contribute to MeHg toxicity that may account for the entire spectrum of pathological effects that occur as a consequence of toxic MeHg exposures. These mechanisms involve both direct effects and indirect outcomes that cause secondary effects or arise as a direct consequence of inhibition of Se dependent enzymes by MeHg binding to intracellular Se.

Synergies of Sequestration (SOS 1)

Enzymes possess substrate binding sites that capture and orient substrate molecules that will be introduced into their active sites. This accelerates their reaction rates and is a major factor in how they catalyze reactions. The selenoenzymes whose function it is to reduce thiols such as those present in thiomolecules are designed to bring the thiol (-SH) moieties into direct proximity with the Se of the Sec of the enzyme active sites. The standard brief nomenclature for glutathione is GSH, which provides an indication of the importance of the molecule's SH group. Although the standard notation for thioredoxin has conventionally been Trx, we will use $T(SH)_2$ as a notation that permits depiction of MeHg association with the two vicinal thiols of the molecule. This also emphasizes the parallels between the chemistry of GSH and $T(SH)_2$. When GSH becomes oxidized, it forms a disulfide between two GSH molecules depicted as GS–SG. In the case of $T(SH)_2$, the vicinal thiols of the molecule form an intramolecular disulfide that can be depicted as TS–S to emphasize the similarity between its chemistry and that of GSH.

MeHg (alternatively termed $HgCH_3$ or CH_3Hg for convenience in certain examples in the following descriptions) readily exchanges its molecular associations from the sulfur of the thiol of the Cys that is its predominant form in fish meat, to the abundant GSH peptide (~5 mM) or $T(SH)_2$ protein (~1 μM) present in cells of the piscivores that consume the fish. These "poisoned substrate" products (GS-$HgCH_3$ and TS-$HgCH_3$) appear likely to specifically inhibit selenoenzymes at rates far greater than otherwise expected. This expectation arises because these MeHg-loaded substrates are directly introduced into the selenoenzymes in the correct orientation to bring the Hg of the MeHg-Cys substrate into close proximity with the Se of the active Sec of their catalytic sites. This biochemical mechanism of expedited MeHg exposure enzyme could synergistically accentuate SOS-1 binding. This mechanism could potentially accelerate the rate of SOS-1 inhibition of Se-dependent enzymes such as thioredoxin reductase (TRxR1) and glutathione peroxidase (GPx) by many log orders since, as suggested by their names, these enzymes are highly interactive with TSH and GSH peptides. Therefore:

- MeHg bound to cysteine thiols in the meat of fish that are consumed will transfer to cysteine thiols of glutathione and thioredoxin within the cells of the consumer.

- As these thiomolecules are acted upon by the selenoenzymes that cycle through them to exchange reducing equivalents, they enter the selenoenzyme in an orientation that brings them into direct contact with Se of the selenocysteine at the enzyme active site.

- Because of high throughputs of glutathione and thioredoxin through selenoenzymes, MeHg transfer from the thiols of these molecules to the selenols of the enzymes will be log orders greater than would be predicted if MeHg encounters with selenoenzyme were diffusion-mediated.

Silencing of Selenoenzymes (SOS 2)

The vulnerability of selenoenzymes to MeHg was first proposed by Ganther et al. (4, 5) and was subsequently demonstrated by Prohaska et al. (6). This mechanism has been increasingly well characterized through the work of Seppanen et al. (6) and Carvalho et al. (1). Consistent with expectations based on this molecular mechanism, Ralston and Raymond (8) showed that supplemental Se was highly effective in preventing interruption of selenoenzyme activities in brain cell lines. These results correspond with the findings of in vivo studies of Watanabe (9, 10) and Stringari et al. (11) that selenoenzyme activities of the fetal brain are extremely vulnerable to high maternal MeHg exposures but protected by increasing maternal Se status. The neurological consequences of high MeHg exposures are consistently associated with the intracellular Hg:Se ratios in brain tissues of exposed animals and humans (12):

- MeHg inhibition of cellular selenoenzymes such as thioredoxin reductase occurs with remarkably high specificity, with an IC_{50} of ~10 nM (1).

- Contrary to earlier assumptions made by toxicologists unfamiliar with Se physiology, MeHg does not generate reactive oxygen species (ROS) (7) through first-order or pseudo-first-order chemical reactions. Instead, MeHg acts through a bimolecular reaction (see above) to selectively inhibit selenoenzymes that normally prevent formation of ROS and reverse oxidative damage to proteins and lipids.

- MeHg-dependent inhibition of glutathione peroxidase in fetal brain and placenta (9, 10) and thioredoxin reductase in cell culture studies (1) is inversely related to Se status (8).

Sequestration of Selenium (SOS 3)

Since the Hg–Se binding product mercury selenide (HgSe) is particularly stable, it is unlikely to degrade through any natural processes other than heating to decomposition temperatures (>300°C). The results of numerous animal studies (e.g., Dietz et al. [13], Huggins et al. [14]) demonstrate that as tissue Hg levels approach a 1:1 stoichiometry with Se, the Se contents of tissues such as brain and endocrine tissues tend to increase to maintain a consistent amount of free Se to support selenoenzyme activities. That the Hg is directly bound to Se has been proven by repeated studies in animals (e.g., Huggins et al. [14]) and recently confirmed in humans (Korbas et al. [12]). The following points are important considerations regarding this molecular mechanism:

- Mercury affinities for Se molecules are ~10^6 times higher than those of analogous sulfur molecules (Dyrssen and Wedborg [15]).

- Selenium physiology results in continuous cycles that involve formation of selenide, the molecule with the highest known Hg affinity. Sulfur has no parallel metabolic cycle that results in formation of sulfide, the next highest affinity Hg binding partner.

- Formation and accumulation of HgSe has been repeatedly demonstrated in brain tissues of seals (Dietz et al. [13]), beluga whales (Dietz et al. [13], Ralston et al., in preparation), and humans (Korbas et al. [12], Huggins and Ralston, unpublished).

- Brains of Hg miners (Huggins and Ralston, unpublished) and people exposed to toxic amounts of Hg (Korbas et al. [12]) show high accumulations of HgSe, a highly stable form that sequesters both elements, but prevents Se from participating in any further aspects of Se-dependent metabolic functions.

- High MeHg exposures induce a severe deficiency of biologically available Se, particularly in brain tissues (Ralston et al. [16, 17]). Although tissue Se levels are not necessarily reduced, Se bound in HgSe is essentially permanently retired in this insoluble, highly unavailable form.

Suicide of Selenium-Deprived Cells (SOS 4)

Although the levels of Se-deprivation in brain and endocrine tissues that occur as a consequence of high MeHg exposures are unlikely to be paralleled by any other environmental challenge, development of an apoptotic mechanism for controlling growth of these tissues during dietary shortfall is entirely consistent with expectations based on evolutionary theory. Growth of brain or endocrine tissues in the absence of adequate selenoenzymes would leave these tissues unprotected from oxidative damage. Even if the level of damage from such unsupported growth did not lead to overt lethality, it would undoubtedly result in early development of tumors and failure to successfully produce offspring. Therefore, the finding that Se-deprivation causes cell death is entirely consistent with expectations and is highly consistent with the level of brain damage that has been observed as a result of toxic MeHg exposures:

- When thioredoxin reductase, an important cellular selenoenzyme, is synthesized without selenocysteine, it is known as GRIM-12, a potent apoptosis (cell suicide) initiator (Anestal et al. [18]).

- Therefore, MeHg sequestration of Se not only deprives cells of selenoenzymes needed to counteract oxidative damage, it appears likely to also cause them to commit suicide.

Sustained Oblivion of Selenoenzyme Synthesis (SOS 5)

Although the biochemical effects related to this molecular mechanism of MeHg toxicity were first predicted by CATM researchers in 2005, the effects have only recently been observed.

The prolonged effects of high MeHg exposures during fetal growth on brain selenoenzyme activities have recently been found to continue through later stages of growth (Stringari et al. [11]) and are expected to remain permanent:

- Selenophosphate synthetase, the selenoenzyme that synthesizes selenophosphate, is a highly vulnerable "choke point" for selenoprotein synthesis.

- In the absence of Se, active selenophosphate synthetase can no longer be synthesized.

- If this occurs, it is unlikely the cell would ever be able to restart selenoenzyme synthesis. Therefore, animals that have experienced high Hg exposures for periods long enough to terminate activity of selenophosphate synthetase are likely to experience sustained loss of selenoenzyme activities.

7.3.3 Relationships Between Hg and Se in Freshwater Fish

Although seafood Se levels are in molar excess of MeHg in all varieties of ocean fish, other than swordfish and certain varieties of shark (Kaneko and Ralston [19]), it is known that maternal consumption of pilot whale meat results in cord blood Hg:Se molar ratios that approach, or exceed, 1:1 (Grandjean et al. [20, 21]). Toxic effects of high MeHg exposures are known to be severe when Hg:Se molar ratios exceed 1:1 in tissues, particularly in the developing fetus. The subtle decrements in selenoenzyme metabolism that may accompany seafood consumption result in extremely low molar Hg:Se ratios in tissues of seafood consumers. Since MeHg risks are proportional to Hg:Se molar ratios in the exposed populations, seafood MeHg exposures are unlikely to remain legitimate subjects of public health concern for much longer. Epidemiological studies are uniformly finding that increasing maternal consumption of ocean fish is accompanied by the beneficial effects that accompany enhanced intakes of long-chain omega-3 fatty acids, Se, iodine, vitamin D, and other essential nutrients result in improved child neurological outcomes (Hibbeln et al. [22]; Davidson et al. [23]). The subtle diminishments of these same endpoints that trend downward in association with increasing MeHg exposures could indicate selenoenzyme impairments begin to become apparent at MeHg:Se molar ratios of ~1:3 or could indicate adverse effects of increasing exposures to other components present in ocean fish. In either case, it is clear that the beneficial effects of maternal consumption of ocean fish are only slightly diminished by these minor adverse effects.

Although most varieties of ocean fish other than shark and swordfish may soon be "off the hook" in regard to MeHg risks, it does not appear that MeHg exposures from freshwater fish consumption will be similarly uniform. Although the majority of freshwater fish originating in the United States will have low MeHg:Se molar ratios similar to ocean fish, certain regions of the country will have fish with markedly higher MeHg:Se molar ratios that may be associated with significantly greater risks. This is primarily because atmospheric Hg deposition, point source influxes, is far more heterogeneous in lakes, rivers, and streams than in the ocean. Similarly, environmental Se availability can vary greatly between even adjacent lakes, and even areas with similar soil Se contents can have vastly different Se availability because of poor Se bioavailability at low soil or water pH.

As described above, inverse relationships between environmental Se availability and Hg contents of lake fish have been noted in natural experiments and intervention studies involving anthropogenically increased Se. However, no previous study has examined the influence of naturally occurring Se on bioaccumulation of Hg in freshwater fish. The purpose of this study was to examine relationships between environmental Se and Hg bioaccumulation in lake fish and compare these influences in fish collected from rivers and streams.

Since tissue Se contents reflect dietary Se intakes, we used fish Se contents as an indirect indicator of environmental Se availability. We hypothesized that formation of insoluble mercury selenide (HgSe) in tissues of prey animals would increase with increased Se availability and that formation of HgSe in tissues of prey would diminish absorption of Hg at each level of predation, decreasing the amount of Hg accumulated in top predators. Therefore, we anticipated increased availability of Se in the food web would be accompanied by diminished Hg bioaccumulation in tissues of top predators.

Eleven species of fish were collected from river and stream sites across the western United States, and their whole body Hg and Se contents were analyzed and evaluated in relation to their weight and length. Relationships between Hg and Se in three piscivorous species (northern pike, northern pikeminnow, and walleye), four herbivore/detritivore species (common carp, white sucker, shorthead redhorse, and black bullhead), and three insectivore species (smallmouth bass, brown trout, and rainbow trout) were assessed and compared to evaluate potential Se-dependent retirement of Hg in freshwater ecosystems (see Table 7-1 and Figures 7-3–7-6).

Table 7-1. Freshwater Fish Species and Size-Dependent Relationships Between Hg and Se

Guild and Species	n	Adjusted R^2	p Value
Piscivores			
Northern Pike	30	0.194	<0.01
Northern Pikeminnow	44	0.078	<0.04
Walleye	44	0.285	<0.0001
Herbivore/Detritivores			
White Sucker	126	0.205	<0.0001
Common Carp	39	0.323	<0.0001
Shorthead Redhorse	19	0.361	<0.01
Channel Catfish	24	–	NS (0.14)
Largescale Sucker	48	–	NS (0.09)
Insectivores			
Smallmouth Bass	52	–	NS
Rainbow Trout	59	–	NS
Brown Trout	74	–	NS

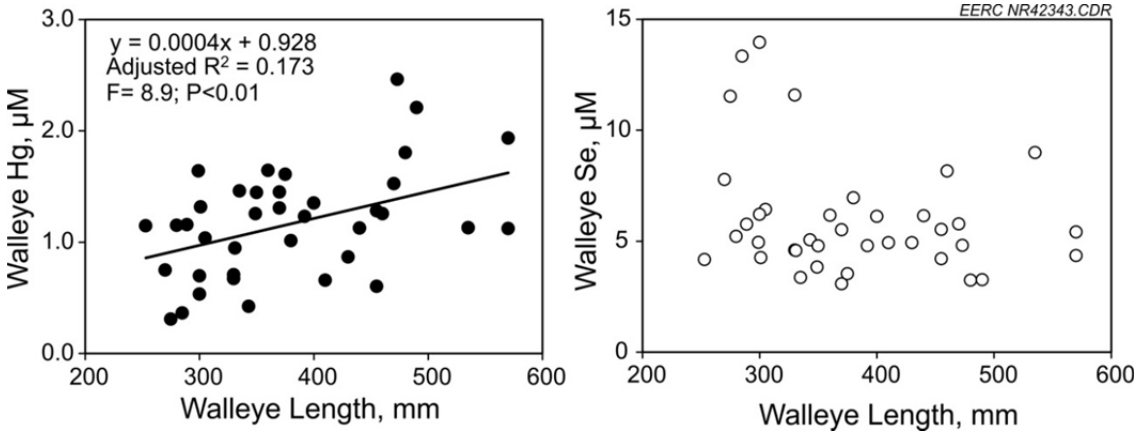

Figure 7-3. Size-dependent relationships between walleye Hg (panel A) and Se (panel B).

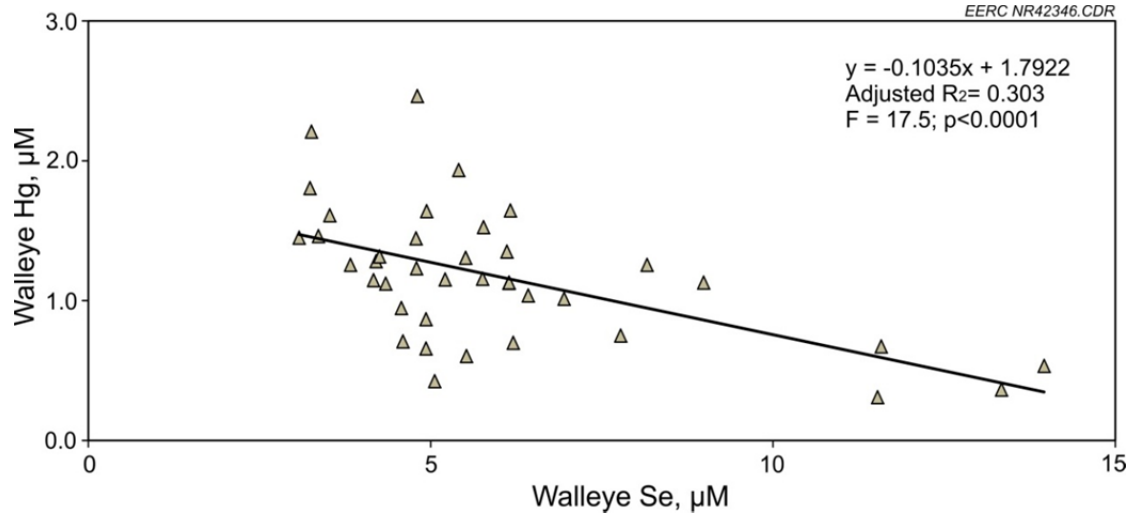

Figure 7-4. Se-dependent effects on Hg bioaccumulation in walleye.

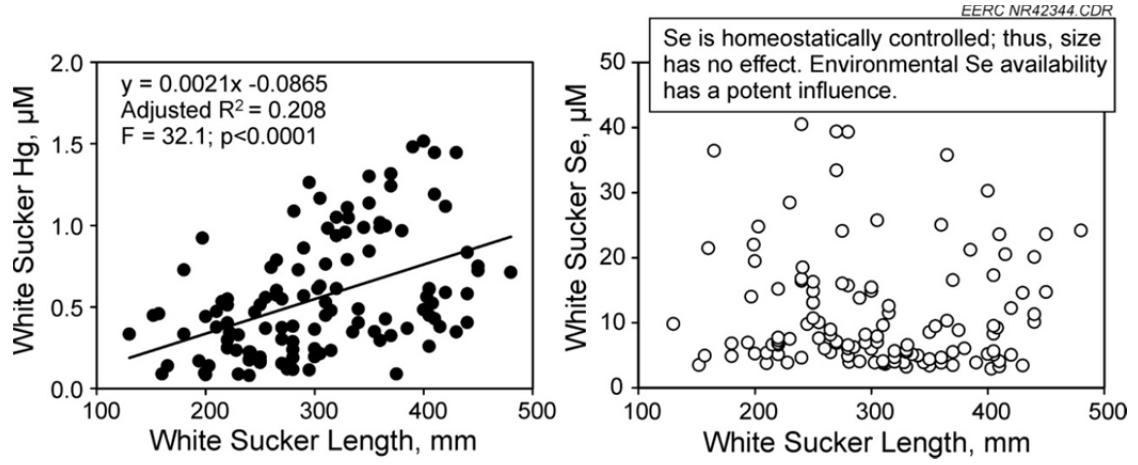

Figure 7-5. Size-dependent relationships between white sucker Hg (panel A) and Se (panel B).

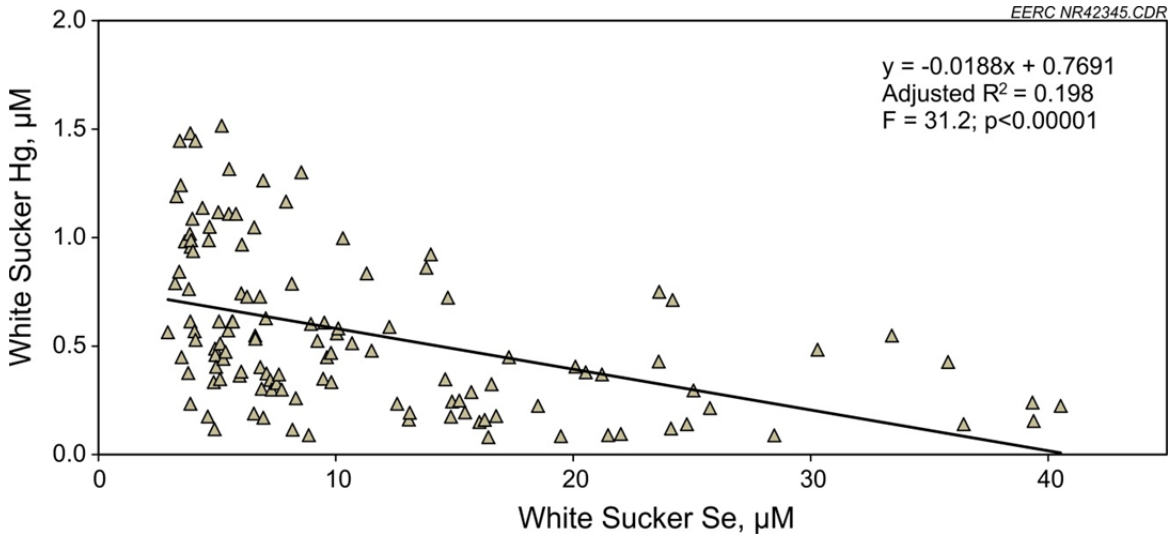

Figure 7-6. Se-dependent effects on Hg bioaccumulation in white sucker.

The Hg contents of 56% of the 659 fish exceeded the wildlife protective Hg threshold, and 12% exceeded the MeHg water quality criterion for the protection of humans. However, Hg occurred in molar excess of Se in only thirteen individual fish, which were all northern pikeminnows. Molar Hg:Se ratios increased significantly with increasing weight and length in all piscivores studied (northern pike, northern pikeminnow, walleye, and smallmouth bass) as well as in four nonpiscivores (common carp, white sucker, shorthead redhorse, largescale sucker).

As shown in Figure 7-3, the concentrations of MeHg increase in relation to increasing fish size ($F = 8.9$, $p<0.01$, adjusted $R^2 = 0.173$), but Se is homeostatically controlled. However, as seen in Figure 7-4, higher Se is associated with lower Hg in fish from rivers/stream of the Western United States ($F = 17.5$, $p <0.0001$, adjusted $R^2 = 0.303$). These findings are consistent with expectations. Part of this effect is associated with the elevated Se contents of smaller fish, but the effect clearly remained consistent among fish of all sizes. Since fish larger than 250 mm in length do not show a significant relationship between size and Se content; only fish larger than that size were used in this study.

As shown in Figure 7-5, the concentrations of MeHg increase in relation to increasing size of white suckers ($F = 32.1$, $p<0.0001$, adjusted $R^2 = 0.208$), but Se is homeostatically controlled. However, as seen in Figure 7-.6, higher Se is associated with lower Hg in fish from rivers/stream of the western United States ($F = 31.2$, $p <0.00001$, adjusted $R^2 = 0.198$). As with walleye, these findings are consistent with expectations. The effect of size was consistent among white suckers of all sizes. Since fish larger than 100 mm in length do not show a significant relationship between size and Se content, only fish larger than that size were used in this study. Table 7-1 provides more information on the fish in the study.

The influence of environmental Se of bioaccumulation of MeHg in fish from rivers and streams was consistently present among piscivores and was also present in most of the species of herbivore/detritivore that were assessed in this study. The p values approached significant

(<0.05) in the cases of channel catfish ($p = 0.14$) and largescale suckers ($p = 0.09$), suggesting that if more fish had been sampled, the effects might have attained statistical significance. Although our initial expectations were that herbivore/detritivores would not show the effects as potently as piscivores, this may have reflected a lack of appreciation of their actual position in the food web.

Since top predators die and are consumed by detritivores, this group would, in actuality, reside at the top of the food web, at least on those occasions when they feed on the decaying remains of "top predators."

Because the insects that are consumed by insectivores can fly in from a wide variety of areas originating outside the aquatic food web, their Se and Hg contents were not expected to reflect the inverse relationship observed in other feeding guilds. It is clear that Hg toxicity risks are proportional to Hg:Se molar ratios. Therefore, Se should be analyzed whenever Hg risk assessments are performed. Our findings indicate that the molar Hg contents of certain piscivorous fish species could rise to exceed those of Se in locations affected by Hg point sources.

In summary, the findings of this study support the hypothesis that increased environmental Se availability is an important determinant of the amount of Hg that will bioaccumulate in freshwater fish from rivers and streams.

Because of the sometimes contrasting heterogeneities of Hg and Se inputs, the MeHg contents in lake fish tend to be highly variable, even among fish of similar sizes that originate from lakes in relatively close geographic proximity (see Table 7-2 and Figure 7-7). Figure 7-7a shows the relationship between fish size and the accumulation of Hg (on a wet weight basis) in 73 northern pike *(Esox lucius*) fillet samples collected from ~18 Minnesota lakes.

Compared to Fishmouth Lake, MeHg bioaccumulation in northern pike from Lower Sakatah Lake is remarkably low. This may arise from lower atmospheric deposition or other inputs or as a result of the higher Se availability in Lower Sakatah Lake. Fish tissue Se is a reliable index of Se availability in an aquatic ecosystem, making it useful for monitoring influx of Se from runoff from natural and anthropogenic sources. On a wet weight basis, Se contents in fillets of northern pike from Fishmouth Lake, 11.2 ± 1.1 μmol Se/kg, were significantly lower (two-tailed t test; $p < 0.0001$) than the 15.8 ± 1.0 μmol Se/kg measured in fillets of fish from Lower Lake Sakatah. This coincides with the observation that MeHg accumulation is inversely related to environmental Se that has been made in previous studies (Chang et al. [24]; Paulsson and Lundberg [25, 26]; Southworth et al. [27, 28]; Belzile et al. [29–32]; Chen et al. [33]; Ralston et al. [34]). However, fish from Greenwood Lake also demonstrated high MeHg bioaccumulation, but, contrary to expectations, their Se contents were not lower but were actually the highest for any lake observed in the study (21.5 ± 2.3 μmol Se/kg).

Fish from Greenwood and Fishmouth Lakes clearly indicate that MeHg bioaccumulation in northern pike is a nonlinear process. Although fish that are 400 mm and longer are acceptably modeled using linear equations, the intercepts for MeHg contents of fish from these lakes are

Table 7-2. Hg and Se Concentrations in Freshwater Flesh of Similar Size by Lake

Name of Lake	µmol Se/g	µmol Hg/g	Hg:Se	Se:Hg	Se HBV
Waboose	9.41 ± 1.28	0.41 ± 0.08	0.04 ± 0.00	23.19 ± 1.67	217 ± 14
Peltier	10.07 ±2.04	0.46 ± 0.13	0.05 ± 0.02	23.48 ± 10.94	248 ± 158
Madison	8.97 ± 0.73	0.56 ± 0.19	0.06 ± 0.03	18.64 ± 10.01	172 ± 106
Lac Qui Parle	3.79 ± 0.10	0.63 ± 0.16	0.14 ± 0.09	19.62 ± 28.57	20 ± 2
Marsh	16.18 ±1.23	0.75 ± 0.10	0.05 ± 0.01	21.99 ± 4.26	359 ± 93
Crow Wing #1	2.82 ± 0.24	0.78 ± 0.16	0.27 ± 0.05	3.72 ± 0.71	10 ± 2
Crow Wing #3	5.75 ± 0.50	0.95 ± 0.11	0.17 ± 0.03	6.10 ± 0.90	35 ± 7
Lower Sakatah	15.99 ±0.99	1.15 ± 0.11	0.07 ± 0.01	14.00 ± 1.91	225 ± 42
Nipisiquit	11.80 ± 3.09	1.61 ± 0.36	0.15 ± 0.06	7.81 ± 3.36	99 ± 61
Phalen	6.32 ± 0.97	1.69 ± 0.42	0.27 ± 0.08	3.94 ± 1.44	25 ± 13
Tetonka	26.38 ± 4.24	1.79 ± 0.27	0.07 ± 0.02	15.10 ± 4.69	408 ± 188
Henderson	11.57 ±0.74	3.26 ± 0.34	0.28 ± 0.01	3.56 ± 0.14	40 ± 1
Harriet	9.81 ± 1.29	3.42 ± 1.89	0.35 ± 0.20	3.48 ± 1.44	33 ± 16
Greenwood	21.50 ±2.32	3.85 ± 1.59	0.18 ± 0.07	6.60 ± 3.26	138 ± 58
Cedar	7.42 ± 0.36	3.95 ± 1.75	0.53 ± 0.22	2.16 ± 1.01	14 ± 9
East Big Rabbit	6.88 ± 0.89	4.17 ± 1.57	0.63 ± 0.31	1.82 ± 0.89	10 ± 10
Fishmouth	11.22 ±1.07	4.40 ± 1.67	0.41 ± 0.17	3.34 ± 2.41	37 ± 34
Windy	9.31 ± 0.08	5.01 ± 1.24	0.48 ± 0.24	2.94 ± 2.39	13 ± 4

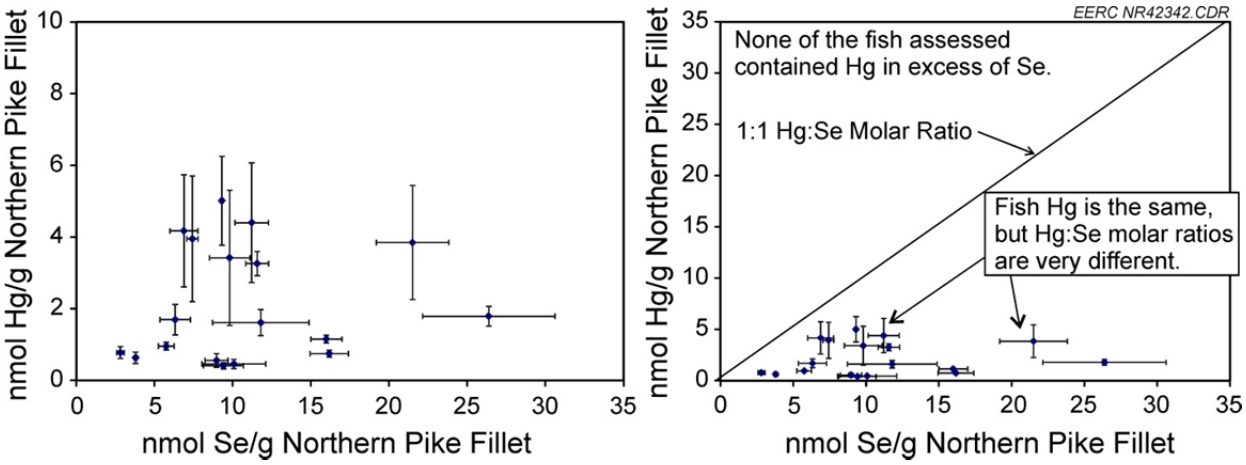

Figure 7-7. Mercury and Se in northern pike from Minnesota lakes. Panel A shows the average ±SD of Hg (Y axis) and Se (X axis) concentrations in northern pike fillets from fish collected from the ~20 lakes included in the study. Panel B shows the same data in relation to the 1:1 Hg:Se molar ratio.

highly negative (a logical impossibility). The data clearly indicate that the observed trends in these lakes are actually nonlinear. In contrast, data on northern pike from Lower Sakatah Lake and from the rivers and streams studied both reflect intercepts that more closely approximate 0.

Although the diagonal line reflecting the Hg:Se equimolar concentration in Figure 7-7B does not define a bright line for health hazards, it does provide a useful index for comparing relative risks related to MeHg exposures.

The heterogeneous nature of MeHg accumulation in lake fish may reflect distinctions in either atmospheric deposition or point source inputs of Hg or could indicate differences in Hg retirement. Panel B of Figure 7-8 shows the relationship between size and Hg accumulation of Hg in whole body homogenates of 29 northern pike samples (wet weight) collected from rivers and streams of the western United States. Although collected from rivers and streams from across North Dakota, South Dakota, and Montana, a much broader geographical range than in the Minnesota lake study, the relationship between length and MeHg accumulation in these samples was significant ($p = 0.05$), although not highly consistent (adjusted $R^2 = 0.131$). The broad range of MeHg concentrations in relation to fish length in northern pike collected in lakes seems to have obscured the more uniform relationship observed in fish collected from rivers and streams. However, based on the known effects of rich Se on Hg bioaccumulation in fish, it appears that the MeHg contents of fish from certain lakes would have been extremely high if not for the enhanced retirement through HgSe formation. In cases where high fish MeHg levels are present, but Se contents are low, it may be that MeHg bioaccumulation could be diminished by restoring Se to normal levels in lakes that have been depleted by excess Hg.

Although relationships between size and MeHg bioaccumulation show little overall consistency between lakes, samples that originated from the same lakes showed highly consistent relationships (adjusted R^2 values ranging from 0.87 to 0.97) in three lakes selected for the current discussion (see Figure 7-8).

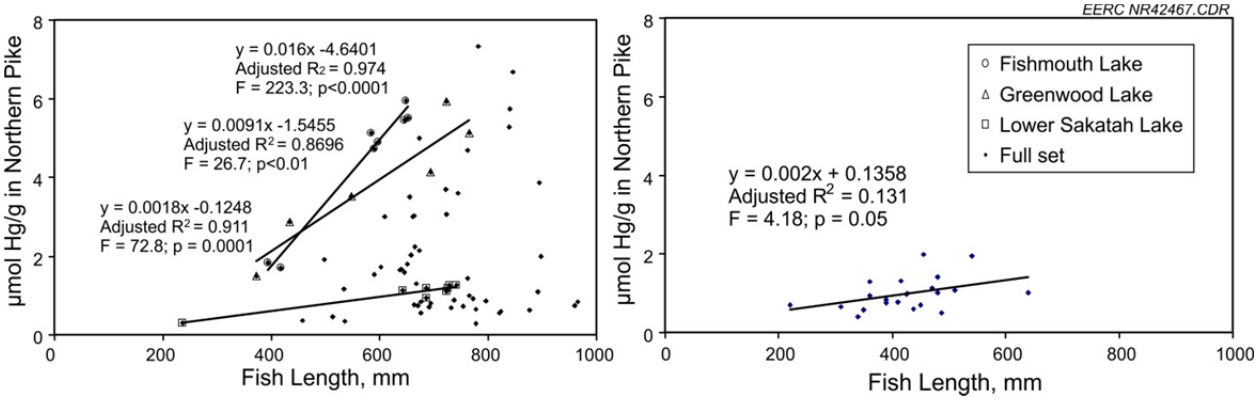

Figure 7-8. Relationships between northern pike length and fillet Hg (Panel A) observed in the Minnesota study and total fish homogenate Hg from the EPA study (Panel B).

Piscivorous wildlife typically consume the entire fish; thus the whole-fish homogenates used in the EPA study are highly appropriate for assessing risks to natural predators. However, because fillet MeHg contents can be estimated from the whole-body homogenate results, risks to human as well as wildlife piscivores can be assessed using this sample type. However, to assess actual risks to humans or wildlife, it is necessary to know the Se content of the fish that are being consumed. The Se contents of freshwater fish will be directly related to the Se status of the food web in their waters of origin. Predatory fish and wildlife from areas with poor environmental Se availability will be at accentuated risk when consuming fish with high MeHg contents. Humans tend to consume foods from a more varied range of geographic origins. Therefore, their Se status is far less dependent on local Se availability, but geographic trends are still noticeable in the United States. The risks to those that depend on subsistence fishing and have increased rates of consumption of locally caught fish are likely to be at greater risk from high-MeHg, low-Se fish since this subpopulation may be more likely to have marginal Se nutritional status due to economic or cultural determinants.

In order to evaluate the risks to human and wildlife consumers, the Se-HBV provides the most complete and reliably accurate indication of relative risks that may accompany fish consumption. Fish with negative Se-HBVs are expected to diminish the Se status of the consumer, while those with positive values improve the consumer's Se status. The magnitude of the negative or positive Se-HBV is intended to reflect the relative risk or benefits of consuming the indicated fish. Although the Se-HBV is, by definition, expressly related to Se status, it is the intention of the health benefit value approach to incorporate the beneficial effects of additional criteria such as omega-3 fatty acid contents and other nutrients as well as potentially adverse effects associated with other components/contaminants that may be present in the food.

Consumption of fish that have similar Hg contents but vastly different Se contents will not be accompanied by similar risks. Similarly, fish with similar Se contents but higher Hg will have lower Se-HBVs, just as fish with similar Hg contents but lower Se. Eating fish with low or negative Se-HBVs are expected to pose risk to consumers, but consumption of fish with highly positive Se-HBVs will tend to counteract MeHg toxicity rather than contribute to causing it. See Figure 7-3 for the effects of size on Se-HBVs of northern pike from the various sample sites examined in this study.

As shown in Figure 7-9A, the Se-HBVs of northern pike diminish as their MeHg burden increases. Although the validity of this assumption will need to be experimentally verified, it appears that fish above a certain size will bioaccumulate MeHg in amounts equal to their Se contents at the sizes indicated as the intercepts shown in the equations in Figure 7-4, and fish that are larger still appear likely to contain MeHg in excess of their Se contents. In Lower Sakatah Lake, the indicated size where this would be expected to occur and Se-HBVs would reach zero and start to have negative values is slightly over 900 mm. Meanwhile in Fishmouth Lake, much smaller pike with lengths over 675 mm would have increasingly negative Se-HBVs and, therefore, pose increasing risks to consumers of their fillets. In the whole-fish homogenates, the intercept at 415 mm indicates that fish above this size would potentially pose risks to wildlife consumers. The variability of Se contents in fish collected from Greenwood Lake make the Se-

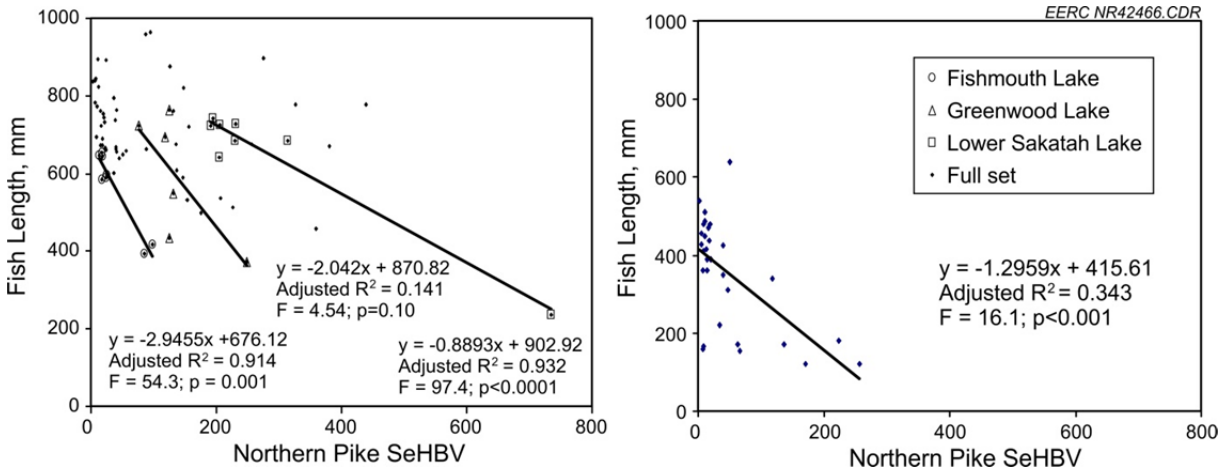

Figure 7-9. Relationships between northern pike length and fillet Se-HBVs (Panel A) observed in the Minnesota study and total fish homogenate Se-HBVs from the EPA study (Panel B).

HBV more variable than in the other cases. It will be important to recognize and quantify all sources of both MeHg and Se variability in freshwater fish before applying the Se-HBV as food safety criteria in relation to protecting public health.

In the meantime, it is also important to note that lakes which have been depleted of Se tend to demonstrate particularly high rates of MeHg bioaccumulation. This results in a highly adverse synergy of accentuated toxicity and accumulation of MeHg that is expected to be relatively uncommon. Until actual surveys are conducted, estimates of less than 2% to as high as 5% of lakes in the United States could be involved. Because of the health risks that might be present, urgent efforts are under way to identify areas where these particular health hazards may exist.

Fortunately, these conditions can be counteracted by supplying natural forms of Se to restore normal levels of Se to these MeHg-depleted ecosystems. These remediation approaches are known to be safe, rapidly effective, and inexpensive. Among both humans and wildlife exposed to MeHg from eating these fish, improving the Se status of the consumer would be a particularly important determinant of the actual risks associated with eating a fish with a negative Se-HBV. If fish from lakes that currently have high MeHg contents and low Se can be changed to fish with much lower MeHg contents and relatively rich Se, this will improve the health of the lake fish as well as wildlife and human consumers of these fish.

7.4 Conclusions

The most important aspects of the seafood and freshwater fish consumption issue involve MeHg binding to Se, the molecular target of MeHg toxicity. Confusion regarding the differences between “MeHg exposures” and “MeHg risks” have arisen because of mistaken assumptions that MeHg exposures were uniformly associated with MeHg risks. However, since adverse effects do not appear to occur until MeHg exposures achieve molar ratios that approach or exceed equimolar stoichiometries with tissue Se concentrations, the Se status of the host is a major factor. Since MeHg exposures from ocean fish consumption seldom result in host tissue Hg:Se

molar ratios that approach, let alone exceed, 1:1, the effects of seafood MeHg exposures are unlikely to be legitimate subjects of public health concern. Since MeHg bioaccumulation and toxicity in freshwater fish are both inversely related to Se, potential risks from MeHg exposures involving human and wildlife remains a subject of concern, as described earlier.

Since 95% of the water bodies that are currently under fish consumption advisories for MeHg appear to actually contain Se in significant molar excess of MeHg, it seems reasonable that the MeHg-related advisories regarding these lakes, rivers, and streams may eventually be repealed. This would have beneficial effects for the public as well as public health agencies. By releasing those lakes, rivers, and streams where MeHg risks do not appear to actually exist from the advisories, the public and public health agencies would be able to focus their attention on locations where MeHg and other hazardous exposures pose serious health risks. This would be a reflection of the progress that has been made to improve understanding of MeHg-related risks as well as the diminishments in atmospheric Hg releases that have already been accomplished. This would appeal to sportsmen, tourists, and the general public as well as to public health agencies and decision makers that would be credited with the substantial progress that has been made in this important area of regulatory activity.

This evaluation of the SeHBVs of freshwater fish from natural water bodies establishes that although fish from many locations compare favorably with ocean fish, their beneficial values decline rapidly with increasing MeHg accumulation. Since Se is known to be far more variable in freshwater bodies than in the ocean, this was expected. Previous work in this area had established that MeHg accumulation in freshwater fish becomes accentuated in fish from water bodies with low Se availability.

The findings of this study indicate that high MeHg accumulation in fish from certain lakes can result in high Hg:Se molar ratios that approach levels potentially associated with adverse health effects, especially in sensitive subpopulations of consumers. However, the relative percentage of water bodies in the United States that may contain fish that pose such risks appear to be quite low, probably fewer than 5% and possibly fewer than 2%. Based on the findings of the most recent epidemiological results from the Seychelles and United Kingdom studies, the results of the current study support the concept that SeHBV criteria provide a superior index of risks as well as benefits associated with fish consumption.

The research initiated through this study is being extended through the EPA Science To Achieve Results (STAR) grant program in a project entitled “Fish Selenium Health Benefit Values in Mercury Risk Management.” Through this study, CATM investigators are contacting all state and federal agencies that analyze mercury levels in fish and requesting any data they may have that report Hg and Se that were concurrently assessed. Through this effort, the findings of the current study are being extended to investigations throughout all available databases. Plans to initiate analysis of fish from potentially problematic areas are under way. That effort will be directed toward determining whether any of these locations have fish with high Hg:Se molar ratios, or if the fish simply have high Hg but not in molar excess of Se. It currently appears that virtually all types of ocean fish other than certain varieties of shark contain Se in molar excess of Hg and are, therefore, more likely to prevent MeHg toxicity than contribute to causing it.

Regions with poor environmental Se availability appear to have freshwater fish with accentuated Hg bioaccumulation and high Hg:Se molar ratios. Fortunately, the fish in such lakes appear likely to respond well to repletion with safe amounts of natural forms of Se. In previous studies, Se-supplemented lakes have responded with diminishments of fish MeHg by more than 75% in less than 3 years (Paulsson and Lundberg [26]). Using similar approaches, the high Hg levels in any U.S. lakes that contain fish with high Hg:Se molar ratios could be effectively remediated through safe and relatively inexpensive additions of natural forms of Se.

7.5 References

1. Carvalho, C.M.L.; Chew, E.-H.; Hashemy, S.I.; Lu, J.; Holmgren, A. Inhibition of the Human Thioredoxin System: A Molecular Mechanism of Mercury Toxicity. *Journal of Biological Chemistry* **2008**, *283* (18), 11913–11923.

2. Peterson S.A.; Ralston N.V.C.; Peck D.V.; Van Sickle J; Robertson J.D.; Spate V.L.; Morris J.S. How Might Selenium Moderate the Toxic Effects of Mercury in Stream Fish of the Western USA? *Environ. Sci. Technol*. **2009**, *43*, 3919–3925.

3. Peterson, S.A.; Ralston, N.V.C.; Whanger, P.D.; Oldfield, J.E.; Mosher, W.D. Selenium and Mercury Interactions in Fish Tissue. *Environmental Bioindicators* **2009**, 4, 318–334.

4. Ganther, H.E.; Goudie, C.; Sunde, M.L.; Kopeckey, M.; Wagner, S., Hoekstra, W. Selenium: Relation to Decreased Toxicity of Methylmercury Added to Diets Containing Tuna. *Science* **1972**, *175*, 1122–1124.

5. Ganther, H.E.; Sunde, M.L. Effect of Tuna Fish and Selenium on the Toxicity of Methylmercury: A Progress Report. *Journal of Food Science* **1974**, *39*, 1–5.

6. Prohaska, J.R.; Ganther, H.E. Interactions Between Selenium and Methylmercury in Rat Brain. *Chemico-Biological Interactions* **1977**, *16*, 155–67.

7. Seppanen. K.; Soininen, P.; Salonen, J.T.; Lotjonen, S.; Laatikainen, R. Does Mercury Promote Lipid Peroxidation? An In Vitro Study Concerning Mercury, Copper, and Iron in Peroxidation of Low-Density Lipoprotein. *Biological Trace Element Research* **2004**, *101* (2), 117–32.

8. Ralston, N.V.C.; and Raymond, L.J. *Selenium's Role in the Seafood Safety Issue*; Final Report to U.S. Department of Energy; Energy & Environmental Research Center: Grand Forks, ND, 2009.

9. Watanabe, C.; Yin, K.; Kasanuma, Y.; Satoh, H. In Utero Exposure to Methylmercury and Selenium Deficiency Converge on the Neurobehavioral Outcome in Mice. *Neurotoxicology and Teratology* **1999**, *21*, 83–88.

10. Watanabe, C.; Yoshida, K.; Kasanuma, Y.; Kun, Y.; Satoh, H. In Utero Methylmercury Exposure Differentially Affects the Activities of Selenoenzymes in the Fetal Mouse Brain. *Environ Res*. **1999**, *80*, 208–14.

11. Stringari, J.; Nunes, A.K.C.; Franco, J.L.; Bohrer, D.; Garcia, S.C.; Dafre, A.L.; Milatovic, D.; Souza, D.O.; Rocha, J.B.T.; Aschner, M.; Farina, M. Prenatal Methylmercury Exposure Hampers Glutathione Antioxidant System Ontogenesis and Causes Long-Lasting Oxidative Stress in the Mouse Brain. *Toxicology and Applied Pharmacology* **2008**, *227*, 147–154.

12. Korbas, M.; O'Donoghue, J.L.; Watson, G.E.; Pickering, I.J.; Singh, S.P.; Myers, G.J.; Clarkson, T.W.; George, G.N. The Chemical Nature of Mercury in Human Brain Following Poisoning or Environmental Exposure. *ACS Chemical Neuroscience* 1 **2010**, *12*, 810–818.

13. Dietz, R.; Riget, F.; Born, E.W. An Assessment of Selenium to Mercury in Greenland Marine Animals. *Science of the Total Environment* **2000**, *245*, 15–24.

14. Huggins F.; Raverty S.A.; Nielsen O.S.; Sharp N.; Robertson J.D.; Ralston N.V.C. An XAFS Investigation of Mercury and Selenium in Beluga Whale Tissues. *Environmental Bioindicators* **2009**, *4*, 291–302.

15. Dyrssen, D.; Wedborg, M. The Sulfur-Mercury(II) System in Natural Waters. *Water, Air, Soil Pollut*. **1991**, *56*, 507–519.

16. Ralston, N.V.C.; Blackwell, J.L.; Raymond, L.J. Importance of Molar Ratios in Selenium-Dependent Protection Against Methylmercury Toxicity. *Biol. Trace Element Res*. **2007**, *119*, 255–268.

17. Ralston, N.V.C.; Ralston C.R.; Blackwell III, J.L.; Raymond, L.J. Dietary and Tissue Selenium in Relation to Methylmercury Toxicity. *Neurotoxicology* **2008**, *29*, 802–811.

18. Anestal, K.; Arner, E.S.J. Rapid Induction of Cell Death by Selenium-Compromised Thioredoxin Reductase 1 But Not by the Fully Active Enzyme Containing Selenocysteine. *J. Biol. Chem.* **2003**, 278, 15966–15972.

19. Ralston N.V.C.; Raverty S.A.; Nielsen O.S.; Blackwell, J.L. III; Sharp N.E.; Robertson, J.D. Selenium and Mercury Concentrations in Neuroendocrine and Somatic Tissues of Beluga Whales (Delphinapterus Leucas). *Environmental Research*, in preparation.

20. Grandjean, P.; Weihe, P.; Jorgenson, P.J.; Clarkson, T.; Cernichiari, E.; Videro, T. Impact of Maternal Seafood Diet on Fetal Exposure to Mercury, Selenium, and Lead. *Archives of Environmental Health* **1992**, *47* (3,) 185–195.

21. Grandjean, P.; Weihe, P.; White, R.F.; Debes, F. Cognitive Performance of Children Prenatally Exposed to "Safe" Levels of Methylmercury. *Environ. Res*. **1998**, *77*, 165–172.

22. Hibbeln, J.R.; Davis, J.M.; Steer, C.; Emmett, P.; Rogers, I.; Williams, C.; Golding, J. Maternal Seafood Consumption in Pregnancy and Neurodevelopmental Outcomes in Childhood (ALSPAC Study): An Observational Cohort Study. *Lancet* **2007**, *369*, 578–585.

23. Davidson, P.W.; Cory-Slechta, D.A.; Thurston, S.W.; Huang, L.S.; Shamlaye, C.F.; Gunzler, D.; Watson, G.; van Wijngaarden, E.; Zareba, G.; Klein, J.D.; Clarkson, T.W.; Strain, J.J.; Myers, G.J. Fish Consumption and Prenatal Methylmercury Exposure: Cognitive and Behavioral Outcomes in the Main Cohort at 17 years from the Seychelles Child Development Study. Neurotoxicology 2011, in press.

24. Chang P.S.S.; Malley, D.F.; Strange, N.E.; Klaverkamp, J.F. The Effects of Low pH, Selenium and Calcium on the Bioaccumulation of 203Hg by Seven Tissues of the Crayfish, Orconectes virilis. *Can. Tech. Rep. Fish Aquat. Sci*. **1983**, *1151*, 45–67.

25. Paulsson, K.; Lundberg, K. The Selenium Method for Treatment of Lakes for Elevated Levels of Mercury in Fish. *Sci Total Environ*. **1989**, *87/88*, 495–507.

26. Paulsson, K.; Lundberg, K. Treatment of Mercury Contaminated Fish by Selenium Addition. *Water Air Soil Pollut*. **1991**, *56*, 833–841.

27. Southworth, G.R.; Peterson, M.J.; Turner, R.R. Changes in Concentrations of Selenium and Mercury in Largemouth Bass Following Elimination of Fly Ash Discharge to a Quarry. *Chemosphere* **1994**, *29*, (1), 71–79.

28. Southworth, G.R.; Peterson, M.J.; Ryon, M.G. Long-Term Increased Bioaccumulation of Mercury in Largemouth Bass Follows Reduction of Waterborne Selenium. *Chemosphere* **2000**, *41* (7), 1101–1105.

29. Belzile, N.; Chen, Y.W.; Xu, R. Early Diagenetic Behaviour of Selenium in Freshwater Sediments. *Appl Geochem* **2000**, *15*, 1439–1454.

30. Belzile, N.; Chen, Y.W.; Gunn, J.M.; Tong, J.; Alarie, Y.; Delonchamp, T.; Lang, C.Y. The Effect of Selenium on Hg Assimilation by Freshwater Organisms. *Can. J. Fish Aquat. Sci*. **2006**, *63*, 1–10.

31. Belzile, N.; Wu, G.J.; Chen, Y.W.; Appanna, V.D. Detoxification of Selenite and Hg by Reduction and Mutual Protection in the Assimilation of Both Elements by Pseudomonas Fluorescens. *Sci Total Environ*. **2006**, *367*, 704–714.

32. Belzile, N.; Chen, Y.W.; Yang, D.Y.; Truong, H.Y.T.; Zhao, Q.-X. Selenium Bioaccumulation in Freshwater and Antagonistic Effect Against Mercury Assimilation. *Environ. Bioindic.* **2009**, *4,* 203–221.

33. Chen, Y.W.; Belzile, N.; Gunn J.M. Antagonistic Effect of Selenium on Mercury Assimilation by Fish Populations near Sudbury Metal Smelters? *Limnol. Oceanogr.* **2001**, *46*, 1814–1818.

34. Ralston, C.R.; Raymond, L.J.; Ralston, N.V.C. Presented at Ecological Society of America, Austin, TX, 2011.

8.0 BIBLIOGRAPHY OF DELIVERABLES/TECHNOLOGY TRANSFER

8.1 Journal Articles

- Under Activity 5, Dr. Nick Ralston submitted a journal article to *Science of the Total Environment* entitled "Selenium and Mercury Concentrations in Neuroendocrine and Somatic Tissues of Beluga Whales (*Delphinapterus Leucas*)."

- Research from Activity 5 is covered in a journal article submitted to *Nutrition Reviews* entitled "The Importance of Mercury–Selenium Interactions in Risks Associated with CH_3Hg Exposure."

- Activity 5 research is covered in the journal article submission entitled "Molecular Neurotoxic Mechanisms of Organic and Inorganic Mercury Forms: Insights from Chemistry and Biochemistry."

- A summary of Activity 5 research showing that mercury in freshwater fish is inversely related to environmental selenium availability is being prepared by CATM–EERC researchers with coauthors from EPA.

- An article was submitted to the *Biological Trace Element Research Journal* entitled "The Nail as a Noninvasive Indicator of Methylmercury Exposures and Mercury/Selenium Molar Ratios in Brain, Kidney, and Livers of Long-Evans Rats," by John Brockman, Laura Raymond, Carla Ralston, David Robertson, Nicole Bodkin, Nicholas Sharp, and Nicholas V.C. Ralston. See citation below:

  Brockman, J.; Raymond, L.J.; Ralston, C.R.; Robertson, J.D.; Bodkin, N.; Sharp, N.; Ralston, N.V.C. The Nail as a Noninvasive Indicator of Methylmercury Exposures and Mercury:Selenium Molar Ratios in Brain, Kidney and Livers of Long-Evans Rats. *Biol. Trace Elem. Res.*, in review.

- A peer-reviewed journal article authored by Ye Zhuang, John Pavlish, Nicholas Lentz, and Lucinda Hamre was published to the special issue of the *International Journal of Greenhouse Gas Control* entitled "Mercury Measurement and Control in a CO-Enriched Flue Gas," Volume 5, p. 5136–5142, 2011. See citation below:

  Zhuang, Y.; Pavlish, J.H.; Lentz, N.B.; Hamre, L.L. Mercury Measurement and Control in a CO_2-Enriched Flue Gas. *International Journal of Greenhouse Gas Control* **2011**, *5S*, S136–S142.

- A journal article authored by Ye Zhuang, Christopher Martin, and John Pavlish was published by *Fuel* entitled "Cobenefit of SO_3 Reduction and Mercury Capture with Activated Carbon Injection in Coal Flue Gas," based on work jointly sponsored by CATM and the Illinois Clean Coal Institute. See citation below:

Zhuang, Y.; Martin, C.L.; Pavlish, J.H.; Botha, F. Cobenefit of SO_3 Reduction on Mercury Capture with Activated Carbon in Coal Flue Gas. *Fuel* **2011**, *90*, 2998–3006.

- A peer-reviewed journal article authored by John H. Pavlish, Lucinda Hamre, and Ye Zhuang was published by *Fuel* entitled "Mercury Control Technologies for Coal Combustion and Gasification Systems."

- Chen, C.; Zhuang, Y.; Wang, C.-B. Enhancement of Direct Sulfation of Limestone by Na_2CO_3 Addition. *Fuel Processing Technology* **2009**, *90* (7–8) 889–894.

- Zhuang, Y.; Chen, C.; Timpe, R.C.; Pavlish, J.H. Investigations on Bromine Corrosion Associated with Mercury Control Technologies in Coal Flue Gas. *Fuel* **2009**, *88* (9), 1692–1697.

- Olson, E.C.; However, J.C.; Senior, C.C.; Suuberg, E.M.; Hurt, R.H.; Wilcox, J.L. Mercury Capture by Native Fly Ash Carbons in Coal-Fired Power Plants. *Prog. Energy Combust. Sci.* **2010**, *36* (4) 510–529. See citation below:

  Hower, J.; Senior, C.; Suuberg, E.; Hurt, R.; Wilcox, J.; Olson, E. Mercury Capture by Native Fly Ash Carbons in Coal-Fired Power Plants. *Prog. Energy Combust. Sci.* **2010**, *36* (4), 510–529.

- Nicholas Ralston, Stephen Raverty, Ole Nielsen, Nicholas Sharp, J. David Robertson, "Selenium and Mercury Concentrations in Neuroendocrine and Somatic Tissues of Beluga Whales (Delphinapterus Leucas)," Submitted to *Science of the Total Environment*, October 5, 2009.

8.2 Presentations

- Dr. Ye Zhuang, Program Area Manager for Activity 2, delivered a presentation for the Air Quality VIII Conference (2011 International Air Quality Conference on Carbon Management, Mercury, Trace Substances, SO_x, NO_x, and Particulate Matter) held in McLean, Virginia, in October 2011. His podium presentation and paper are entitled "Mercury Measurement and Control in Coal Gasification Applications." See citation below:

  Zhuang, Y.; Olson, E.S.; Thompson, J.S.; Lentz, N.B.; Pavlish, J.H.; Holmes, M.J. Mercury Measurement and Control in Coal Gasification Application. In *Proceedings of Air Quality VIII: An International Conference on Carbon Management, Mercury, Trace Substances, SO_x, NO_x, and Particulate Matter*; Arlington, VA, Oct 24–27, 2011.

- Dr. Chris Martin, Program Area Manager for Activity 3 delivered a presentation for the Air Quality VIII Conference entitled "Impacts of Condensation on Selenium Transport and Capture." See citation below:

  Martin, C.L.; Pavlish, J.H.; Zhuang, Y. Impacts of Condensation on Selenium Transport and Capture. In *Proceedings of Air Quality VIII: An International Conference on Carbon*

Management, Mercury, Trace Substances, SO_x, NO_x, and Particulate Matter; Arlington, VA, Oct 24–27, 2011.

- Dr. Nick Lentz, for Activity 4, gave a presentation for the Air Quality VIII Conference entitled "Development of a Multielement Sorbent Trap Sampling Method." See citation below:

  Lentz, N.B.; Pavlish, J.H. Development of a Multielement Sorbent Trap Sampling Method. In *Proceedings of Air Quality VIII: An International Conference on Carbon Management, Mercury, Trace Substances, SO_x, NO_x, and Particulate Matter*; Arlington, VA, Oct 24–27, 2011.

- Dr. Ralston provided a platform presentation at the 10th International Conference on Mercury as a Global Pollutant, held July 24–29 in Halifax, Nova Scotia. His presentation was entitled "The Physiological and Environmental Implications of Mercury–Selenium Interactions."

- Dr. Ralston delivered a presentation entitled "Selenium's Pivotal Role in Molecular Mechanisms of Mercury Toxicity" at the 2nd International Selenium Conference in Suzhou, China, on October 24, 2011.

- CATM Director John Pavlish presented research outcomes of this subtask's mercury control research in a presentation entitled "Enhancing Mercury Capture to Meet Global Mercury Reductions with Sorbent Enhancement Additives" at the Mercury Emissions from Coal (MEC) Conference in Krugers Gate, South Africa, held May 18–20, 2011. This international working group was opened to outside participants this year.

- Ye Zhuang, Program Area Manager for Activity 2, gave a presentation on work funded through this project at the Clearwater Conference, held June 5–9, 2011, at Clearwater, Florida. The title of his presentation was "Transformation of Hazardous Air Pollutants in Oxygen-Fired Coal Combustion with Flue Gas Recycling." See citation below:

  Zhuang, Y.; Pavlish, J.H. Transformation of Hazardous Air Pollutants in Oxygen-Fired Coal Combustion with Flue Gas Recycling. Paper presented at the 36th International Technical Conference on Clean Coal & Fuel Systems, Clearwater, FL, June 5–9, 2011.

- Activity 3 Program Area Manager, Christopher Martin, gave a presentation entitled "Identifying Factors That Limit Mercury Capture with Sorbent Injection" in May at the 2011 Electric Power Conference. This presentation to utility professionals was based on research conducted under CATM, including the work that was funded by this subtask; it covered the CATM-developed model for mercury and AC interactions to the situation of in-flight mercury capture.

  Martin, C.L.; Pavlish, J.H.; Olson, E.S. Identifying Factors that Limit Mercury Capture with Sorbent Injection. Presented at Electric Power 2011, Rosemont, IL, May 10–12, 2011.

- CATM researchers gave a presentation at the Electric Utility Environmental Conference on January 31, 2011, entitled "Development of a Multielement Sorbent Trap Sampling Method."

- Dr. Nicholas Ralston presented "Molecular Mechanisms of Irreversible Inhibition of Selenoenzymes by High Methylmercury Exposures" at the 50th International Society of Toxicology Meeting on March 8, 2011, in Washington, D.C.

- Dr. Ralston, under Activity 5, chaired the Mercury–Selenium Session at the Hawaii Seafood 2010 Conference on October 20–22, 2010, in Honolulu, Hawaii, at which time he gave outcomes of CATM research in a presentation named "Methylmercury Is an Irreversible Inhibitor of Brain Selenoenzymes with Vital Functions."

- At the International Seafood and Health meeting in Melbourne, Australia, on November 7, 2010, Dr. Ralston described CATM research findings in a presentation entitled "Selenium's Role in Seafood Safety Issues Regarding Mercury."

- Dr. Ralston presented CATM research at the EPA-sponsored Quicksilver Summit in Anchorage, Alaska, on October 28, 2010, entitled "Mercury Bioaccumulation and Toxicity Are Inversely Related to Selenium."

8.3 Workshops, Working Group Involvement, and Round-Table Discussions

- Dennis Laudal presented a 1-day workshop to engineering students at the University of North Dakota to explain mercury behavior, transformations, and control technologies. His workshop also provided information on regulatory actions concerning trace metals. This workshop was delivered in November 2011. See citation below:

  Laudal, D.L. Mercury in Combustion Flue Gas. Presented to the University of North Dakota Engineering Department, Grand Forks, ND, Nov 8 and 10, 2011.

  Laudal, D.L. Mercury in Combustion Flue Gas. Presented to the University of North Dakota Engineering Department, Grand Forks, ND, Nov 8 and 10, 2011.

- CATM Director, John Pavlish, and Dr. Nick Lentz delivered a workshop at the Air Quality VIII Conference covering mercury control mechanisms, control technologies, and measurement. See citation below:

  Pavlish, J.H.; Lentz, N.B. Measurement and Control of Mercury, Trace Metals, and Halogens. Presented at Preconference Workshop 2 of Air Quality VIII: An International Conference on Carbon Management, Mercury, Trace Substances, SO_x, NO_x, and Particulate Matter, Arlington, VA, Oct 23, 2011.

- Dr. Nicholas Ralston, Program Area Manager for Activity 5, continued his work for the EPA SAB panel considering the mercury issue and assisted in preparation of the SAB summary that was submitted to EPA.

- Dr. Ralston took part in the EPA Science Advisory Board meetings during the week of June 13–17, 2011, where the panel reviewed current mercury environmental research.

- CATM Director John Pavlish presented outcomes of CATM's mercury control research in an oxycombustion environment at a keynote address entitled "Mercury Measurement and Control in a CO_2-Enriched Flue Gas" at the Workshop on SO_2/SO_3/Hg/Corrosion Issues under Oxyfuel Combustion Conditions in London, England, on January 25, 2011.

- John Pavlish disseminated technical mercury control information to the audience at the EXPPERTS USA Workshop. The presentation was entitled "Mercury Control and Technology Considerations" and was given March 23, 2011, in St. Louis, Missouri.

- Dr. Ralston's descriptions of CATM research findings are now available on the Seafood Services Australia Web site in a presentation entitled "Seafood's Secret Ingredient to Protect Our Health" (www.seafood.net.au/page/?pid=1434&nid=403). This was recorded during the International Seafood and Health meeting in Melbourne, Australia.

- Dr. Ralston's descriptions of CATM research-related findings are available on the Hawaii Seafood Web site, www.hawaii-seafood.org/Symposium-Statement/Speakers-Extended/in (http://hawaii-seafood.org/symposium/videos/view-flash?speaker=nick_ralston_phd).

- Dr. Ralston assisted in the coordination of and chaired the 4th International Selenium–Mercury Interactions Symposium at the 31st SETAC North America Conference in Portland, Oregon, on November 9, 2010.

- CATM's Director, Mr. Pavlish, shared experimental results from this research at the International Mercury Emissions from Coal (MEC7) conference on June 18, 2010, at the Strathclyde University, Glasgow, in Scotland, United Kingdom. The presentation title was "Mercury Measurement and Control in a CO_2-Enriched Flue Gas." See citation below:

  Pavlish, J.H. Mercury Measurement and Control in a CO_2-Enriched Flue Gas. Presented at the 7th International Workshop on Mercury Emissions from Coal (MEC7), Glasgow, Scotland, June 16–18, 2010.

8.4 Brochures, Fact Sheets, Newsletters, and Book Chapters

- Fact sheets were prepared, along with a Web site, to provide additional information that is an outcome of the research conducted under the outreach project "Seafood Treasures of the Hawaii and the U.S. Pacific Island Fisheries," which is a collaboration with the National Oceanographic and Atmospheric Association and Prairie Public Broadcasting. Resource materials can be accessed at www.undeerc.org/fish.

- Nick Ralston, Alex Azenkeng, and Laura Raymond prepared a book chapter detailing research outcomes from Hg–Se interaction research (2011). The book chapter is entitled "Selenium Modulates the Neurotoxic Effects of Methylmercury." The book is

Methylmercury and Neurotoxicity of the Current Topics in Neurotoxicity series, edited by M. Aschner and S. Ceccatelli.

- A technical newsletter was prepared and submitted to the CATM list that covers the scientific highlights concerning mercury that were given at the Air Quality Conference held in Washington, D.C., in October 2009. This newsletter can be found at the Web site www.undeerc.org/CATM. See Citation below:

  Center for Air Toxic Metals®. *CATM® Technical Newsletter* 2010, *14* (1).

8.5 Patents

Technology transfer is critical to move research from the laboratory to the commercial domain. Toward this goal, DOE-funded research under this subtask resulted in the filing of one provisional patent during the course of this work, noted below:

- Measurement of Multimetals and Total Halogens in a Gas Stream. Inventors: Nicholas B. Lentz and John H. Pavlish. Assigned to the Energy & Environmental Research Center Foundation, Grand Forks, North Dakota. A full patent application is pending.

APPENDIX A

LEACHING RESULTS FOR INDIVIDUAL ELEMENTS

TABLE OF CONTENTS

LIST OF FIGURES

Continued…

LIST OF FIGURES (continued)

Continued…

LIST OF FIGURES (continued)

Continued…

LIST OF FIGURES (continued)

Continued…

LIST OF FIGURES (continued)

Continued…

LIST OF FIGURES (continued)

APPENDIX A1

ARSENIC

LIST OF FIGURES

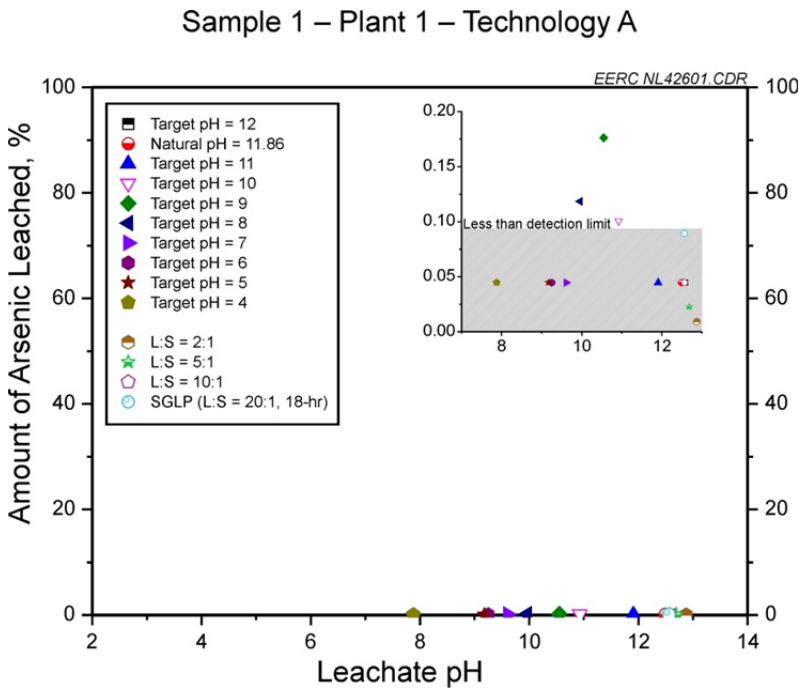

Figure A1-1. Percent of total arsenic leached from Sample 1 – Plant 1 – Technology A.

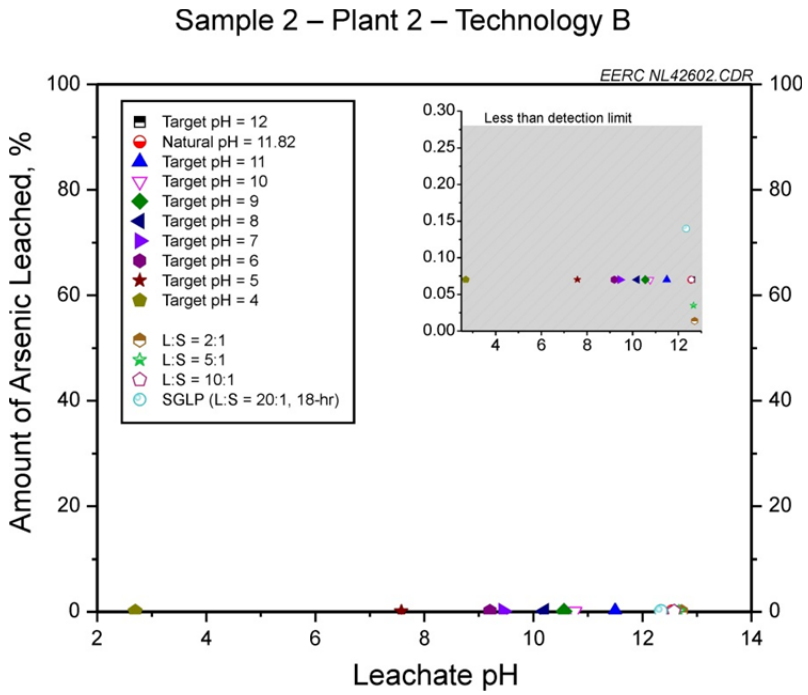

Figure A1-2. Percent of total arsenic leached from Sample 2 – Plant 2 – Technology B – all values less than the leachate detection limit.

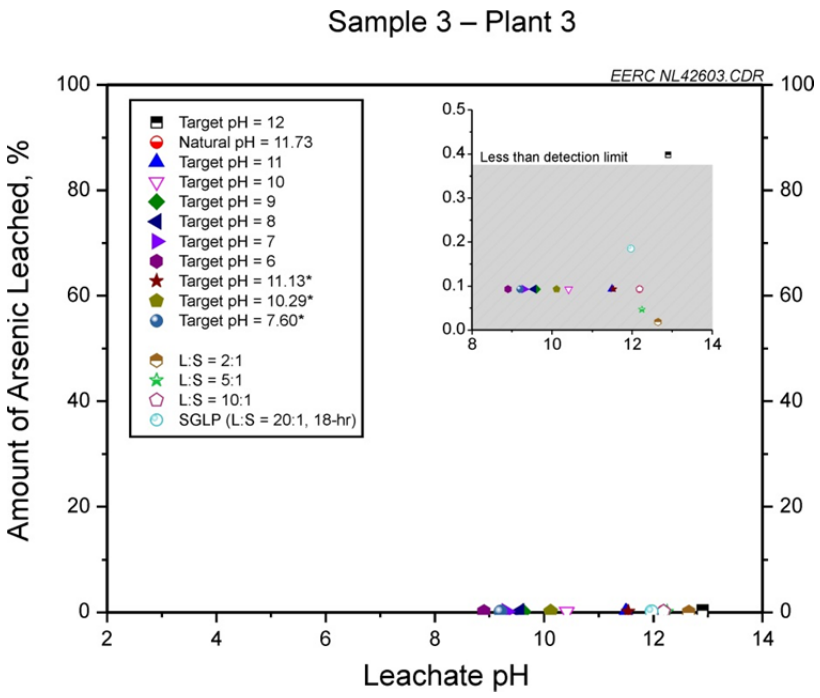

Figure A1-3. Percent of total arsenic leached from Sample 3 – Plant 3.

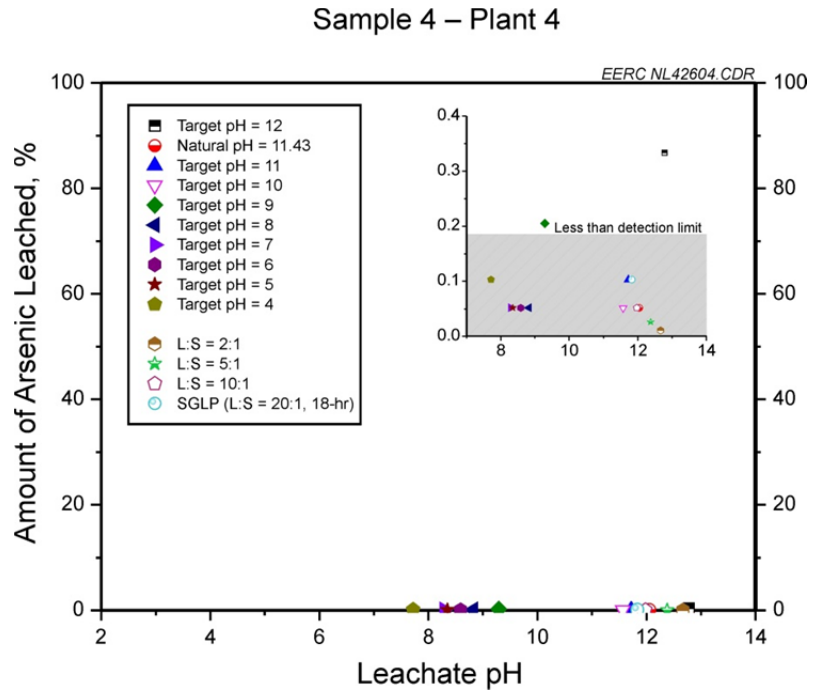

Figure A1-4. Percent of total arsenic leached from Sample 4 – Plant 4.

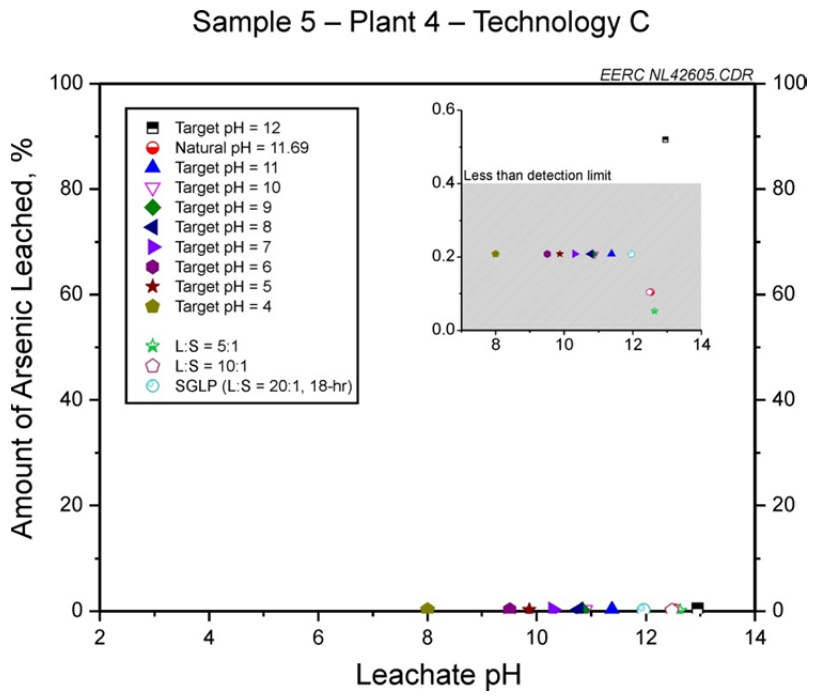

Figure A1-5. Percent of total arsenic leached from Sample 5 – Plant 4 – Technology C.

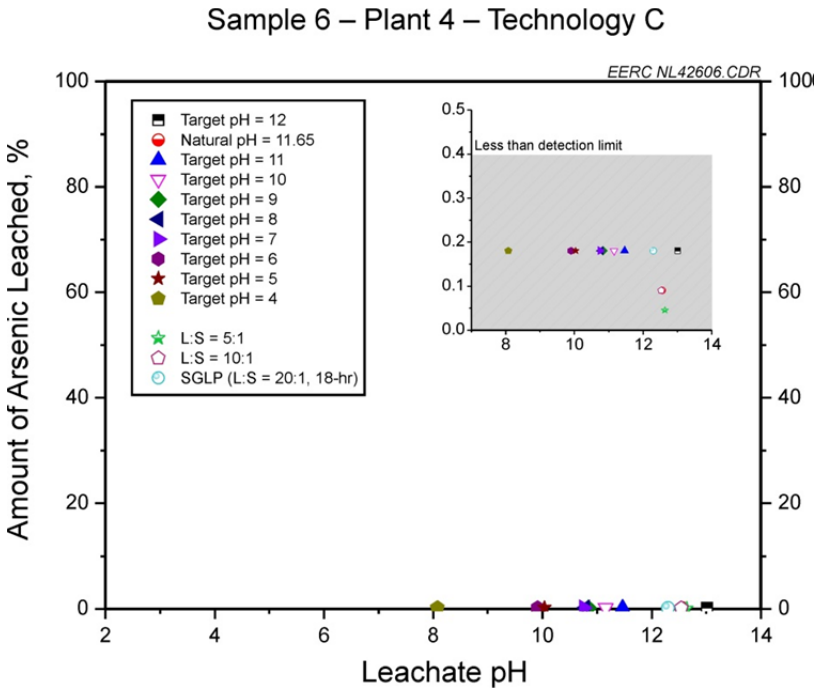

Figure A1-6. Percent of total arsenic leached from Sample 6 – Plant 4 – Technology C – all values less than the leachate detection limit.

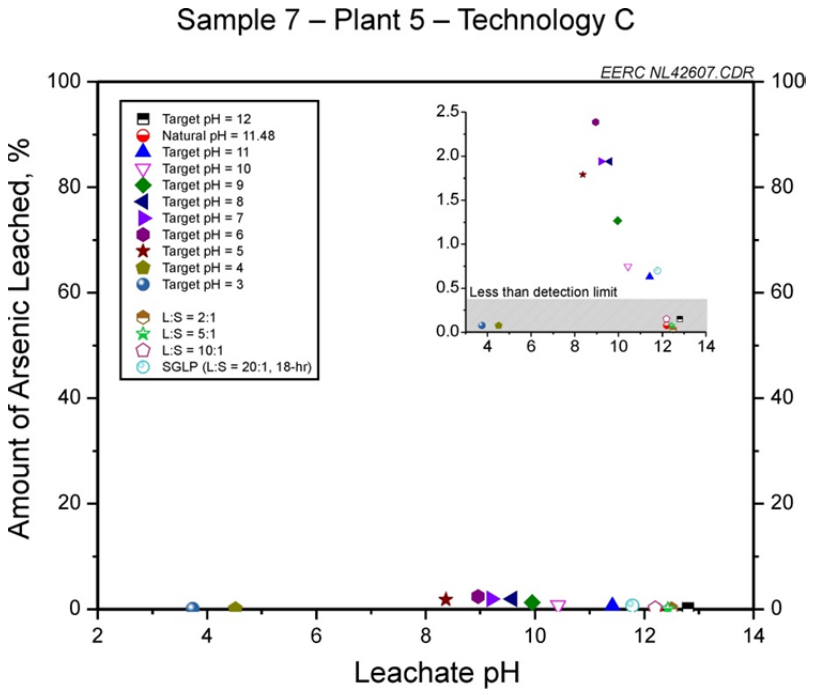

Figure A1-7. Percent of total arsenic leached from Sample 7 – Plant 5 – Technology C.

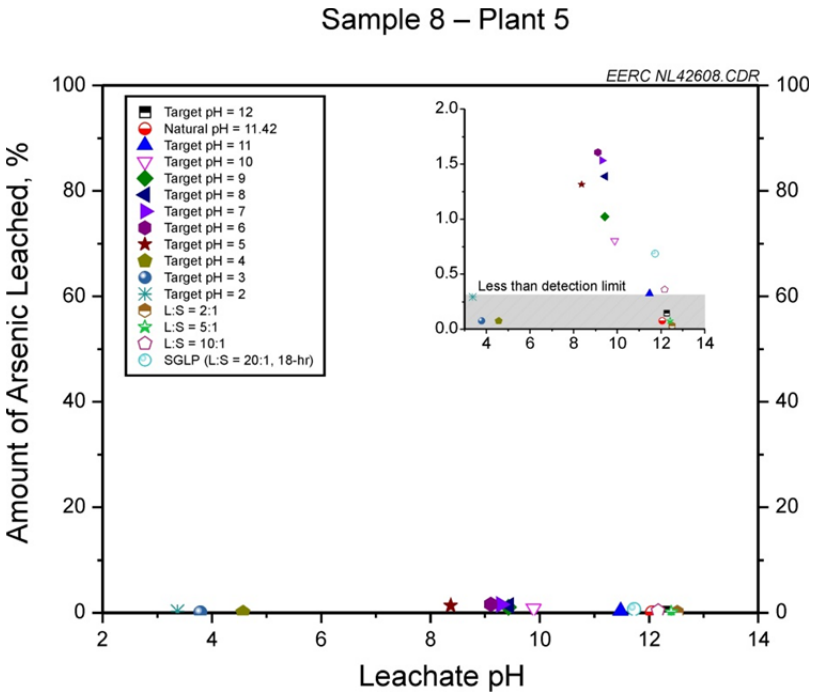

Figure A1-8. Percent of total arsenic leached from Sample 8 – Plant 5.

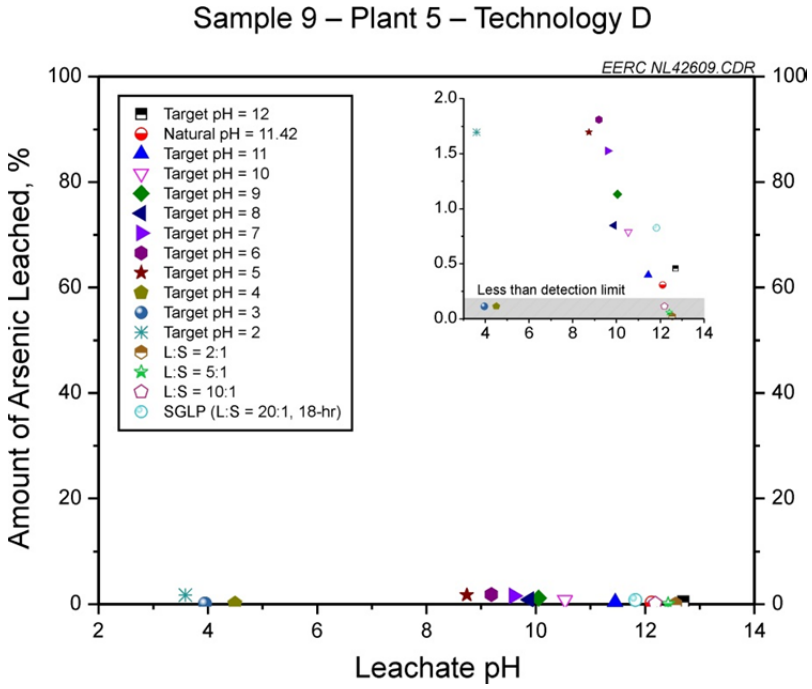

Figure A1-9. Percent of total arsenic leached from Sample 9 – Plant 5 – Technology D.

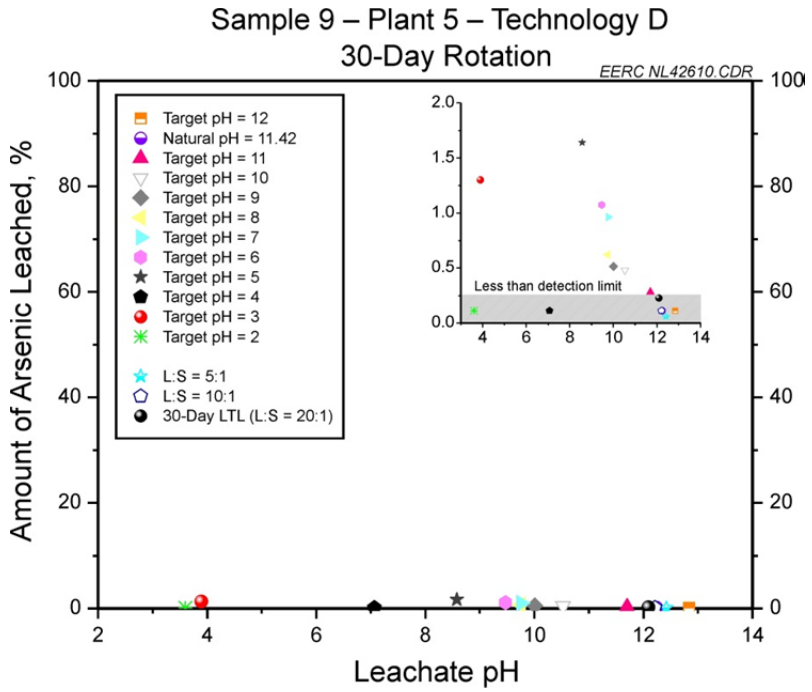

Figure A1-10. Percent of total arsenic leached from Sample 9 – Plant 5 – Technology D – 30-day extension of all leaching tests.

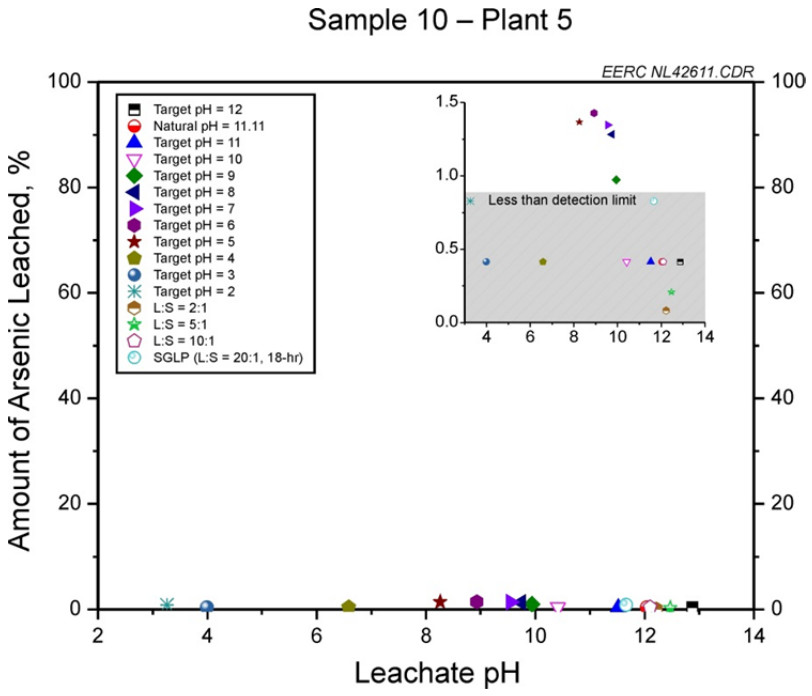

Figure A1-11. Percent of total arsenic leached from Sample 10 – Plant 5.

APPENDIX A2

CADMIUM

LIST OF FIGURES

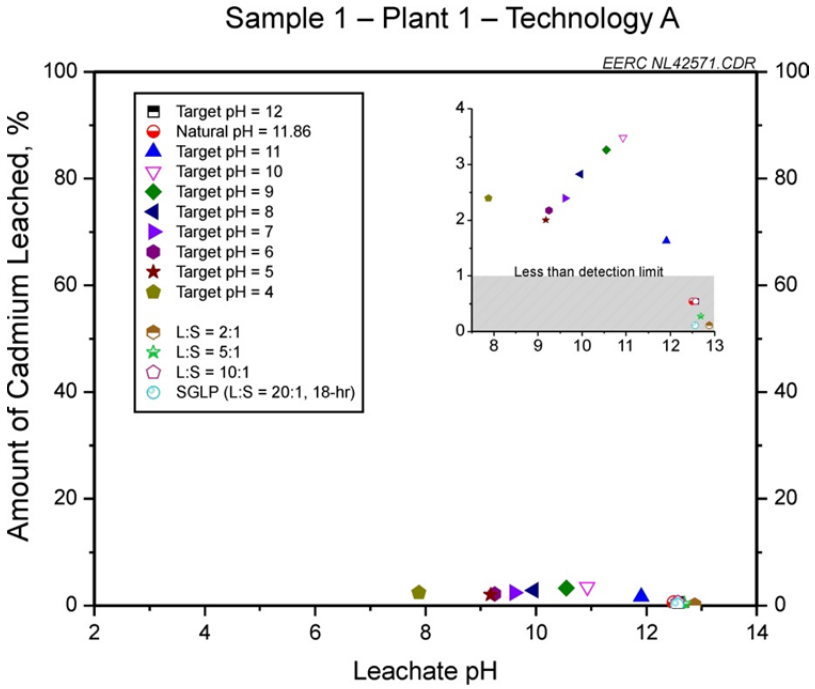

Figure A2-1. Percent of total cadmium leached from Sample 1 – Plant 1 – Technology A.

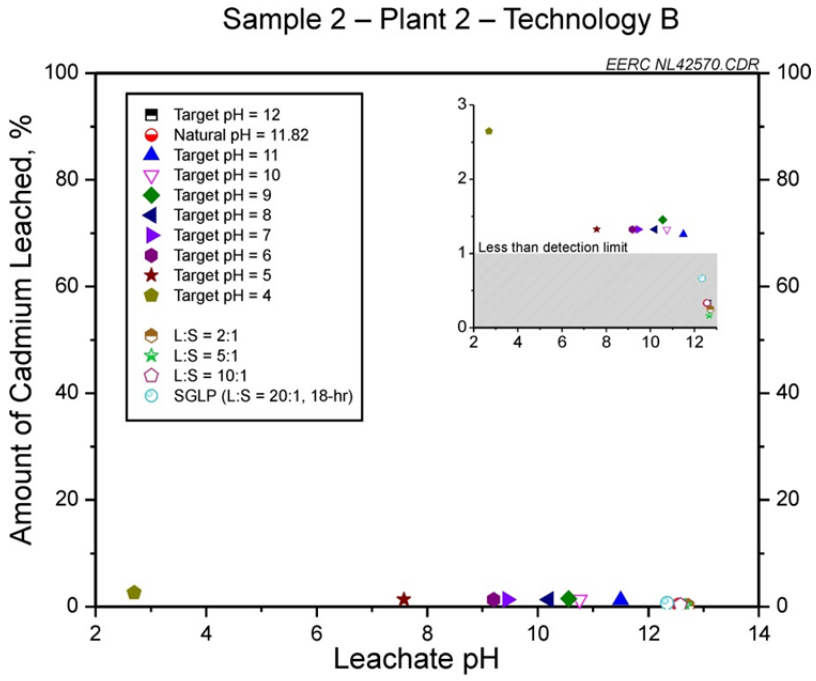

Figure A2-2. Percent of total cadmium leached from Sample 2 – Plant 2 – Technology B.

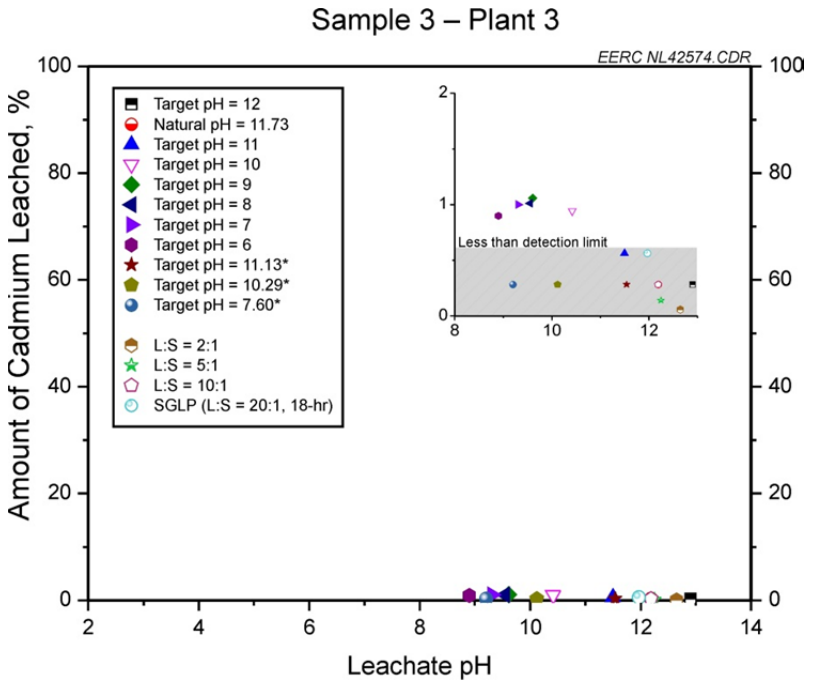

Figure A2-3. Percent of total cadmium leached from Sample 3 – Plant 3.

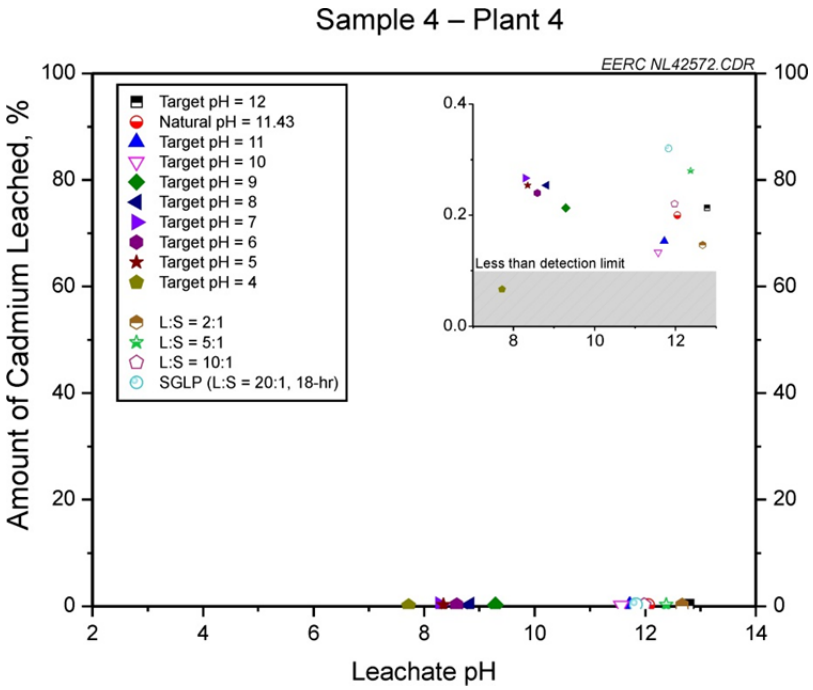

Figure A2-4. Percent of total cadmium leached from Sample 4 – Plant 4.

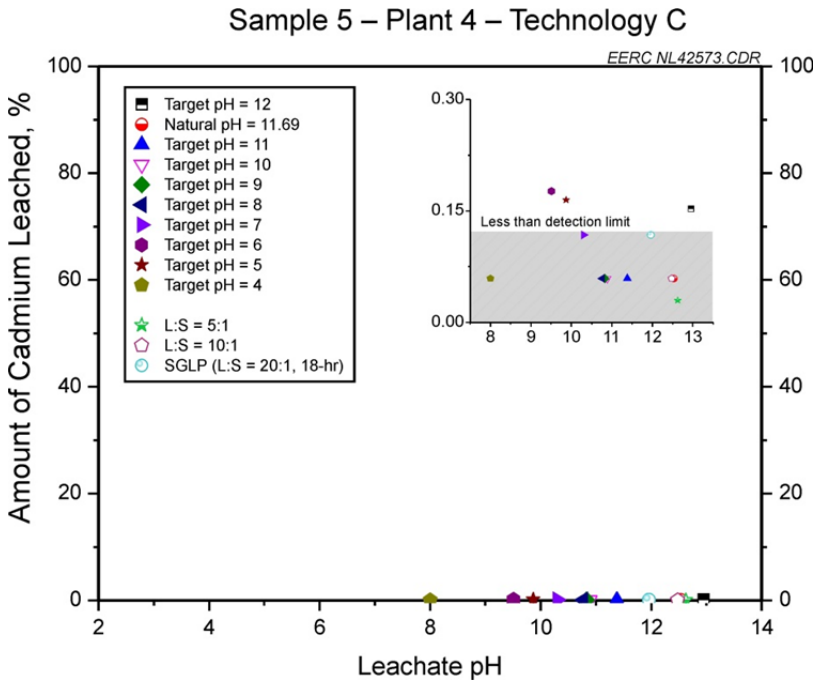

Figure A2-5. Percent of total cadmium leached from Sample 5 – Plant 4 – Technology C.

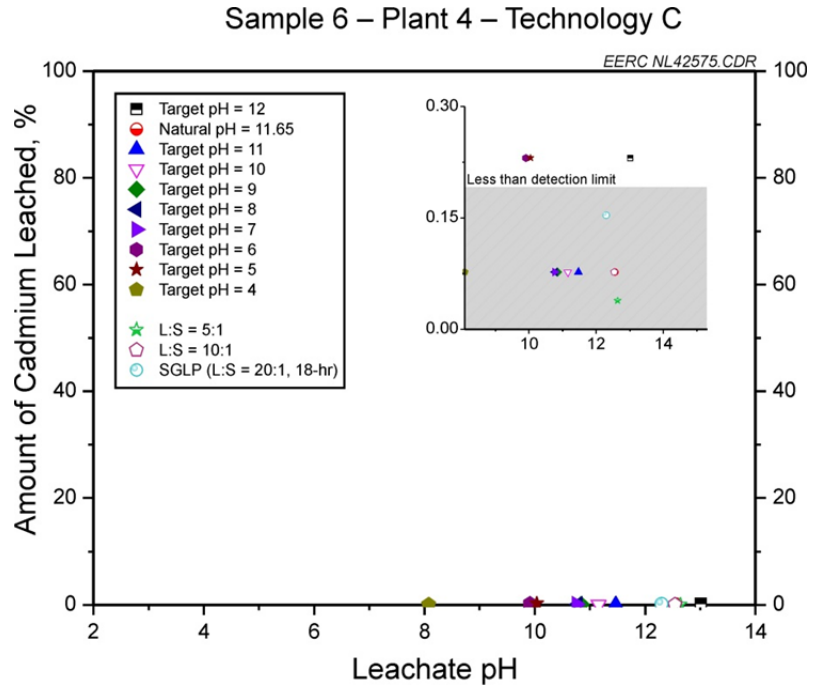

Figure A2-6. Percent of total cadmium leached from Sample 6 – Plant 4 – Technology C.

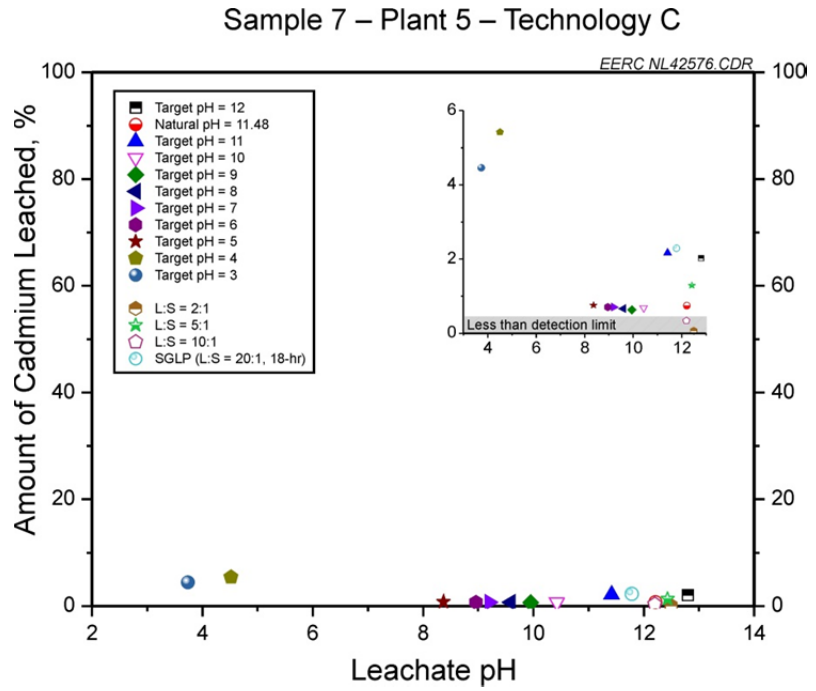

Figure A2-7. Percent of total cadmium leached from Sample 7 – Plant 5 – Technology C.

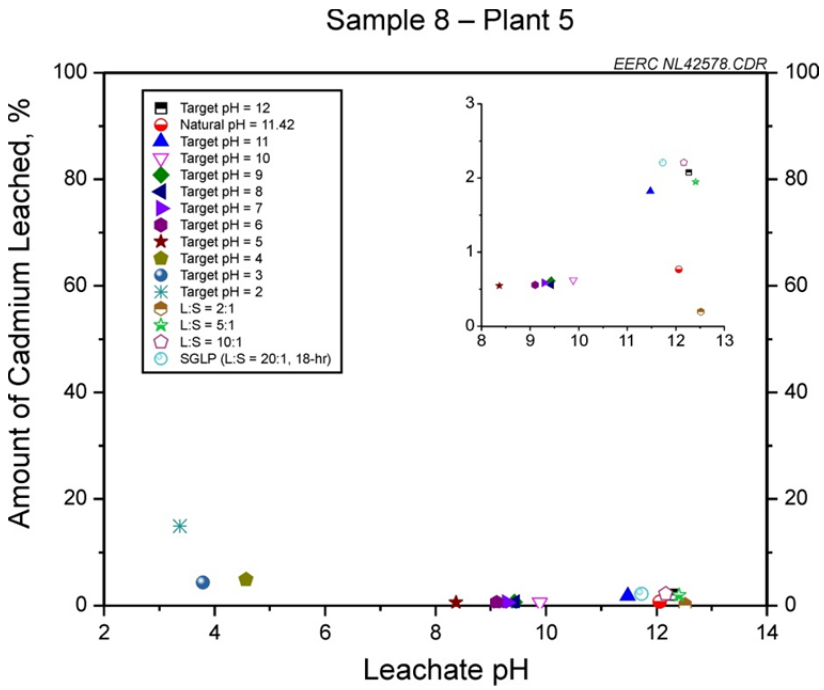

Figure A2-8. Percent of total cadmium leached from Sample 8 – Plant 5. The inset contains only values less than 3% and over the pH range of 8–13.

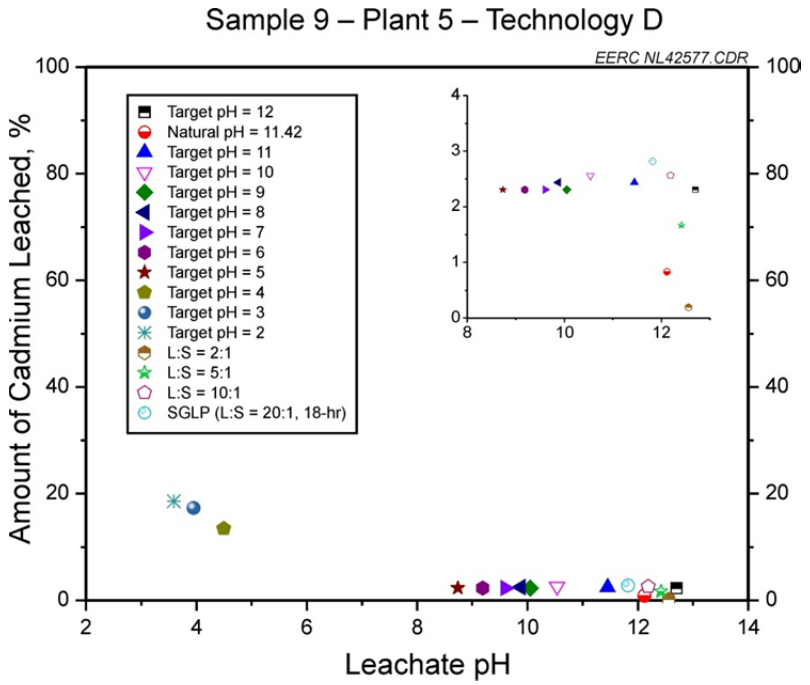

Figure A2-9. Percent of total cadmium leached from Sample 9 – Plant 5 – Technology D. The inset contains only values less than 4% and over the pH range of 8–13.

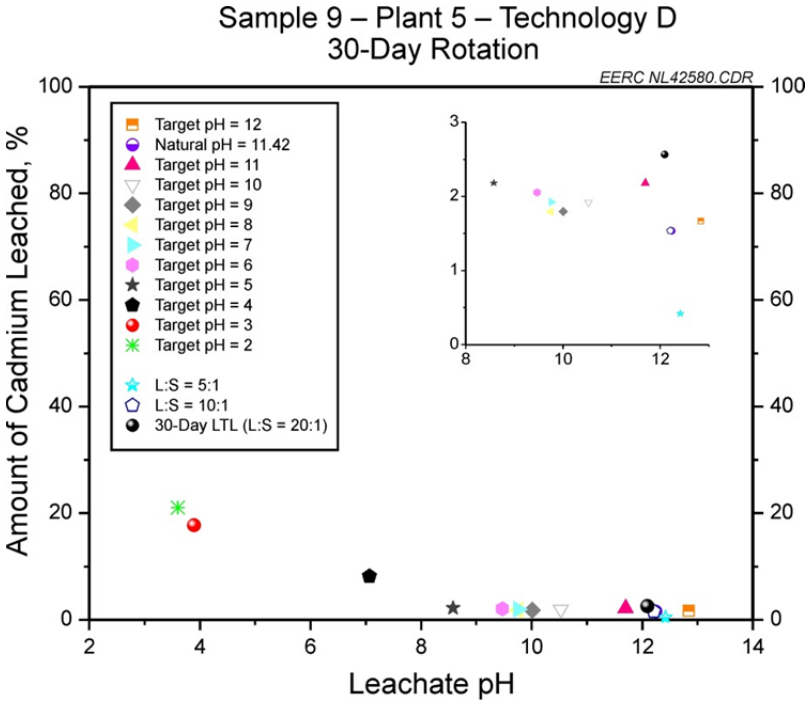

Figure A2-10. Percent of total cadmium leached from Sample 9 – Plant 5 – Technology D – 30-day extension of all leaching tests. The inset contains only values less than 3% and over the pH range of 8–13.

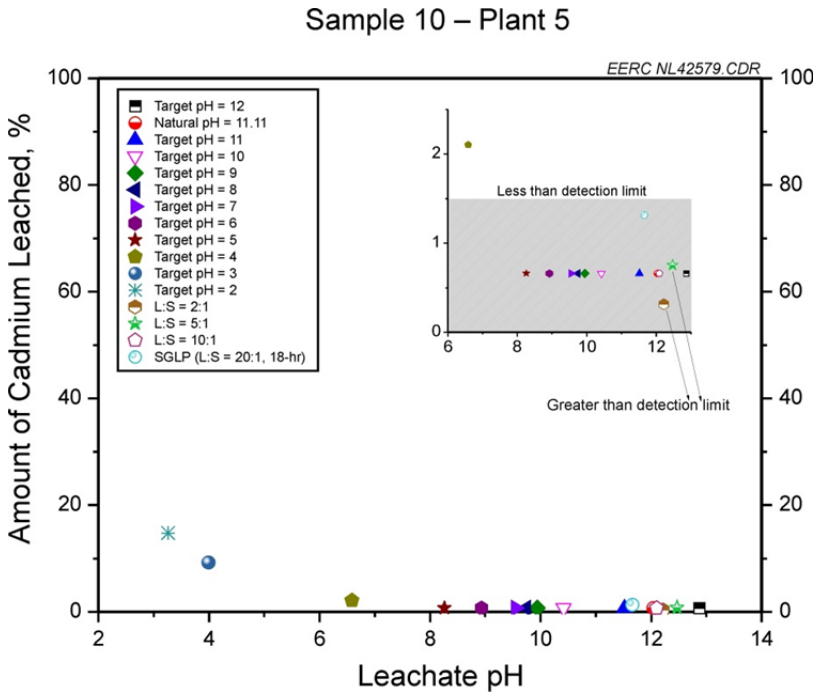

Figure A2-11. Percent of total cadmium leached from Sample 10 – Plant 5. The inset contains only values less than 2.5% and over the pH range of 6–13. The 2:1 and 5:1 liquid-to-solid ratio leaching samples had leachate concentrations above the detection limit; however, the low liquid-to-solid ratios resulted in percent of cadmium leached lower than the 10:1 and 20:1 liquid-to-solid ratios.

APPENDIX A3

CHROMIUM

LIST OF FIGURES

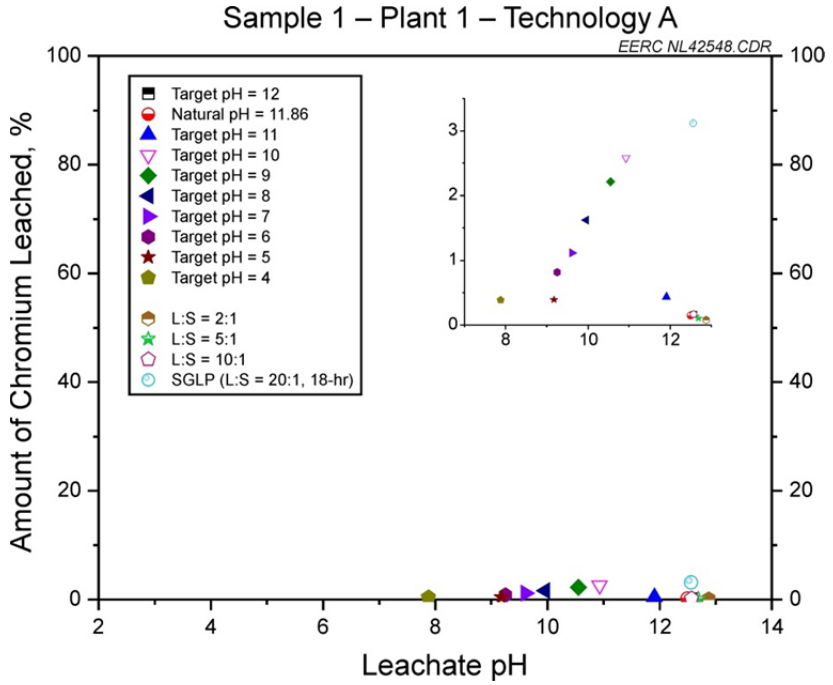

Figure A3-1. Percent of total chromium leached from Sample 1 – Plant 1 – Technology A.

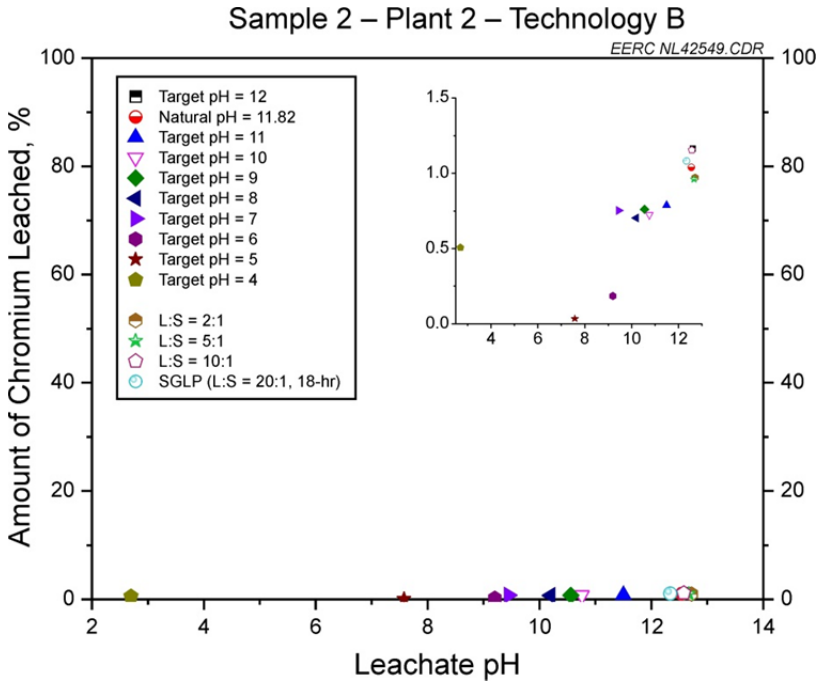

Figure A3-2. Percent of total chromium leached from Sample 2 – Plant 2 – Technology B.

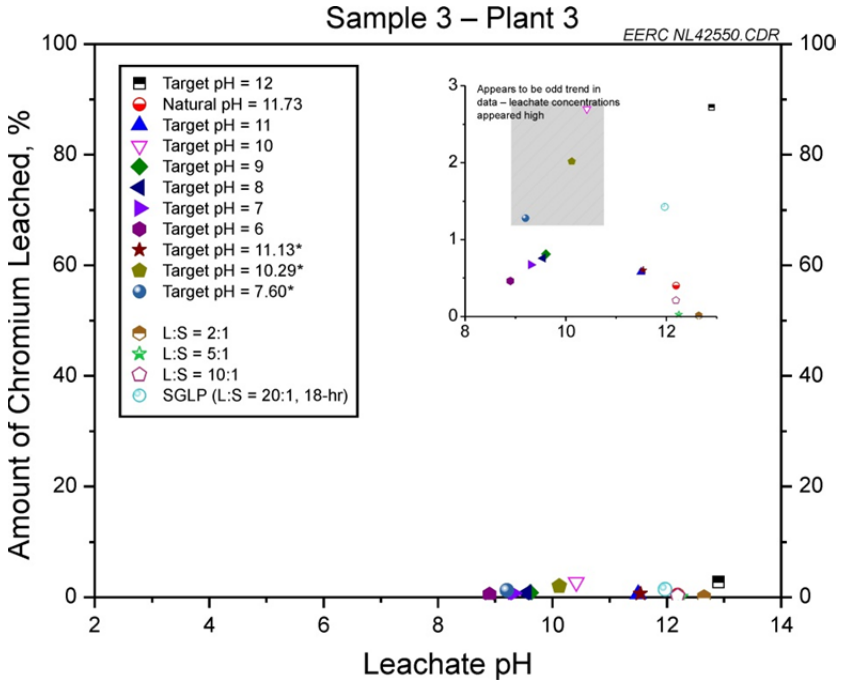

Figure A3-3. Percent of total chromium leached from Sample 3 – Plant 3. The data points for the target pH 7.60, 10.29, and 10 leachates appear unreliable because these do not fit in with the apparent data trend.

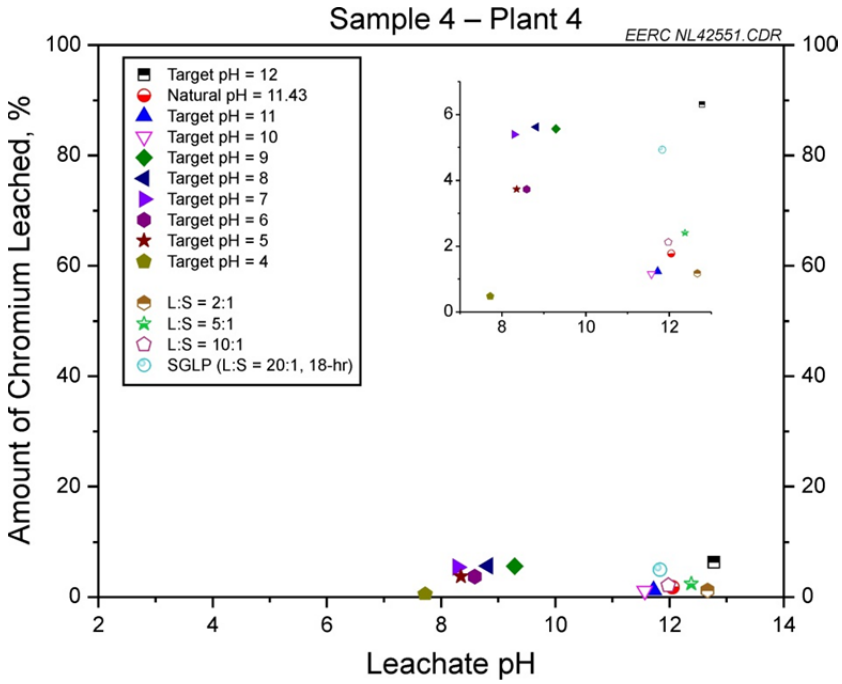

Figure A3-4. Percent of total chromium leached from Sample 4 – Plant 4.

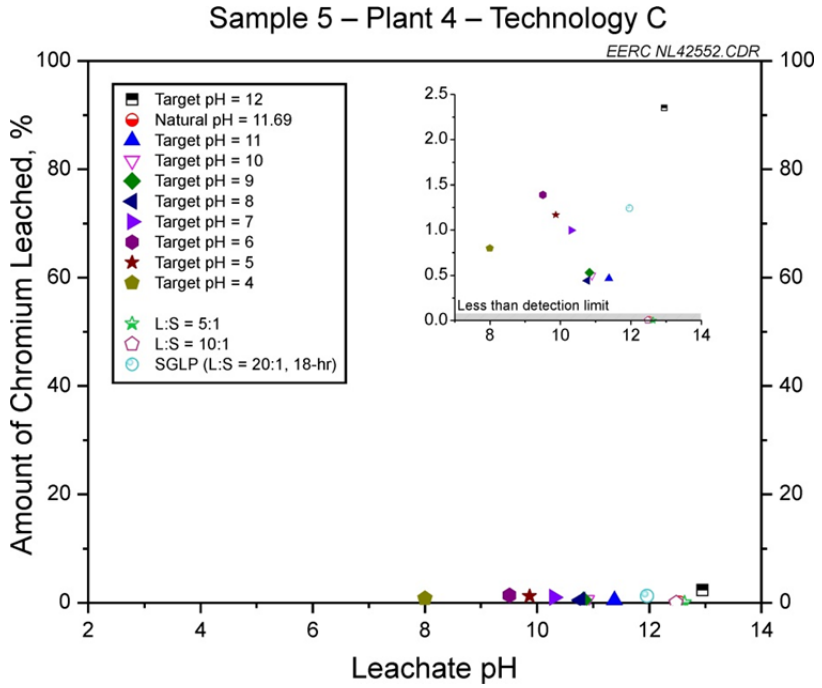

Figure A3-5. Percent of total chromium leached from Sample 5 – Plant 4 – Technology C.

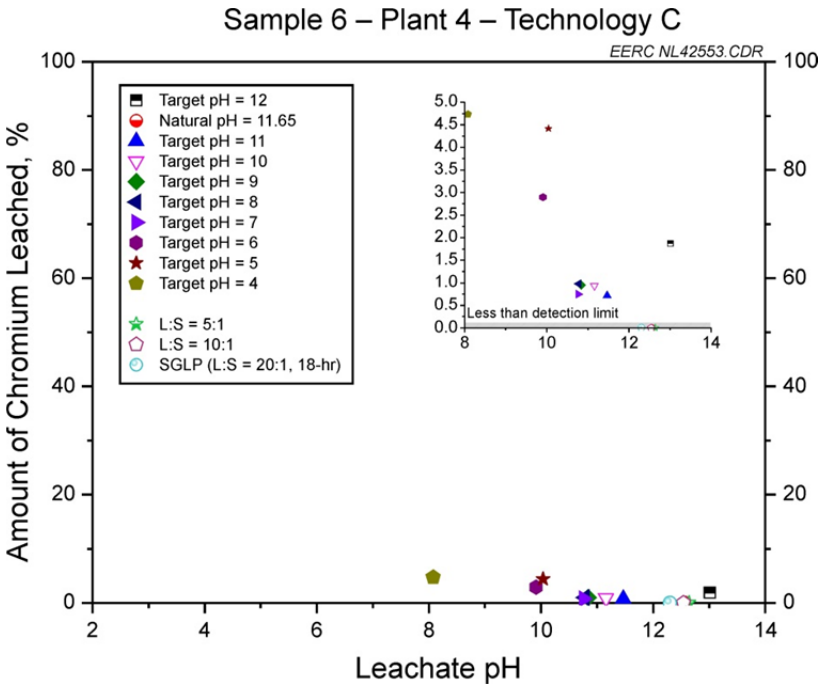

Figure A3-6. Percent of total chromium leached from Sample 6 – Plant 4 – Technology C.

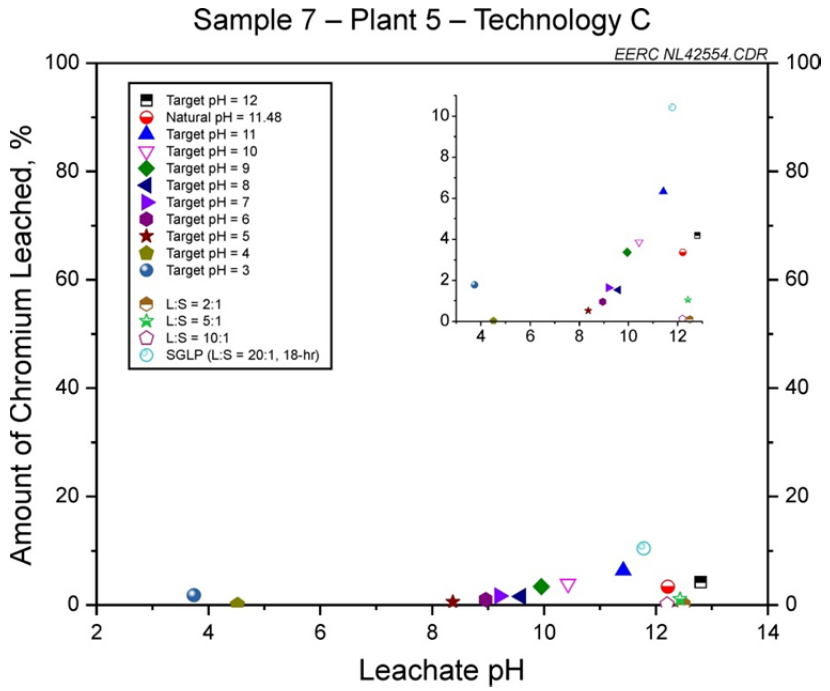

Figure A3-7. Percent of total chromium leached from Sample 7 – Plant 5 – Technology C.

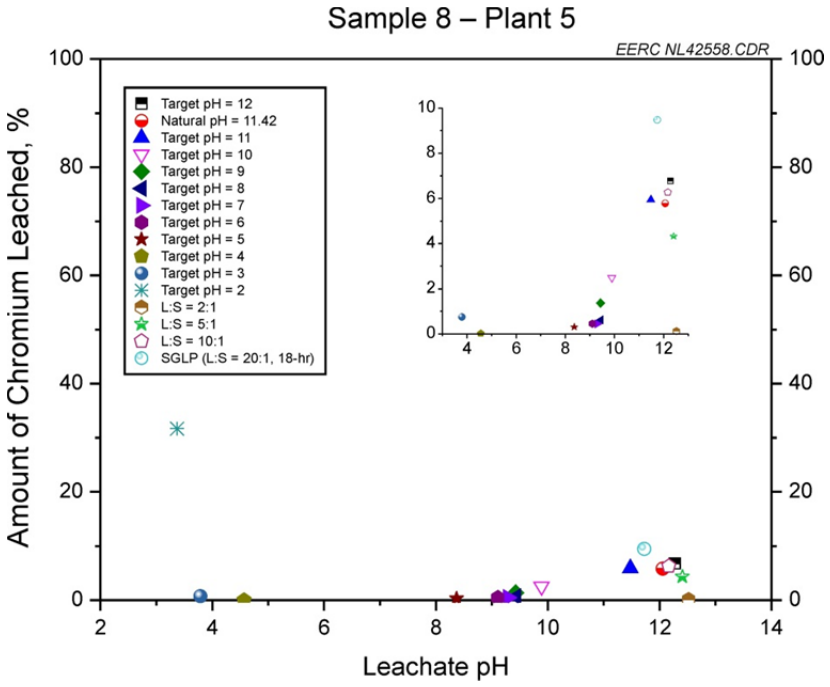

Figure A3-8. Percent of total chromium leached from Sample 8 – Plant 5. The inset contains only values less than 10%.

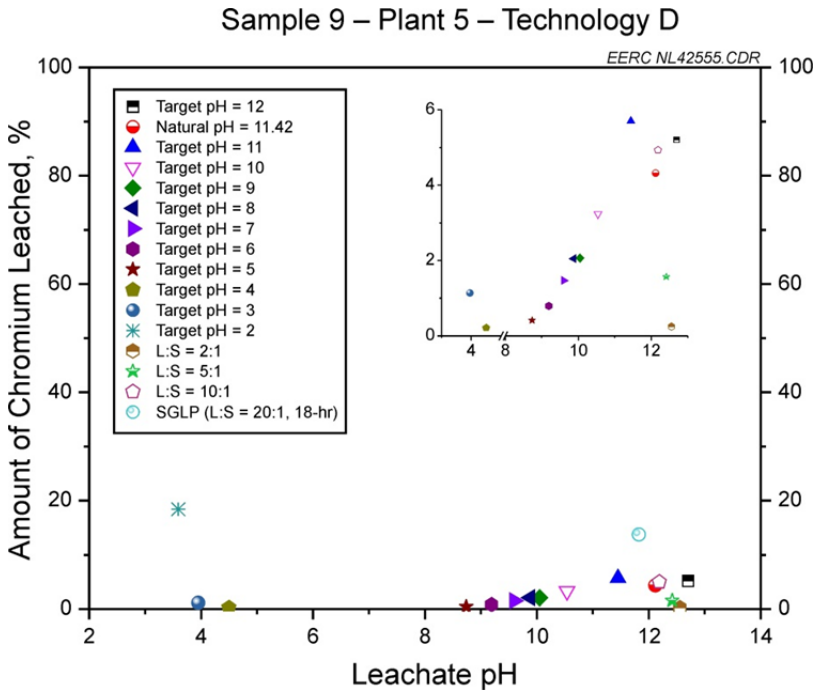

Figure A3-9. Percent of total chromium leached from Sample 9 – Plant 5 – Technology D. The inset contains only values less than 6%. The inset contains an axis break from leachate pH 5 to 8.

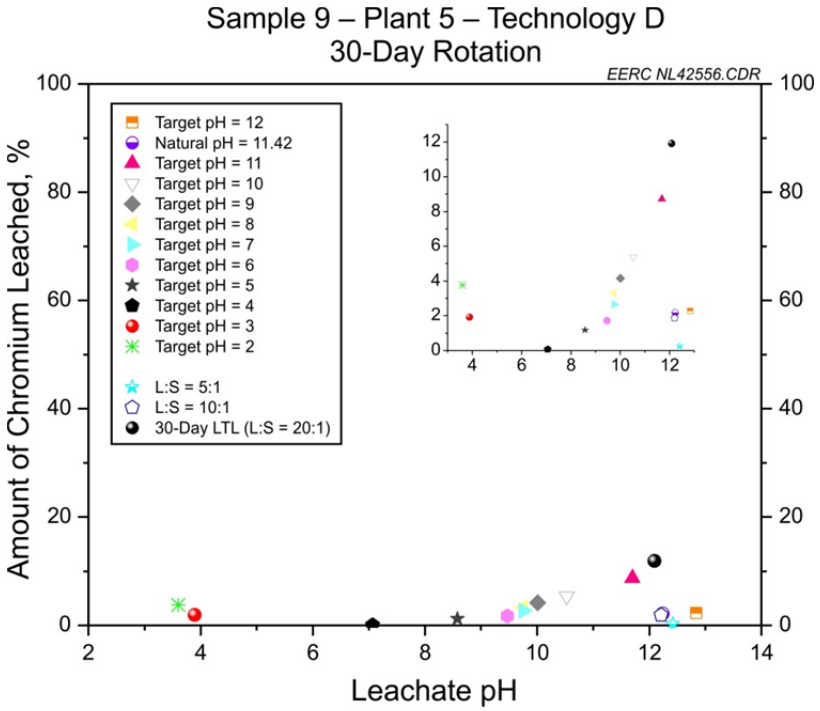

Figure A3-10. Percent of total chromium leached from Sample 9 – Plant 5 – Technology D – 30-day extension of all leaching tests.

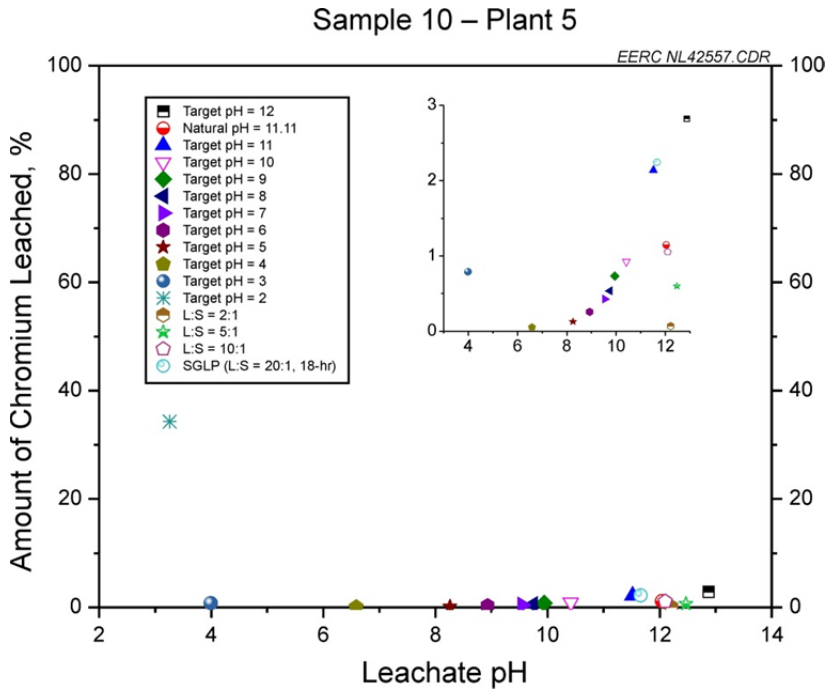

Figure A3-11. Percent of total chromium leached from Sample 10 – Plant 5. The inset contains only values less than 3%.

APPENDIX A4

MERCURY

LIST OF FIGURES

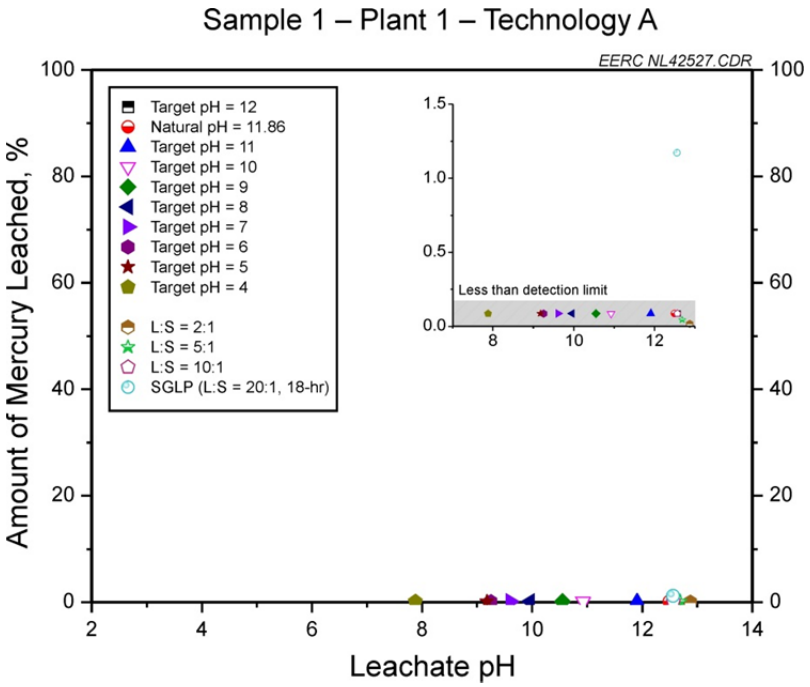

Figure A4-1. Percent of total mercury leached from Sample 1 – Plant 1 – Technology A.

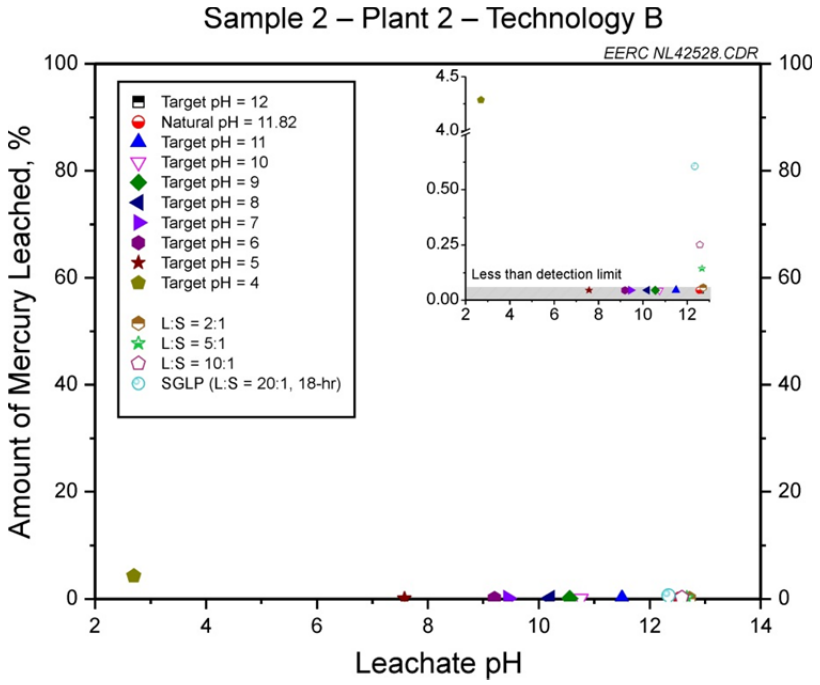

Figure A4-2. Percent of total mercury leached from Sample 2 – Plant 2 – Technology B. The inset contains an axis break from 0.75% to 4%.

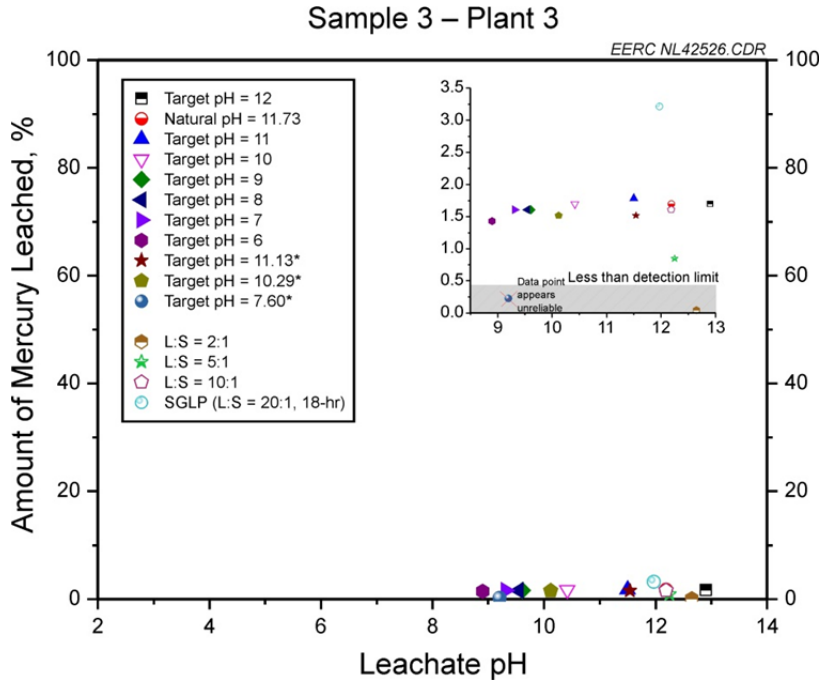

Figure A4-3. Percent of total mercury leached from Sample 3 – Plant 3. The data point for target pH 7.60 appears unreliable because it does not fit in with the apparent data trend.

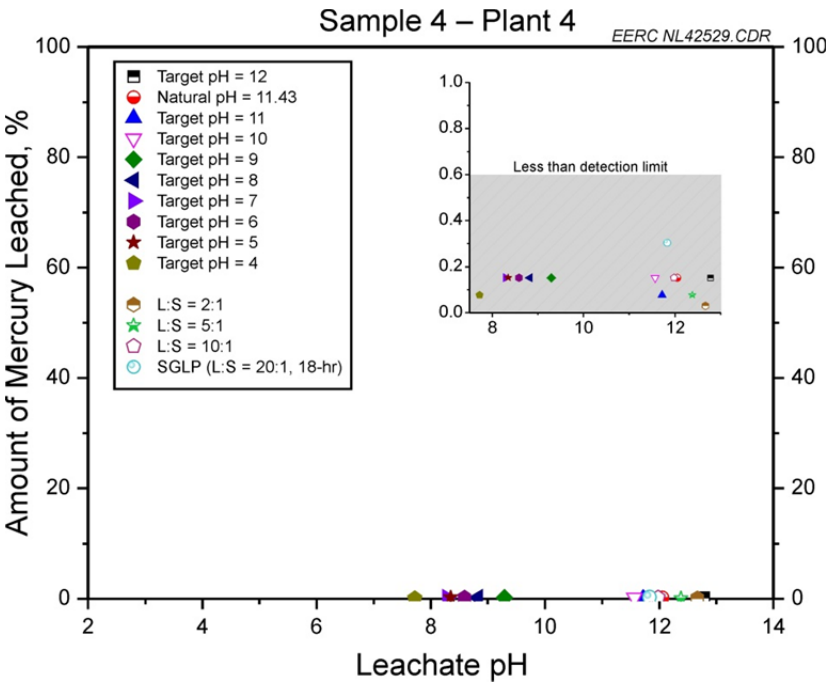

Figure A4-4. Percent of total mercury leached from Sample 4 – Plant 4 – all values less than the leachate detection limit.

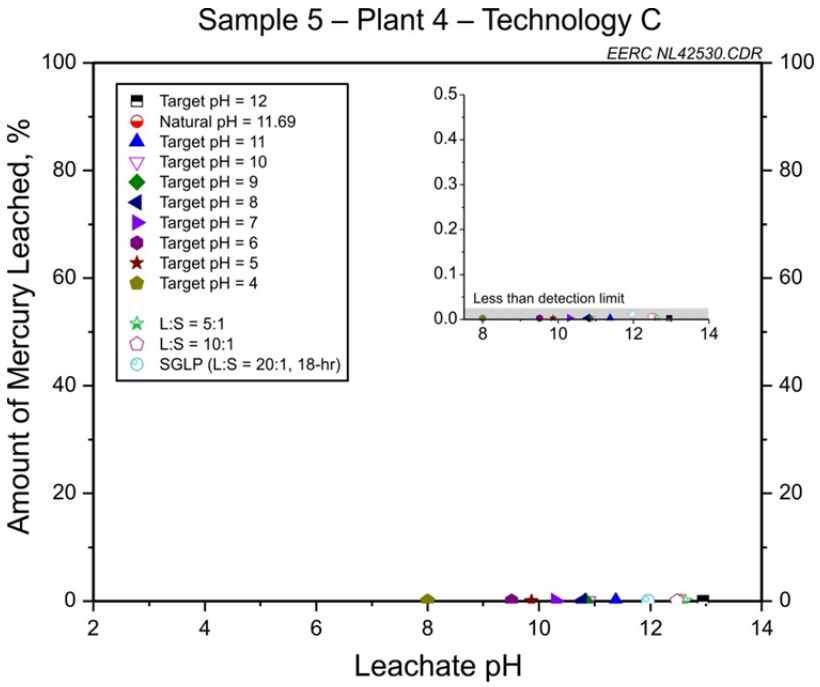

Figure A4-5. Percent of total mercury leached from Sample 5 – Plant 4 – Technology C – all values less than the leachate detection limit.

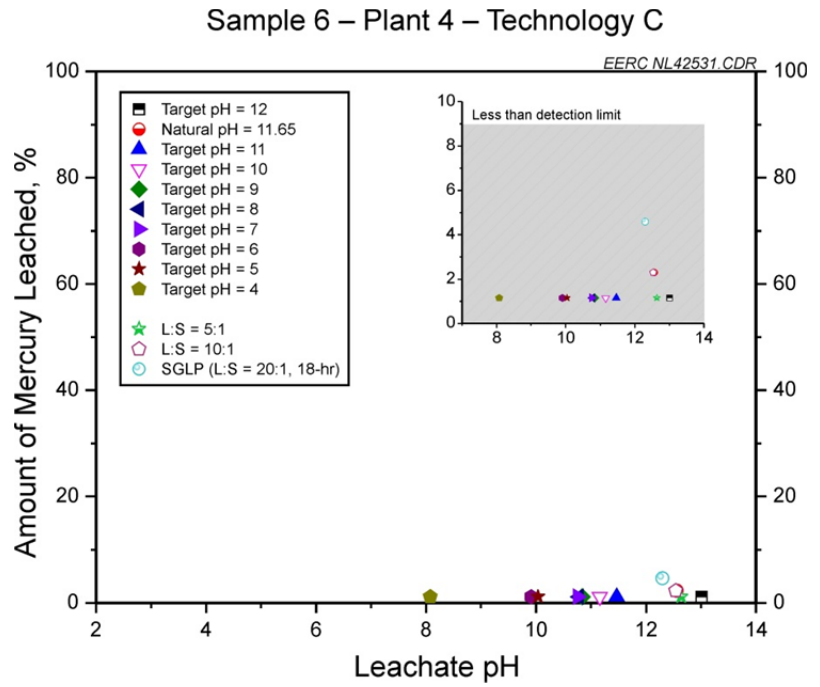

Figure A4-6. Percent of total mercury leached from Sample 6 – Plant 4 – Technology C – all values less than the leachate detection limit.

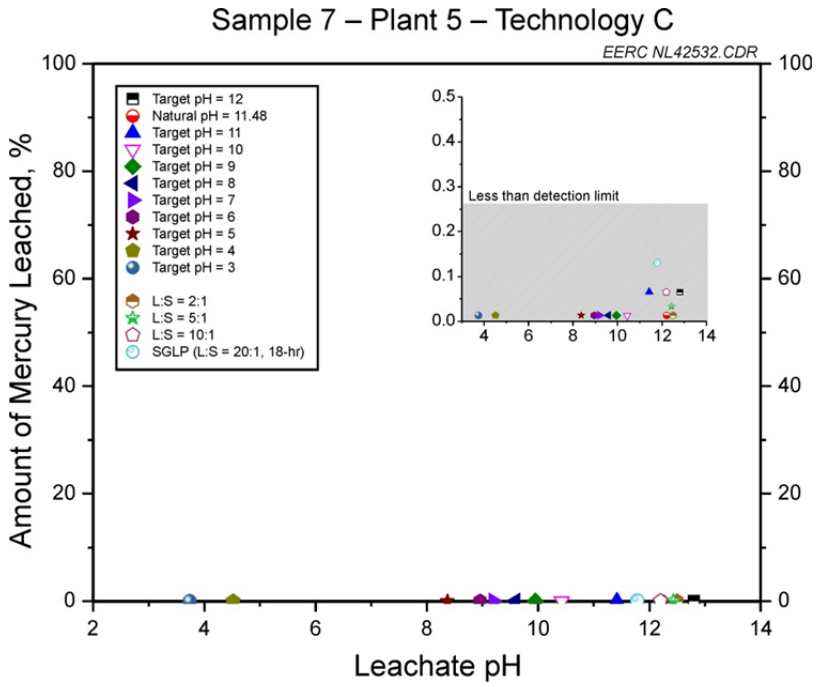

Figure A4-7. Percent of total mercury leached from Sample 7 – Plant 5 – Technology C – all values less than the leachate detection limit.

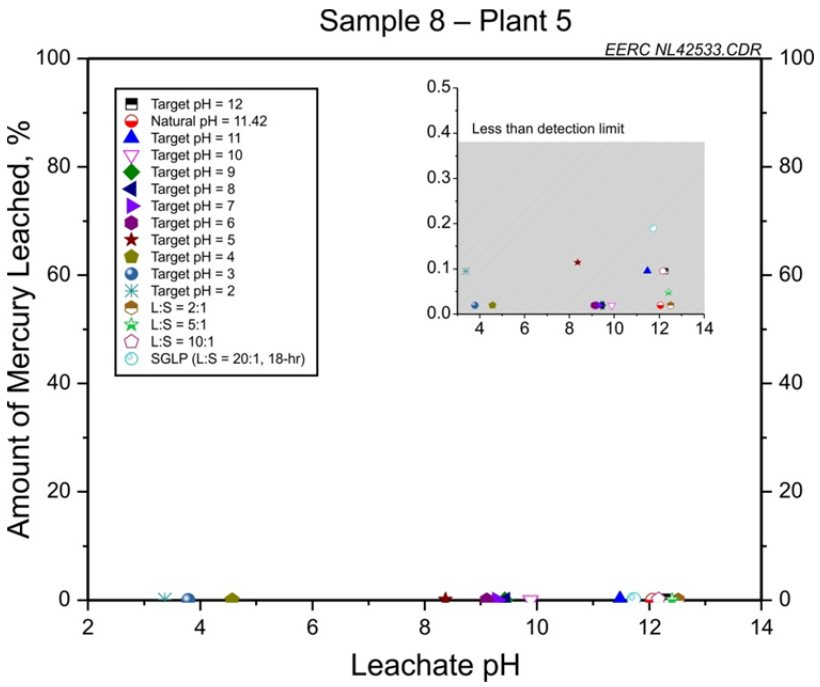

Figure A4-8. Percent of total mercury leached from Sample 8 – Plant 5 – all values less than the leachate detection limit.

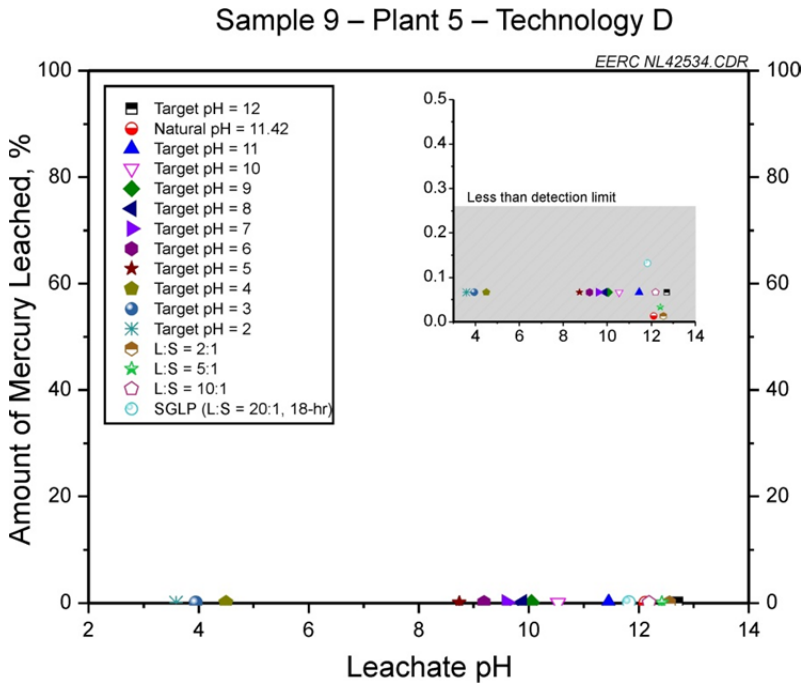

Figure A4-9. Percent of total mercury leached from Sample 9 – Plant 5 – Technology D – all values less than the leachate detection limit.

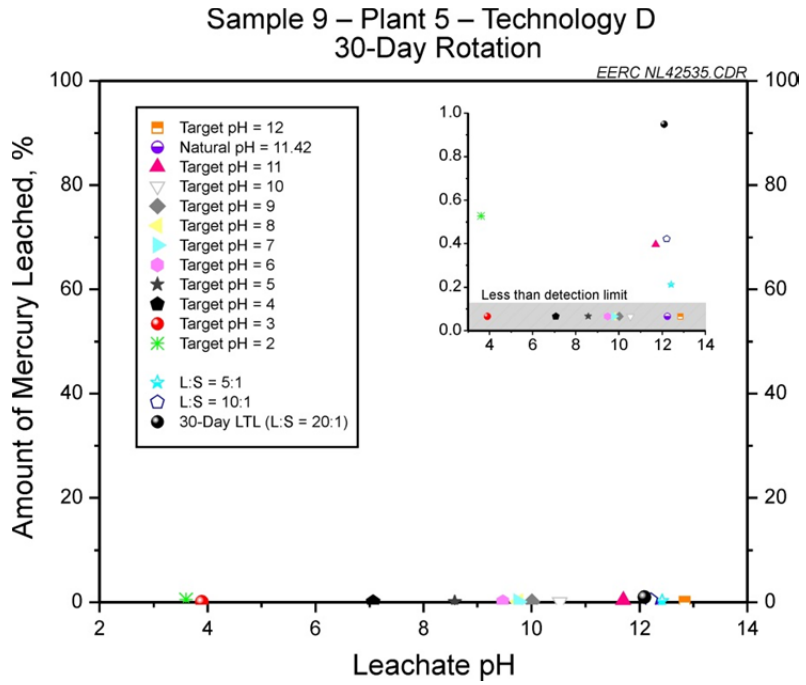

Figure A4-10. Percent of total mercury leached from Sample 9 – Plant 5 – Technology D – 30-day extension of all leaching tests.

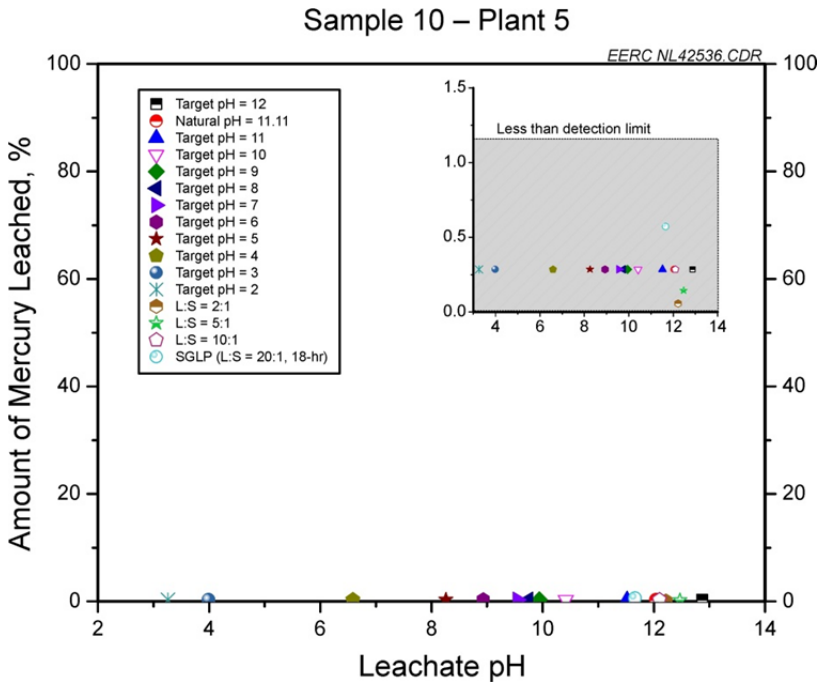

Figure A4-11. Percent of total mercury leached from Sample 10 – Plant 5 – all values less than the leachate detection limit.

APPENDIX A5

NICKEL

LIST OF FIGURES

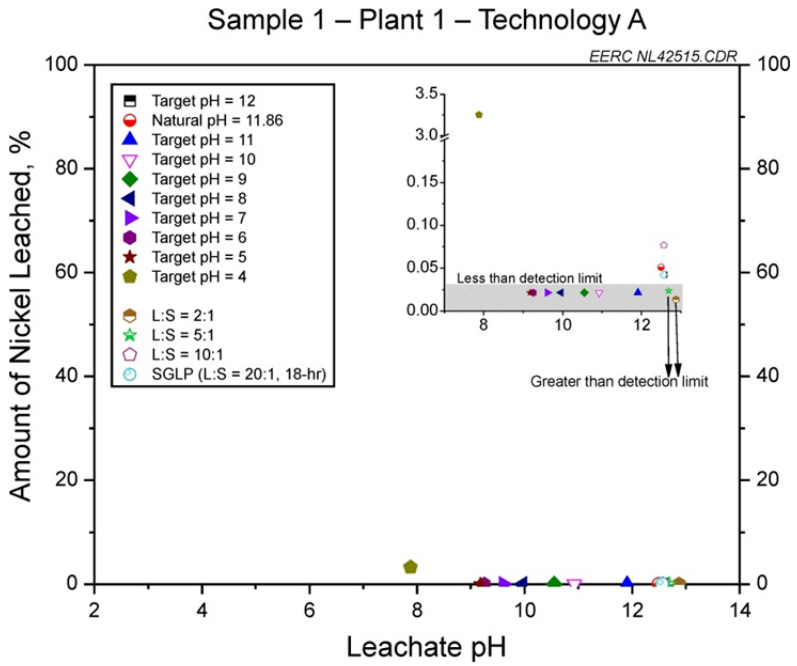

Figure A5-1. Percent of total nickel leached from Sample 1 – Plant 1 – Technology A – with y-axis break in inset. The 2:1 and 5:1 liquid-to-solid ratio leaching samples had leachate concentrations above the detection limit; however, the low liquid-to-solid ratios resulted in percent of nickel leached lower than the 10:1 and 20:1 liquid-to-solid ratios.

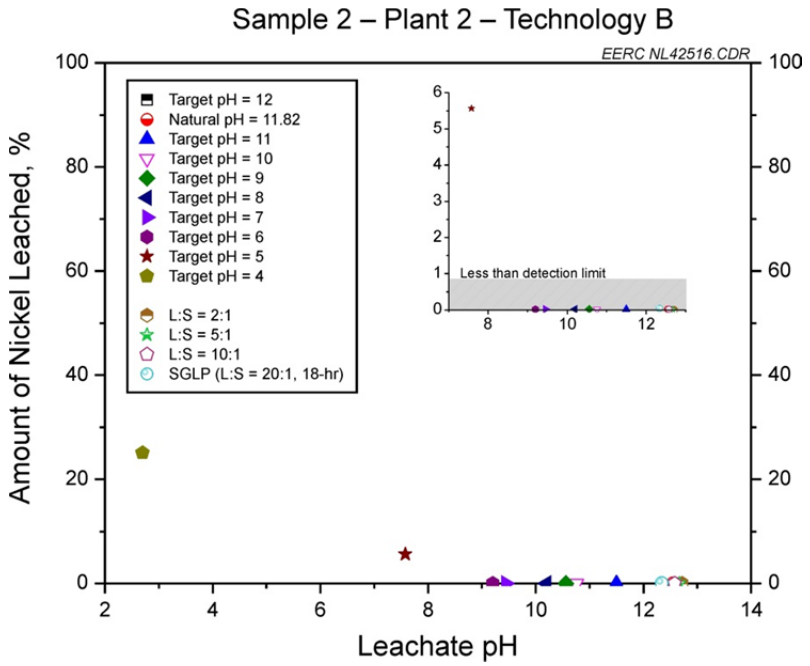

Figure A5-2. Percent of total nickel leached from Sample 2 – Plant 2 – Technology B. The inset contains only values less than 6%.

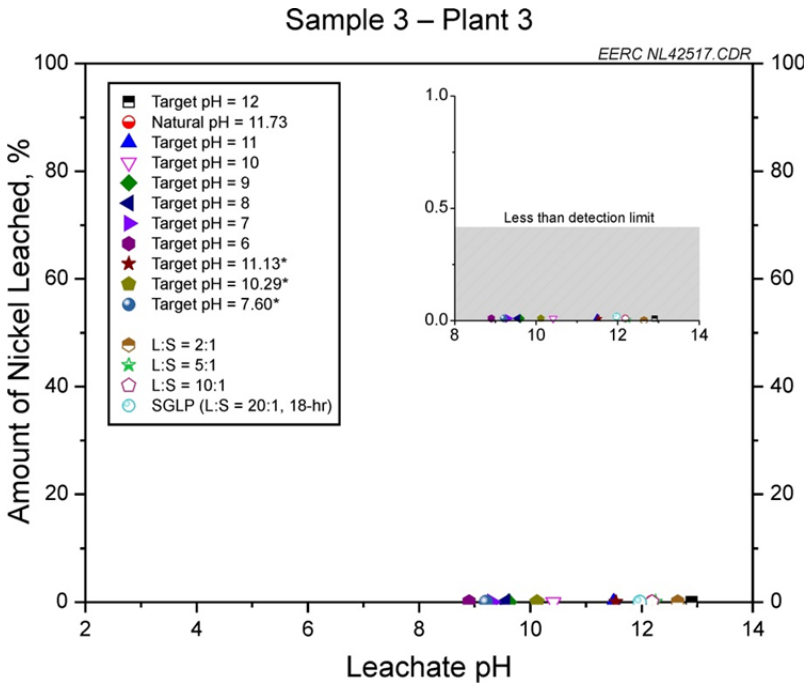

Figure A5-3. Percent of total nickel leached from Sample 3 – Plant 3 – all values less than the leachate detection limit.

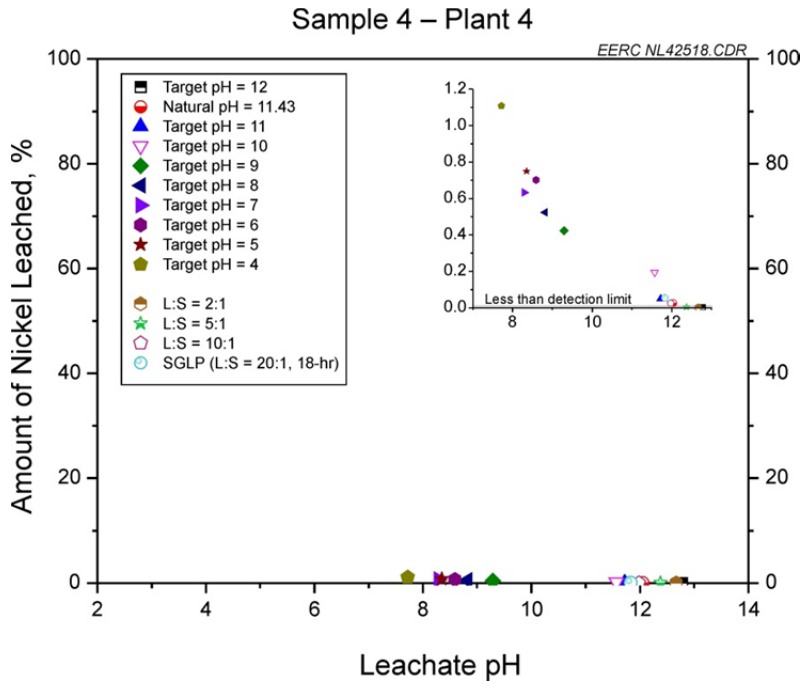

Figure A5-4. Percent of total nickel leached from Sample 4 – Plant 4.

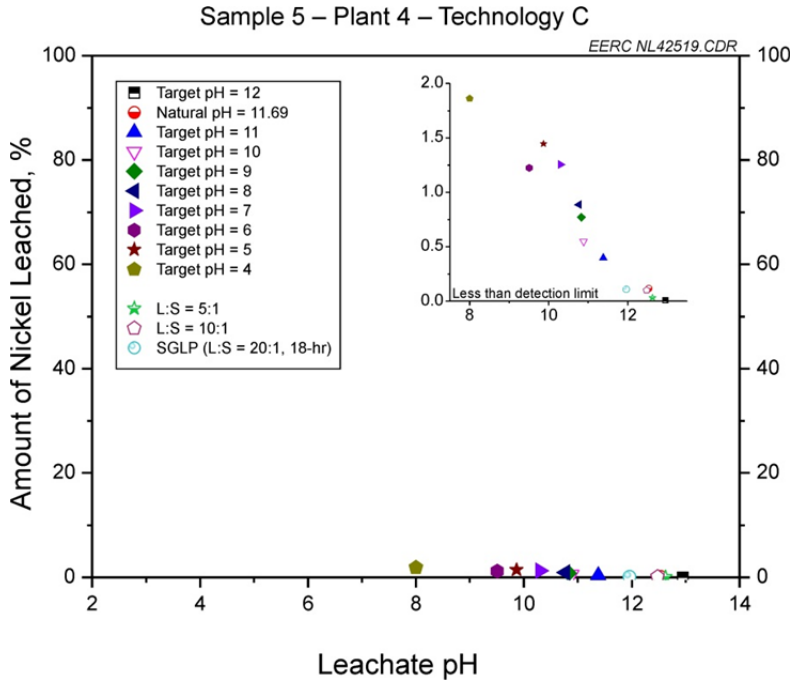

Figure A5-5. Percent of total nickel leached from Sample 5 – Plant 4 – Technology C.

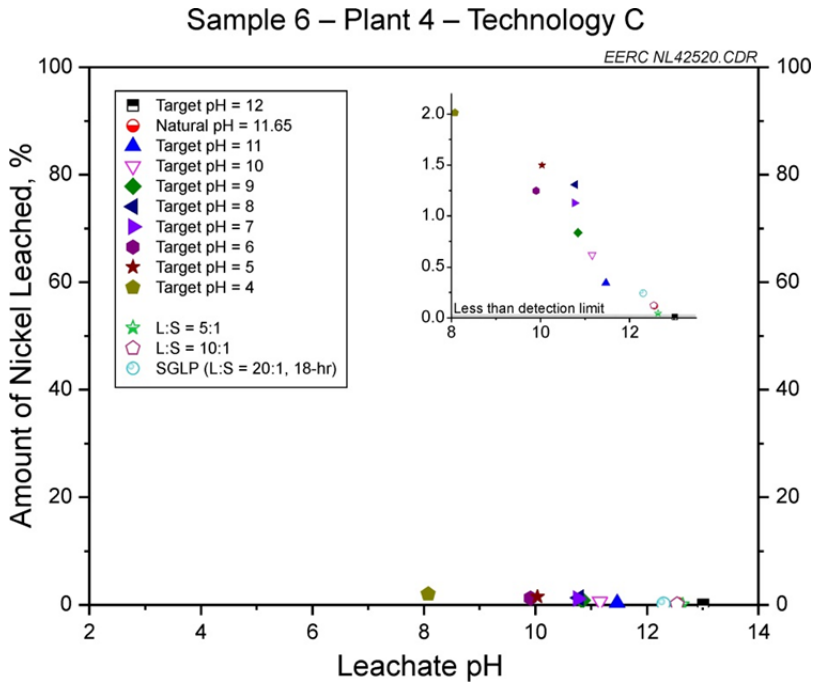

Figure A5-6. Percent of total nickel leached from Sample 6 – Plant 4 – Technology C.

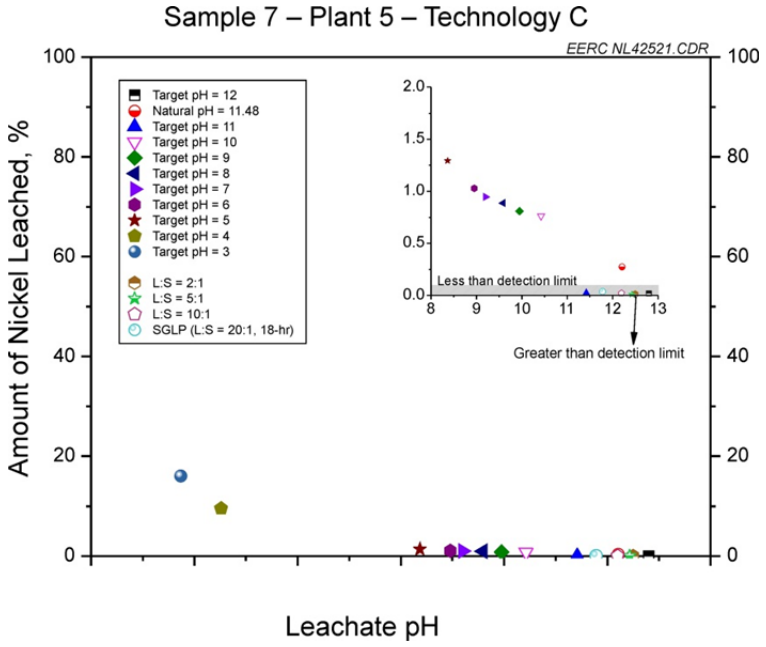

Figure A5-7. Percent of total nickel leached from Sample 7 – Plant 5 – Technology C. The inset contains only values less than 2% and over the pH range of 8–13. The 2:1 liquid-to-solid ratio leaching sample had a leachate concentration above the detection limit; however, the low liquid-to-solid ratio resulted in percent of nickel leached lower than the other liquid-to-solid ratios.

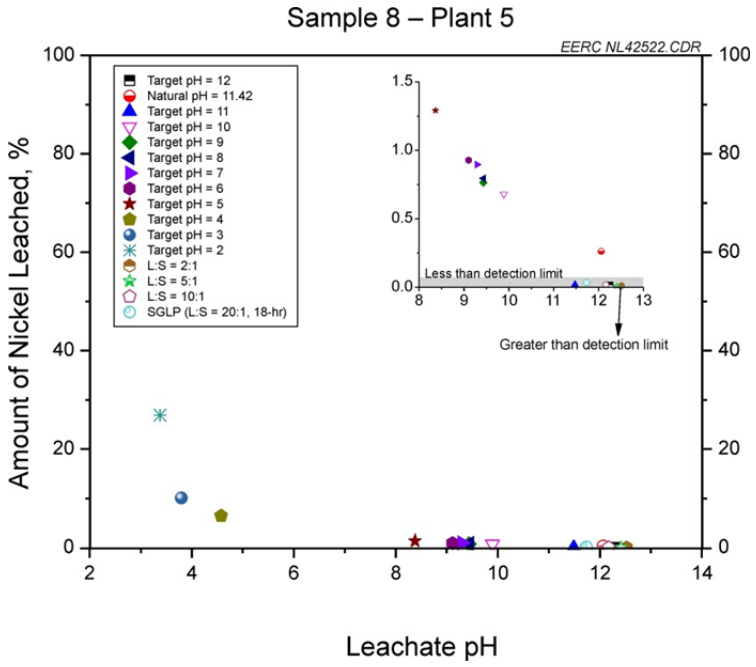

Figure A5-8. Percent of total nickel leached from Sample 8 – Plant 5. The inset contains only values less than 1.5% and over the pH range of 8–13. The 2:1 liquid-to-solid ratio leaching sample had a leachate concentration above the detection limit; however, the low liquid-to-solid ratio resulted in percent of nickel leached lower than the other liquid-to-solid ratios.

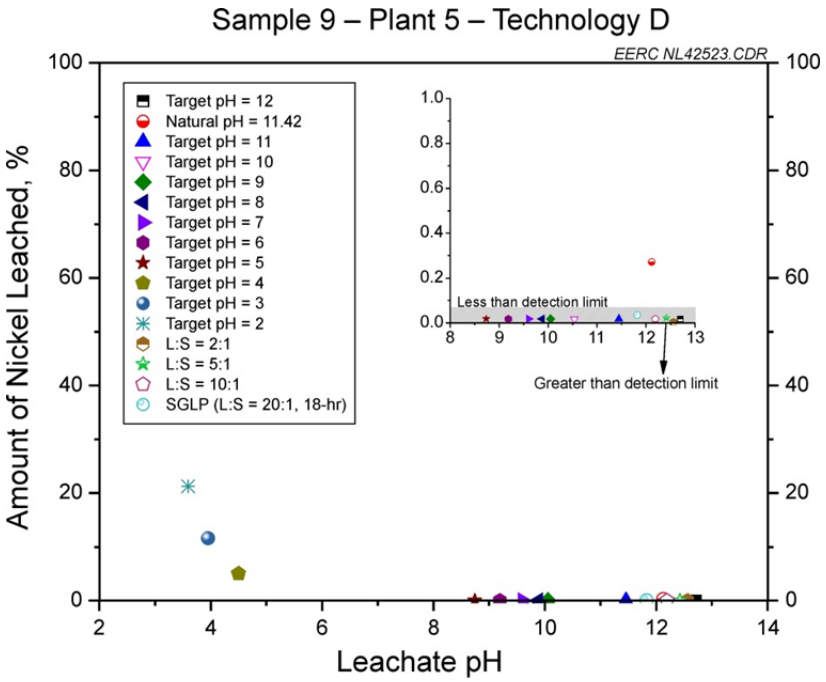

Figure A5-9. Percent of total nickel leached from Sample 9 – Plant 5 – Technology D. The inset contains only values less than 1% and over the pH range of 8–13. The 5:1 liquid-to-solid ratio leaching sample had a leachate concentration above the detection limit; however, the low liquid-to-solid ratio resulted in percent of nickel leached lower than the other liquid-to-solid ratios.

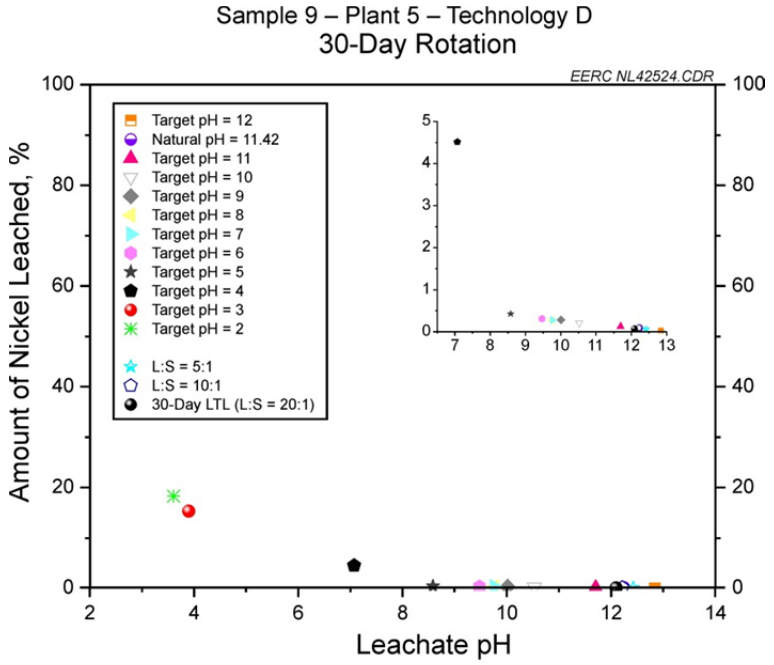

Figure A5-10. Percent of total nickel leached from Sample 9 – Plant 5 – Technology D – 30-day extension of all leaching tests. The inset contains only values less than 5% and over the pH range of 6.5–13.

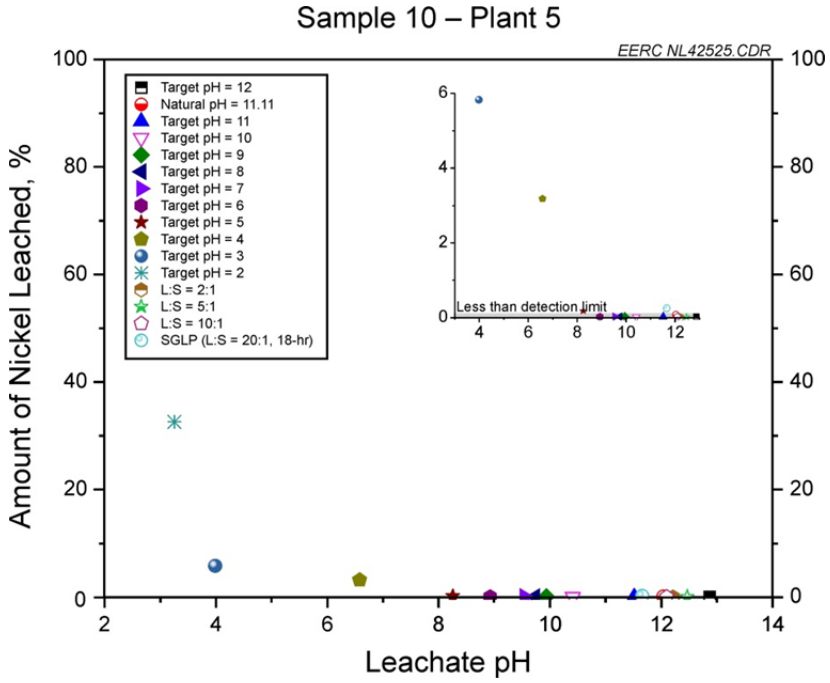

Figure A5-11. Percent of total nickel leached from Sample 10 – Plant 5. The inset contains only values less than 6%.

APPENDIX A6

SELENIUM

LIST OF FIGURES

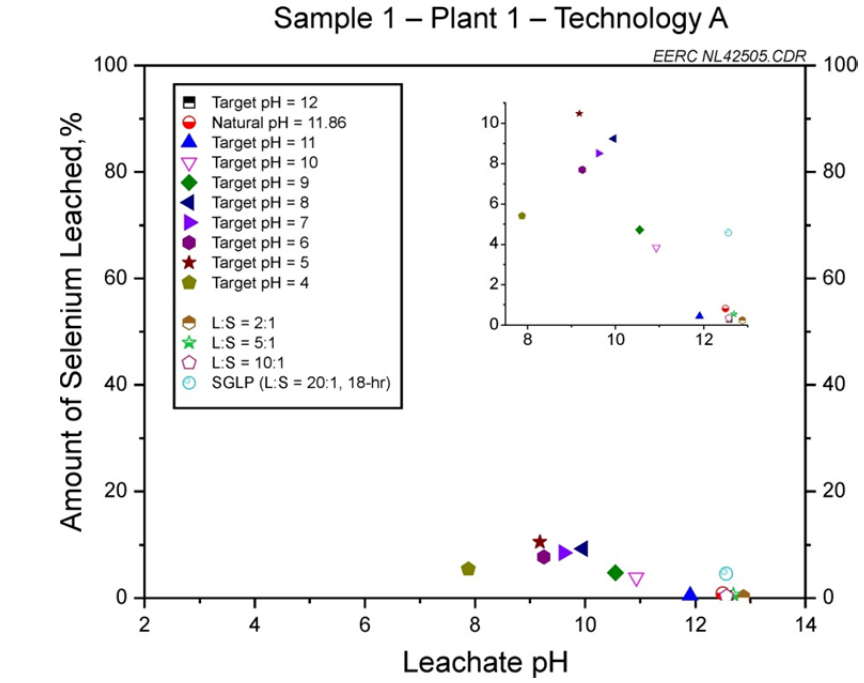

Figure A6-1. Percent of total selenium leached from Sample 1 – Plant 1 – Technology A.

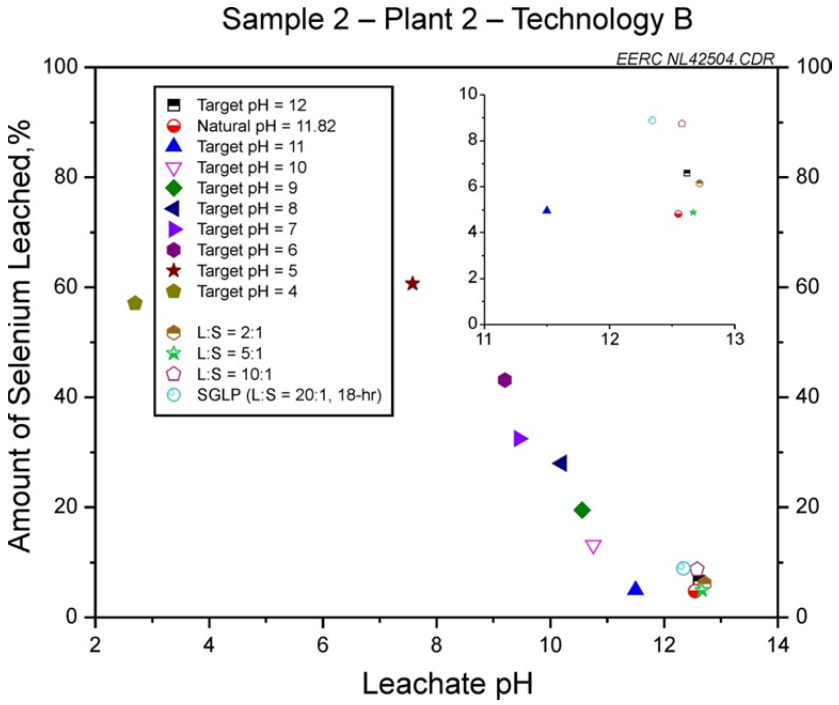

Figure A6-2. Percent of total selenium leached from Sample 2 – Plant 2 – Technology B. The inset contains only values less than 10%.

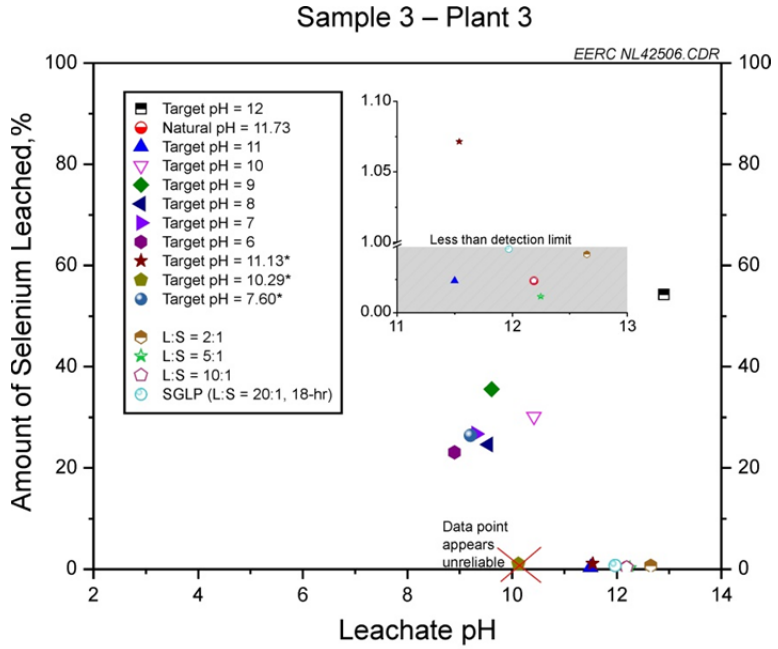

Figure A6-3. Percent of total selenium leached from Sample 3 – Plant 3. The inset contains only values less than 1.10% and over the pH range of 11–13. The data point for target pH 10.29 appears unreliable because it does not fit in with the apparent data trend.

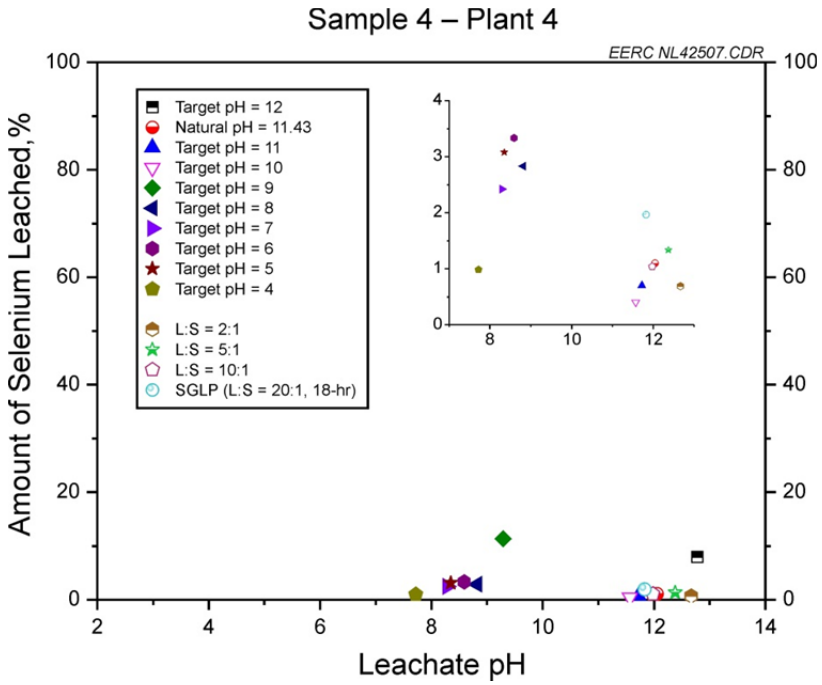

Figure A6-4. Percent of total selenium leached from Sample 4 – Plant 4. The inset contains only values less than 4%.

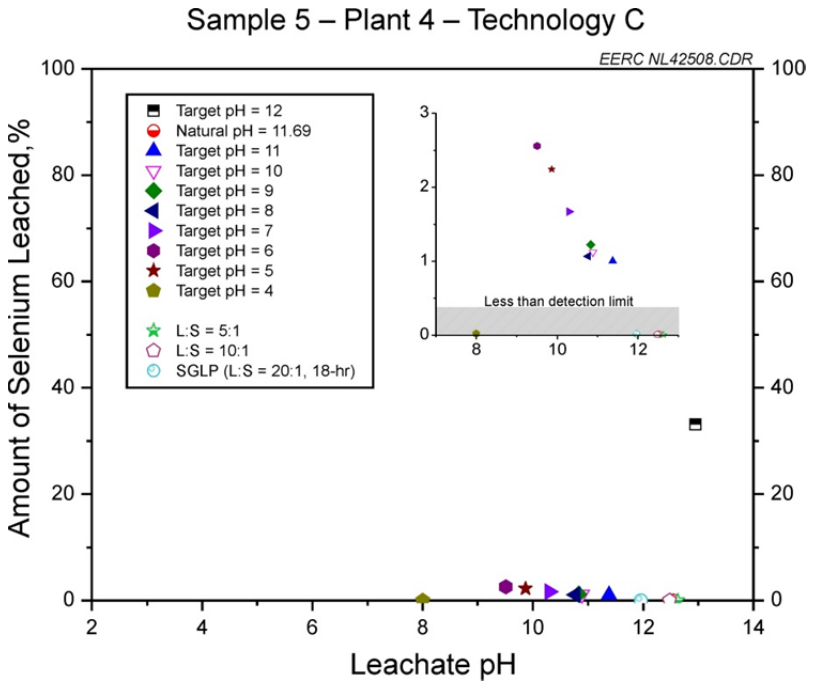

Figure A6-5. Percent of total selenium leached from Sample 5 – Plant 4 – Technology C. The inset contains only values less than 3%.

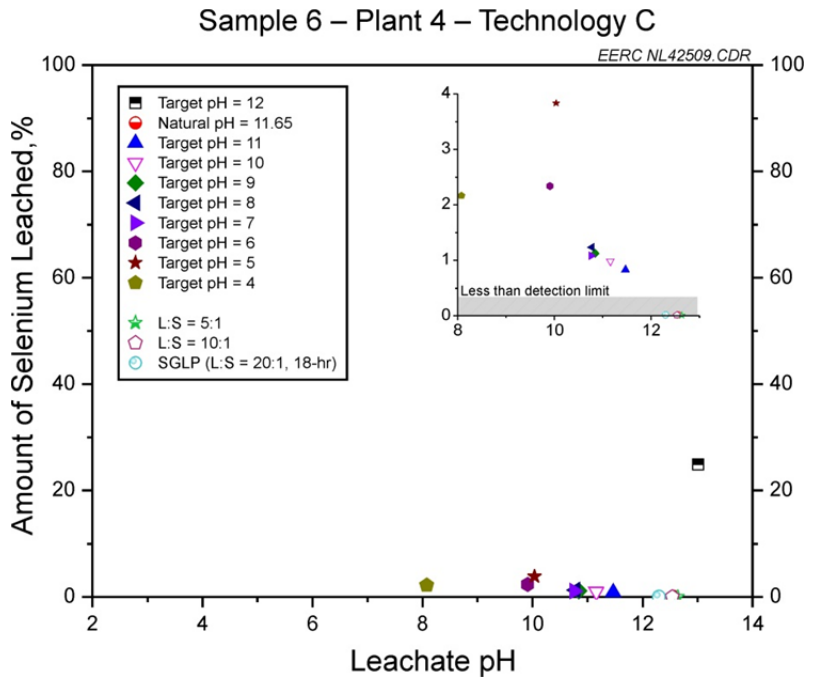

Figure A6-6. Percent of total selenium leached from Sample 6 – Plant 4 – Technology C. The inset contains only values less than 4%.

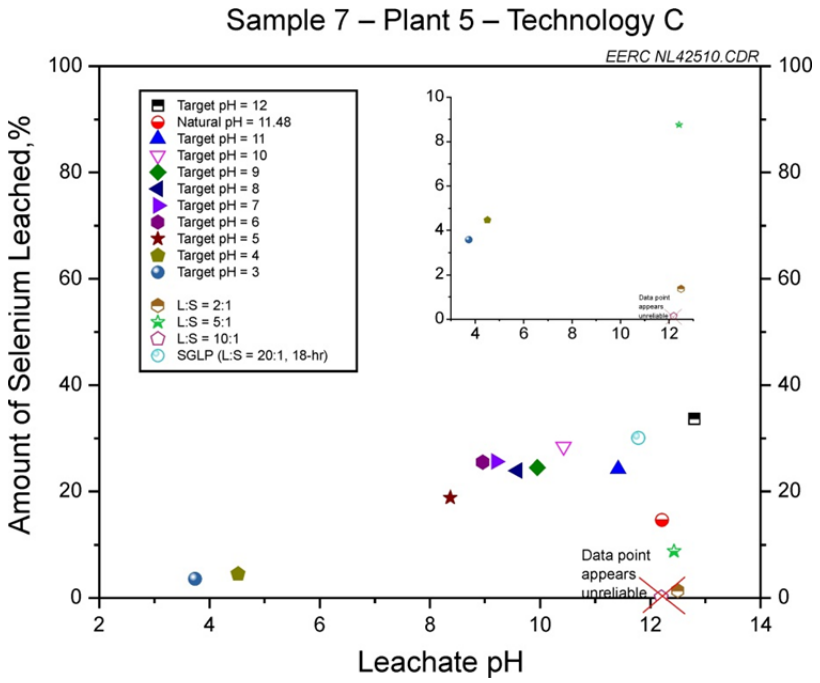

Figure A6-7. Percent of total selenium leached from Sample 7 – Plant 5 – Technology C. The inset contains only values less than 10%. The data point for the 10:1 liquid-to-solid ratio leachate appears unreliable because it is greater than 10% different than the natural pH sample, which is a duplicate.

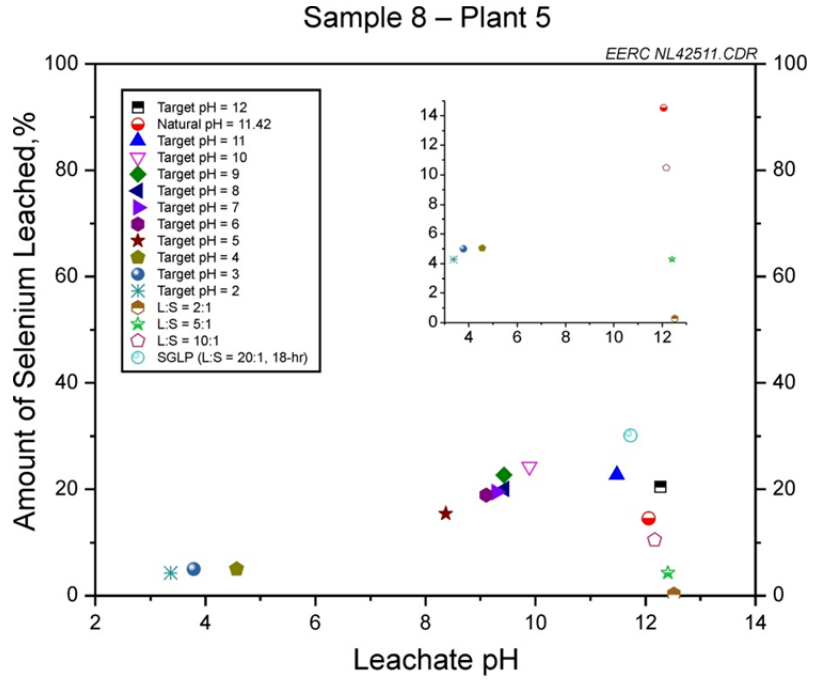

Figure A6-8. Percent of total selenium leached from Sample 8 – Plant 5. The inset contains only values less than 15%.

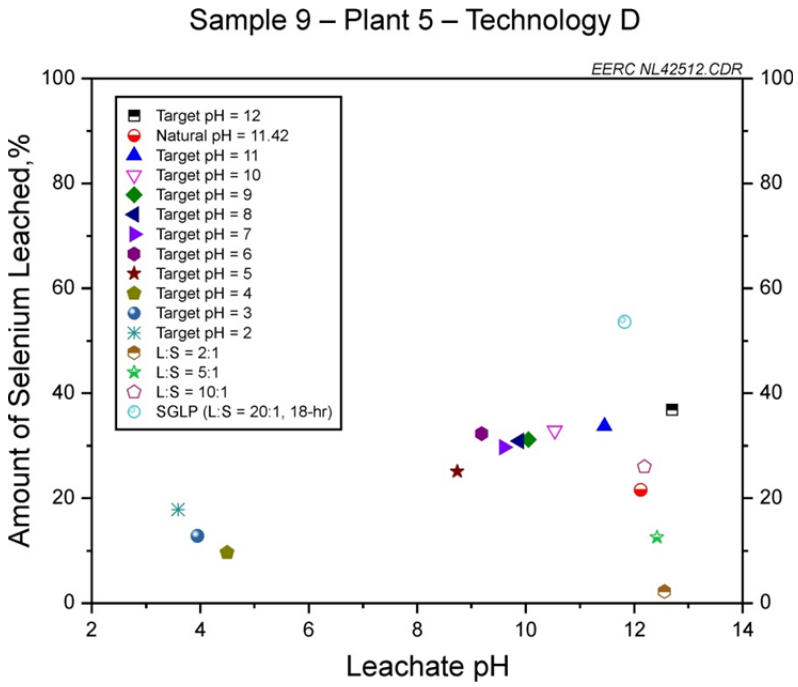

Figure A6-9. Percent of total selenium leached from Sample 9 – Plant 5 – Technology D.

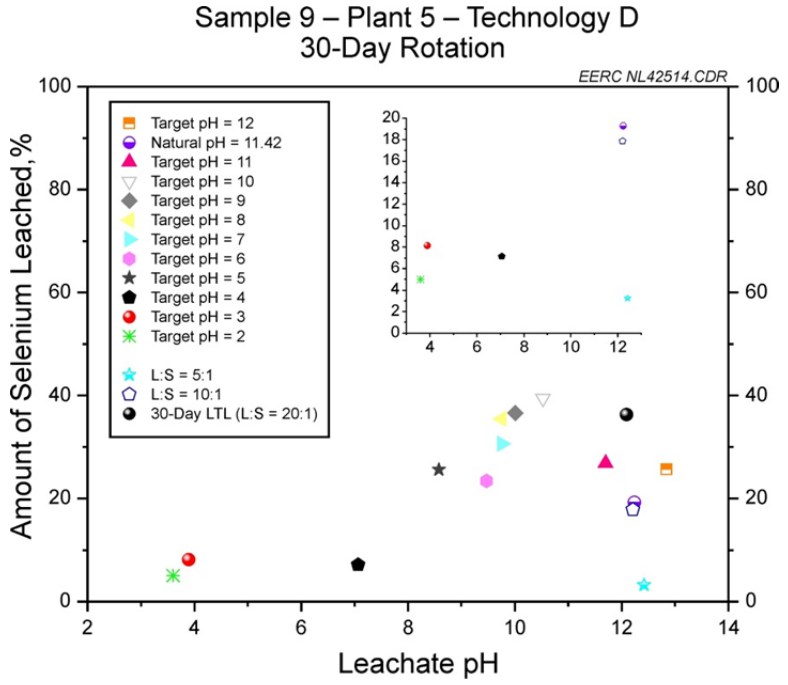

Figure A6-10. Percent of total selenium leached from Sample 9 – Plant 5 – Technology D – 30-day extension of all leaching tests. The inset contains only values less than 20%.

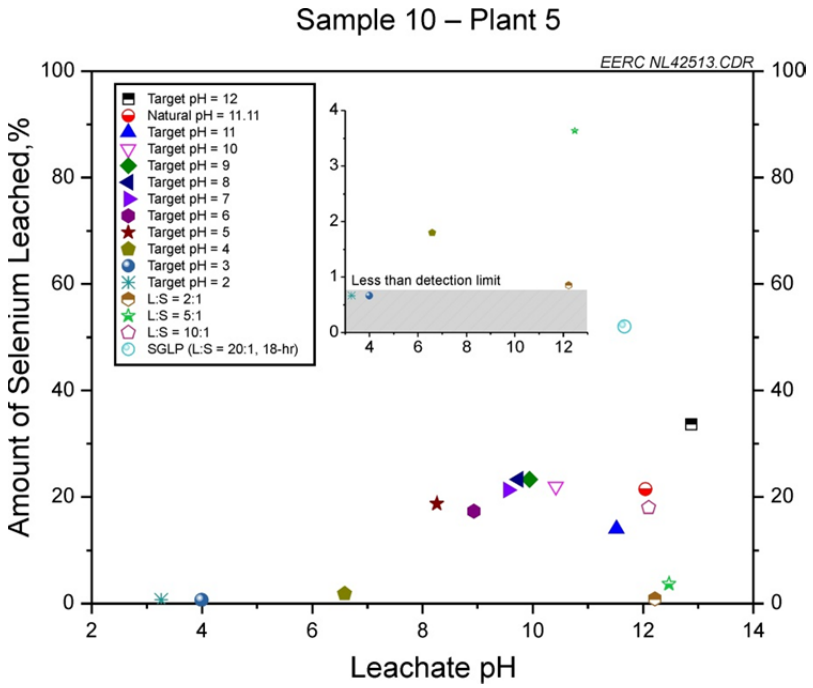

Figure A6-11. Percent of total selenium leached from Sample 10 – Plant 5. The inset contains only values less than 4%.

APPENDIX A7

SULFUR AS SULFATE

LIST OF FIGURES

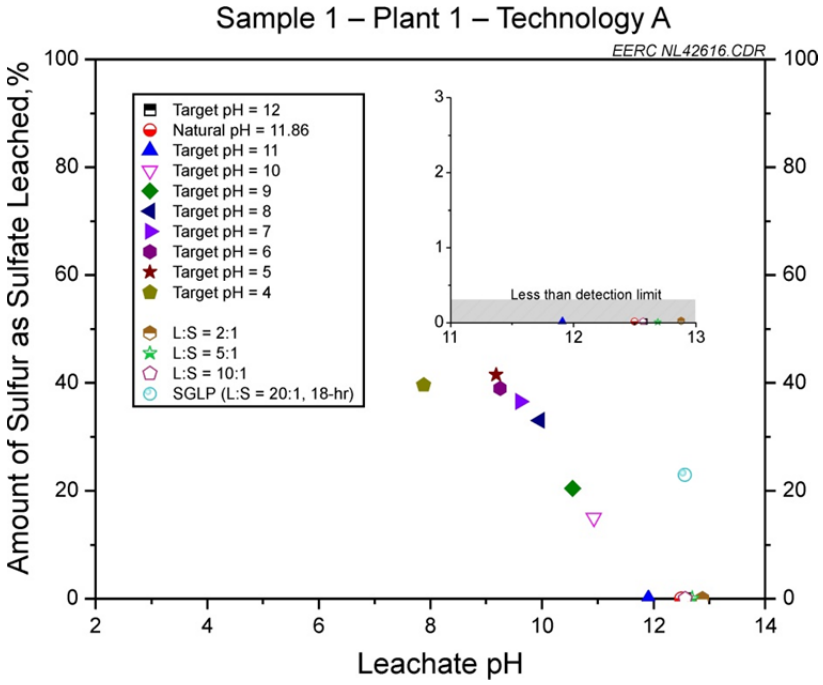

Figure A7-1. Percent of total sulfur as sulfate leached from Sample 1 – Plant 1 – Technology A. The inset contains only values less than 3%.

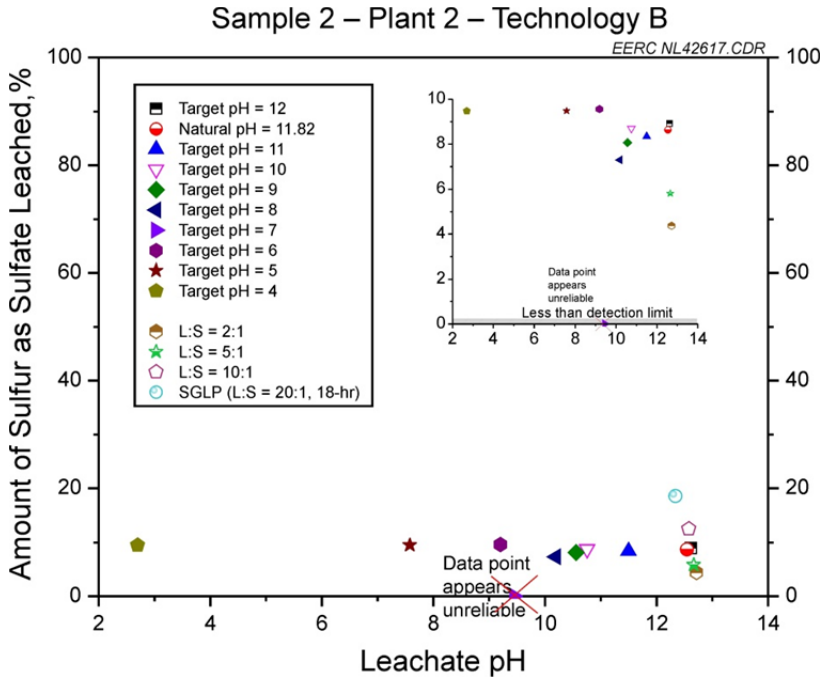

Figure A7-2. Percent of total sulfur as sulfate leached from Sample 2 – Plant 2 – Technology B. The inset contains only values less than 10%. The data point for target pH 7 appears unreliable because it does not fit in with the apparent data trend.

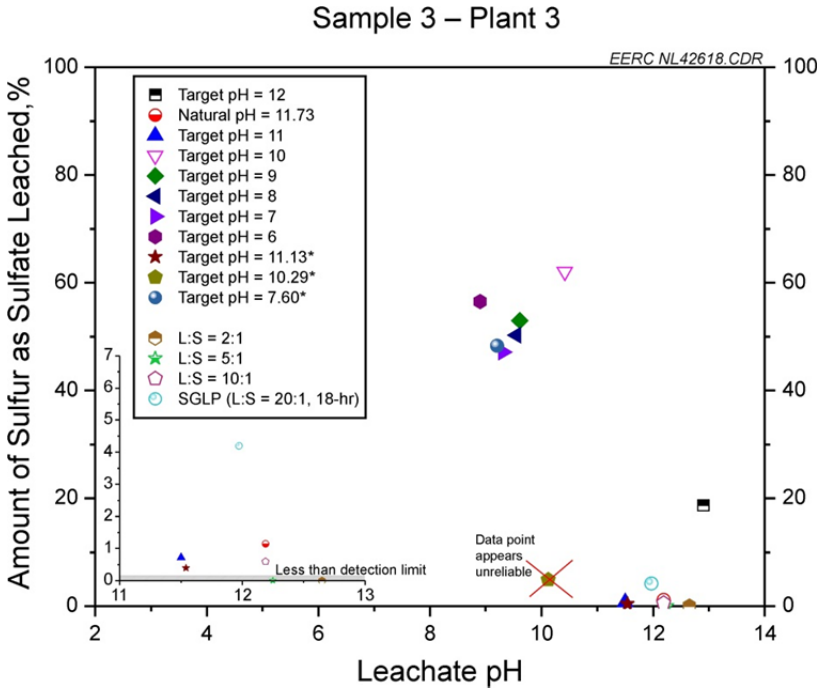

Figure A7-3. Percent of total sulfur as sulfate leached from Sample 3 – Plant 3. The inset contains only values less than 7% and over the pH range of 11–13. The data point for target pH 10.29 appears unreliable because it does not fit in with the apparent data trend.

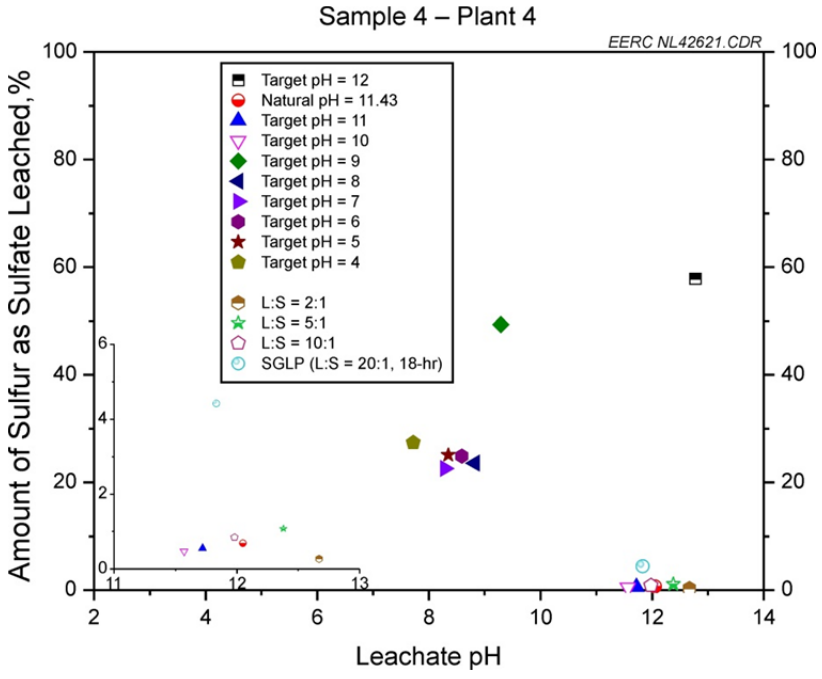

Figure A7-4. Percent of total sulfur as sulfate leached from Sample 4 – Plant 4. The inset contains only values less than 6% and over the pH range of 11–13.

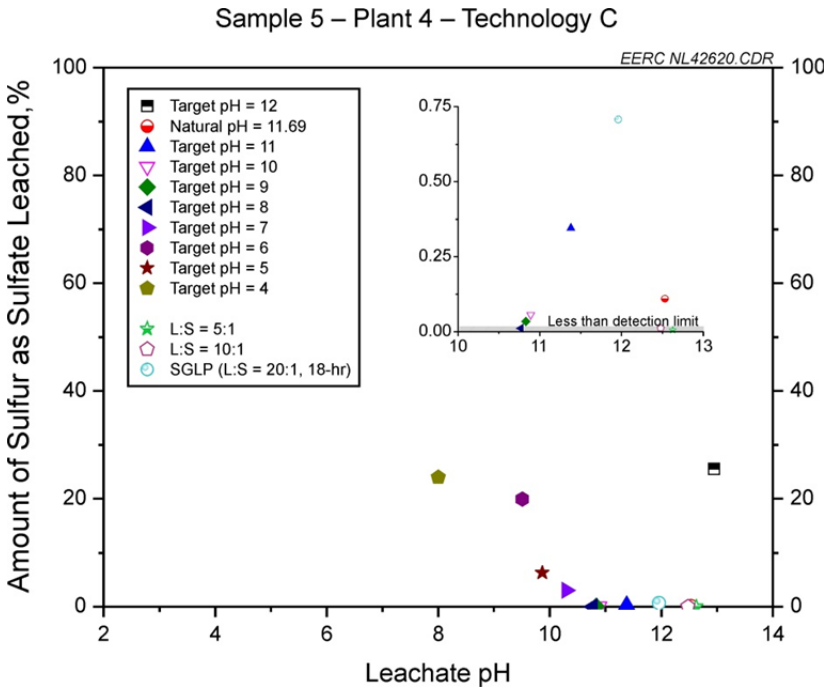

Figure A7-5. Percent of total sulfur as sulfate leached from Sample 5 – Plant 4 – Technology C. The inset contains only values less than 0.75%.

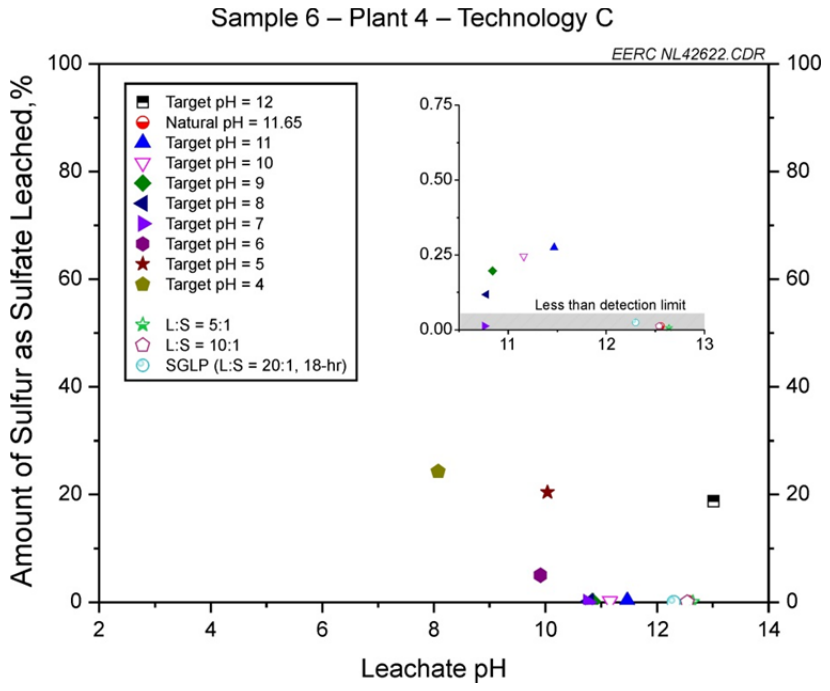

Figure A7-6. Percent of total sulfur as sulfate leached from Sample 6 – Plant 4 – Technology C. The inset contains only values less than 0.75%.

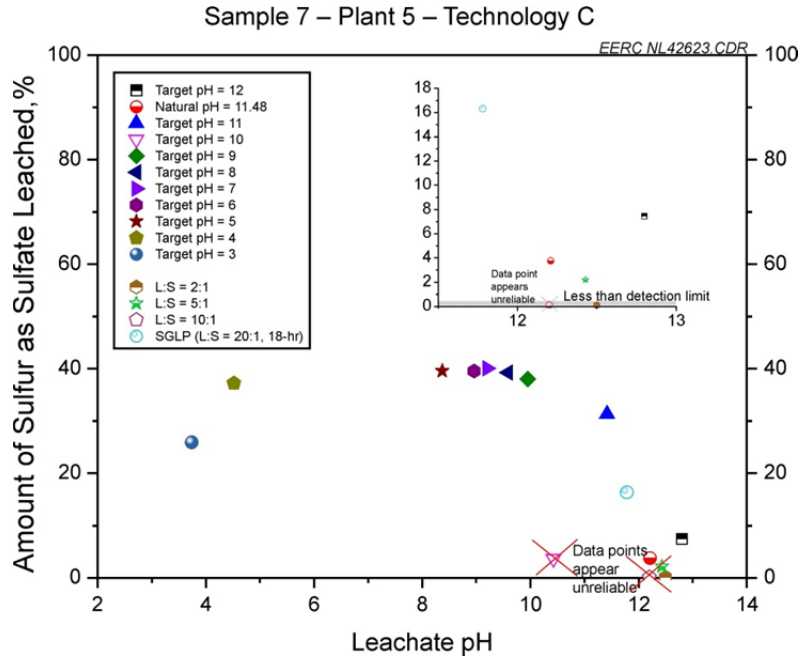

Figure A7-7. Percent of total sulfur as sulfate leached from Sample 7 – Plant 5 – Technology C. The inset contains only values less than 18% and over the pH range of 11.5–13. The data point for target pH 10 appears unreliable because it does not fit in with the apparent data trend. The data point for the 10:1 liquid-to-solid ratio leachate appears unreliable because it is greater than 10% different than the natural pH sample, which is a duplicate.

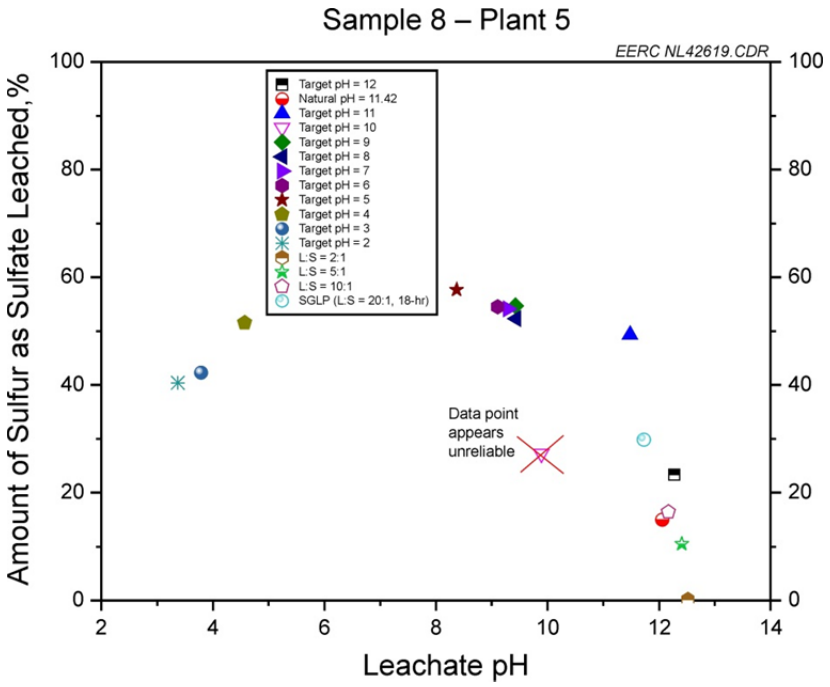

Figure A7-8. Percent of total sulfur as sulfate leached from Sample 8 – Plant 5. The data point for target pH 10 appears unreliable because it does not fit in with the apparent data trend.

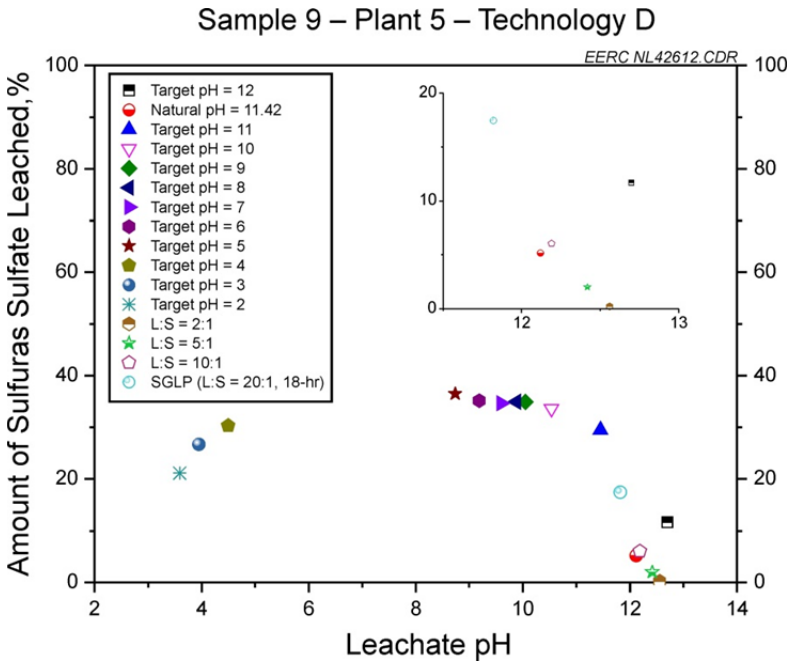

Figure A7-9. Percent of total sulfur as sulfate leached from Sample 9 – Plant 5 – Technology D. The inset contains only values less than 20% and over the pH range of 11.5–13.

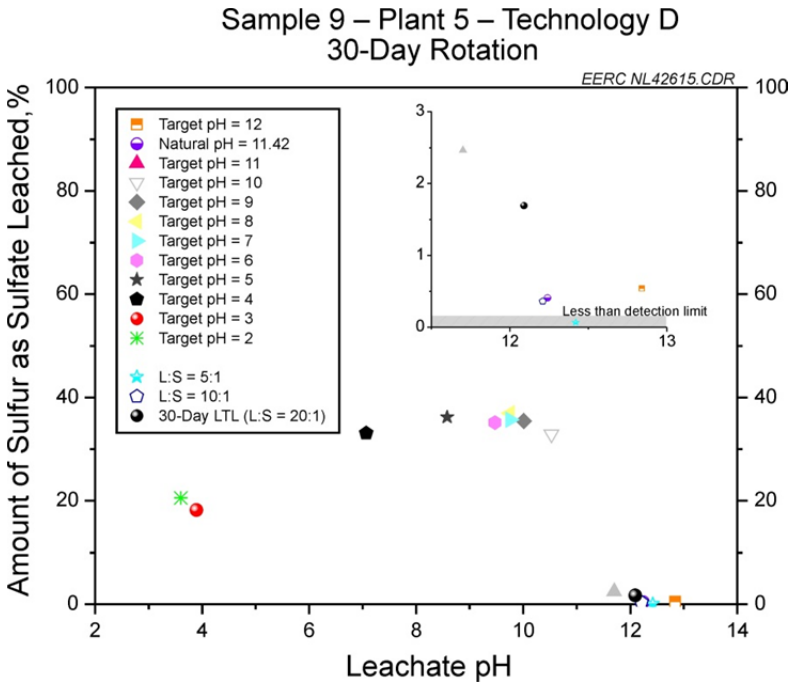

Figure A7-10. Percent of total sulfur as sulfate leached from Sample 9 – Plant 5 – Technology D – 30-day extension of all leaching tests. The inset contains only values less than 3% and over the pH range of 11.5–13.

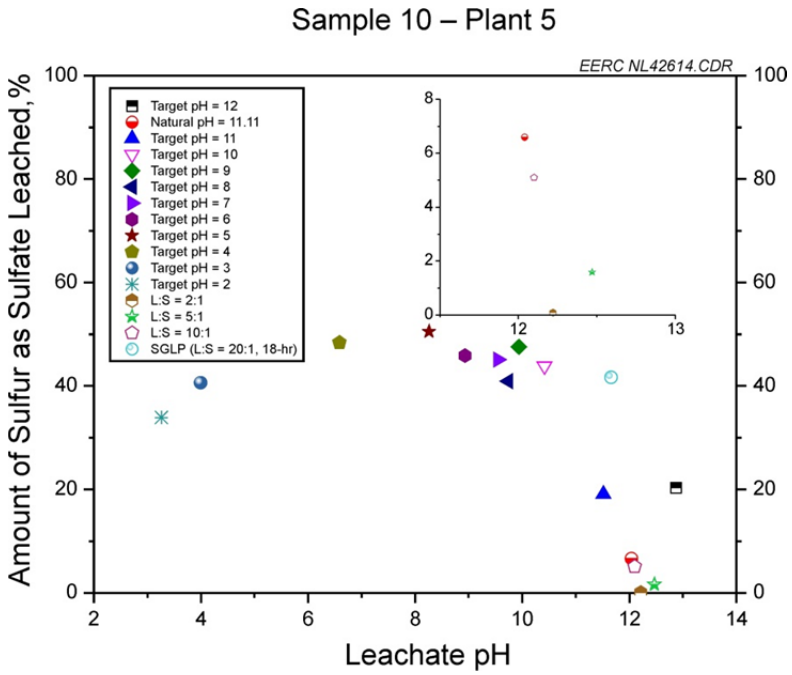

Figure A7-11. Percent of total arsenic leached from Sample 10 – Plant 5. The inset contains only values less than 8% and over the pH range of 11.5–13.

APPENDIX A8

BERYLLIUM, COBALT, AND MANGANESE

LIST OF FIGURES

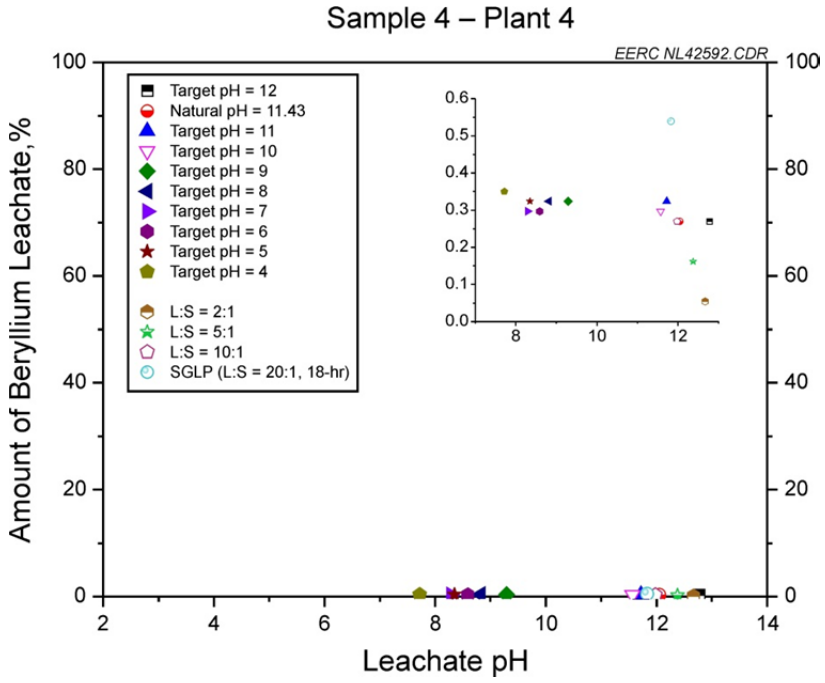

Figure A8-1. Percent of total beryllium leached from Sample 4 – Plant 4.

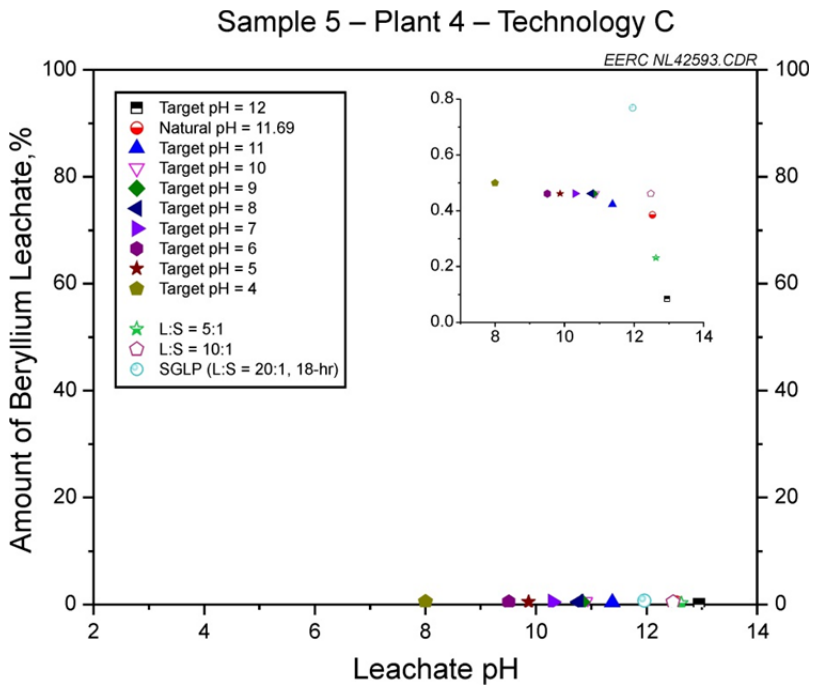

Figure A8-2. Percent of total beryllium leached from Sample 5 – Plant 4 – Technology C.

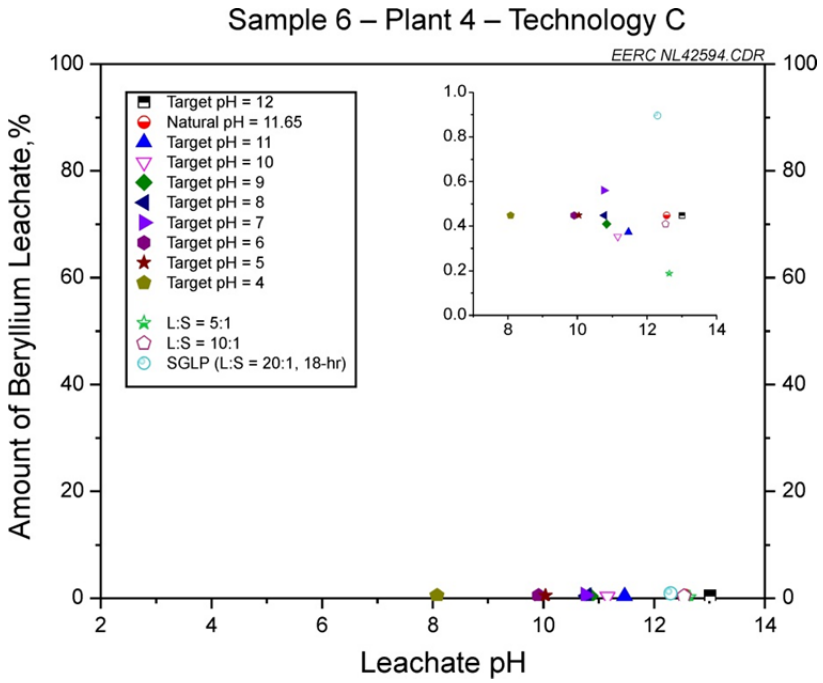

Figure A8-3. Percent of total beryllium leached from Sample 6 – Plant 4 – Technology C.

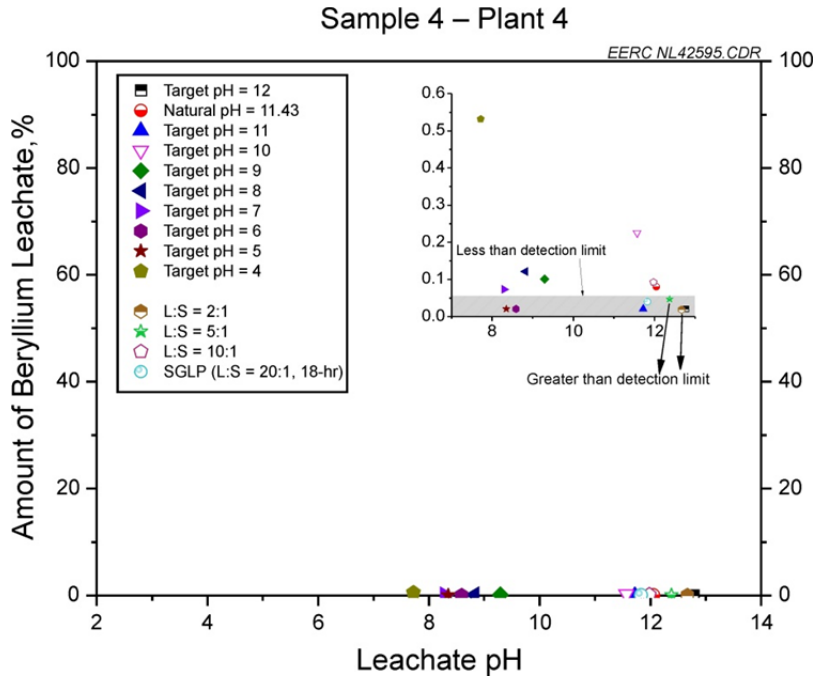

Figure A8-4. Percent of total cobalt leached from Sample 4 – Plant 4. The 2:1 and 5:1 liquid-to-solid ratio leaching samples had leachate concentrations above the detection limit; however, the low liquid-to-solid ratios resulted in percent of cobalt leached lower than the 10:1 and 20:1 liquid-to-solid ratios.

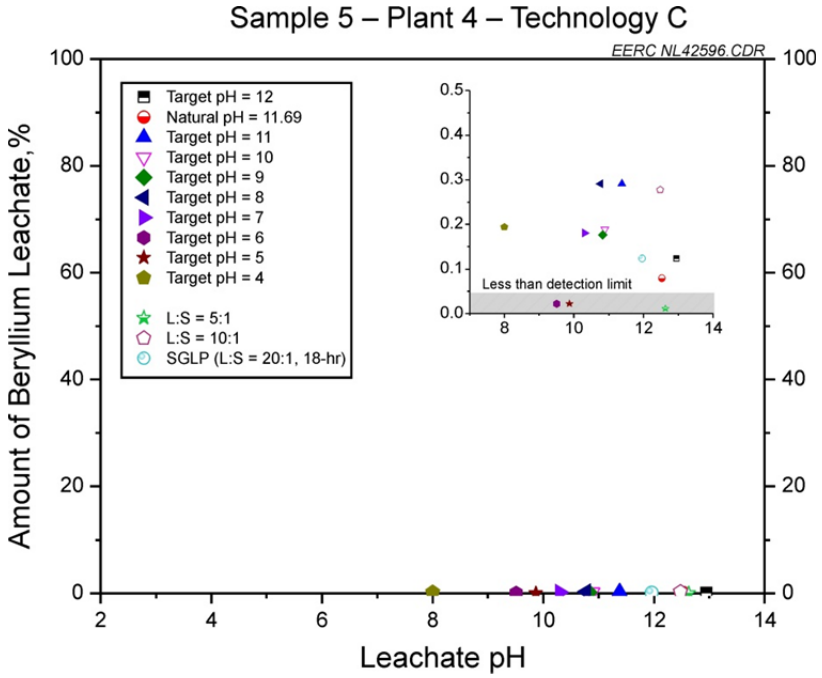

Figure A8-5. Percent of total cobalt leached from Sample 5 – Plant 4 – Technology C.

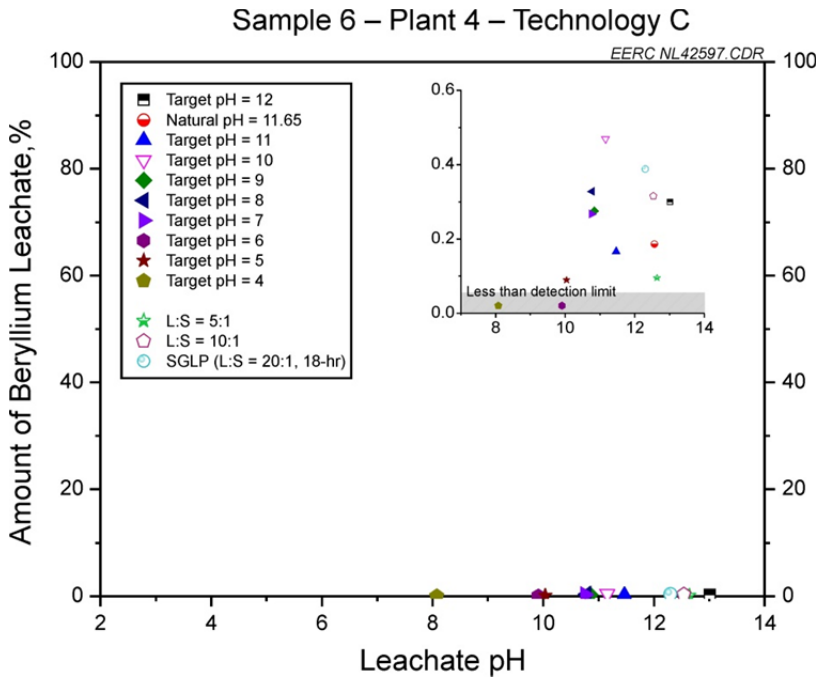

Figure A8-6. Percent of total cobalt leached from Sample 6 – Plant 4 – Technology C.

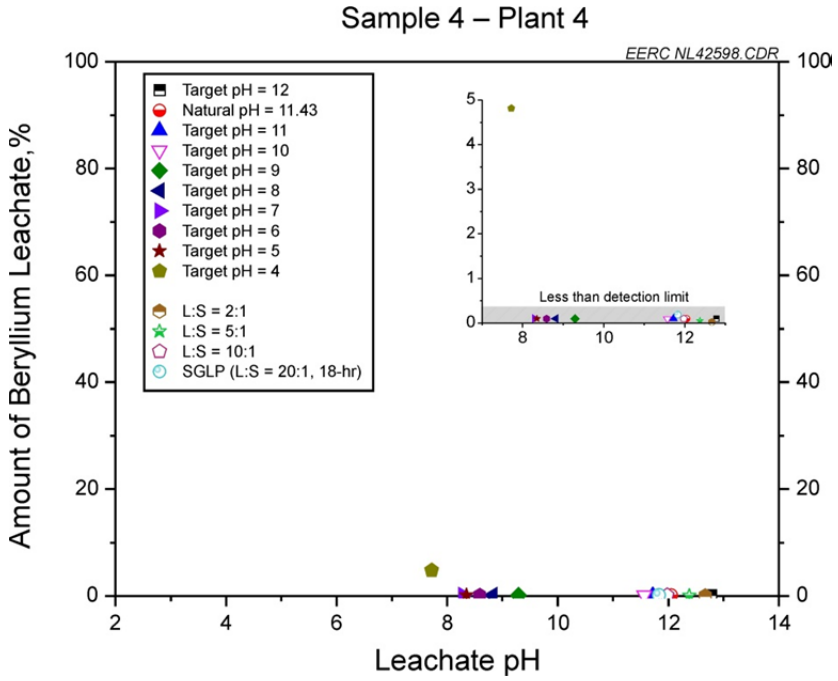

Figure A8-7. Percent of total manganese leached from Sample 4 – Plant 4.

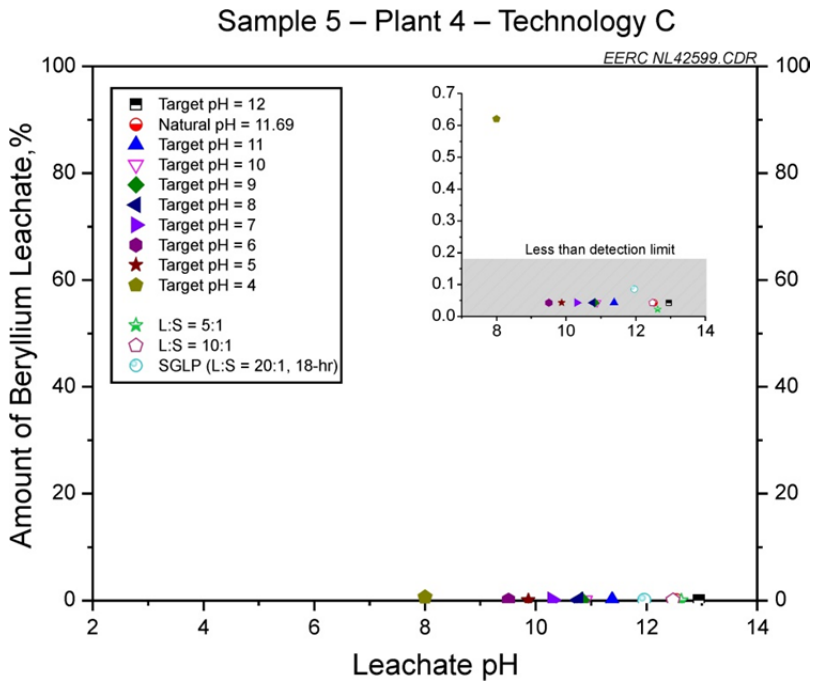

Figure A8-8. Percent of total manganese leached from Sample 5 – Plant 4 – Technology C.

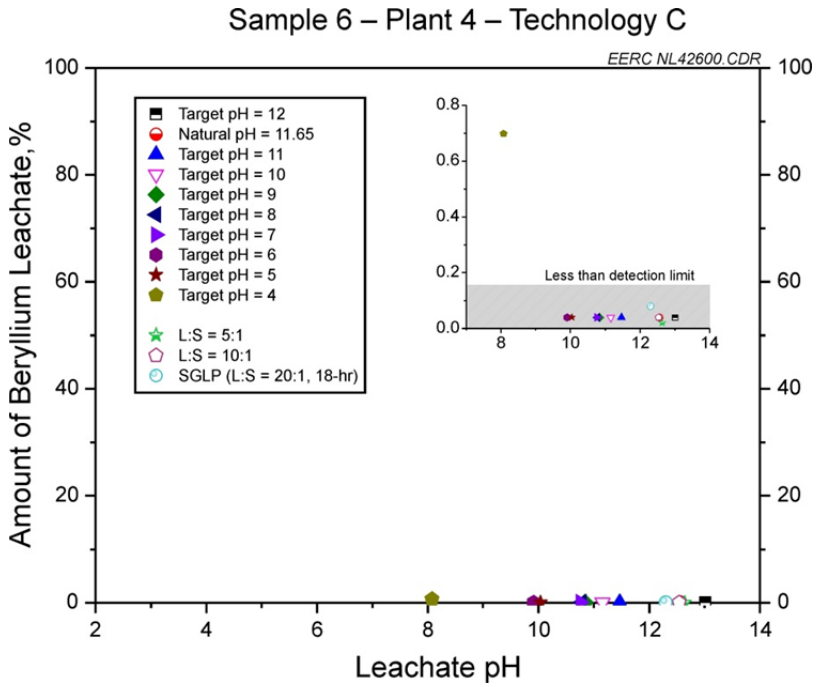

Figure A8-9. Percent of total manganese leached from Sample 6 – Plant 4 – Technology C.

APPENDIX A9

BROMIDE

LIST OF FIGURES

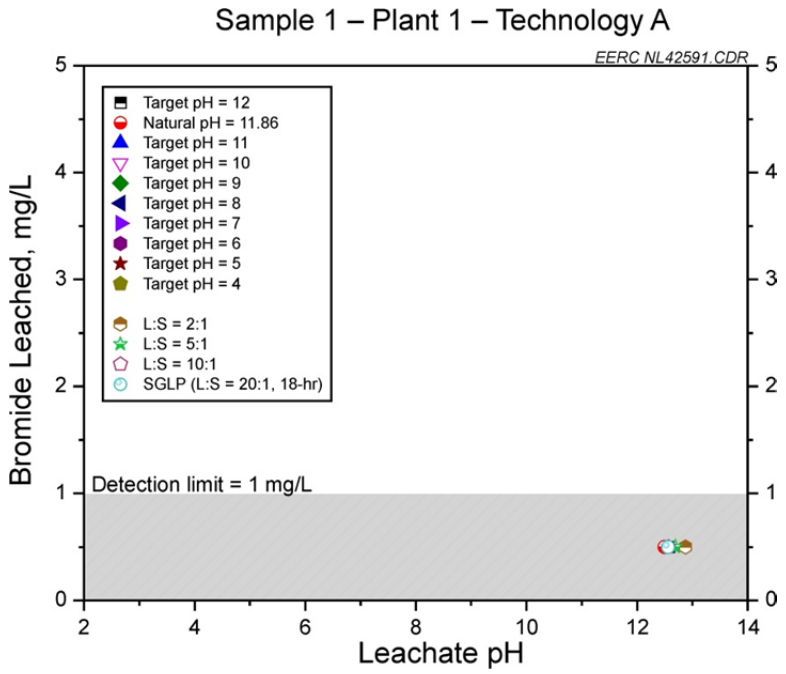

Figure A9-1. Bromide leached from Sample 1 – Plant 1 – Technology A – all values less than the leachate detection limit.

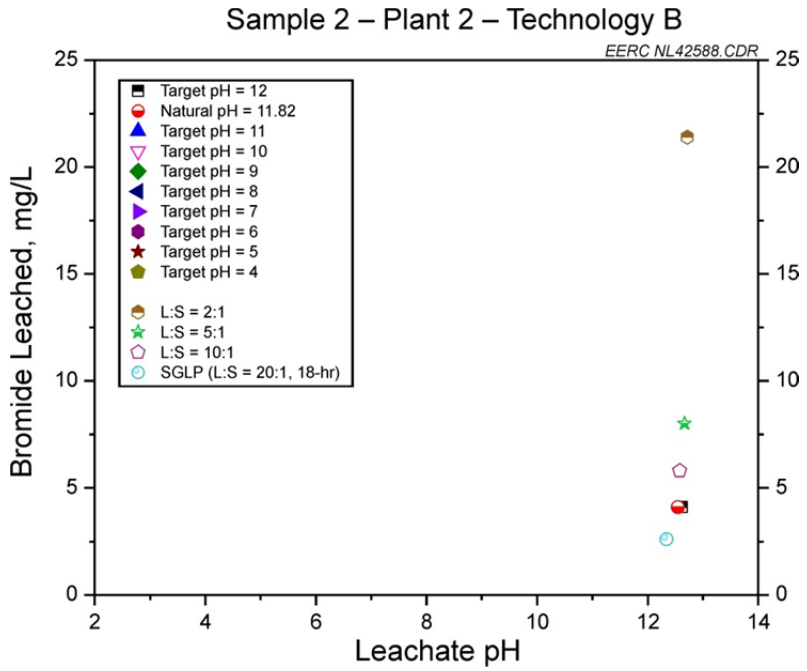

Figure A9-2. Bromide leached from Sample 2 – Plant 2 – Technology B.

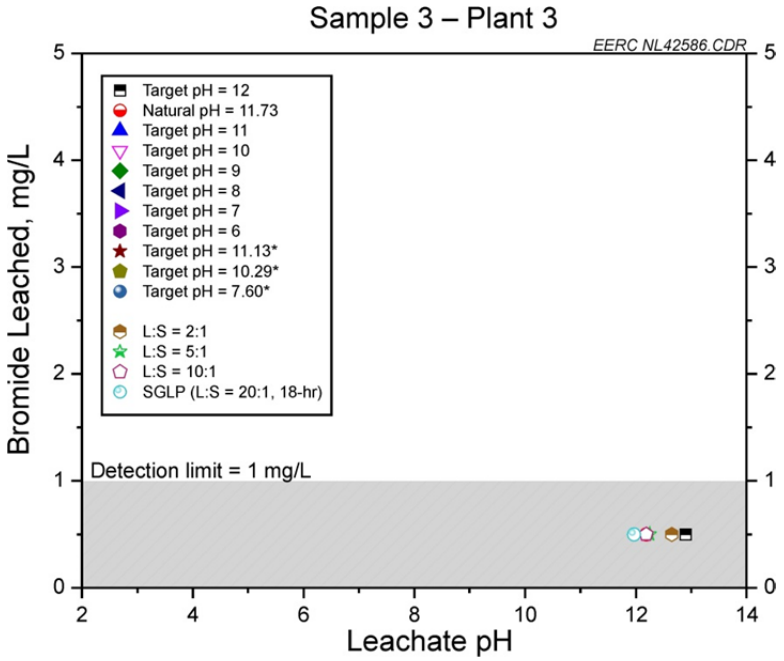

Figure A9-3. Bromide leached from Sample 3 – Plant 3 – all values less than the leachate detection limit.

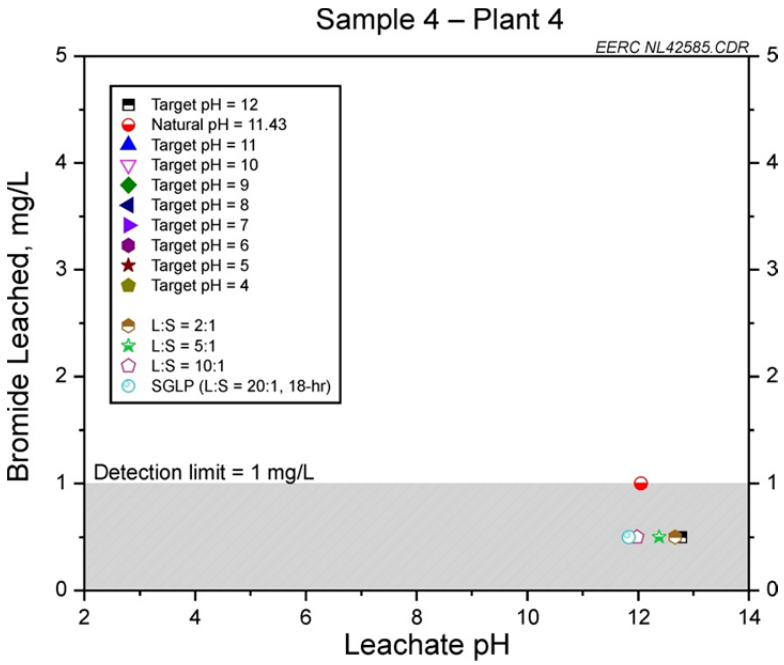

Figure A9-4. Bromide leached from Sample 4 – Plant 4.

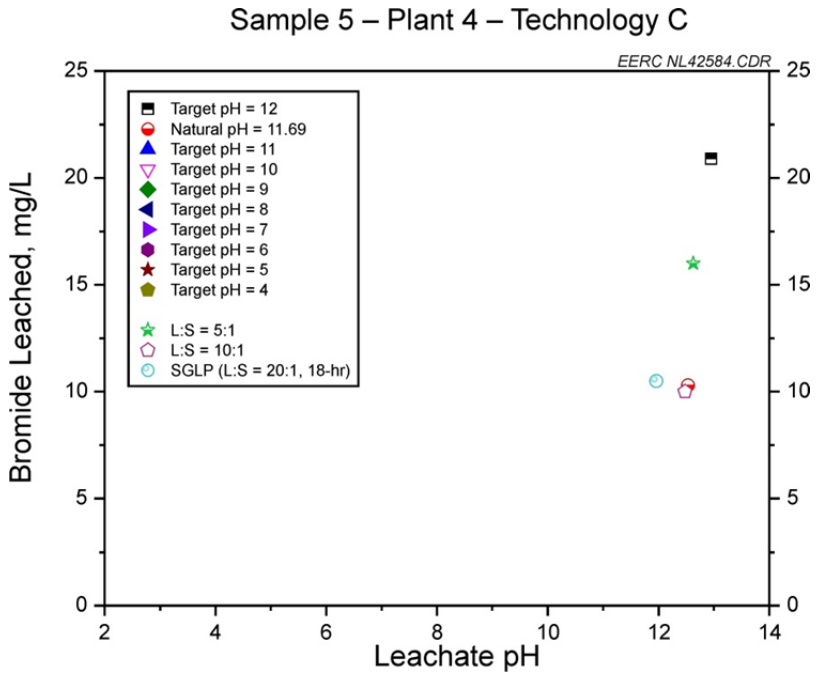

Figure A9-5. Bromide leached from Sample 5 – Plant 4 – Technology C.

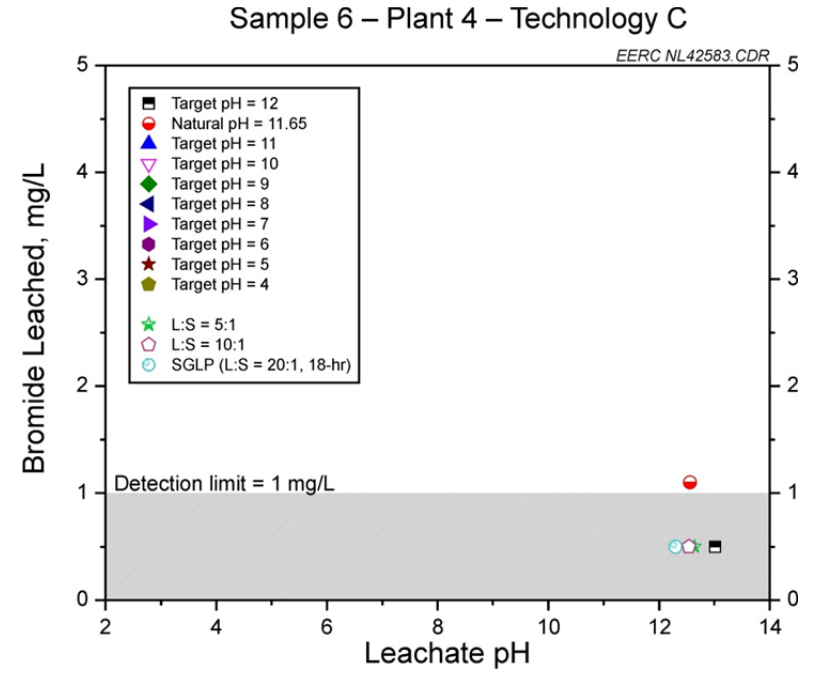

Figure A9-6. Bromide leached from Sample 6 – Plant 4 – Technology C.

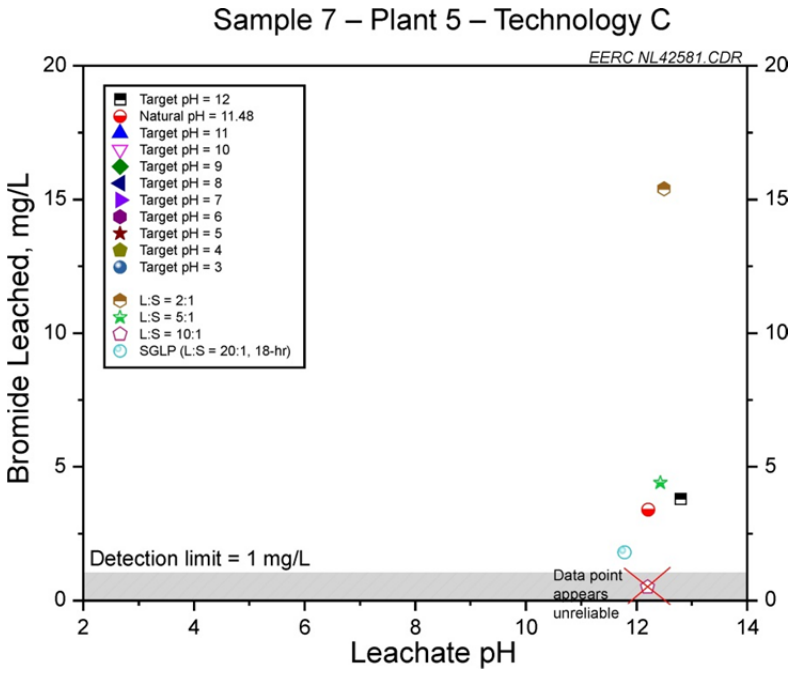

Figure A9-7. Bromide leached from Sample 7 – Plant 5 – Technology C. The data point for the 10:1 liquid-to-solid ratio leachate appears unreliable because it is greater than 10% different than the natural pH sample, which is a duplicate and it does not fit in with the apparent data trend.

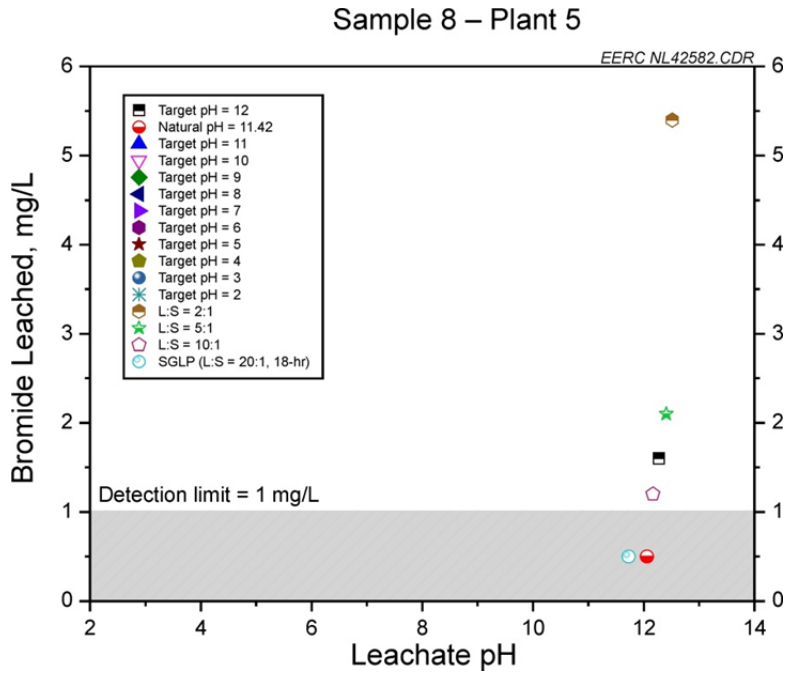

Figure A9-8. Bromide leached from Sample 8 – Plant 5.

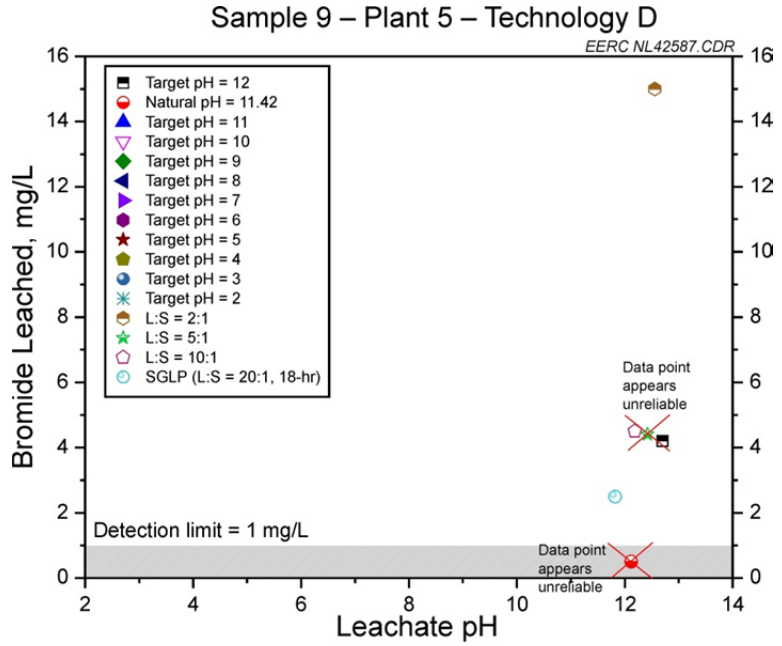

Figure A9-9. Bromide leached from Sample 9 – Plant 5 – Technology D. The data point for the natural pH sample appears unreliable because it is greater than 10% different than the 10:1 liquid-to-solid ratio leachate, which is a duplicate, and it does not fit in with the apparent data trend. The data point for the 5:1 liquid-to-solid ratio leachate sample appears unreliable because it does not fit in with the apparent data trend.

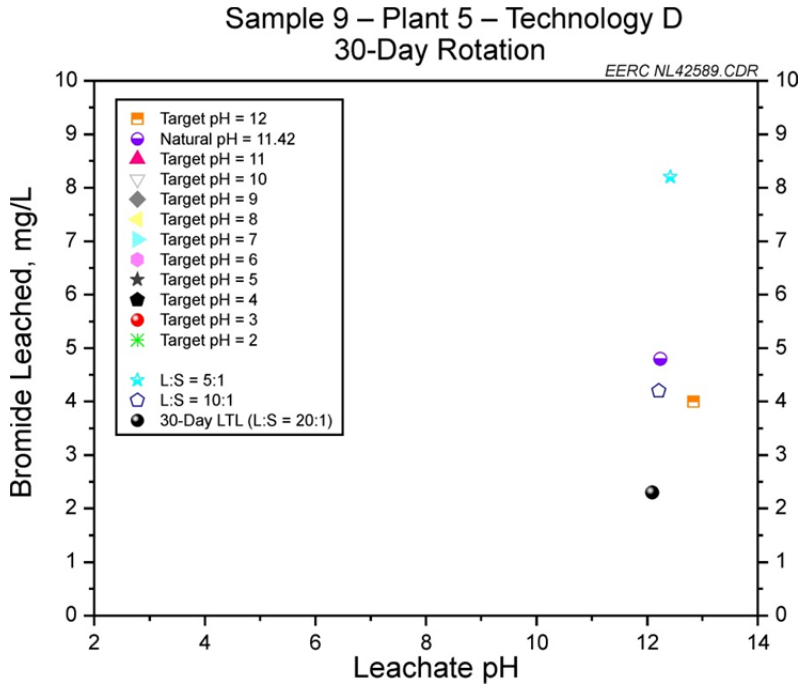

Figure A9-10. Bromide leached from Sample 9 – Plant 5 – Technology D – 30-day extension of all leaching tests.

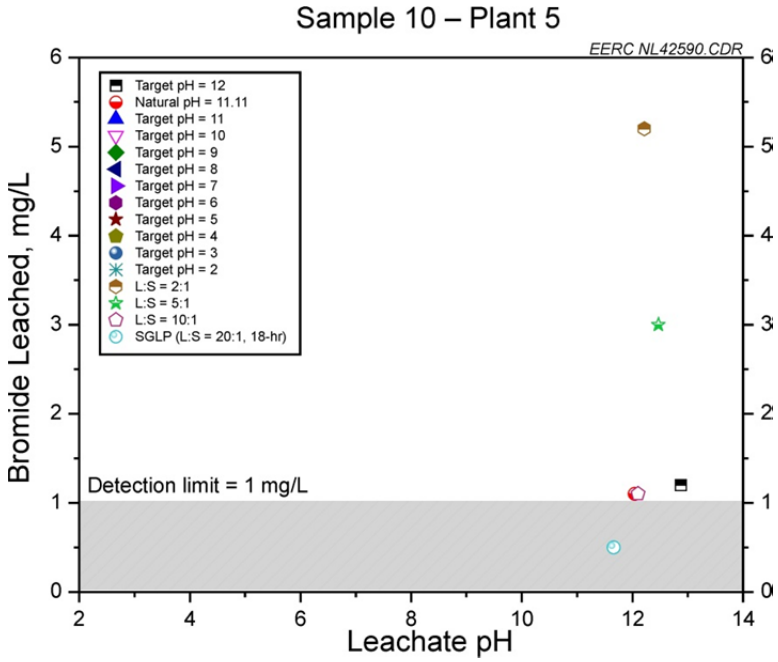

Figure A9-11. Bromide leached from Sample 10 – Plant 5.

APPENDIX A10

CHLORIDE

LIST OF FIGURES

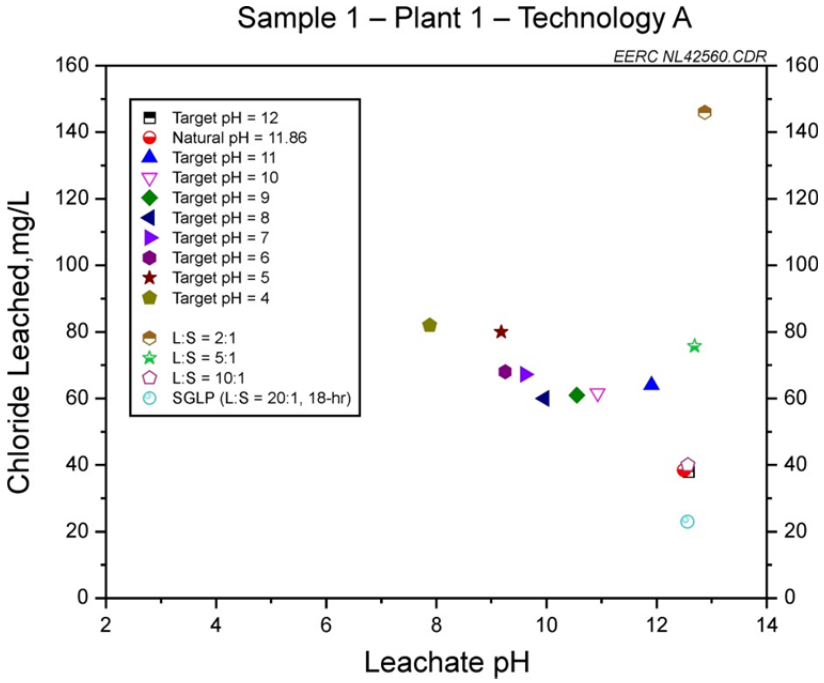

Figure A10-1. Chloride leached from Sample 1 – Plant 1 – Technology A.

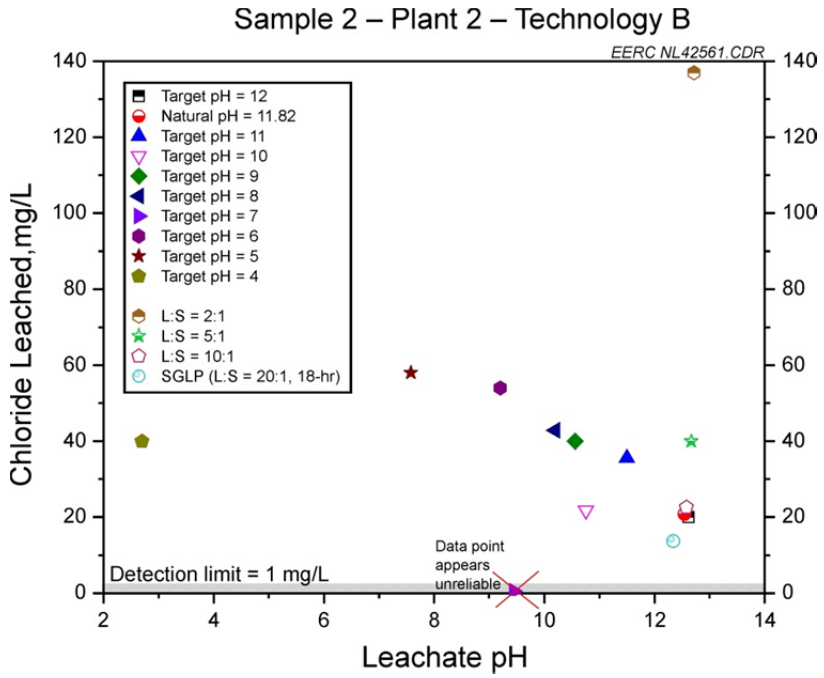

Figure A10-2. Chloride leached from Sample 2 – Plant 2 – Technology B. The data point for target pH 7 appears unreliable because it does not fit in with the apparent data trend.

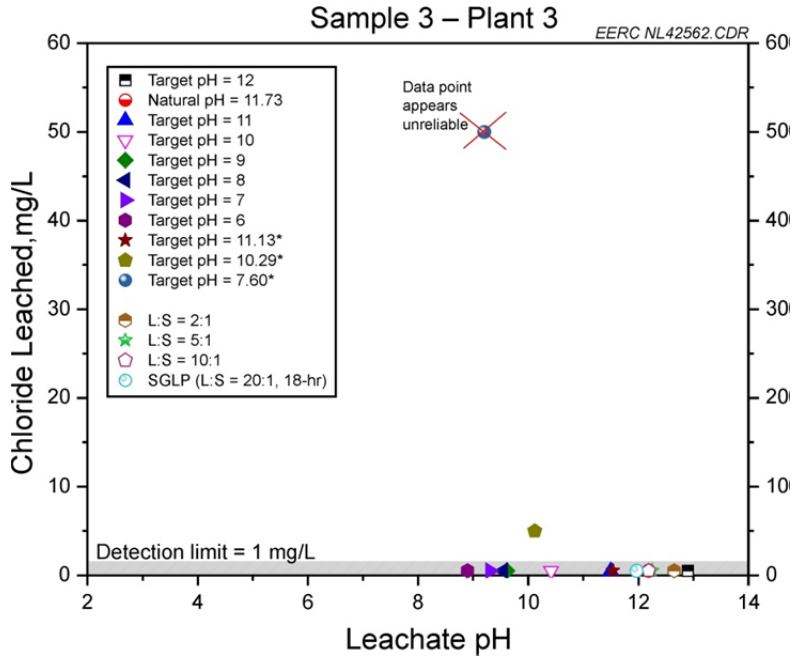

Figure A10-3. Chloride leached from Sample 3 – Plant 3. The data point for target pH 7.60 appears unreliable because it does not fit in with the apparent data trend.

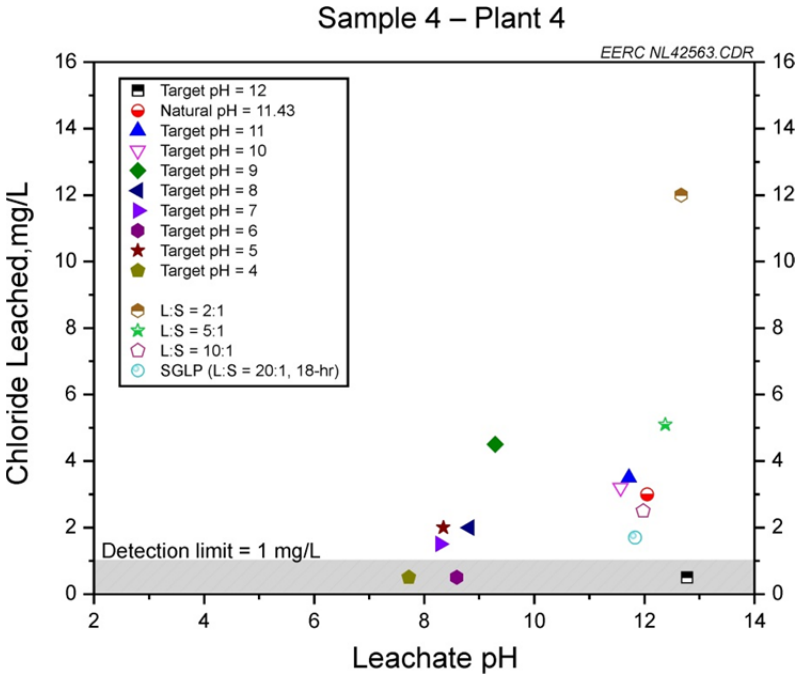

Figure A10-4. Chloride leached from Sample 4 – Plant 4.

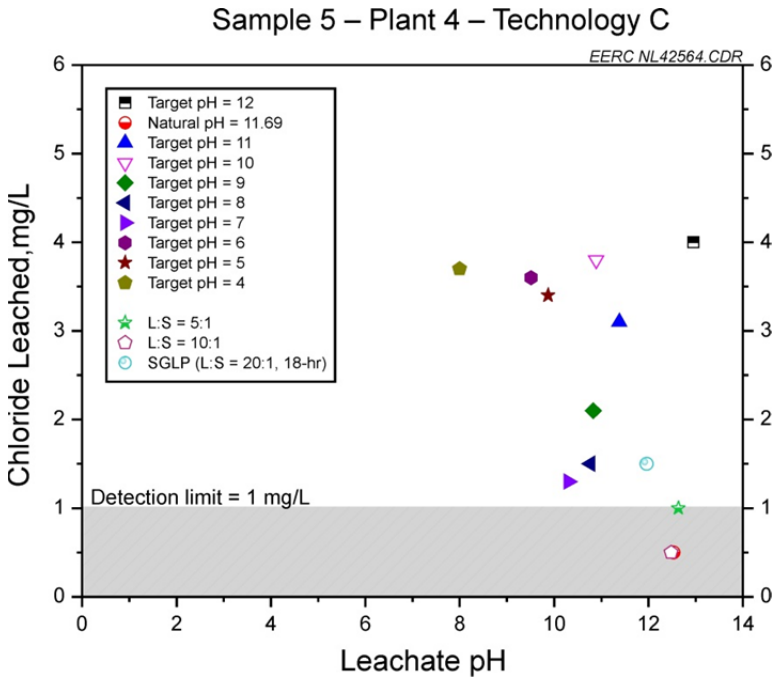

Figure A10-5. Chloride leached from Sample 5 – Plant 4 – Technology C.

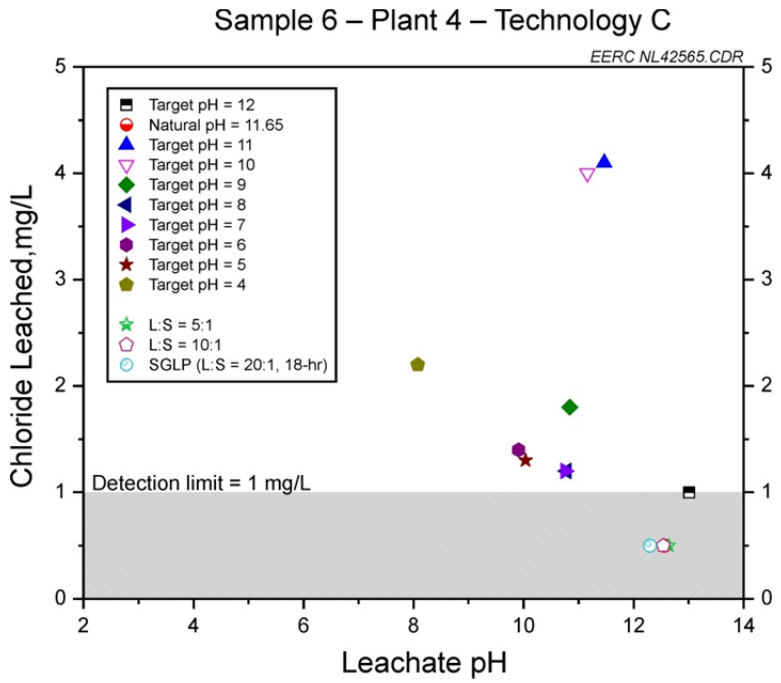

Figure A10-6. Chloride leached from Sample 6 – Plant 4 – Technology C.

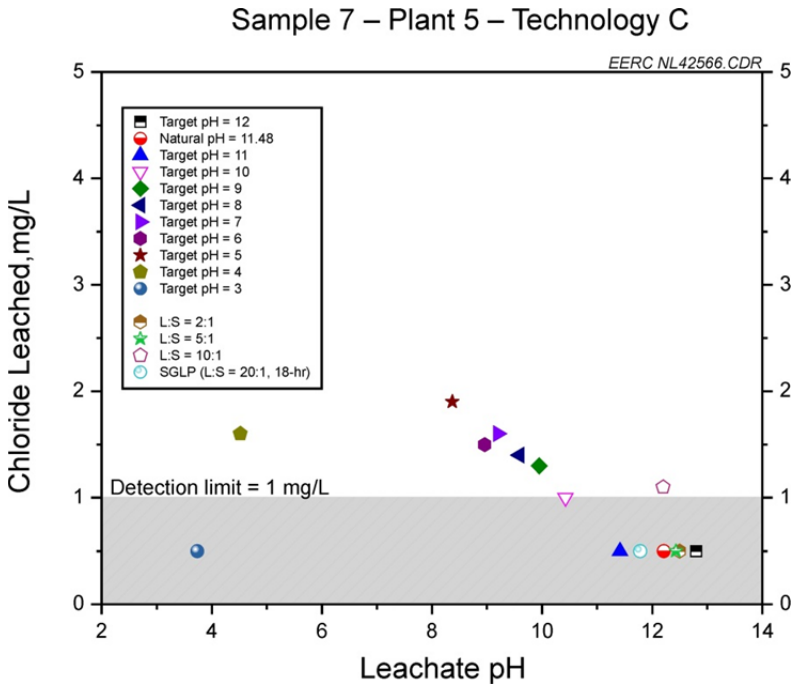

Figure A10-7. Chloride leached from Sample 7 – Plant 5 – Technology C.

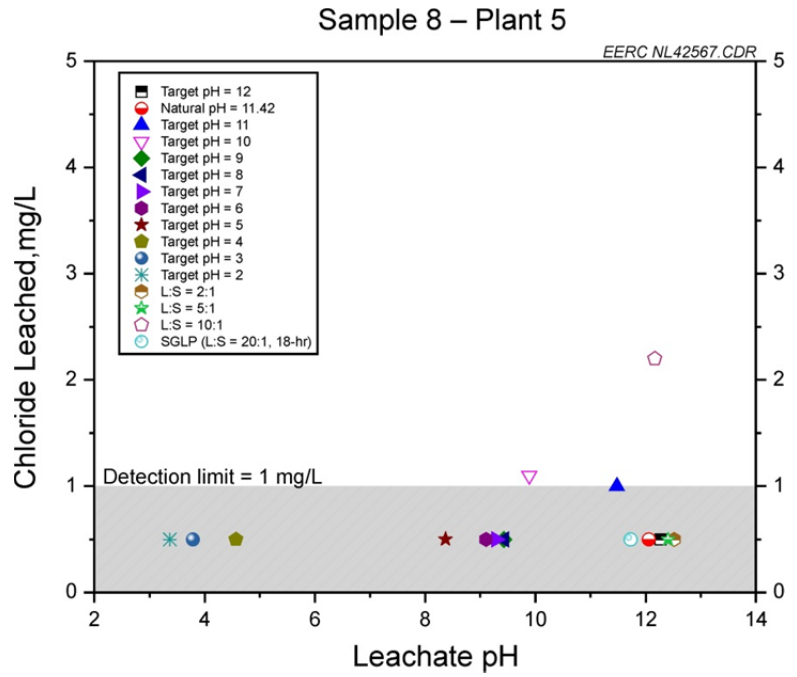

Figure A10-8. Chloride leached from Sample 8 – Plant 5.

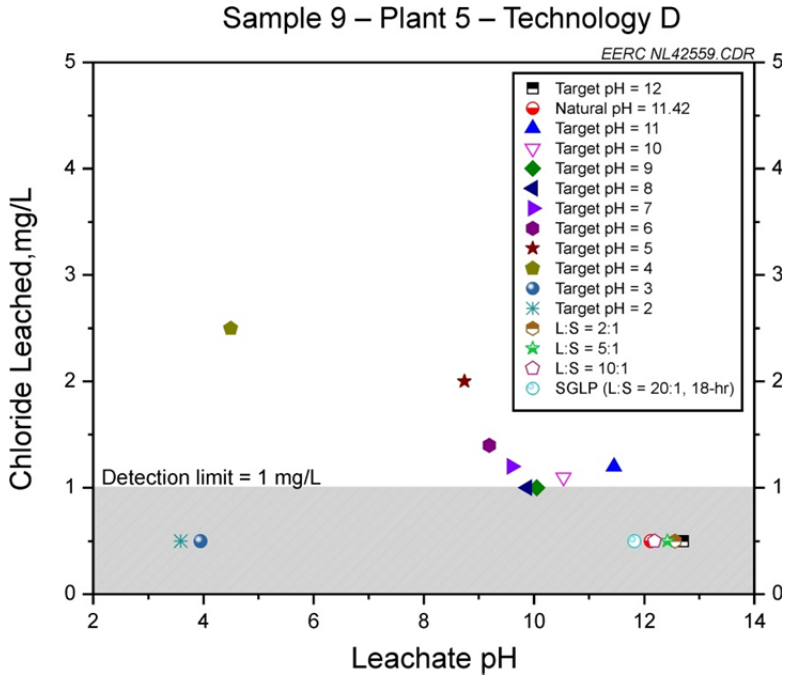

Figure A10-9. Chloride leached from Sample 9 – Plant 5 – Technology D.

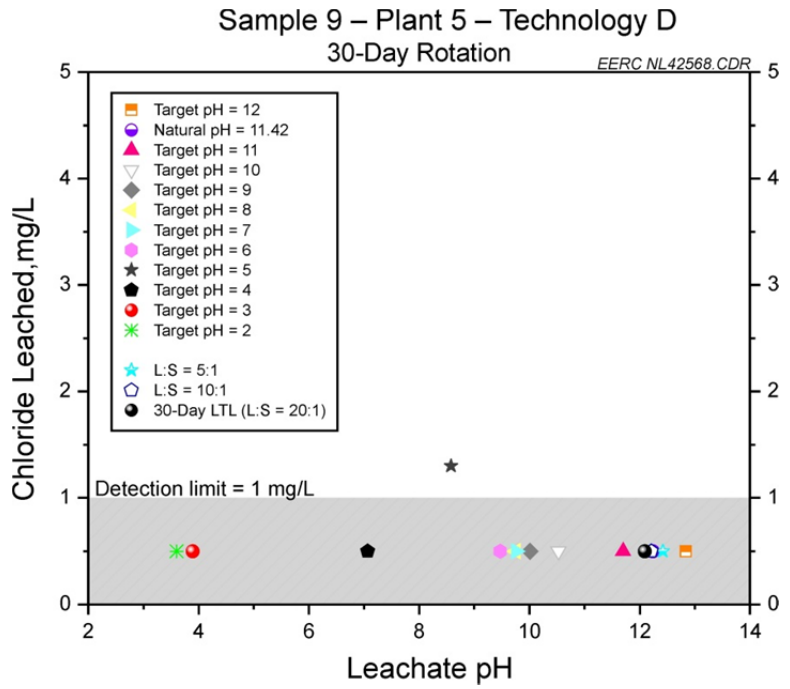

Figure A10-10. Chloride leached from Sample 9 – Plant 5 – Technology D – 30-day extension of all leaching tests.

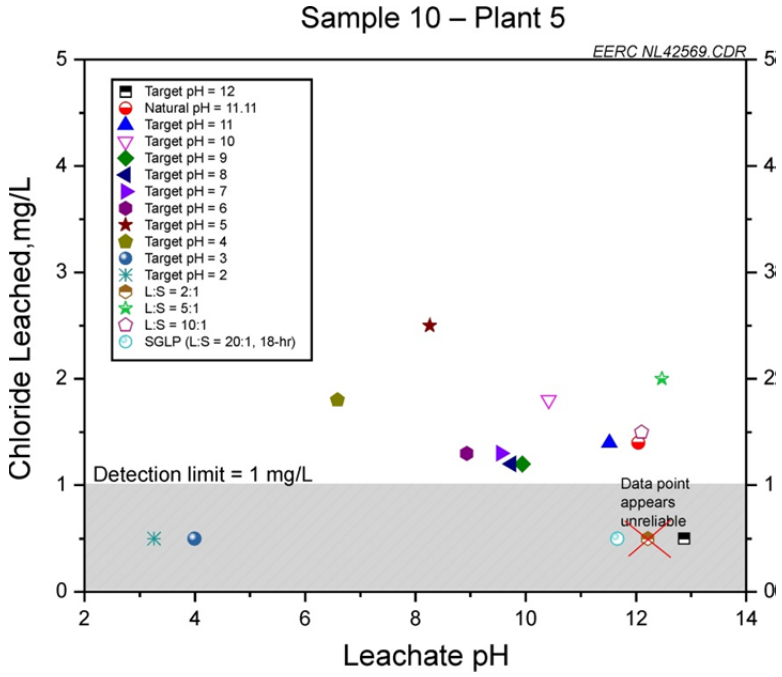

Figure A10-11. Chloride leached from Sample 10 – Plant 5. The data point for liquid-to-solid ratio 2:1 appears unreliable because it does not fit in with the apparent data trend.

APPENDIX A11

FLUORIDE

LIST OF FIGURES

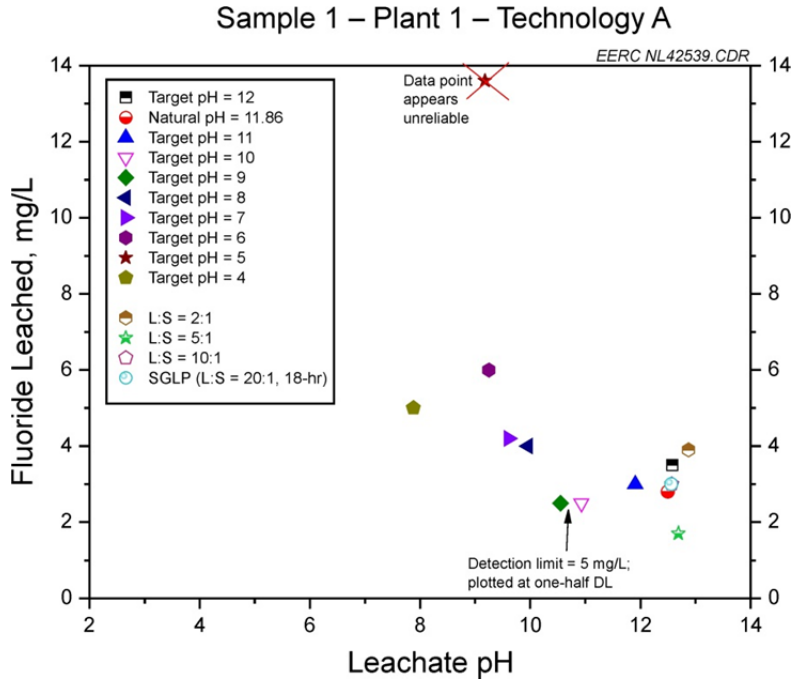

Figure A11-1. Fluoride leached from Sample 1 – Plant 1 – Technology A. The data point for target pH 5 appears unreliable because it does not fit in with the apparent data trend. The data points at target pH 9 and 10 had a higher detection limit than other leachates in the data set.

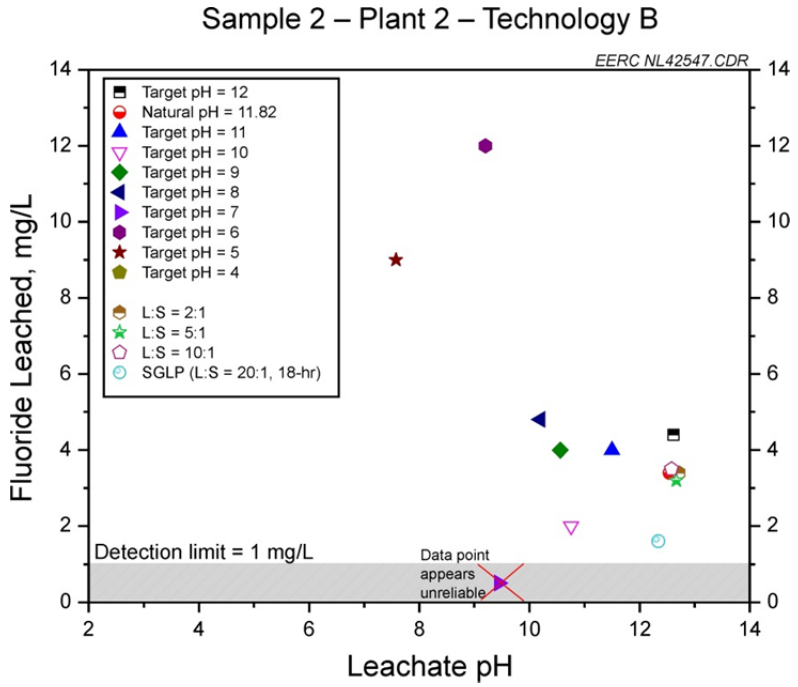

Figure A11-2. Fluoride leached from Sample 2 – Plant 2 – Technology B. The data point for target pH 7 appears unreliable because it does not fit in with the apparent data trend.

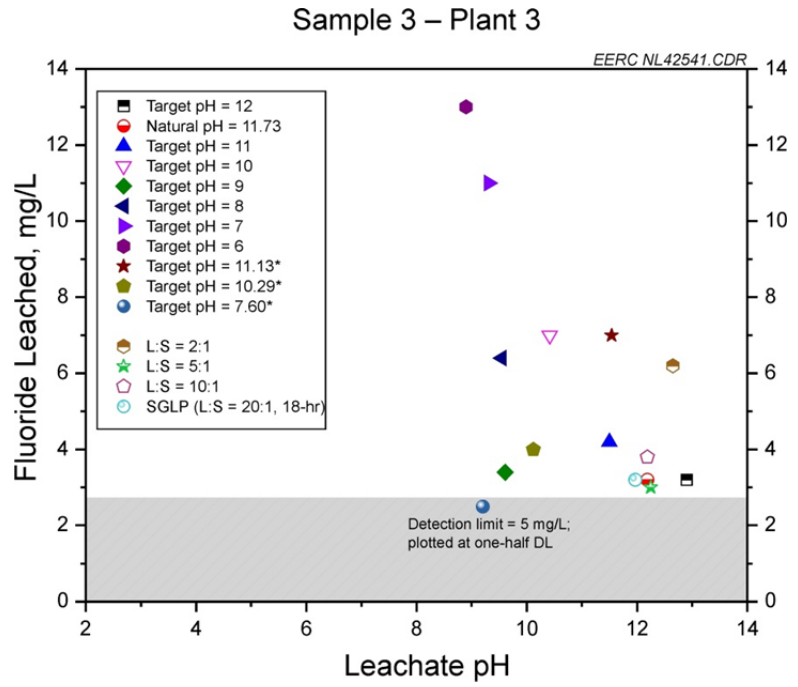

Figure A11-3. Fluoride leached from Sample 3 – Plant 3. The data point at target pH 7.60 had a higher detection limit than other leachates in the data set.

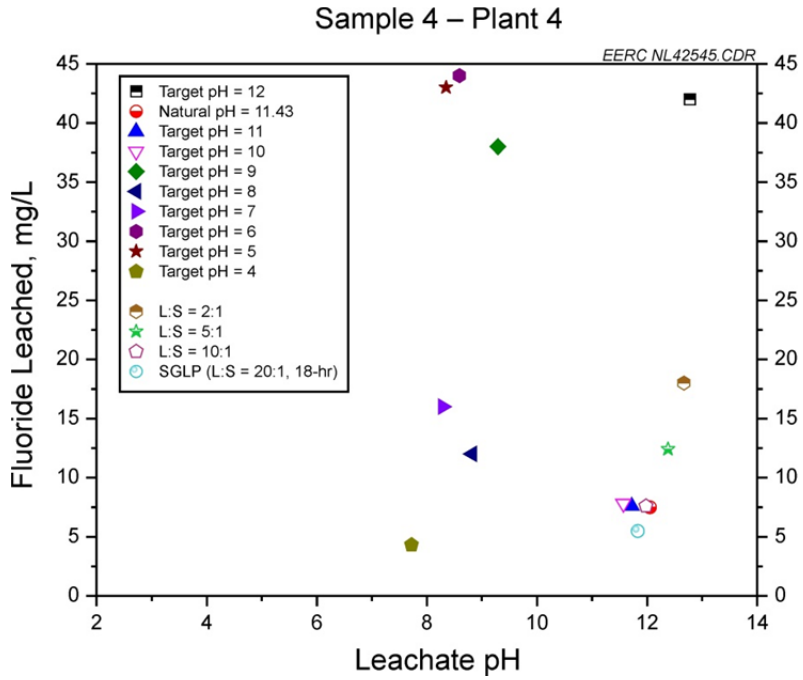

Figure A11-4. Fluoride leached from Sample 4 – Plant 4.

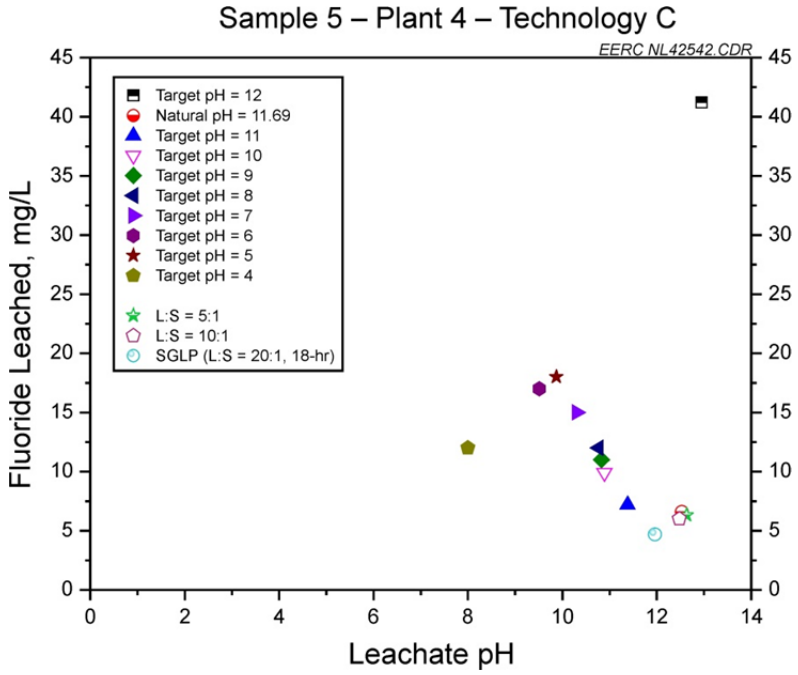

Figure A11-5. Fluoride leached from Sample 5 – Plant 4 – Technology C.

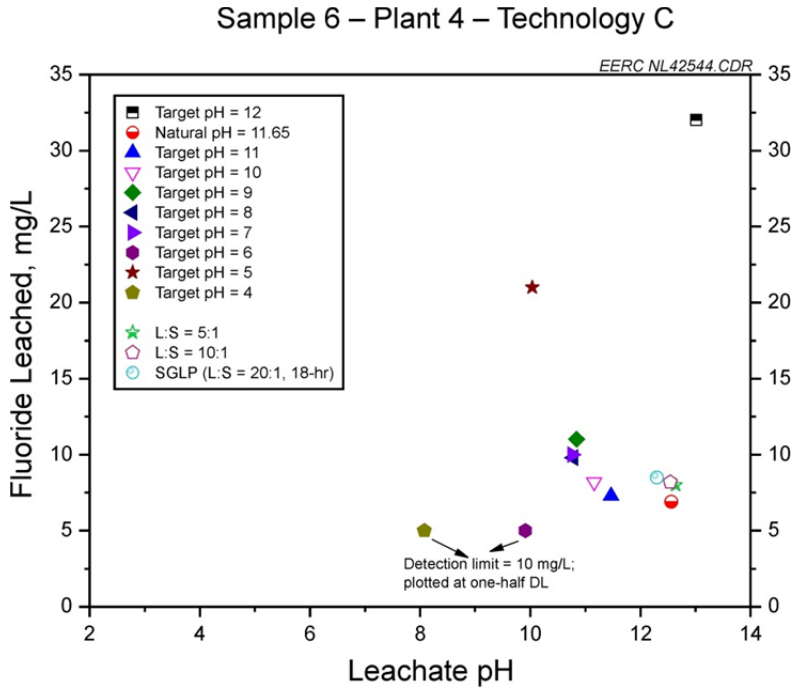

Figure A11-6. Fluoride leached from Sample 6 – Plant 4 – Technology C. The data points at target pH 4 and 6 had a higher detection limit than other leachates in the data set.

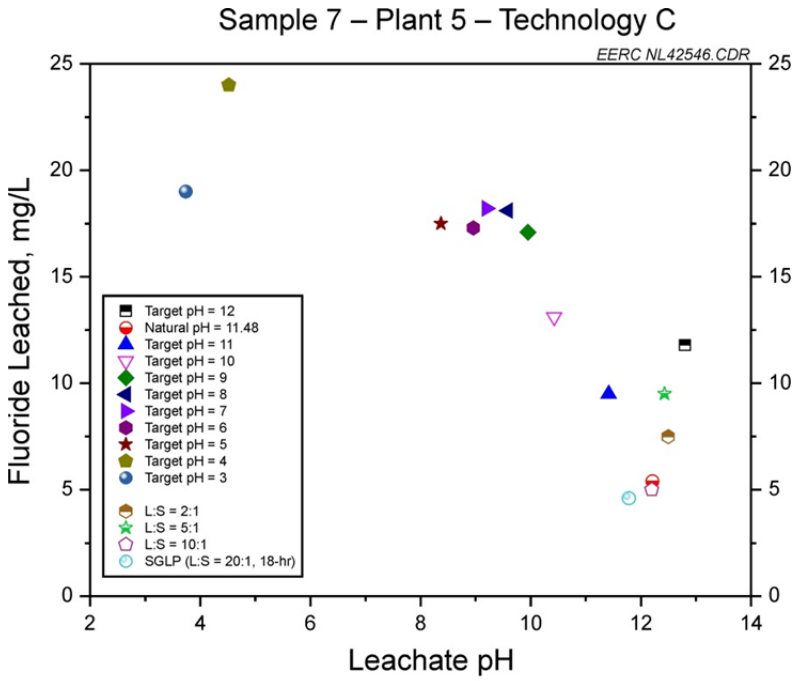

Figure A11-7. Fluoride leached from Sample 7 – Plant 5 – Technology C.

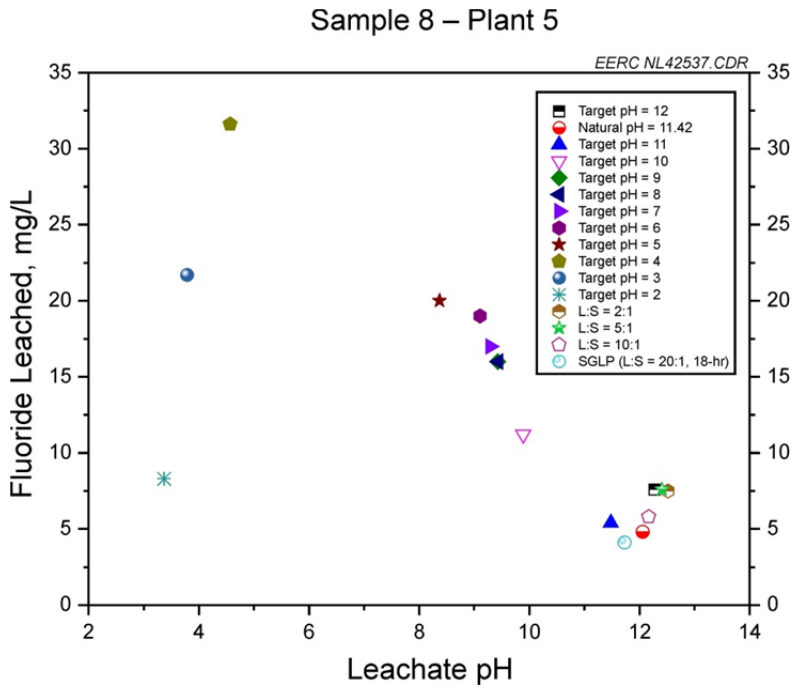

Figure A11-8. Fluoride leached from Sample 8 – Plant 5.

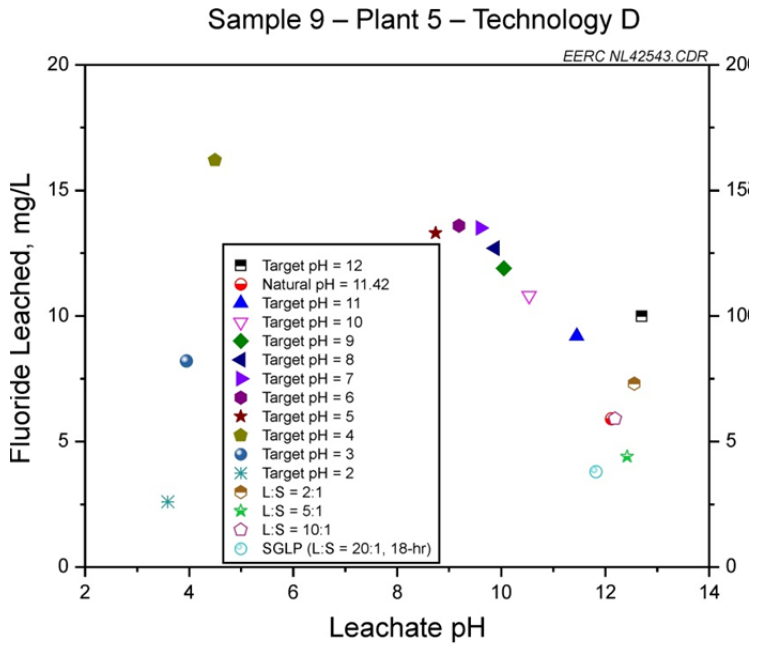

Figure A11-9. Fluoride leached from Sample 9 – Plant 5 – Technology D.

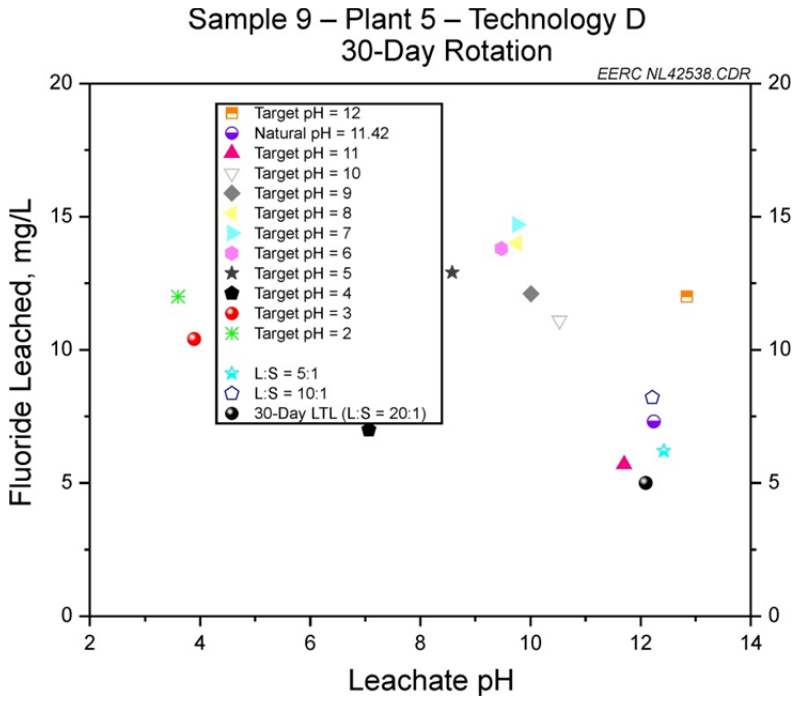

Figure A11-10. Fluoride leached from Sample 9 – Plant 5 – Technology D – 30-day extension of all leaching tests.

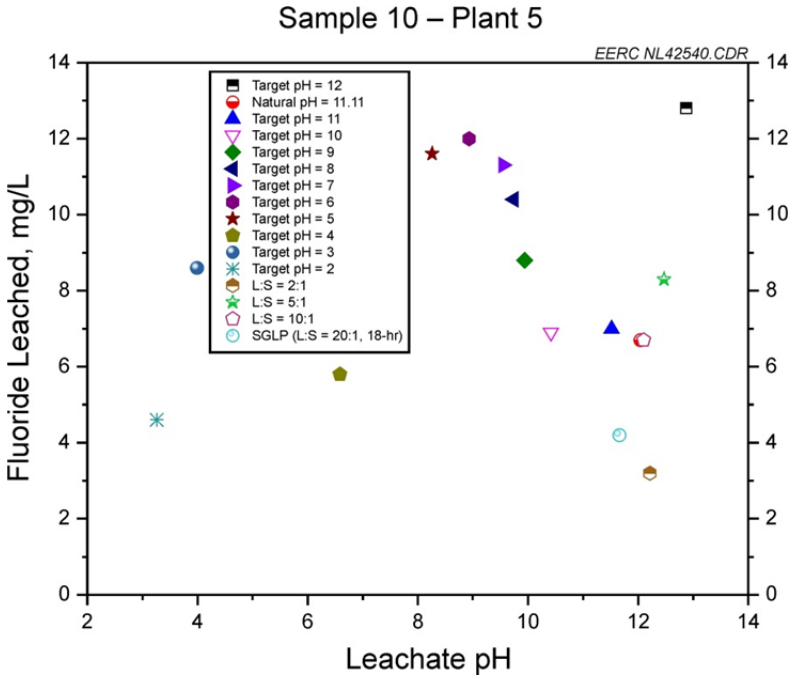

Figure A11-11. Fluoride leached from Sample 10 – Plant 5.